Coupling quantum dot circuits to microwave cavities

Matthieu Delbecq

ÉCOLE NORMALE SUPÉRIEURE

Département de Physique

THÈSE de DOCTORAT de L'UNIVERSITÉ PARIS VI

Spécialité : Physique Quantique

présentée par

Matthieu DELBECQ

Pour obtenir le titre de
DOCTEUR de l'UNIVERSITÉ PARIS VI

Sujet de la thèse :

COUPLING QUANTUM DOT CIRCUITS TO MICROWAVE CAVITIES

Soutenue le 17 septembre 2012 devant le jury composé de :

M.	Christopher BAUERLE	Rapporteur
M.	Andreas WALLRAFF	Rapporteur
M.	Markus BÜTTIKER	Examinateur
M.	Pascal SIMON	Examinateur
M.	Jean-Michel RAIMOND	Examinateur
M.	Takis KONTOS	Directeur de thèse

Contents

Acronyms

2DEG	Two-dimensional electron gas
AC	Alternative current
AFM	Atomic force microscope
CNT	Carbon nanotube
CPW	Coplanar waveguide
CVD	Chemical vapour deposition
DC	Direct current
EM	Electromagnetic
IF	Intermediate frequency
IPA	Isopropanol
LO	Local oscillator
MIBK	Methyl-iso-butyl ketone
PMMA	Poly methyl methacrylate
QD	Quantum dot
QED	Quantum electrodynamics
CQED	Cavity quantum electrodynamics
cQED	circuit quantum electrodynamics
RF	Radio frequency
SEM	Scanning electron microscope
SWNT	Single wall carbon nanotube
TLS	Two-level system

Notations

k or k_B	Boltzmann constant. Usually written k unless confusion is possible with an index
g or λ	Electron-photon coupling
V_g	Gate voltage
V_{sd}	Source-drain or bias voltage
V_{AC}	High frequency voltage, associated to the resonator voltage

Introduction

In the last years, two particular fields of mesoscopic physics have been developed and studied independently. These are circuit quantum electrodynamics (cQED) and quantum dots (QD) devices. The former is a solid state implementation of cavity quantum electrodynamics (CQED) which studies the light matter interaction at its most elementary level, down to single atom and photon [1]. The dipole interaction between the atom and the photon field induces entanglement between the two systems. This entangled state, which constitutes one of the most intriguing aspect of quantum mechanics, is in principle controllable by adjustment of either the atom or photon field properties. Increase of the coupling strength between the two involved systems is achieved by confining the photon field inside a high finesse cavity, leading to the so-called Cavity QED (CQED). A scheme of such optical CQED experiment [2] is presented in figure 1.

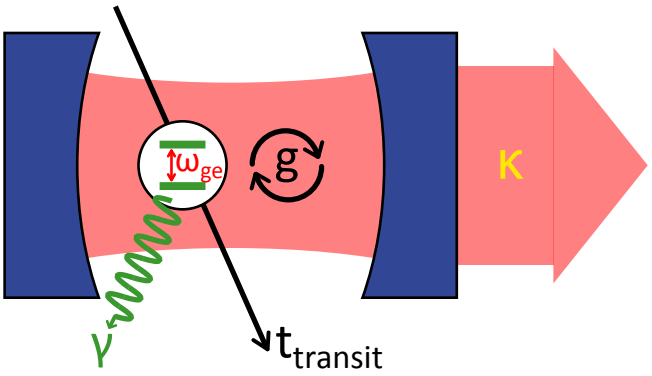

FIGURE 1: Scheme of an optical CQED experiment. An optical field single mode is formed inside a laser driven cavity with damping rate κ. Atoms fall inside the cavity during a transit time $t_{transit}$ and interacts with the cavity mode with a coupling strength g. The excited state of the atomic system has a decay rate γ.

A laser drives an optical cavity while atoms are sent into the cavity. The atom, which can be seen as a two-level system (TLS) is coupled to the cavity photon field by a coupling strength g. The presence of the atom in the cavity induces a modification of the electromagnetic (EM) mode. This change is monitored via the field transmitted out of the cavity. In this situation, the state of the atom is determined by the modifications of

the optical field. It can also be performed the other way round, as detecting the state of the outgoing atom can give information on the photon state inside the cavity[3].

Recently, CQED experiments have found a new playground with on-chip electrical circuits, leading to circuit QED (cQED) [4]. The optical 3D cavity and atom are respectively replaced by coplanar waveguide (CPW) resonator in the microwave range (∼GHz) and superconducting circuits behaving as artificial atoms as depicted in figure 2. The pioneer work in this field has been performed at Yale in 2004 [5] and has opened a new field of investigation in condensed matter and mesoscopic physics. The generated keen interest of cQED comes from the relatively small size of the resonator (of the order of 1cm) and the possibility to scale up the devices with many artificial atoms. These systems allow to play with the most uncanny aspects of quantum mechanics [6, 7], but also offer a practical way to perform quantum computing [4, 8, 9]. Today, this architecture is seen as one of the most promising to produce the highly desired quantum computer.

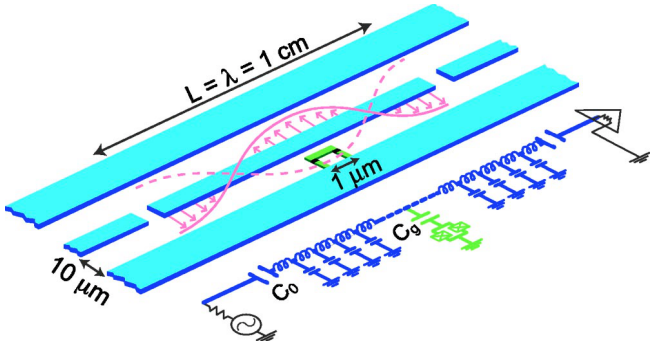

FIGURE 2: Scheme of a cQED device. The superconducting coplanar waveguide resonator is represented in blue. It consists of a transmission line cut at two ends which creates the confined mode of the EM field (in pink), in regard with the ground plane. A superconducting circuit behaving as an artificial atom is placed in the gap of the resonator, at an anti-node of the electric field. The typical characteristic length of such device are labelled on the structure. The equivalent lumped element description of the device is depicted as well. This figure is taken from [4].

The objective of this thesis is to replace the superconducting circuit behaving as artificial TLS by a QD device, in a cQED architecture. QD studies started in the late 80's [10, 11], and have undergone a vivid development thanks to progress in nanofabrication techniques. They are made of confined electronic islands where strong electronic interactions occur, and as such, can be seen as complex artificial atoms. Contrarily to atoms, the properties of QD's discrete spectrum are tunable in-situ via external parameters applied by local electrodes. By monitoring the current passing through such structures, one can have access to the spectroscopy and microscopic aspect of this complex electronic system. Such studies have been extensively carried out since the mid 90's, primarily

in two-dimension electronic gases (2DEG) [12]. Different new host materials have been developed, such as carbon nanotubes (CNT) [13] or single molecules like $C60$ fullerenes [14]. The strong electronic interactions of QD systems gives rise to an intrinsic wealth of behaviour that explains the wide success that they have met since their first studies.

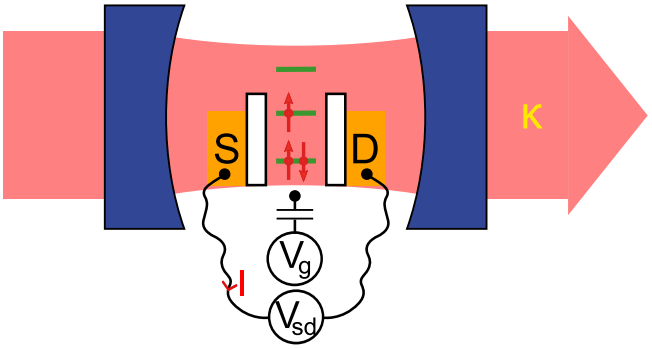

FIGURE 3: Scheme of a CQED experiment with QD devices inside the cavity. The quantum dot is represented by its intrinsic discrete energy levels (in green) coupled to source and drain electrodes (in orange) by tunnel barriers. Current can passe through the QD when a finite bias voltage is applied between the source and drain electrodes. Similarly, the electronic levels energies can be adjusted by tuning the potential of a gate electrode. The transmitted EM field of the cavity is affected both in amplitude and phase by the state of the QD.

Interestingly, most studies have focused on the DC behaviour of QD devices. The merge of such systems with cQED architectures, as depicted in figure 3, would give a tool to probe the strong electronic interactions at higher frequencies. In particular, the quantum capacitance of the quantum dot, which is not accessible by conventional transport measurement, is directly read out via the dispersive shift of the cavity. The applications of such hybrid device mixing cQED with QD are twofold. On the one hand, it offers a new device to perform quantum computation (CNT based spin qbit coupled to microwave cavity for example [15]). On the other hand it offers a playground to simulate on-chip condensed matter situations where electronic degrees of freedom are coupled to a bosonic bath. In both cases, the cavity can play the role of a quantum bus to couple distant QDs.

In this thesis, the material that has been chosen to make QD is the single wall carbon nanotube (SWNT). The versatility of SWNT QD devices makes them particularly good candidates for leading to both quantum computation and purely condensed matter experiments. Indeed, these devices allow to easily reach the three transport regimes available in QDs : Fabry-Perot [16], Coulomb blockade [17, 18] and Kondo [19]. Furthermore, different kind of electrodes can be used to form hybrid devices, extending the range of applications of SWNT QDs. For example, they can be contacted with superconducting electrodes to create Cooper pair splitters [20, 21], with ferromagnetic electrodes for spintronic purposes [22–24] or for making spin qbits [15]. It should be noted that

simultaneously to the work that is presented in this manuscript, other groups have been working on similar hybrid device architecture, with 2DEG QDs [25, 26], with InAs nanowire [27], or with lumped element resonator and SWNT double QD [28]. This shows the growing interest for such hybrid devices in the mesoscopic community.

The implementation of SWNT QD inside superconducting coplanar resonator meets major nanofabrication challenges. First of all, superconductivity, especially at finite frequency, and SWNT growth by CVD are rather incompatible. Furthermore, compared to cQED with superconducting circuits that are fully designed by lithography, SWNT processes require a lot of post selection. However, this last point is compensated by the much smaller size of SWNT QD ($\sim 1\mu$m) compared to standard superconducting qbits like transmon ($\sim 100\mu$m [29]). This allows a priori for contacting more QDs in a single cavity.

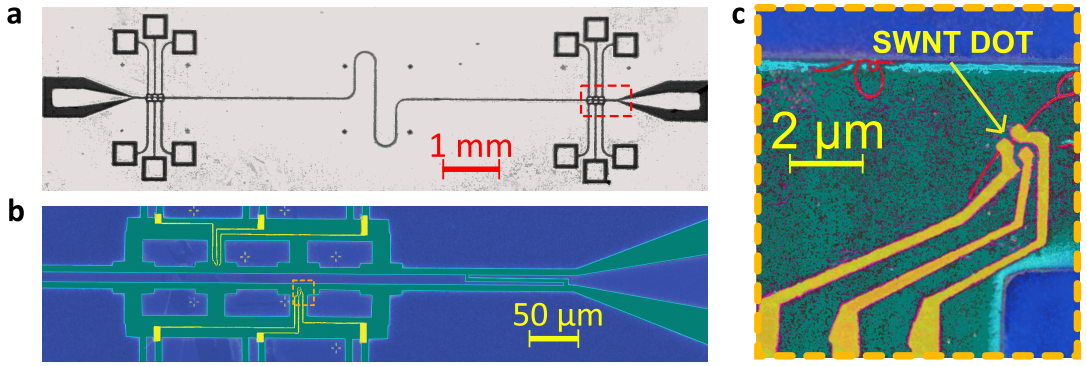

FIGURE 4: **a :** photograph of a CPW resonator in Nb/Pt or Al. **b :** optical micrograph close up in false colors of the ground plane openings where the SWNT QDs are contacted. The superconductor is in blue and the dielectric in green. **c :** SEM micrograph in false colors of the contacted QD with source, drain and gate electrodes. The blue represent the superconductor (transmission line and ground plane), the yellow is for the Pd electrodes, the SWNT is in red and the dielectric in green.

The samples made in this thesis all share the same typical pattern shown in figure 4. The centimetric superconducting CPW resonator is presented in figure 4 (a). It consists of a meander transmission line facing a ground plane. The left and right pads consist of the RF pads that connect the resonator to the external drive and read-out lines. 4 sets of 3 DC lines with their contacting pads are also visible, allowing to connect and measure up to 4 QDs inside one single cavity. These QD devices lie in the 5 μm gap of the resonator, as shown in figure 4 (c). SWNT are grown by chemical vapour deposition. Post selected tubes (considering their orientation relative to the transmission line as well as their thickness) are contacted in the standard 3 electrodes geometry : source, drain and gate electrodes, similarly to single electron transistors [30, 31]. Here the contacting metal is

palladium (Pd), which is a normal metal offering good contact to the SWNT. It is thus straightforward to make similar samples with different kind of electrodes, ferromagnetic or superconducting as mentioned above. This constitutes a substantial advantage for exploring a wide variety of physics situations with only one device pattern.

The experimental results that have been obtained in this thesis concern normal metal to SWNT hybrid structures, coupled to microwave resonators. The first objective was to investigate the coupling between the two systems and to probe afterwards with the microwave field the strong electronic interactions taking place in QDs. The first sample giving results was generous enough to provide both, as shown in figure 5 [32]. The DC spectroscopy (differential conductance) of figure 5 (a) exhibits Coulomb diamonds in the gate voltage V_G bias voltage V_{sd} plane. Kondo effect is also observable, as the zero bias bright line in the middle of a Coulomb diamond is a clear signature of such a phenomenon. The rich physics of the Kondo effect in QDs [33] constitutes the epitome of electronic interactions. Indeed, this effect arises due to many body interactions, and as such has become a breeding ground for both theoretical developments and experimental investigations.

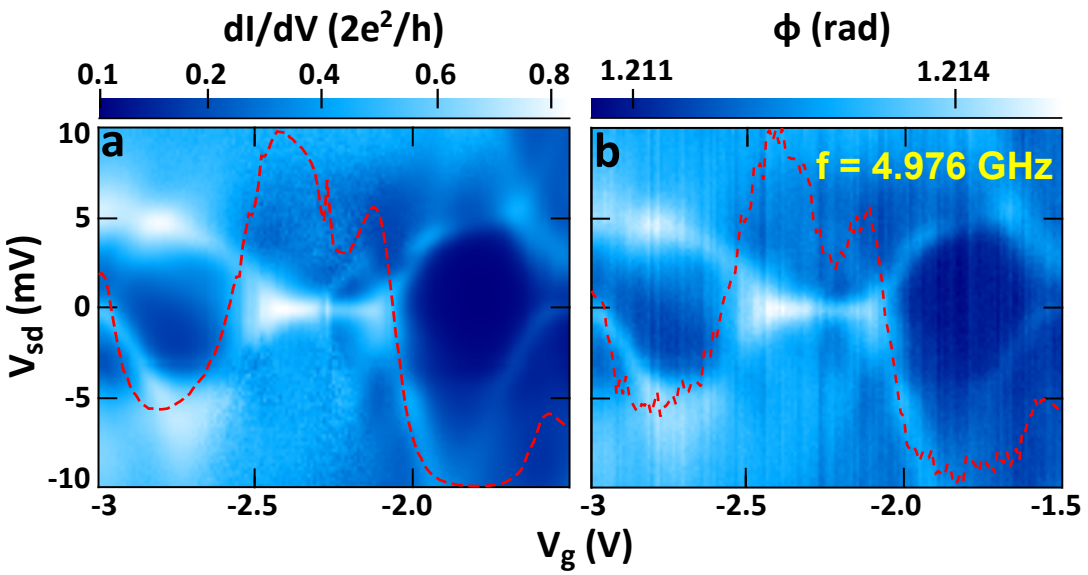

FIGURE 5: **a :** Color scale plot of the differential conductance of the SWNT QD *NTRES33bZ4D* in units of $2e^2/h$ in the gate/bias voltages plane. Three Coulomb diamonds are visible and a Kondo ridge at zero bias is observed in the middle diamond. **b :** Color scale plot of the phase of the microwave field transmitted through the cavity at $f = 4.976$GHz taken simultaneously with (**a**). In both plots, the dashed red line is a cut at zero bias. From the phase signal, the electron-photon coupling strength is estimated to be $g \sim 100$MHz (see details in chapter 4).

Simultaneously to the low frequency measurements, the phase of the RF signal transmitted through the cavity is measured, as showed in figure 5 (b). The RF phase spectroscopy

strikingly shows the same behaviour as the standard low frequency spectroscopy, indicating that the cavity is well coupled to the QD. One could argue that the phase spectroscopy is redundant with the differential conductance as in the RF SET setup [34]. But contrarily to the latter setup where the SET is galvanically coupled to a lumped element resonator, the SWNT QD here is capacitively coupled to the CPW resonator. The information acquired in the phase is thus directly related to the QD quantum capacitance, giving therefore insights on the interactions taking place in the system, at GHz frequency. It was especially found that the quantum capacitance does not drop on the Kondo ridge contrarily to what was commonly expected [35].

The coupling g between the cavity and the QD can be estimated from such measurements. However, a more straightforward way to observe and determine g is achieved by studying the QD levels evolution with the number of photons in the cavity. This AC-Stark shift-like experiment is presented in figure 6 for a Fabry-Perot QD (a) and a Coulomb blockaded QD (b). The electronic levels of the QDs split in a funnel shaped pattern. This indicates a direct coupling of the cavity mode to the QD levels, similarly to what is observed in standard cQED, even though the microwave power involved here is much higher [29].

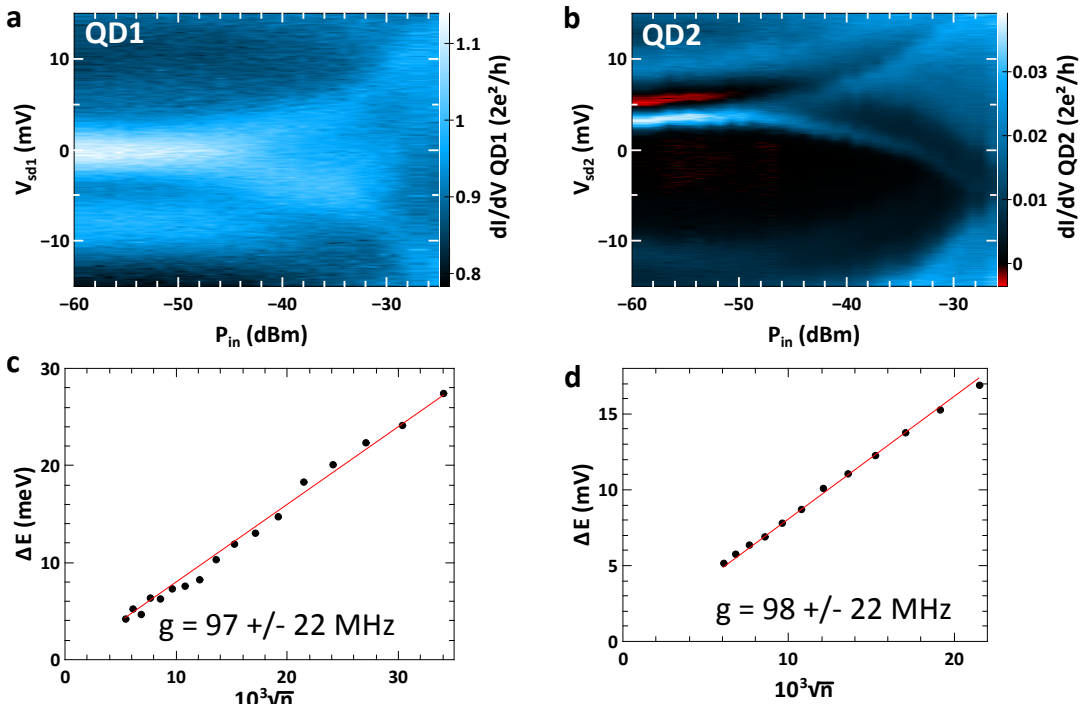

FIGURE 6: Energy level splitting versus power at the input port of the microwave cavity for a Fabry-Perot QD (**a**) and a Coulomb blockade QD (**b**). The color code is the differential conductance of the measured QD. **c** and **d :** Energy level spacing respectively taken from (a) and (b), plotted versus the square root of the mean number of photons in the cavity. The linear dependence fit of the data (in red) gives the coupling parameter g as its slope.

The spacing ΔE between the split levels behaves as $\Delta E = 2g\sqrt{\bar{n}}$ (see figure 6 (c) and (d)). Therefore, this measurement is a direct read-out of the coupling g, found to be of about 100MHz for all the devices that have been studied. This measurement is consistent with the estimations that have been done in the case of the Kondo QD [32]. Furthermore, this rather high value is comparable to the couplings observed in standard cQED [4]. It indicates that the strong coupling regime is achievable for such devices as it requires $g > [\kappa, \gamma]$, with κ and γ the decoherence rates of the cavity mode and the "atomic" system (see figure 1). Reaching this regime is necessary to perform coherent manipulations of the atom-photon coupled system. Therefore, the results obtained in this thesis pave the way to cQED manipulation of QD devices, especially awaited for the spin qbits architecture [15]. The experimental setup of this thesis is however not suitable for reaching the quantum limit for cavity photons, hence coherent manipulation. Nevertheless, it allows to explore other aspects of this rich architecture.

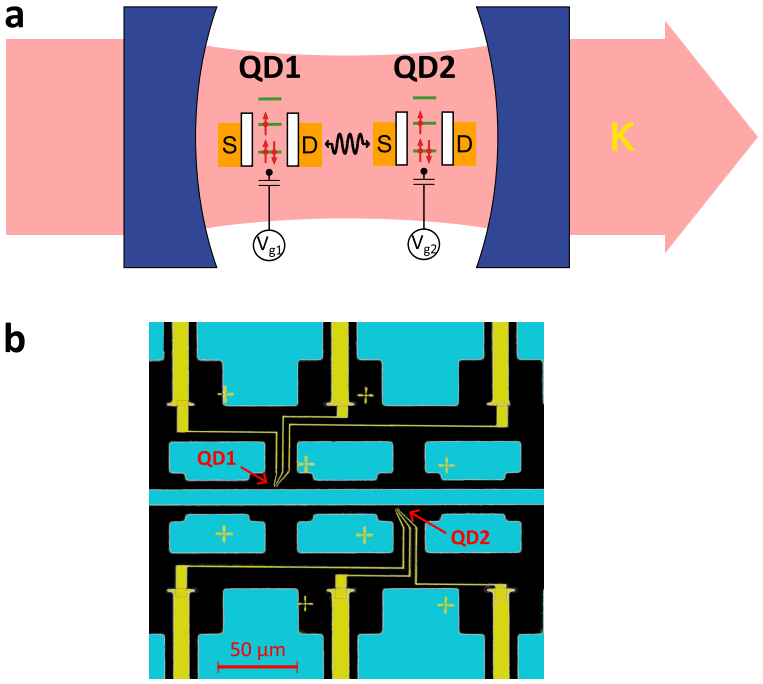

FIGURE 7: **a :** Scheme of two separate QDs interacting inside a microwave cavity. Both QDs are independently tuned and interact with the cavity mode. A distant interaction between the QDs can be mediated via the cavity photons. **b :** Optical micrograph in false colors of a device showing 2 QDs (yellow electrodes) embedded inside the same CPW superconducting resonator (in blue). The 2 QDs share the same anti-node of the electric field and are separated by about 80μm.

As shown by the photograph of figure 4 (a), the devices have been designed from the beginning to host up to 4 QDs. The interaction between multiple controlled electronic systems in a microwave cavity pushes a step further the applications of such hybrid devices. It is fundamental for quantum computation perspectives where, among other

things, several qbits are needed to perform gate operations [36, 37]. It also constitutes an effective on-chip quantum simulator of condensed matter situations. Figure 7 (a) presents a scheme depicting a cQED experiment with two QDs. As both QDs are coupled to the microwave field, they should also interact via cavity photons. The concept of photons is used for commodity here, like phonons in condensed matter. The field is indeed classical. Once again, the independent tunability and standard low frequency measurements of each QD will reveal itself a crucial aspect of the setup to decipher the mechanisms involved in this coupling at distance.
The experimental realization of 2 QDs cQED device is shown in figure 7 (b). Two SWNT QDs are embedded inside a superconducting CPW resonator, separated by about 80 μm. Even tough they share the same anti-node of the electric field, they are separated by roughly 200 times their own characteristic lengths. It must be emphasized that the two QDs are made of two different SWNTs, both being contacted independently. As such, contrarily to double QD devices, they should be considered as independent systems in the absence of cavity. The most direct and intuitive way to probe the distant interaction between the two QDs is by independently tuning their respective gates and monitor the differential conductance of each. Figure 8 (a) shows such a spectroscopy for one of the two QDs of the device. The electronic levels of this QD exhibit non trivial behaviours as they encounter crossings and anticrossings when driving the gate of the other QD. This allows to assess that the interaction between the two QDs is not a direct crosstalk as every energy level would behave similarly in this case. It can be shown that the slope of QD2 levels is the signature of the distant interaction between the two QDs, and more precisely is explained by a polaronic shift. Such a model, taking into account both the polaronic shift and the levels splitting is presented in figure 8 (b). Most of the spectroscopic features observed in (a) are reproduced, indicating that the mechanisms involved are understood.

This general introduction addressed the main ideas and challenges that have been treated in this thesis. The main results have been presented as well in order to beckon the interested reader to go further into the technical details discussed in the main text. It is divided in six chapters :
In chapter 1, the two different “tools” used in this thesis are introduced. They consist of SWNT QDs and microwave CPW resonator. They respectively can be thought of being an electron box and a photon box. The basic knowledge necessary to understand the present work are addressed. In particular, the three different electronic transport regimes observable in SWNT QDs. For the microwave resonator part, the discussion will focus on the lumped element description as it is essential for latter understanding of the coupling between the QD and the cavity.

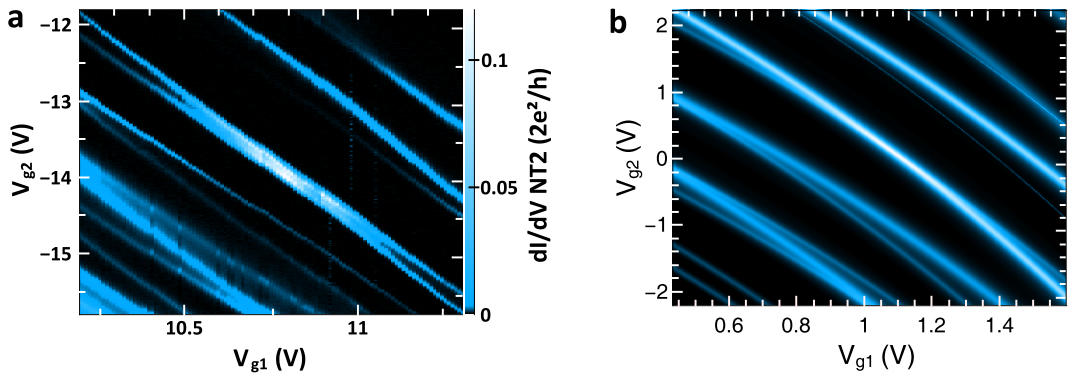

FIGURE 8: **a :** Differential conductance spectroscopy of one of the two QDs embedded inside the microwave cavity. The measurement is performed versus the independent gate voltages of each QD, V_{g1} and V_{g2}. QD2 levels undergo a slope versus V_{g1} and crossing levels are visible as well. **b :** Modelling of (a), using the theoretical model developed in chapter 5.

In chapter 2, a brief theoretical description of the AC response, which probes the quantum capacitance of QDs, is addressed. In the first place, the discussion will focus on the non-interacting case, corresponding to the Fabry-Perot regime. In this situation, the Landauer-Büttiker formalism and scattering theory is used. In the second part, the interacting case of Coulomb blockade is treated. It relies there on the equation of motion (EOM) of the Green function treatment. Although it allows for treating the Coulomb blockade regime precisely, it cannot treat the Kondo effect.

In chapter 3, the experimental realization of the experiment is developed. In a first part, the nanofabrication and clean room processes to make the device are detailed. In a second part, the measurement setup is described with details.

In chapter 4, the coupling of the QD to the cavity is discussed. The nature and strength of the coupling will be addressed. The three different transport regimes (Fabry-Perot, Coulomb blockade and Kondo) are studied. The Kondo situation is particularly investigated, as the measurement of the quantum capacitance of the QD in this regime is particularly new.

In chapter 5, the distant interaction between QDs circuits is discussed. The photon mediated interaction between the two artificial atoms is several orders of magnitude higher than what could be expected from direct coupling. The origin of the distant coupling, relying on polaronic shifts, will be discussed in details.

In chapter 6, preliminary results about quantum capacitance in the out of equilibrium regime are presented. Although incomplete, these show a peculiar behaviour that needs further study.

Chapter 1

Electron box and photon box

The purpose of this chapter is to briefly present the basic concepts of both SWNT electronic transport and CPW resonator properties. These two systems are the two tools that we will use to probe the physics of electron-photon coupling in stronlgy correlated electronic systems. They have been independently extensively studied. Works on electronic transport through quantum dot (QD) structures started in the mid 90's with two-dimensional electronic gases (2DEG) quantum dot [38]. QD devices consist of model systems to probe mesoscopic physics where quantum effects become dominant for electronic transport. Thanks to their tunability, these systems are ideally suited to confront theory and experiments. It is thus relatively easy to test theoretical results with experiments. Various transport regime can be observed in these systems. Fabry-Perot (2DEG [39], CNT [16]) where electronic interactions are neglected but correction to current is due to quantum interferences, Coulomb blockade (2DEG [38], CNT [17, 18]) where electronic interactions dominate transport and Kondo physics (2DEG [40], CNT [19]) where many-body interactions emerge.

Superconducting CPW resonators have been developed and studied for resonant detection since the mid 90's [41][1]. However, it is relatively recently that the quantum limit has been reached. The field of quantum electrodynamics (QED) was boosted by the possibility to perform quantum computing. Cavity QED (CQED) was first developed with Rydberg atoms and optical cavities [3]. The need for small and possible scalable devices lead to the development of circuit QED (cQED) where superconducting two-level systems (TLS) are embedded in CPW resonator. The first notable step in this way was done at Yale in 2004 [5] where the strong coupling regime between a single microwave photon and a TLS was observed. In this thesis, the dispersive read-out technique offered by such device is used to probe new dynamical aspects of CNT QDs.

[1]The principle of resonant detection has a wide range of applications in various field, as for atomic force microscope (AFM) or electron spin resonance (ESR) for example.

1.1 Electronic transport through carbon nanotube quantum dots

Mesoscopic physics was first developed on the study of low dimensionality disordered medium at low temperature where weak localization occurs for example. Quantum corrections to classical transport laws become relevant in such systems. Thanks to the arrival of nanostructures such as 2DEGs or CNTs, a second generation of mesoscopic systems could be studied which offers the tunability. Classical laws of transport as Ohm's law or Drude's model of a diffusive conductor do not apply. Indeed, at these scales, the phase coherence of electrons cannot be neglected. This introduces dominant quantum contribution to the conduction of the device, due to electronic interferences.

1.1.1 Characteristic lengths of CNT QDs

A carbon nanotube is a nanostructure characterized by its diameter and its length. The former is of the order of one nanometer for a single wall carbon nanotube (SWNT) which are the nanostructures that we will study in this thesis. The comparison to the Fermi wavelength of SWNT electrons ($\lambda_F \sim 0.74$nm for an armchair CNT, see [42]) justifies the one dimensional character of CNTs. The two other relevant lengths are the mean free path l_m and the phase coherence length l_ϕ. As mentioned above, l_ϕ is to be compared to the length of the nanostructure L to assess its mesoscopic behaviour. It represents the length over which the electron is coherent and is thus subject to electronic interferences. Quantum effects are observed when $L \leq l_\phi$ at low temperature, which is easily accessible in CNT as their phase coherence length is of the order of few microns. The mean free path characterizes the distance between two elastic collisions. These do not affect the phase coherence, hence the mesoscopic behaviour of the conductor. The comparison of the mean free path to the length of the conductor gives two kinds of transport regimes. When $l_m < L$, the conductor is diffusive and when $L < l_m$, it is ballistic. Diffusive mesoscopic conductors lead to correction of the conductance such as Aharonov-Bohm ring experiment [43]. For QDs systems, the quantum effects are dominant as the correction to the conductance is inversely proportional to the number of conduction channel $\delta G \propto G_0/N$. It becomes particularly important in the case of CNTs that only have 4 conduction channels.

1.1.2 Energy scales

Electronic properties and transport of QD devices result from the interplay between several energy scales. The confinement of the system gives rise to a discrete particle

spectrum. For CNT, already confined in two directions, this can be obtained by contacting the CNT with electrical contacts along the 1D direction on a length $L < l_\phi$ [17, 18]. The resulting level spacing Δ is directly given by the interference condition $\Delta = hv_F/L$. This is referred as the orbital energy of the QD in reference to atomic orbitals. Indeed, this energy quantization gives QDs the behaviour of artificial atoms. The charging energy E_C is the second important energy scale of QDs. It is related to electronic interactions due to Coulomb interaction and represents the energy cost to add an electron on the electronic island that is the QD. Geometrical capacitances of the device characterize the charging energy as $E_C \sim e^2/C$. The third important energy in these systems is the energy level broadening Γ due to the coupling to the leads. It is related to the overlapping of electronic bands of the leads and the quantum dot spectrum. It is also directly related to the transmission rate $\Gamma/\hbar$, thus the transparency of the tunnel barriers that couple the QD to the leads. The last energy scale involved is temperature T. The level separation and electronic interactions can only be observed if kT is lower than Δ or E_C. It is thus remarkable that QD devices allow for such studies with temperature reachable in the lab. For 2DEG QDs, the energies involved require dilution fridge temperature range (T ∼20 mK) while for CNT QDs, a simple ^{4}He refrigerator (T ∼ 1.4 - 4.2K) is enough to observe the emergence of the quantum world.

The interplay between these different energy scales gives rise to a rich set of various transport regimes [44]. The typical energies that we observe in our CNT QDs are $\Delta \sim$ 5 meV (L ≈ 500 nm, $v_F \approx 8.10^5 \text{m.s}^{-1}$), $E_C \leq 10$ meV, $\Gamma \lesssim 1$ meV. The temperature is an extrinsic parameter, which in the case of this thesis is 1.5K, corresponding to kT ≈ 130μeV.

1.1.3 From two-level system to complex artificial atoms

cQED was developed for coupling of a TLS to a microwave cavity in order to reproduce in condensed matter what had already been done in atomic physics and CQED. The TLS behaviour of the superconducting circuit allows for qbit operations, hence quantum computation[2]. QD devices, by the natural quantization of their energy levels, can also behave as TLS. More importantly, they present a rich spectrum similar to atoms, which parameters such as interactions, spin degree of freedom [22] or orbital degree of freedom [46] can be controlled in situ via external parameter like voltage sources or magnetic field. Therefore, the combination of cQED techniques with the manipulation of these complex artificial atoms offer the possibility to simulate on-chip the light-matter interaction.

[2]Superconducting circuit acting as TLS qbit rely on Josephson junctions circuits, like in the flux qbit [45] or transmon qbit [29]. The TLS behaviour is obtained thanks to the non-linearity of the Josephson inductance.

1.1.4 Three different transport regimes

In this subsection, the basics concepts of the three different transport regimes that have been studied in this thesis are addressed. First, two regimes are separated by the presence or not of electronic interactions. This gives the limit between coherent transport and Coulomb blockaded transport. The former arises when the transmission Γ from lead to QD is high and the charging energy E_C is much smaller than all other energies involved in the following sequence $E_C \ll kT \ll \Gamma \lesssim \Delta$. On the other hand, Coulomb blockade regime appears when the charging energy becomes dominant over Γ and kT in the following sequence Γ, $kT \ll E_C \lesssim \Delta$. An interesting way of viewing the separation between the two different regimes is given in [11] : to observe Coulomb blockade, thus discrete charges on the QD, the quantum fluctuations in the number of charges due to tunnelling events must be much smaller than one over the time scale of measurements. This can be translated in the Heisenberg uncertainty relation as $\Delta E \Delta t = (e^2/C)R_t C > h$, with, $R_t$the tunnel resistance of the barrier related to Γ. To observe discrete charge, R_t must be much larger than h/e^2 =25.8 kΩ in addition to $e^2/C \gg kT$.

A valuable property of SWNT QDs is that they offer the possibility to reach these different regimes. Semiconductor SWNTs push this even further as it is even possible to observe them in one sample by only varying the gate voltage electrode V_G as shown in figure 1.1. Both Γ and E_C are affected by the variation of V_G. The wave vector $\vec{k}$ is modified by the modification of the energy of the QD[3]. The transmission coefficient from one medium to another can be written $t_{12} = \frac{2\sqrt{k_1 k_2}}{k_1+k_2}$, which is directly related to Γ. The charging energy is also affected by a variation of V_G as it modifies the density of states/number of charges on the dot, hence the capacitance of the electronic island towards source and drain electrodes. Self consistent calculations ([48–50]) show a gradual decrease of E_C with increasing V_G, and an especially sharp dependence near the zero charge occupancy[4]. Semiconductor SWNTs present a gap with a really low density of states, thus a low capacitance in regard of the leads resulting in a high charging energy. This region is therefore suitable for observing Coulomb blockade regime. On the other hand, the high density of states available out of the gap leads to a small charging energy that can be overcome by kT and Γ, thus providing Fabry-Perot physics.

[3]The dispersion relation at low energy for a SWNT, near dirac points is given by [47] $E_k = \pm\sqrt{(hv_F k)^2 + \left(\frac{E_i^g}{2}\right)^2}$, with E_i^g the energy separation for each sub band.

[4]Such strong variation of E_C has been observed in QDs close to zero charge filling, see e.g. [38].

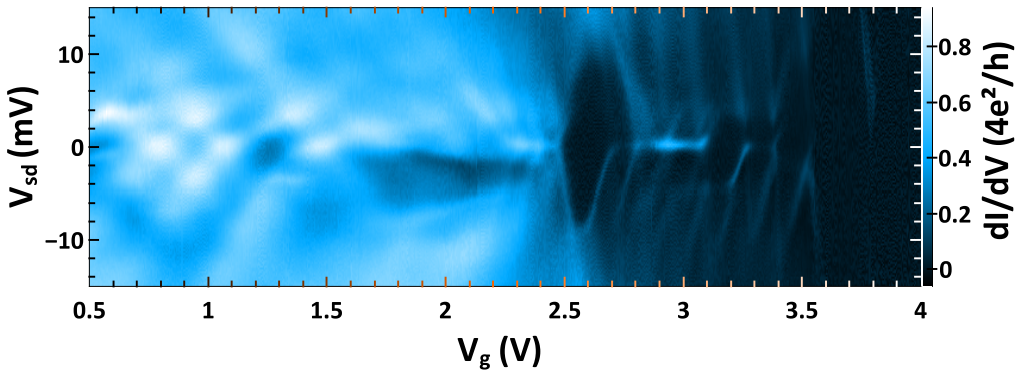

FIGURE 1.1: Semiconductor SWNT QD spectroscopy taken in the lab by T. Delattre. Fabry-Perot regime is observed at low gate voltage while Coulomb blockade regime is observed at higher gate voltage. In between appears a Kondo ridge, signature of many-body effect in the system.

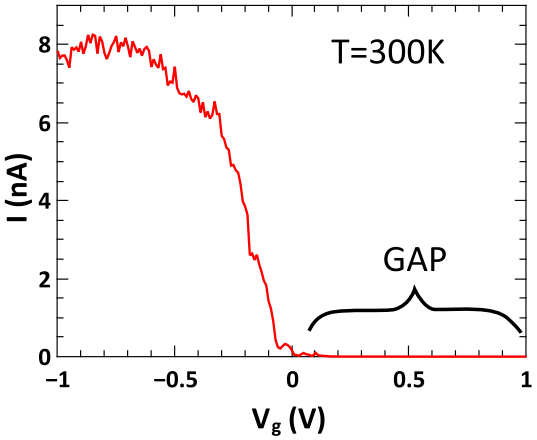

FIGURE 1.2: Semiconductor SWNT QD current versus gate voltage V_G taken at room temperature T=300K. A gap is observed for $V_G \geq 0$V. In this region, the electronic gas of the QD is depleted of charge carriers.

Fabry-Perot regime

The Fabry-Perot regime can be observed when the following hierarchy of energy is established in the system

$$E_C \ll kT \ll \Gamma \lesssim \Delta \tag{1.1}$$

which is represented in figure 1.3.

As already mentioned, in this regime, electronic interactions, being the smallest energy of the system are neglected. The problem reduces to quantum scattering by a coherent mesoscopic conductor. However, the finite temperature is crucial here to overcome interactions. In principle, at zero temperature, interactions are always present and can even dominate the transport in the system, as emphasized by the Kondo effect.

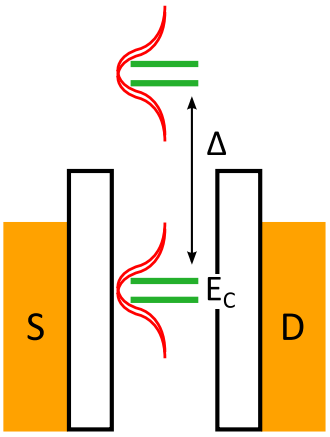

FIGURE 1.3: Scheme of the different energy scales involved the Fabry-Perot regime. Orbitals are separated by the level spacing Δ. The level broadening Γdue to the coupling of the QD to the leads is much larger than the charging energy and temperature.

Landauer-Büttiker formalism The Landauer-Büttiker approach of electronic transport for mesoscopic conductors is based on a scattering approach. It is particularly well suited to understand the transport in the Fabry-Perot regime. The transport properties are related to the scattering properties of the system, which are assumed to be known from a quantum-mechanical calculation. This methods applies to non-interacting systems in the stationary regime but it is possible to extend it to interacting systems in the case of finite frequency study (see [51, 52]). The strength of this theory is that the system may be either at equilibrium or in a non-equilibrium state, which is encoded via the Fermi-Dirac distribution of the contacts of the conductor. The trick developed by Büttiker is to consider the potential created by the island capacitance not as interactions but as a global constant potential that shift the energy of the QD.
Two reservoirs are connected by a mesoscopic conductor. These two reservoirs, labelled $\alpha = \mathrm{L}, \mathrm{R}$, are large enough so they can be described by degenerated Fermi gases from their Fermi-Dirac distribution at temperature T_α and chemical potential μ_α

$$f_\alpha(E) = \frac{1}{e^{\frac{E-\mu_\alpha}{kT_\alpha}} + 1} \tag{1.2}$$

Current through a single scatterer A quantum coherent, perfect, one-dimensional conductor of infinite length is considered. The density of state for spinless electrons of velocity v, per unit of length and energy is $g(E) = 2/(hv(E))$. The number of electrons passing through the conductor per unit of time and energy is thus $g(E) \times v(E)/2 = 1/h$. Under voltage polarization V, the resulting current through the system is then

$$I = e \times \frac{1}{h} \times (\mu_L - \mu_R) = \frac{e^2}{h} V \tag{1.3}$$

The conductance of such system is $G = I/V = e^2/h = G_0$ which is the conductance quantum $G_0 \approx 38.7\mu$ S$\approx 25.8\text{k}\Omega^{-1}$. The conductance of a quantum wire is thus the conductance quantum multiplied by the number of conduction channel. For SWNTs, the spin and valley degeneracies lead to a conductance $4G_0$.
The presence of a diffusive impurity on the conductor is now considered. The probability for an electron of energy E to pass through the impurity is $D(E)$. The Pauli exclusion principle is intrinsically taken into account in the problem via the Fermi distribution of the reservoirs that enclose the impurity. The probability for an electron from the left reservoir to pass through the impurity into the right reservoir is $D(E)f_L(E)(1-f_R(E))$ and reciprocally for an electron coming from the right. Thus the Landauer formula for the current through the impurity

$$\begin{aligned} I &= \frac{e}{h} \int \big(D(\epsilon) f_L(\epsilon)(1 - f_R(\epsilon)) - D(\epsilon) f_R(\epsilon)(1 - f_L(\epsilon)) \big) d\epsilon \\ &= \frac{e}{h} \int D(\epsilon)(f_L(\epsilon) - f_R(\epsilon)) d\epsilon \end{aligned} \tag{1.4}$$

When taking $D(E) = 1$, the result for a perfect conductor is recovered. The treatment of several impurities on the conductor is made easier by using a second quantization formalism, which is particularly useful for treating many body problems. This is enclosed in the scattering matrix formalism which offers a useful tool for multiple impurity problems.

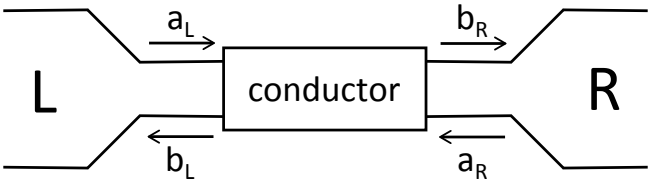

FIGURE 1.4: Two reservoirs L and R coupled by a mesoscopic conductor represented by its scattering matrix

As shown in figure 1.4, the scattering matrix S links the incoming waves function to the outgoing waves function (from the conductor point of view). These wave functions are here represented by creation and annihilation operators of electron with energy E, $a^\dagger(E)$ and $a(E)$ (resp. $b^\dagger(E)$ and $b(E)$) for incoming waves (resp. outgoing). The relation between all these operators is the following

$$\begin{pmatrix} b_L \\ b_R \end{pmatrix} = S \begin{pmatrix} a_L \\ a_R \end{pmatrix} \quad \text{with} \quad S = \begin{pmatrix} r & t' \\ t & r' \end{pmatrix} \tag{1.5}$$

In the case of multichannel transport, each creation and annihilation operator is in fact an array of N_α operators of the same type (considering that there are N_α channel for reservoir α), and the coefficient of the scattering matrix are block diagonal of dimension the number of channels. The coefficients r and r' describe electron reflection back to the left and right reservoirs, respectively, while the off-diagonal coefficients t and t' describe the transmission through the conductor. The unitarity of the S-matrix guarantees the current conservation. The current operator in lead α can be written within the second quantification formalism as [53]

$$\hat{I}_\alpha(t) = \frac{e}{h} \sum_n \int dE dE' (\hat{a}^\dagger_\alpha(E)\hat{a}_\alpha(E') - \hat{b}^\dagger_\alpha(E)\hat{b}_\alpha(E')) e^{(E-E')t/\hbar} \tag{1.6}$$

The multi terminal case will be studied in more details in chapter 2. Using equation 1.1.4 and some calculation steps (see Appendix **??**), the average current writes

$$\langle I_L \rangle = \frac{e}{h} \int Tr(s^\dagger_{RL}(E) s_{RL}(E))(f_L(E) - f_R(E)) dE \tag{1.7}$$

with s_{RL} the block matrix corresponding to $\hat{b}_L = s_{LL}\hat{a}_L + s_{RL}\hat{a}_R$. The average current in this situation expressed in terms of transmission coefficient as

$$\langle I_L \rangle = \frac{e}{h} \sum_n \int D_n(E)(f_L(E) - f_R(E)) dE \tag{1.8}$$

where the $D_n(E)$ are the eigenvalues of $s^\dagger_{RL}(E)s_{RL}(E)$. At zero temperature, the differential conductance of the system is thus

$$G_{diff} = \left. \frac{\partial \langle I_L \rangle}{\partial V} \right|_{V=0,T=0} = \frac{e^2}{h} \sum_n D_n \tag{1.9}$$

Electronic Fabry-Perot The SWNT QD is geometrically designed to behave as an electronic cavity. In the non-interacting regime where electrons are well represented by wave functions, the source and drain contacts can be thought as electronic mirrors.

These actually must be described as diffusive scatterers with transmission D, which is encoded in the following scattering matrix

$$s_\alpha = \begin{pmatrix} \sqrt{1-D_\alpha}e^{i\phi_\alpha} & -i\sqrt{D_\alpha} \\ -i\sqrt{D_\alpha} & \sqrt{1-D_\alpha}e^{-i\phi_\alpha} \end{pmatrix} \tag{1.10}$$

where α represent either the left or right contact and ϕ_α is the phase acquired by an electron during reflection. This matrix is unitary, as required by current conservation law. For the sake of simplicity, only one channel of conduction is considered. The two spin channels can be considered degenerate while the orbital channels should be treated independently. Indeed, defects in the atomic structure of the SWNT generate an finite coupling between the K and K' orbitals which are thus usually non-degenerate [54]. The SWNT is here described by a purely coherent conductor with no dissipation and only a propagation term

$$s_{SWNT} = \begin{pmatrix} 0 & e^{i\delta} \\ e^{i\delta} & 0 \end{pmatrix} \tag{1.11}$$

where δ is the classical phase acquired during propagation $\delta = kL = E/(\hbar v_F)L$. The calculation relies on the combination of these three scattering matrices. Unfortunately, this formalism does not allow for direct multiplication of matrices and one must either transform each matrix in a transfer matrix or simply solve the system. The calculation details are given in appendix A. The overall transmission coefficient of the system is found to be

$$s_{RL} = \frac{\sqrt{T_L T_R}e^{i\delta}}{1 - e^{i(2\delta-\phi_L-\phi_R)}\sqrt{(1-T_L)(1-T_R)}} \tag{1.12}$$

This expression shows a Fabry-Perot like behaviour with an interference condition being $2\delta - \phi_L - \phi_R = 2n\pi$. By developing near a resonance $\delta_n = n\pi + (\delta_L + \delta_R)/2$ with small transmissions T_α, the scattering matrix simply rewrites as

$$s_{\alpha\beta} = e^{i\frac{\phi_\alpha+\phi_\beta}{2}}\left(\delta_{\alpha\beta} - i\frac{\sqrt{\Gamma_\alpha\Gamma_\beta}}{\Delta E}\right) \tag{1.13}$$

with $\Delta E = E - E_n + i\Gamma/2$, $E - E_n = (\hbar v_F)/L(\phi - \phi_n)$, $\Gamma = \Gamma_L + \Gamma_R$ and $\Gamma_\alpha = T_\alpha(\hbar v_F)/(2L)$. This simplified S matrix (1.13) is going to be useful for evaluating the quantum capacitance of the device investigated in this thesis. This will be developed with more details in chapter 2. The calculation of the transmission coefficient in energy

$D = s^{\dagger}_{RL} s_{RL}$ has a Lorentzian expression which gives nothing else than the Breit-Wigner formula. While this development is useful for understanding the behaviour of the system close to a level resonance, it implies very small transmission of the tunnel barriers. In the previous discussion about energy scales in the QD and the different transport regime, it has been pointed out that the Fabry-Perot regime required, to be observed, to have large tunnelling transmission to overcome interactions in the QD.
With this expression, the differential conductance of the system under gate and bias voltage can be calculated. The problem is made easier by considering a symmetric bias with respect to both contact as $V_{L/R} = \pm V/2$. The SWNT chemical potential is supposed to be at equilibrium with the chemical potentials of the leads, thus remains unchanged due to symmetric bias. Spin degeneracy is also assumed. In this situation, equation 1.8 rewrites

$$\langle I_L \rangle = \frac{2e}{h} \sum_n \int D_n(E + \alpha V_G)(f_L(E + \alpha V_G + \frac{eV}{2}) - f_R(E + \alpha V_G - \frac{eV}{2}))dE \quad (1.14)$$

with $\alpha = C_G/C_\Sigma$ the capacitance lever arm of the gate electrode. For T=0, the Fermi distribution derivative is $\partial_V f_\alpha(E + \alpha V_G - eV_\alpha) = e\partial_V(V_\alpha)\delta(E + \alpha V_G - eV_\alpha)$. The differential conductance is thus

$$\frac{\partial \langle I \rangle}{\partial V} = \frac{2e^2}{h} \sum_n \frac{1}{2} D_n(\alpha V_G + \frac{eV}{2}) + \frac{1}{2} D_n(\alpha V_G - \frac{eV}{2}) \quad (1.15)$$

The differential conductance of such a device is shown in figure 1.5. It exhibits the typical checkerboard pattern of Fabry-Perot interferometer. The orbital spacing of the QD is directly readable from the spacing between two resonances in bias voltage.

Coulomb blockade regime

When the charging energy becomes dominant in the problem, transport through the device exhibits charge discretization. The energy hierarchy is now $kT,\ \Gamma < E_C,\ \Delta$. In this regime, transport is governed by the addition energy E_a needed to add or remove an electron from the electronic island formed by the QD. This addition energy consists of two contributions which are the charging energy and the orbital spacing $E_a = E_C + \Delta$ with $E_C = e^2/C_\Sigma$ and $\Delta = (hv_F)/(2L)$.

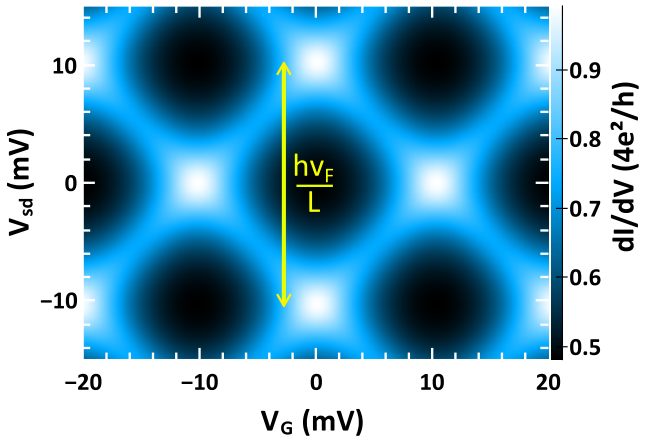

FIGURE 1.5: Colorplot of the differential conductance of a SWNT QD in the Fabry-Perot regime. The spin and orbital channels are degenerate and the transmission coefficient of each contact is taken to be $T_\alpha = 0.7$. The differential conductance is expressed in unit of $4e^2/h$, the maximum possible value for four conduction channels. The energy separation between two resonances in bias voltage directly gives the orbital spacing of the QD.

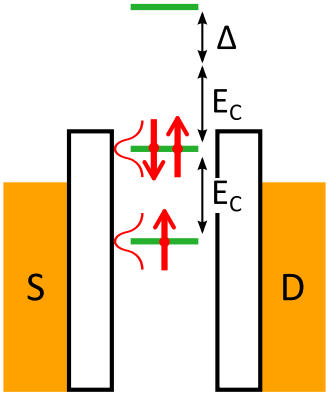

FIGURE 1.6: Scheme of the different energy scales involved the Coulomb blockade regime.

QD in the Coulomb blockade regime offers a rich experimental and theoretical playground. Indeed, such device acts as a tunable impurity with strong electronic interactions. The total Hamiltonian

$$H = H_D + H_\alpha + H_T^\alpha \tag{1.16}$$

with the dot Hamiltonian H_D

$$H_D = \sum_{\kappa,\sigma} \xi_{\kappa\sigma} \hat{d}^\dagger_{\kappa\sigma} \hat{d}_{\kappa\sigma} + U \hat{n}_{\kappa,\sigma}(\hat{n}_{\kappa,\sigma} - 1) \tag{1.17}$$

, the lead α Hamiltonian H_α

$$H_\alpha = \sum_{k_\alpha,\sigma} (\epsilon_{k_\alpha,\sigma} - \mu_\alpha) \hat{c}^\dagger_{k_\alpha,\sigma} \hat{c}_{k_\alpha,\sigma} \tag{1.18}$$

and the tunnelling Hamiltonian from one lead α to the dot H_T^α

$$H_T^\alpha = \sum_{k_\alpha,\kappa,\sigma} t_{k_\alpha,\kappa,\sigma} \hat{d}^\dagger_{\kappa\sigma} \hat{c}_{k_\alpha,\sigma} + t^\star_{k_\alpha,\kappa,\sigma} \hat{c}^\dagger_{k_\alpha,\sigma} \hat{d}_{\kappa\sigma} \tag{1.19}$$

can be simplified to a single impurity level in the Anderson model [55]

$$H = \sum_\sigma \xi_d \hat{d}^\dagger_\sigma \hat{d}_\sigma + U \hat{n}_{d\uparrow} \hat{n}_{d\downarrow} + H_L + H_R + \sum_{k_\alpha \sigma} t_{k_\alpha} \hat{d}^\dagger_\sigma \hat{c}_{k_\alpha,\sigma} + h.c \tag{1.20}$$

The competition between the different energies involved in the problem is adjustable by varying external parameter such as gate voltage or temperature. Being a simple model, the Anderson Hamiltonian is before hand a rich model that can account for many different situations. Each situation requires special care and hypothesis. In the current chapter, the discussion will focus on the sequential tunnelling regime where $\Gamma \ll kT$. This situation is useful for understanding the transport mechanism in this regime as well as the spectroscopic pattern of differential conductance. Chapter two will address the treatment of the Anderson model with the equation of motion technique (EOM). This method is more rigorous but diverges at half filling for $\Gamma \gg kT$. This divergence is due to the emergence of Kondo physics. Interestingly, Meir and Wingreen [56] derived a Landauer formula for the current and conductance of this impurity with electronic interactions.

Master equation treatment The sequential tunnelling regime is well suited for a master equation approach. In this regime, $\Gamma \ll kT$ so that the charge is strongly localized on the QD. The current thus only happens via sequential hopping events from the leads to the QD and from the QD to the leads.

Similarly to the Landauer-Büttiker formalism, a strength of the master equation approach is the possibility to treat the out-of equilibrium regime, when applying bias voltage. It consists of solving an equation of conservation for probabilities of levels occupation in the QD. The case of one orbital is treated, with double occupancy. The levels are thus $\{0, \uparrow, \downarrow, \uparrow\downarrow\}$. The master equation is

$$\frac{d\vec{P}}{dt} = M\vec{P} \tag{1.21}$$

with

$$\vec{P} = \begin{pmatrix} p_0 \\ p_\uparrow \\ p_\downarrow \\ p_{\uparrow\downarrow} \end{pmatrix} \quad \text{and} \quad M = \begin{pmatrix} -(\Gamma^+_\uparrow + \Gamma^+_\downarrow) & \Gamma^-_\uparrow & \Gamma^-_\downarrow & 0 \\ \Gamma^+_\uparrow & -(\Gamma^-_\uparrow + \tilde{\Gamma}^+_\downarrow) & 0 & \tilde{\Gamma}^-_\downarrow \\ \Gamma^+_\downarrow & -(\Gamma^-_\downarrow + \tilde{\Gamma}^+_\uparrow) & 0 & \tilde{\Gamma}^-_\uparrow \\ 0 & \Gamma^+_\downarrow & \Gamma^+_\uparrow & -(\tilde{\Gamma}^-_\uparrow + \tilde{\Gamma}^-_\downarrow) \end{pmatrix} \tag{1.22}$$

with $\Gamma^\pm_{\alpha\sigma} = \gamma_\alpha f^\pm_\alpha$ with $\alpha = L/R$, V_α the potential applied on the lead, thus $f^\pm_\alpha = f(\pm\xi + V_\alpha)$. The plus or minus upper script represents tunnelling events that increase or decrease the charge on the QD by one unit. Finally, $\tilde{\Gamma}$ represents events involving the double occupancy level so that their energy is $\xi + U$. The current is given by

$$I_\alpha = e\sum_\sigma \underbrace{\tilde{\Gamma}^+_\alpha p_{\bar{\sigma}}}_{N\to N+1} + \underbrace{\Gamma^+_\alpha p_0}_{N-1\to N} - \underbrace{\Gamma^-_\alpha p_\sigma}_{N\to N-1} - \underbrace{\tilde{\Gamma}^+_\alpha p_{\uparrow\downarrow}}_{N+1\to N} \tag{1.23}$$

Solving the stationary system $d_t\vec{P} = \vec{0}$, the expression of the current writes (see appendix B for details)

$$I = \frac{2e}{h}\frac{\gamma_L\gamma_R}{\gamma_L+\gamma_R}\frac{\Gamma^+\left[\tilde{f}^+_L\tilde{f}^-_L - \tilde{f}^+_R\tilde{f}^-_R\right] + \tilde{\Gamma}^-\left[f^+_L f^-_L - f^+_R f^-_R\right]}{\Gamma^+ + \tilde{\Gamma}^-} \tag{1.24}$$

with $V_{L/R} = \pm V/2$. The current and differential conductance through such a single level QD is represented in figure 1.7. In the linear regime when $eV/2 \ll kT$, the Fermi distribution expands as

$$f(x \pm \frac{eV}{2}) = f(x) \pm \frac{eV}{2}\frac{1}{4kT\cosh^2\frac{x}{2kT}} \tag{1.25}$$

the current can be rewritten as

$$I = \frac{2e^2}{h}\frac{\gamma_L\gamma_R}{\gamma_L+\gamma_R}V\left[\frac{\Gamma^+}{\Gamma^+ + \tilde{\Gamma}^-}\frac{1}{4kT\cosh^2\frac{\xi+U}{2kT}} + \frac{\tilde{\Gamma}^-}{\Gamma^+ + \tilde{\Gamma}^-}\frac{1}{4kT\cosh^2\frac{\xi}{2kT}}\right] \tag{1.26}$$

and the corresponding linear conductance

$$G_{\text{linear}} = \frac{2e^2}{h}\frac{\gamma_L\gamma_R}{\gamma_L+\gamma_R}\left[\frac{\Gamma^+}{\Gamma^+ + \tilde{\Gamma}^-}\frac{1}{4kT\cosh^2\frac{\xi+U}{2kT}} + \frac{\tilde{\Gamma}^-}{\Gamma^+ + \tilde{\Gamma}^-}\frac{1}{4kT\cosh^2\frac{\xi}{2kT}}\right] \tag{1.27}$$

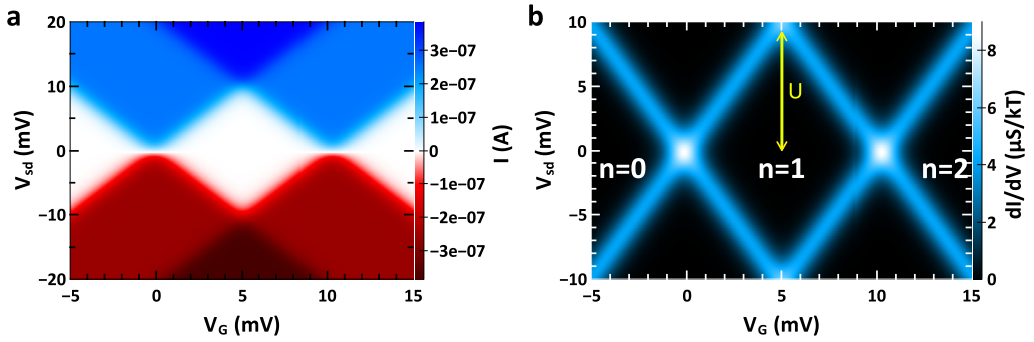

FIGURE 1.7: single level QD with double occupancy current (**a**) and differential conductance (**b**) in the gate/bias voltages plane. U=10 meV, γ=100μeV and T=5K.

As shown in figure 1.7 (b), the conductance of the QD in the Coulomb blockade regime exhibits a diamond pattern known as the Coulomb diamond pattern. The expression 1.1.4 shows that the conductance peak height scales as $1/kT$. The smaller kT, the thinner and higher the peaks. One can read off the spectrum from the gate/bias voltage plane conductance map. The height of a diamond in bias voltage gives two times the charging energy U and the width of the diamond edges gives kT[5]. In each diamond, the current is constant and the conductance zero. A number of charges N is localized on the QD and one charge is added or removed when crossing from one diamond to the next. Only one single orbital has been considered here on the QD, thus the number of charge varies from 0 to 2 as shown on the figure. To visualize the addition energy spectrum that comprises both U and Δ, is is instructive to compute the same approach with two orbitals. This situation is represented in figure 1.8. The QD state can be expressed with two numbers (Θ, N_Θ), with Θ the orbital and N_Θ the number of charges on this orbital. The diamond pattern shows a new periodicity as every time we pass to a new orbital, the addition energy is $\Delta + U$, thus forming wider Coulomb diamonds.

The spectroscopy calculation for figure 1.8 shows the richness of QD devices. The inner quantum structure of the energy levels is directly observable with simple measurements of current and/or conductance[6].

[5]This apply for true sequential tunnelling situation. Experimentally the width of the diamond edge is $\max(\Gamma, kT)$.

[6]Single electron transistor SET for their part also exhibits Coulomb diamonds. However, the electronic island being metallic has a high density of states available, thus a level separation $\delta_s \ll E_C$. The inner level structure and its richness is out of reach for laboratory temperature.

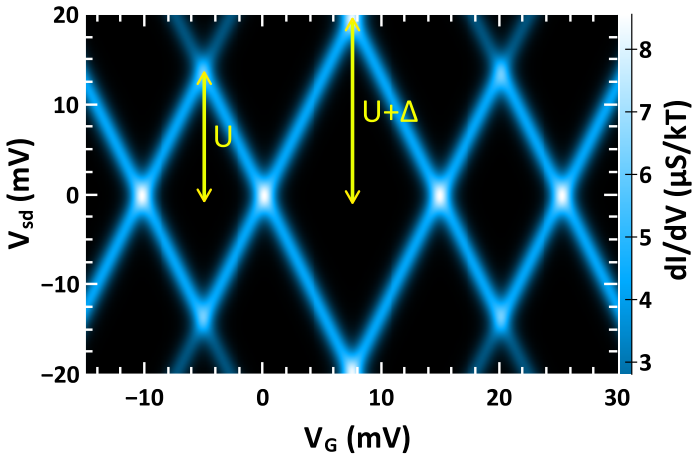

FIGURE 1.8: two levels QD with double occupancy differential conductance (**b**) in the gate/bias voltages plane. Δ= 5meV, U=10 meV, γ=100μeV and T=5K.

Beyond sequential tunnelling The transport through the QD in the sequential regime has been addressed. In this regime, the couplings from the leads to the QD levels Γ are small,compared to the charging energy E_C. When the tunnel couplings becomes higher and closer to the charging energy, the transport can happen via virtual states. This regime is called the co-tunnelling regime because two electrons are involved. These co-tunnelling events, resulting from quantum virtual states consist of one single quantum process. During this process, an excess electron lies on the QD for a short time[7]. Elastic co-tunneling and inelastic co-tunnelling (see [33]) can be observed. In the first case, the incoming electron arrives on the outgoing electron level. In the second case, the incoming electron arrives on a level with excess energy ΔE and the observation of such process requires to overcome ΔE by applying a finite bias voltage $eV > \Delta E$.

Kondo physics

A special case of co-tunnelling is when the QD has a non zero spin in its fundamental state. This happens *e.g.* when only one electron stands on the last occupied level of the QD. This leads to the spin $S = 1/2$ Kondo effect. In this situation, the virtual quantum process involved is a spin-flip of the spin of the last electron of the dot. During this event, there is no charge fluctuation on the QD.

First experimental signatures of the Kondo effect where found in 1930 on metallic alloys with magnetic impurities [57]. It was only thirty years later in 1964 that Jun Kondo gave a theoretical description and understanding of the phenomenon [58]. The resistivity of metals drops with temperature, due to the freezing of electron-phonon interaction first

[7] this time is related to the Heisenberg relation $\Delta E \Delta t > h$ with ΔE the excess energy of this process.

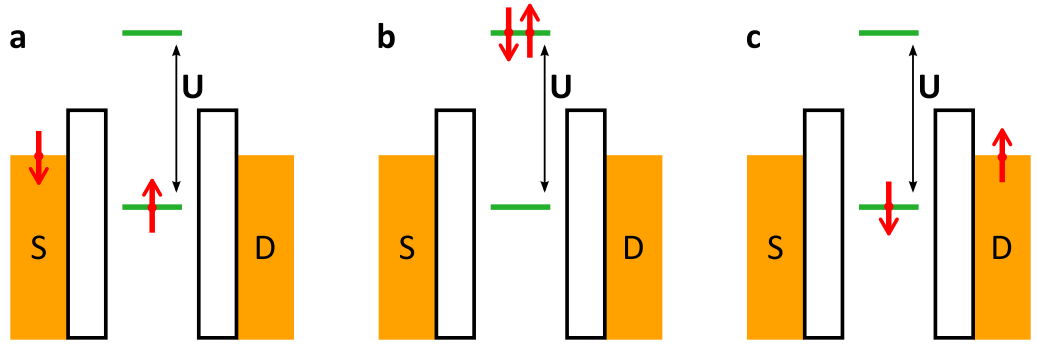

FIGURE 1.9: One of the possible process involved in Kondo S=1/2 effect for QD. The process starts in the real state (**a**) with one electron on the dot with spin up and one conduction electron on the left electron with spin down. Step (**b**) is a virtual state with double occupancy of the dot. In the final step (**c**), one electron leaves the QD and the remaining electron on the dot is spin down. The overall process results of a spin-flip of the electron spin on the QD

and elelctron-electron interaction at lower temperature. The resistivity then saturates to a value that depends on the number of residual defects of the crystal. In the presence of magnetic impurities, the resistivity increases again under a certain temperature around 10K [57, 59]. The solution proposed by Kondo relies on an anti-ferromagnetic coupling between the conduction electron and the magnetic impurities. He found that the resistance should diverge logarithmically as the temperature decreases. Only the emergence of renormalization group theory could remove this divergence behaviour, as was done by Wilson in 1975 [60]. One important feature of Kondo physics is its universality with respect to only one characteristic energy, the Kondo temperature T_K (see e.g. [61]). It means that whatever the device, only T_K governs its dependence. Another important aspect of this phenomenon is the concept of Kondo cloud, formed by the conduction electrons that screen the magnetic impurity. Up to now, there exists no experimental observation of the existence of the Kondo cloud. It would especially be important to measure the dynamic of the cloud to have access to the microscopic establishment of the regime.

The problem is old and seems closed. However, the development of QD devices lead to what has been called the "Kondo revival" [62]. The spin of the QD, which in the simplest case is $S = 1/2$, can be considered as a magnetic impurity toward the conduction electrons of the leads. In these devices, the current is blocked and the screening of the spin impurity by the Kondo cloud leads to an increase of conductance instead. The success of this revival relies for one part on the vast variety of possible device, such as magnetic adatoms on metallic surfaces [63], GaAlAs/GaAs 2DEG QDs [40], C60 molecules [14] and CNTs [19]. The other strength of the QD devices is the tunability of magnetic impurity in situ. This allow to study the Kondo effect at the single impurity

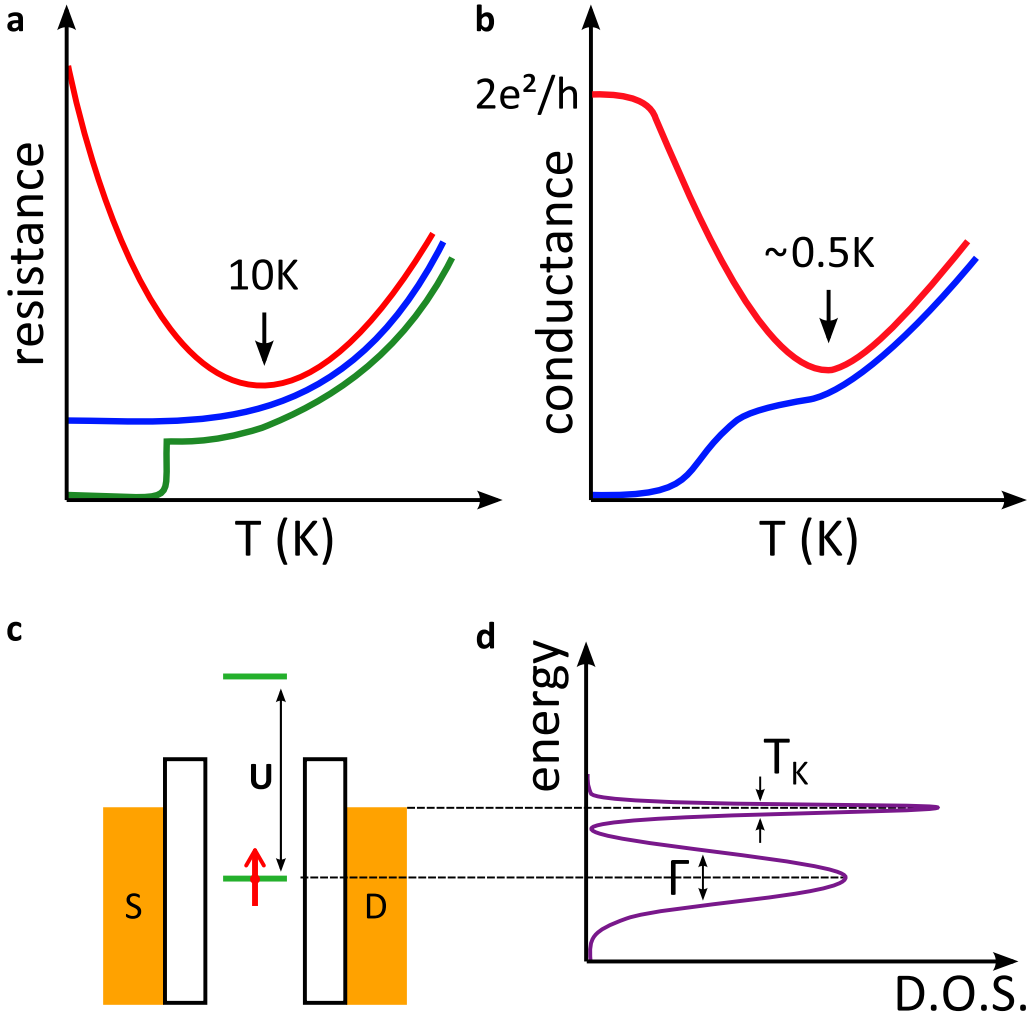

FIGURE 1.10: **a :** Temperature evolution of the resistance of a normal metal (blue), superconductor (green) and alloy with magnetic impurities (red).**b :** Temperature evolution of the conductance of a QD device when a magnetic impurity is localized on the QD, e.g. in the case of spin 1/2 when the number of electron is even (blue) or odd (red) nd Kondo effect appear. **c :** Scheme of the QD associated with the density of states (**d**). A sharp peak appears in the density of state at the chemical potential of the leads.

level and control the different parameters of the problem.

Success of Kondo physics is made by both its many-body and universal behaviour. It is hard to solve theoretically and a large amount of publications has been produced on the topic [33, 64]. The influence of AC-field has has been treated theoretically in some works like [35, 65]. Although the success of Kondo physics in nanostructures, only few attempts to measure the effects of AC field have been undertaken. Kogan measured satellite Kondo peaks at bias voltages corresponding to the frequency of the AC field $\epsilon = \pm h\nu$ [66]. The quantum quench of Kondo correlations in optical QD was studied in [67]. The Kondo resonance disappears with the detuning of the laser frequency with respect to T_K, in an universal way (it only depends on $\Delta\nu/T_K$). In both of these

works, the problem is treated as a photo-assisted process. Recently, the noise of a Kondo dot, made of CNT, has been measured at finite frequency, of the order of the Kondo temperature [68]. In this thesis, the cQED architecture allowed for dispersive measurements of the AC microwave field. This will give new information compared to low frequency measurements as we shall detail in chapter 4.

1.2 circuit Quantum Electrodynamics in the dispersive regime

In this thesis, measurements in the dispersive regime are performed. In this regime the cavity frequency is far detuned from the energy level separations in the artificial atom. The two systems thus do not exchange energy but only shift their respective energy. The information on the interactions between the two systems is usually read from the frequency shift of the cavity, also called the cavity pull. The coupling between the artificial atom and the microwave field is a dipole coupling. A change in the electronic state of the artificial atom modifies its polarizability, thus shift the frequency of the cavity. In the case of TLS, the treatment of this effect is easily done quantum mechanically, leading to the expression of both the cavity pull and AC-stark shift which describes the shift of the TLS resonance. In this work, it is more appropriate to describe the coupling of the QD and the cavity in a classical way. There are two reasons for that :

1. As in this thesis, the working temperature is rather high ($T \sim 1.5K$[8]) as well as the power excitation, the microwave field can be treated classically. The resonator itself can be described by classical lumped elements related to the geometrical properties of the cavity.

2. The coupling between the cavity and the QD is a priori a capacitive coupling. The electronic state and interactions of the QD are related to the quantum capacitance C_Q of the QD. This quantum capacitance, which varies with the different parameters that control the QD such as the gate and bias voltage, can thus be directly added in the classical description of the resonator.

The result are the same and the cavity frequency shift is interpreted as a capacitance shift of the QD. Note that in contrast to standard cQED where the artificial TLS is non dissipative[9], QDs offer a dissipative channel for the microwave field. In result, the cacity frequency shift is due both to a capacitive and a dissipative effect, as it will be discussed in greater details in chapter 4.

[8] the thermal occupation of a 6GHz resonator at 1.5K is about 5 photons
[9] the TLS is made of lossless superconducting circuit.

1.3 On-chip superconducting microwave resonator

1.3.1 Transmission line resonator

On-chip superconducting resonators are the electronic counterpart of optical cavity. They can be formed using a transmission line in which an electromagnetic field propagates. The CPW geometry allows to confine the electric $\vec{E}$ and magnetic $\vec{B}$ fields in the dielectric gap separating the transmission line and the ground plane, as shown in figure 1.11 (b). Within the gap, the electric field is within the plane while the magnetic field is perpendicular to the plane. Cuts in the transmission line act as electronic counterparts to optic mirrors. They are capacitive elements[10] which impedance is strongly mismatched from the transmission line impedance. This results in transmission and reflection of the microwave field at these coupling gaps. When cut at two ends, a transmission line will thus behave as a microwave Fabry-Perot with high quality factor due to the low loss of superconducting materials[11].

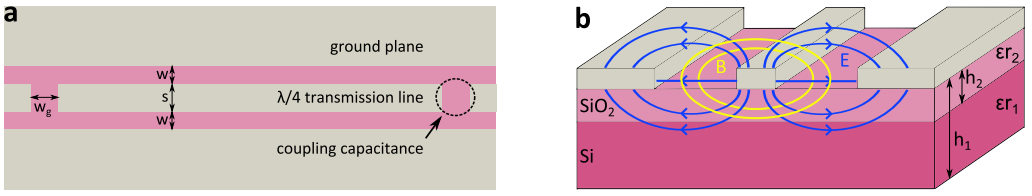

FIGURE 1.11: Schematics of an on-chip CPW geometry. (a) view from the top showing the central conductor $\lambda/2$ transmission line of width s separated from the ground plane by a gap of width w. The coupling capacitances that play the role of electronic mirrors in our cavity are also represented as gaps in the central conductor of width w_g. (b) view from the side of the chip showing the dielectric substrat which is usually oxidized (Si/SiO_2). Both electric and magnetic field distribution are represented in the vicinity of the central conductor, respectively in blue and yellow.

1.3.2 Lumped elements approximation

A capacitively coupled CPW transmission line is schematically represented in figure 1.11 (a). The resulting resonator's fundamental frequency is given by

[10] the two sides of the transmission line in regard of each other's are two metallic plates that form a capacitance.

[11] Superconductor are lossless in the DC regime. However, under AC drive, quasiparticles lying in the gap of the superconductor are accelerated, opening a dissipative channel in parallel to the lossless superconducting channel of cooper pairs. The imaginary part of this new channel is a kinetic inductance, which study can be found in appendix C for a particular sample, while the real part is a dissipative channel.

$$f_0 = \frac{c}{\sqrt{\epsilon_{eff}}} \frac{1}{2l} \tag{1.28}$$

with c the speed of light in vacuum, ϵ_{eff} the effective permittivity of the CPW line and l the length of the resonator. The phase velocity of the CPW line is given by $v_{ph} = c/\sqrt{\epsilon_{eff}} = 1/\sqrt{L_l C_l}$ where L_l and C_l are respectively the inductance and capacitance per unit length of the resonator as described in figure 1.12. Considering only the geometric contribution to these quantities, one finds [69]

$$L_l = \frac{\mu_0}{4} \frac{K(k_0')}{K(k_0)}, \quad C_l = 4\epsilon_0 \epsilon_{eff} \frac{K(k_0)}{K(k_0')}.$$

where K is the complete elliptic integral of the first kind with the geometric arguments

$$k_0 = \frac{w}{w+2s} \quad k_0' = \sqrt{1-k_0^2}.$$

Using conformal mapping theory, one can determine the characteristic impedance Z_0 of the line

$$Z_0 = \frac{30\pi}{\sqrt{\epsilon_{eff}}} \frac{K(k_0')}{K(k_0)} = \sqrt{\frac{L_l}{C_l}}$$

The main properties of the resonator are thus only determined by the geometric pattern of the CPW[12].

RLC model

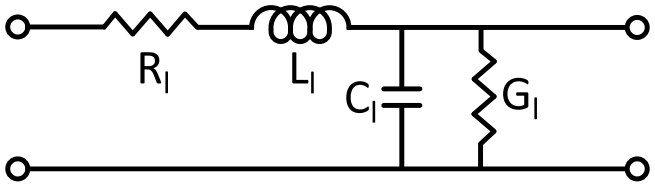

FIGURE 1.12: Schematics of a transmission line model with lumped elements in units per length.

[12]These expressions will reveal useful for determining the resonator's gap capacitance from SEM micrograph.

The resonator can be described by a RLC equivalent circuit. A transmission line of length $l = \lambda_0/2$, open at both ends, is considered. The impedance of the line is thus given by [70]

$$Z_{TL} = Z_0 \frac{1 + i\tan(\beta l)\tanh(\alpha l)}{\tanh(\alpha l) + i\tan(\beta l)} \tag{1.29}$$

$$\approx \frac{Z_0}{\alpha l + \frac{\pi}{\omega_0} i(\omega - \omega_0)} \tag{1.30}$$

where α is the attenuation constant related to the losses in the material, β is the propagation constant and Z_0 is the transmission line impedance. Equation (1.30) holds in the vicinity of cavity resonance $\omega = \omega_0 + \Delta\omega$ with $\Delta\omega \ll \omega_0$, and also $\alpha l \ll 1$ as the losses are negligible. The addition of coupled capacitance to both ends of this transmission line will form the cavity. For practical use, a RLC equivalent circuit to this transmission line can be found, if the latter approximation is valid :

$$Z_{RLC} = \left(\frac{1}{i\omega L_n} + i\omega C + \frac{1}{R}\right)^{-1} \tag{1.31}$$

$$= \frac{R}{1 + iRC\omega_0\left(\frac{\omega}{\omega_0} - \frac{\omega_0}{\omega}\right)}$$

$$\approx \frac{R}{1 + i2RC(\omega - \omega_0)} \tag{1.32}$$

with the following expressions for the circuit elements

$$L_n = \frac{2L_l l}{n^2\pi^2} \qquad C = \frac{C_l l}{2} \qquad R = \frac{Z_0}{\alpha l} \tag{1.33}$$

Here n refers to the cavity mode. The resonator frequency is adjusted with the inductance element as $\omega_n = n\omega_0 = 1/\sqrt{L_n C}$. In the following, only the first mode $n = 1$ is treated, so that the inductance of the line is $L = 2L_l l/\pi^2$. Note that the exact expression of the resonator's impedance (1.31) will be useful afterwards to properly take into account the coupling of the resonator to the QD. This point will be addressed with details in chapter 4.

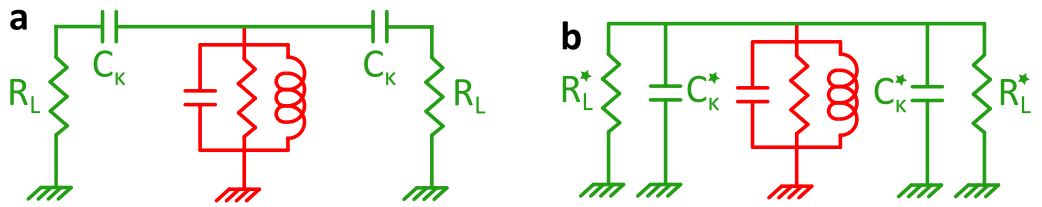

FIGURE 1.13: **a :** Equivalent RLC circuit of the resonator transmission line (red) coupled to the environnement via coupling capacitance C_κ and loaded impedance R_L (green). **b :** Same circuit with Norton equivalent lumped elements for the coupling impedance.

Quality factor

Equations (1.30) and (1.32), obtained for $\omega \approx \omega_0$ and small losses have a Lorentzian lineshape. This expression form is very convenient to express the resonator frequency and quality factor. The latter reads

$$Q_{int} = \frac{\pi}{2\alpha l} = \omega_0 RC \tag{1.34}$$

which directly gives $R = \frac{2Z_0 Q_{int}}{\pi}$. As mentioned above, the transmission line resonator is coupled to the environment via two capacitances acting as highly reflective mirrors. The environment is made out of two RF transmission lines (input and output) that are adapted to an usual impedance of 50Ω. The presence of the coupling capacitance C_κ in series with the load resistance $R_L = 50\Omega$ will slightly shift the resonance frequency of the resonator as well as introduce an external quality factor to the whole. In order to easily find these new expressions, it is useful to transform the coupling impedance from serie connection to parallel connection as shown in figure 1.13

$$Z_{coupling} = R_L + \frac{1}{i\omega C_\kappa} = \left(\frac{1}{R_L^\star} + i\omega C_\kappa^\star\right)^{-1} \tag{1.35}$$

with

$$R_L^\star = R_L \frac{1+\omega_0^2 C_\kappa^2 R_L^2}{\omega_0^2 C_\kappa^2 R_L^2} \qquad \text{and} \qquad C_\kappa^\star = C_\kappa \frac{1}{1+\omega_0^2 C_\kappa^2 R_L^2} \tag{1.36}$$

Now that all the elements of the circuit are in parallel, the capacitance and resistance of the RLC circuit are modified as follow

$$\frac{1}{R'} = \frac{1}{R} + \frac{2}{R_L^\star} \qquad C' = C + 2C_\kappa^\star \tag{1.37}$$

The resonance frequency is thus shifted as

$$\omega_0' = \frac{1}{\sqrt{LC'}} = \frac{1}{\sqrt{L(C+2C_\kappa^\star)}} \approx \omega_0 \left(1 - \frac{C_\kappa}{C}\frac{1}{1+\omega_0^2 C_\kappa^2 R_L^2}\right) \tag{1.38}$$

The coupling capacitance is in the range of fF while the resonator capacitance is in the range of pF, hence the last approximation. For typical resonators as the one used in this thesis, $C \approx 0.8pF$ and $C_\kappa \approx 4fF$ yielding a frequency shift of $-30MHz$. The measured quality factor of the coupled resonator is then the loaded quality factor

$$\begin{aligned} Q_L = \omega_0' R' C' &= \omega_0 \frac{1}{\sqrt{1+\frac{C_\kappa}{C}\frac{2}{1+\omega_0^2 C_\kappa^2 R_L^2}}} \frac{C+2C_\kappa^\star}{\frac{1}{R}+\frac{2}{R_L^\star}} \\ &\approx Q_{int}\frac{1}{1+2\frac{R}{R_L^\star}} \end{aligned} \tag{1.39}$$

Thus, within the same approximation as above, an external quality factor Q_{ext} can be defined by the following relation

$$\frac{1}{Q_L} \approx \frac{1}{Q_{int}} + \frac{1}{Q_{ext}} \tag{1.40}$$

with

$$Q_{int} = \omega_0 RC \quad \text{and} \quad Q_{ext} = \frac{\omega_0 R_L^\star C}{2} \tag{1.41}$$

The measured quality factor deviates from the internal quality factor due to the coupling capacitances. This will be investigated in more details in the following section.

Furthermore, the shape of the behaviour of the loaded impedance is well approximated by the following Lorentzian

$$Z^{\star}_{RLC} \approx \frac{R'}{1 + i2R'C'(\omega - \omega'_0)} \approx \frac{R'}{1 + i2Q_L\frac{\omega-\omega'_0}{\omega'_0}} \tag{1.42}$$

1.3.3 Scattering theory approach

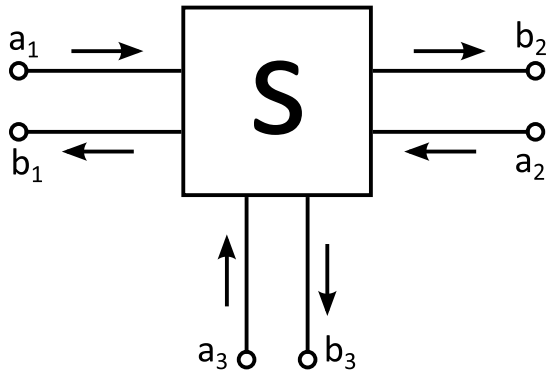

FIGURE 1.14: Schematics scattering theory model. The scattering element S is connected to the environnement via N ports containing both inputs a_i and outputs b_i.

The transmitted field is the measured quantity in the experiments of this thesis. It is therefore necessary to express the output field as a function of the input field that is applied at the input port of the resonator. The problem is properly described by considering propagating waves. Scattering theory allows to find the transmissions and reflections parameters of a system as the coefficients of the so called scattering matrix. This theory allows to take into account an arbitrary number of ports n connecting the system to the environment. In order to achieve this, the voltage and current at port i read

$$\begin{cases} V_i = g(a_i + b_i) \\ I_i = \dfrac{1}{g}(a_i - b_i) \end{cases} \tag{1.43}$$

with $g = \sqrt{R_L}$. The a_i and b_i coefficients are respectively the input and output coefficients at each port i, with respect to the scattering theory conventions. For the coupled RLC resonator, the following S matrix is found

$$S_{res} = \frac{1}{(g^2+Z_\kappa)(g^2+Z_\kappa+Z_{RLC})}\begin{pmatrix} Z_\kappa^2+2Z_{RLC}Z_\kappa-g^4 & 2g^2Z_{RLC} \\ 2g^2Z_{RLC} & Z_\kappa^2+2Z_{RLC}Z_\kappa-g^4 \end{pmatrix}$$

with $Z_\kappa = 1/i\omega C_\kappa$. The transmission from port 1 to port 2 is

$$S_{21} = \frac{2}{2+\frac{2}{i\omega C_\kappa R_L}+\frac{1}{R_L Z_{RLC}}\left(\frac{1+i\omega C_\kappa R_L}{i\omega C_\kappa}\right)^2} \tag{1.44}$$

It is convenient to express S_{21} with a simple Lorentzian expression, function of the coupled resonator impedance $Z^\star_{RLC}$. (cf equation (1.42)) The calculation is made easier by considering $Y^\star_{RLC} = \frac{1}{Z^\star_{RLC}}$ and replacing $C_\kappa = C^\star_\kappa \frac{1+\omega_0^2 C^{\star 2}_\kappa R^{\star 2}_L}{\omega_0^2 C^{\star 2}_\kappa R^{\star 2}_L}$ and $R_L = R^\star_L \frac{1}{1+\omega_0^2 C^{\star 2}_\kappa R^{\star 2}_L}$ for the simplifications. Finally,

$$\begin{aligned} S_{21} &= Z^\star_{RLC}\frac{2}{R^\star_L}\left(\frac{-1+\omega_0'^2 C_\kappa^2 R_L^2}{1+\omega_0'^2 C_\kappa^2 R_L^2}+i\frac{\omega_0' C_\kappa R_L}{1+\omega_0'^2 C_\kappa^2 R_L^2}\right) \\ &\approx -Z^\star_{RLC}\frac{2}{R^\star_L} \\ &\approx -\frac{Q_L/Q_{ext}}{1+2iQ_L\frac{\omega-\omega_0'}{\omega_0'}} \end{aligned} \tag{1.45}$$

The last approximation holds for $C_\kappa \ll 1/\omega_0' RL$ which is satisfied for $C_\kappa \leq 100fF$ with the parameters of our resonators.

Here it has been showed that the transmission of the system is proportional to the coupled impedance of the resonator, as long as the coupling capacitance is not too high. It is much more convenient to calculate the impedance than the scattering matrix of the system. Thus, every element that can be model by electronic lumped elements, inserted inside the cavity will directly add up in parallel to the resonator impedance. It allows to very quickly understand the effect of any coupling between the cavity and this external system on the transmitted field.

1.3.4 Coupling regimes

Equation (1.40) shows that the loaded quality factor can be expressed as the internal quality factor and an external quality factor added in parallel. As $\omega_0^2 C_\kappa^2 R_L^2 \ll 1$, the external quality factor can be simplified as

$$Q_{ext} \approx \frac{C}{2\omega_0 R_L C_\kappa^2} \propto C_\kappa^{-2} \tag{1.46}$$

Following this, the value of the coupling capacitance strongly affects the value of Q_{ext}. Thus, the choice of the coupling parameter is crucial to determine the regime of the device. Indeed, the resonator can either be dominated by the coupling quality factor or the internal quality factor. A critical behaviour is obtained for $Q_{int} = Q_{ext}$ which is obtained for

$$C_\kappa^{(c)} = \frac{1}{\omega_0 \sqrt{R_L(2R - R_L)}} \tag{1.47}$$

The behaviour of the transmitted signal and loaded quality factor in the three different regime is depicted in figure 1.15.

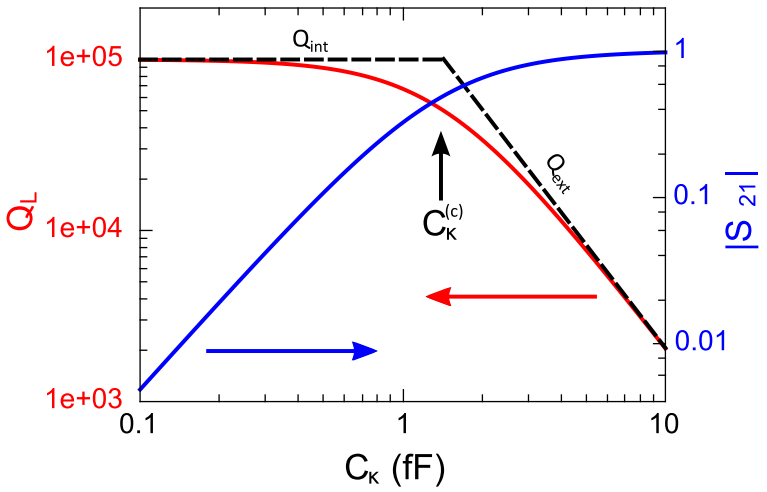

FIGURE 1.15: Loaded quality factor Q_L (red) and transmission amplitude $|S_{21}|$ (blue) of the coupled resonator of internal quality factor $Q_{int} = 10^5$ versus the coupling capacitance C_κ. The loaded quality factor and the transmission amplitudes undergo an opposite variation versus C_κ giving rise to a critical coupling value $C_\kappa^{(c)}$.

Coupling regimes

- **Over coupled regime**

  When $Q_{ext} \ll Q_{int}$, the loaded quality factor is approximatively Q_{ext}. This regime is obtained for high coupling capacitance $C_\kappa \gg C_\kappa^{(c)}$. The transmission tends to reach unity on resonance as C_κ increases while the quality factor of the resonance decreases. The Lorentzian approximation doesn't hold for too high coupling capacitances.

- **Critically coupled regime**

  For $C_\kappa = C_\kappa^{(c)}$, $Q_{ext} = Q_{int} = 2Q_L$. The transmission is exactly 1/2 at the resonance.

- **Under coupled regime**

  When $Q_{int} \gg Q_{ext}$, the loaded quality factor is approximatively Q_{int}. This regime is reached for $C_\kappa \ll C_\kappa^{(c)}$. The transmission decreases towards zero as C_κ decreases while the quality factor asymptotically tends to Q_{int}. **Note that the devices of this thesis are this regime.**

1.3.5 Quantum description

The classical description of CPW resonator is well adapted to quickly understand the behaviour of such cavities with an intuitive point of view. However, as the temperature and the excitation of the device are lowered, a quantum description is needed to properly describe its properties. Even tough the quantum limit for the cavity is not reached in this thesis, it is important to briefly describe it for two reasons :

1. like for phonons in solids, the quantum language is practical.

2. this description allows to determine the number of photons in the cavity. This will be particularly useful in the discussion of chapter 4.

LC harmonic oscillator

As superconducting transmission line are considered here, the losses can be neglected in the system. It is model by an LC circuit as described in figure 1.16. The losses will be introduced after as damping terms. It is convenient to use the phase $\phi = \int_{-\infty}^{t} V(\tau)d\tau$ for the description of the system. The corresponding Lagrangian of the circuit reads

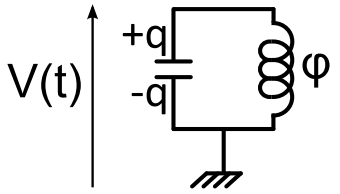

FIGURE 1.16: LC cirucuit under a voltage $V(t)$. The useful parameters to describe its behavior are the charge q on the condensator plates and the phase ϕ of the inductance.

$$\mathcal{L} = \frac{C\dot{\phi}^2}{2} - \frac{\phi^2}{2L} \tag{1.48}$$

The charge on the capacitor's plate reads $q = C\frac{\partial\phi}{\partial t}$. Replacing ϕ and q respectively by phase and charge operators $\hat{\phi}$ and $\hat{q}$, the Hamiltonian writes

$$H = \frac{\hat{q}^2}{2C} + \frac{\hat{\phi}^2}{2L} \tag{1.49}$$

$\hat{q}$ and $\hat{\phi}$ are conjugate operators and play the role of the position $\hat{x}$ and momentum $\hat{p}$ of a mechanical oscillator, therefore $[\hat{\phi}, \hat{q}] = i\hbar$. This Hamiltonian can be written in the canonical form of a harmonic oscillator

$$H = \hbar\omega_0(\hat{a}^\dagger\hat{a} + 1/2) \tag{1.50}$$

with $\hat{a} = \frac{Z_0\hat{q} - i\hat{\phi}}{\sqrt{2\hbar Z_0}}$ the annihilation operator in the mode $\omega_0 = \frac{1}{\sqrt{LC}}$ and $Z_c = \sqrt{\frac{L}{C}}$ is the characteristic impedance of the line. A useful representation of the field is a phase plane representation for any polar angle θ as

$$\hat{X}_\theta = \frac{\hat{a}e^{-i\theta} + \hat{a}^\dagger e^{i\theta}}{2} \tag{1.51}$$

Given two angles separated by $\pi/2$, this defines the in-phase and out-of-phase quadratures I and Q which obey $[I, Q] = i/2$.

Input/Output theory

The input/output theory is a quantum version of the scattering theory previously used to determine the cavity transmission. The input and output coefficients in the different ports of the system of equation (1.43) are replaced by creation and annihilation operators of bosonic modes. The full description of the quantum input/output theory can be found in [71] and the interested reader should refer to this review for more details. Here only the main results, that will reveal useful later, are discussed. The overall system can be described by the following Hamiltonian

$$H = H_{sys} + H_{bath} + H_{int} \tag{1.52}$$

H_{sys} describes the cavity, H_{bath} describes the field outside the cavity and H_{int} describes the coupling between the external field and the internal field of the cavity.

$$\begin{aligned} H_{sys} &= \hbar\omega(1/2 + \hat{a}^\dagger\hat{a}) \\ H_{bath} &= \hbar \int d\omega \hat{b}^\dagger(\omega)\hat{b}(\omega) \\ H_{int} &= i\hbar \int \kappa(\omega)[\hat{b}^\dagger(\omega)\hat{a} - \hat{a}^\dagger\hat{b}(\omega)] \end{aligned}$$

Operators $\hat{a}$ and $\hat{b}$ are bosonic creation and annihilation ($\hat{a}^\dagger$ and $\hat{a}^\dagger$) operators respectively for the cavity mode ω_0 and the environment bath. The interaction Hamiltonian describes the coupling between the external bath and the cavity via a coupling parameter $\kappa(\omega)$. The cavity is coupled to the environment by several ports. The input and output ports are two of them which are designed to address and drive the cavity, thus two couplings κ_{in} and κ_{out}. The losses are taken into account by considering a third port κ_L. With respect to the cavity, these couplings describe the rate at which photons are lost via the different ports, thus are related to damping of the cavity. The damping can be assumed to be due to markovian processes, thus independent of the frequency and can be written $\kappa_i(\omega) = \sqrt{\gamma_i/(2\pi)}$.

The equation of motion (EOM) of operator $\hat{a}$ gives

$$\dot{\hat{a}}(t) = -i\omega_0\hat{a}(t) - \sum_i \frac{\gamma_i}{2}\hat{a}(t) - \sum_i \sqrt{\gamma_i}\hat{b}_{in,i}(t) \tag{1.53}$$

and for each ports

$$\hat{b}_{out,i}(t) - \hat{b}_{in,i}(t) = \sqrt{\gamma_i}a(t) \tag{1.54}$$

In order to express the output mode from the input mode directly, in the case of two ports plus one port for losses (γ_L), the signal is considered to come to the cavity via port 1, and to be transmitted via port 2 (meaning that $\hat{b}_{in,2}(t) = 0$). The previous equations are solved with the help of Fourier transform and give

$$\hat{a}(\omega) = -\frac{2\sqrt{\gamma_1}}{\gamma_1 + \gamma_2 + \gamma_L - 2i(\omega - \omega_0)}\hat{b}_{in,1}(\omega) \tag{1.55}$$

$$\hat{b}_{out,2}(\omega) = -\frac{2\sqrt{\gamma_1\gamma_2}}{\gamma_1 + \gamma_2 + \gamma_L - 2i(\omega - \omega_0)}\hat{b}_{in,1}(\omega) \tag{1.56}$$

Equation (1.56) has the same structure as the classical equation (1.45). This shows the direct parallel between the classical and quantum description of the system. The average intra-resonator number of photon, at resonance is found to be

$$\bar{n} = \frac{4\gamma_1}{\hbar\omega_0(\gamma_1 + \gamma_2 + \gamma_L)^2}P_{in} \tag{1.57}$$

where $P_{in/out}(\omega) = \hbar\omega|\beta_{in/out}|^2$ with β the amplitude of the microwave field associated to $\hat{b}$. Assuming that the dampings of ports 1 and 2 are identical, equation (1.57) rewrites, with experimental relevant parameters, as

$$\bar{n} = \frac{2\sqrt{P_{in}P_{out}}}{hf_0\Delta f} \tag{1.58}$$

1.3.6 Link between classical and quantum description

As expected, both the electronic and quantum treatments lead to Lorentzian cavity transmission expressions close to resonance. The first approach gives a classical picture of the cavity behaviour via electronic lumped elements. The second approach allows to treat the problem in term of photons and is useful when the cavity is driven in the quantum regime (10 mK range temperature and low excitation power) or when one wants to express parameters in terms of photons number. Both approach rely on the same concept of a coupled transmission line to environment. The coupling capacitance and the coupling parameter γ_i are thus linked. The coupling constant γ_i is the ratio between the power dissipated in the coupling capacitance and the energy stored in the transmission line [72]

$$\gamma_i = \frac{P_{diss,i}}{E_{stored}} = \frac{1/2|V_i|^2 \Re(1/Z_i)}{1/4 C_{res}|V_i|^2} = \frac{2\omega_0^3 Z_0^2 C_\kappa^2}{\pi(1+\omega_0^2 Z_0^2 C_\kappa^2)} = \frac{\omega_0}{2Q_{ext}} \tag{1.59}$$

As the external quality factor has been defined with the two symmetric coupling capacitance of the cavity ($C_{\kappa,L} = C_{\kappa,R}$), one finds that $\gamma_L + \gamma_R = \omega_0/Q_{ext}$ as expected. We then also find $\gamma_L = 1/(RC)$. The damping inside the resonator is due to resistive losses through the capacitance of the transmission line. To thermally set the cavity in its ground state $|0\rangle$, it is necessary to cool it down to millikelvin range temperatures. Now, it is possible to estimate the power needed to add one photon to this state. Considering standard parameters; a coupling capacitance $C_\kappa = 4fF$, a resonance frequency $\omega_0 = 6GHz$, a characteristic line impedance $Z_0 = 50\Omega$ and a loaded quality factor $Q_L = 10000$, with the help of equation (1.57) $P_{in,1\ photon} = -125dBm$ corresponding to an excitation amplitude of $V = 100nV$.

Chapter 2

Dynamical response of a quantum dot

This chapter addresses the dynamical response of single QDs in different situations. As it will be emphasized, this dynamical response is related to the quantum capacitance of the dot. It is particularly necessary as it will be confronted to the experimental results later. Carbon nanotubes allow for studying different transport regimes with no electronic interactions (Fabry-Perot) or with electronic interactions (Coulomb blockade). In the first section, the non-interacting case is discussed. It offers the possibility to solve the problem exactly. In the second section, the interacting case is developed. It is particularly important as experiments are performed in this situation. Only the Coulomb blockade is treated, with an equation of motion (EOM) technique applied to the electronic Green's functions. This allow for an acute description of this regime but do not describe the Kondo physics.

2.1 Non interacting case

In this section, the non-interacting case is discussed . This situation allows for understanding the behaviour of the QD in the Fabry-Perot regime. The problem is treated by adapting the work of Prêtre, Thomas and Büttiker [52] with the Landauer-Büttiker formalism.

2.1.1 Dynamical conductance

With the help of the scattering matrix S, it is possible to express the current and the conductance of the system. The multi-terminal case is considered. The expression of the conductance is derived from the expression of the current operator

$$\hat{I}_\alpha(t) = \frac{e}{h}\int dE dE' (\hat{a}^\dagger_\alpha(E)\hat{a}_\alpha(E') - \hat{b}^\dagger_\alpha(E)\hat{b}_\alpha(E'))e^{(E-E')t/\hbar} \tag{2.1}$$

The current is expressed as the difference between the occupation number of the incident carriers in the conductor α and the occupation number of outgoing carriers in the same conductor (this expression can be found by carrying out the integral with $E' = E + \hbar\omega$ and setting $\hat{n}^+_\alpha = \hat{a}^\dagger_\alpha(E)\hat{a}_\alpha(E)$ and $\hat{n}^-_\alpha = \hat{b}^\dagger_\alpha(E)\hat{b}_\alpha(E)$). The conductance writes

$$g^{(m)}_{\alpha\beta}(\omega) = \frac{e^2}{h}\int dE \frac{f^{(m)}_\beta(E) - f^{(m)}_\beta(E+\hbar\omega)}{\hbar\omega}\Big(\delta_{\alpha\beta} - s^\star_{\alpha\beta}(E)s_{\alpha\beta}(E+\hbar\omega)\Big) \tag{2.2}$$

which is the expression of the external conductance in conductor m from reservoir β to reservoir α. This expression shows that only carriers close to the Fermi surface participate to conduction of current. The conductance is now expanded up to second order for small ω which is justified by the fact that the working frequency is f_0 ≈6GHz, which is negligible compared to the energies in the QD (Δ ∼5meV ≡ 1.2 THz). One finds

$$g^{(m)}_{\alpha\beta}(\omega) \;=\; g^{(m)}_{\alpha\beta}(0) - i\omega e^2\frac{dN_{\alpha\beta}}{dE} + \omega^2 e^4\Big(\frac{dN_{\alpha\beta}}{dE}\Big)^2 R_{\alpha\beta} \tag{2.3}$$

with $g^{(m)}_{\alpha\beta}(0)$, $\frac{dN^{(m)}_{\alpha\beta}}{dE}$ and $R^{(m)}_{\alpha\beta}$ respectively given by equations (**??**), (**??**) and (**??**). Here $\frac{dN_{\alpha\beta}}{dE}$ is a partial density of states, so that $e^2\frac{dN_{\alpha\beta}}{dE}$ has the dimension of a capacitance which is called the quantum capacitance C_q. $R_{\alpha\beta}$, having the dimension of a resistance is related to the charge relaxation resistance of the system. These notations are helpful for the construction of an electronic equivalent circuit.

2.1.2 Electronic equivalent circuit

The system

The studied system is represented in figure 2.1. A CNT based QD is connected to two electrodes and capacitively coupled to a gate.

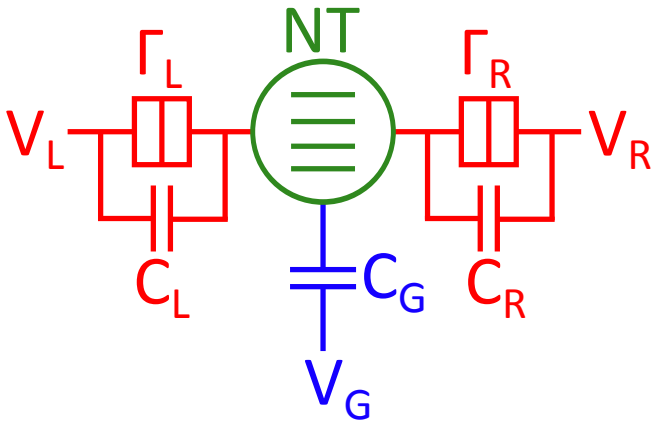

FIGURE 2.1: The physical system. A nanotube NT is connected to two reservoirs L and R via two tunnel barriers Γ_L et Γ_R, in parallel with two capacitance C_R and C_L. The CNT is also capacitively coupled to a gate G.

The conductance matrix $\mathcal{G}_{\alpha\beta}$ allows one to calculate the current at a contact (reservoir) α with the applied potentials to contacts β via

$$I_\alpha = \sum_\beta \mathcal{G}_{\alpha\beta}\delta V_\beta \tag{2.4}$$

Here the contacts α are the left, right and gate electrodes. Nevertheless, it is necessary first to determine what is called the true conductance of the system including interactions (see [52]). This true conductance is determined self consistently, considering the geometry of the system. The following expression, which is fully derived in [52], is necessary

$$g_{\alpha\beta}^{(mn)}(\omega) = \delta_{mn} g_{\alpha\beta}^{ext(m)}(\omega) - \Big[\sum_\gamma g_{\alpha\gamma}^{ext(m)}(\omega)\Big](M^{-1})_{mn}(\omega)\Big[\sum_\delta g_{\delta\beta}^{ext(n)}(\omega)\Big] \tag{2.5}$$

The conductance with superscript *ext* is the external conductance previously determined and the M matrix is $M_{mn}(\omega) = \delta_{mn}\sum_{\alpha\beta} g_{\alpha\beta}^{ext(m)}(\omega) - i\omega C_{mn}$ where C_{mn} is the geometric capacitance matrix. This description accounts for the displacement currents that re-equilibrates the charge distribution in the system. The capacitance matrix writes

$$C = \begin{pmatrix} C_\Sigma & -C_L & -C_R & -C_G \\ -C_L & C_L & 0 & 0 \\ -C_R & 0 & C_R & 0 \\ -C_G & 0 & 0 & C_G \end{pmatrix} \begin{matrix} NT \\ L \\ R \\ G \end{matrix}$$

with $C_\Sigma = C_L + C_R + C_G$. M takes into account both the geometric and the quantum capacitance. Equation (2.5), shows that the response of the conductor contains the contribution of charge carriers coming from reservoir β through conductor n and entering reservoir α from conductor m. Indeed, the two partial sums in the expression, linked by the matrix M mixes the different conductances with coupling capacitances between the different conductors.

In order to account correctly for the screening, it is necessary to consider additional conductors independently from the reservoirs. The three reservoirs L, R and G are linked to the nanotube via wires L, R and G with a capacitances in between. Reservoirs L and R are also linked to each other via the nanotube itself, which has been previously determined by the Fabry-Perot scattering matrix. Figure 2.1 has to be modified into figure 2.2.

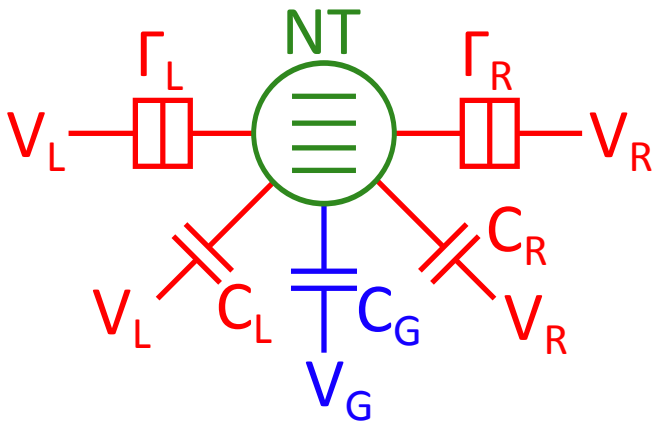

FIGURE 2.2: Equivalent circuit

Thus, when the conductor superscript is NT, equation (1.13) linking L and R only is used. When the conductor superscript is L, R or G, a simple scalar phase factor $e^{i\phi_R}$, $e^{i\phi_L}$ and $e^{i\phi_G}$ being due to total reflection at the conductor interface is used. The model has been settled and each term has been defined. The dynamical response of the system is now calculated.

Solving the system

In order to determine the conductance matrix, the expression of current in each contact (or reservoir) is needed. It is obtained with the following expression

$$I_\alpha = \sum_n \sum_{\beta m} g_{\alpha\beta}^{(mn)} \delta V_\beta^{(n)} \tag{2.6}$$

where $\delta V_\beta^{(n)}$ is the potential applied to the contact between reservoir β and conductor n. This expression corresponds to intuition as the total current in a reservoir is the sum of all the currents (conductance $\times$ potential) that reach this reservoir. The sum over the conductor n is separated from the sum over the conductor m in order to make the next step clearer. Then, as already mentioned, the conductance matrix will be derived from

$$I_\alpha = \sum_\beta \mathcal{G}_{\alpha\beta}\delta V_\beta \tag{2.7}$$

From this point, a first approximation has to be made, which is not too restrictive as it is to consider that the conductors L, R and G being macroscopic, they possess many conducting channels N. This number of channels being a prefactor of the partial density of state of eq. (2.3), it is reasonable to state that all the terms containing this partial density of state $\frac{dN_{m\neq NT}}{dE} \gg 1$. This will greatly simplify every further expression. Moreover, due to the trivial scattering matrices of L, R and G, many contributions will be zero and for example, the determination of I_L only requires $I_L = I_L^{(NT)} + I_L^{(L)}$ with

$$I_L^{(NT)} = (g_{LL}^{(NT,NT)} + g_{LL}^{(NT,L)})\delta V_L^{(NT)} + (g_{LR}^{(NT,NT)} + g_{LR}^{(NT,R)})\delta V_R^{(R)} + g_{LG}^{(NT,G)}\delta V_G^{(G)}$$

$$I_L^{(L)} = (g_{LL}^{(L,L)} + g_{LL}^{(L,NT)})\delta V_L^{(NT)} + (g_{LR}^{(L,R)} + g_{LR}^{(L,NT)})\delta V_R^{(R)} + g_{LG}^{(NT,G)}\delta V_G^{(G)}$$

Thus, $\mathcal{G}$ is built up to the second order in ω, coefficient by coefficient. This conductance matrix shows several physical aspects that are expected. First, there are non zero terms at first order only between reservoirs L and R, via the tunnelling resonant barriers. Indeed, the capacitive coupling between the gate and the nanotube prevents from any current propagation at zero frequency. Second, it is found that the geometric capacitances of the circuit are modified by a quantum correction proportional to the density of states inside the carbon nanotube. The charges in the nanotube create a screening effect that acts as a capacitive effect and adds up parallel to the other capacitances of the system.

Note that the final expression must fulfil current conservation ($\sum_\alpha \mathcal{G}_{\alpha\beta} = 0$) and gauge invariance ($\sum_\beta \mathcal{G}_{\alpha\beta} = 0$) that states that an overall potential shift does not affect the behaviour of the system. One can check that these two properties are fulfilled in the expression of $\mathcal{G}$

The main result of this calculation is the expression of the finite frequency conductance of the SWNT QD due to the gate electrode

$$\mathcal{G}_{GG} = -i\omega C_\mu + \omega^2 R_q C_\mu^2 \tag{2.8}$$

An expression of the form of equation (2.3) is found, as expected. C_μ is the total electrochemical capacitance of the wire *vis-a-vis* the gate G and R_q is the charge relaxation resistance. The electrochemical capacitance C_μ is defined by the sum of the mean orbital level spacing Δ and the charging energy as $e^2/C_\mu = \Delta + e^2/C$. This energy corresponds to the energy one needs to add a charge in the nanotube. The other important result is the value of the CNT QD quantum capacitance which is found to be

$$C_Q = \frac{2e^2}{\pi\Gamma} \tag{2.9}$$

which is consistent with the result found in [52]. In the simple case where $C_L = C_R = 0$ and the system is at resonance so that $\Delta(E) = i\Gamma/2$ in equation (1.13), C_μ is equal to C_G in parallel with C_Q, and $R_q = \frac{h}{2e^2}$, which is half the quantum of resistance.

Equivalent circuit

From the expression of $\mathcal{G}$, it is possible to fully determine the equivalent electronic circuit of our system. However this circuit is only valid up to second order in ω. A triangle circuit (as shown in figure 2.3 (a)) is considered. By successively turning on one potential (and letting the other two being equal to zero), a relation between the current at each contact and the different impedances for this potential is obtained. This leads to the expression of the three impedances of the circuit.

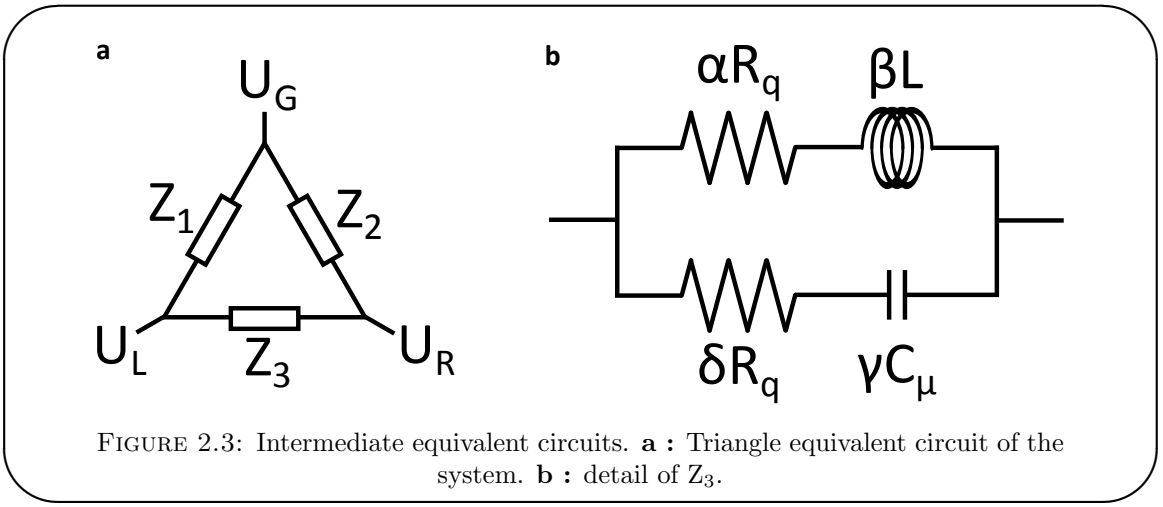

FIGURE 2.3: Intermediate equivalent circuits. **a :** Triangle equivalent circuit of the system. **b :** detail of Z_3.

The impedances Z_1 and Z_2 have the same structure of a resistance proportional to R_q in series with a capacitance proportional to C_μ

$$\frac{1}{Z_{1(2)}} = \frac{1}{A_{1(2)}R_q} + j\omega C_\mu B_{1(2)} \tag{2.10}$$

while the impedance Z_3 has the structure shown in figure 2.3 (b) where $L = R_q^2 C_\mu$. For the sake of simplicity, the case at zero temperature with symmetric barriers ($\Gamma_L = \Gamma_R = \Gamma/2$) is now considered. Moreover, the two reservoirs L and R are taken at the same chemical potential $\mu_L = \mu_R = 0$, meaning that the system is not biased. Being at T=0 induces $\frac{df_L^{(NT)}}{dE} = \frac{df_R^{(NT)}}{dE} = -\delta(E)$, which in combination with non resonant regime introduces Lorentzian terms in all the coefficients of $\mathcal{G}$

$$\lambda(E_0, \Gamma) \quad = \quad \lambda \quad = \quad \frac{\Gamma^2/4}{E_0^2 + \Gamma^2/4}$$

which is equal to unity at resonance. Then, by considering the ratio of the geometric capacitance over the nanotube quantum capacitance, balanced with the resonance weight λ,

$$\chi_i = \frac{1}{\lambda}\frac{\pi\Gamma C_i}{2e^2} = \frac{1}{\lambda}\frac{C_i}{C_Q} \tag{2.11}$$

with i =L, R, G. The total electrochemical capacitance C_μ, the relaxation resistance R_q and the Luttinger parameter g of the system write

$$C_\mu = C_G \frac{1 + \chi_L + \chi_R}{1 + \chi_L + \chi_R + \chi_G} \tag{2.12}$$

$$R_q = \frac{h}{2e^2}\frac{1}{1 + \chi_L + \chi_R} \tag{2.13}$$

$$\frac{1}{g^2} = \frac{1 + \chi_L + \chi_R + \chi_G}{\chi_G(1 + \chi_L + \chi_R)} \tag{2.14}$$

The Luttinger parameter g reflects the interactions of the Luttinger liquid. It ranges from 1 (no interactions) to 0[1] and is related to the density of states of the conductor [73]. It gives direct information on the electron-electron interaction strength and has been measured in CNT [74]. In order to evaluate the orders of magnitude, numerical

[1] g can be re-expressed in the more common expression $g = \frac{1}{\sqrt{1+\frac{C_Q}{C_G}}}$.

values consistent with the experiments are taken, $C_G = 4\text{aF}$, $C_\Sigma = 8\text{aF}$ and $\Gamma = 1\text{meV}$. In order to visualize the effects of asymmetries of the lateral capacitances C_L and C_R, they are respectively set to 2.1aF and 2aF. The behaviours of R_q and C_μ are shown in figure 2.4.

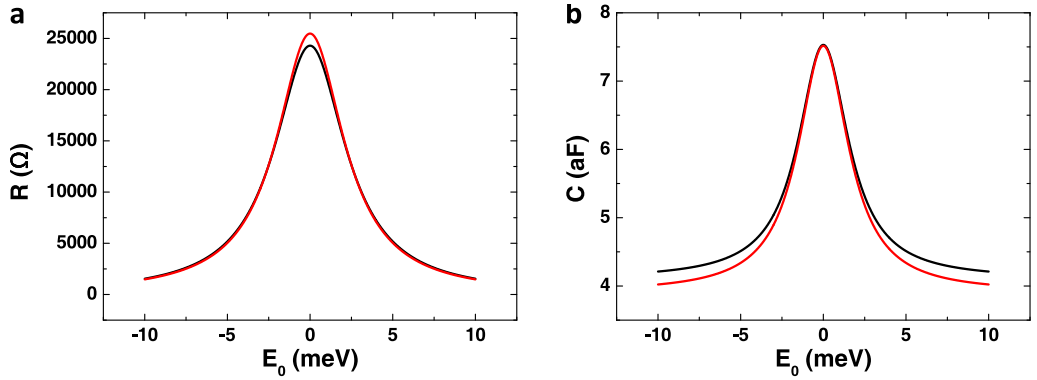

FIGURE 2.4: Simulation of the value of resistances R_L (black) and R_R (red) (**a**) and capacitances C_L (black) and C_R (red) (**b**), as defined in figure **??** in appendix **??** section **??**. C_L=2.1aF, C_R=2aF, C_G=3.9aF, Γ=1meV and E_0 ranges from -10meV to 10meV.

2.2 Interacting case with EOM

In this section, interactions are considered in the problem in order to treat Coulomb blockade regime. In the non-interaction situation, it has been shown that the quantum capacitance of the QD is $C_Q = \frac{2e^2}{\pi\Gamma}$. The electronic interactions affect significantly this quantity. The calculation is performed by using the equation of motion (EOM) technique applied to the electronic Green's function. This technique allows for treating the Coulomb blockade regime rigorously, even for $\Gamma \gtrsim kT$. Therefore it covers the non-interacting case ($U = 0$) as well as the sequential regime where $\Gamma \ll kT$. The latter has been treated in chapter 1 to describe the Coulomb blockade pattern, with a master equation approach. The quantum capacitance of the QD in this regime can be calculated[2] to be $C_Q \propto \frac{e^2}{kT}$. However, the EOM technique does not allow for treating the Kondo regime.

2.2.1 Model and Hamiltonian

The CNT is contacted by two source drain electrodes and is driven by a gate electrode in a SET configuration. It is also capacitively coupled to an AC voltage source which

[2]Considering a single occupation level, one finds $C_Q = \frac{e^2}{kT}\frac{e^{\epsilon/kT}}{\left(2+e^{\epsilon/kT}\right)^2}$. This peaks to $C_Q(max) = \frac{e^2}{8kT}$.

is the CPW resonator. In the Coulomb blockade regime, the charge on the island is quantized as $Q_{island} = -ne$ where n is the number of electrons on the dot and e is the absolute value of electronic charge as shown in figure 2.5.

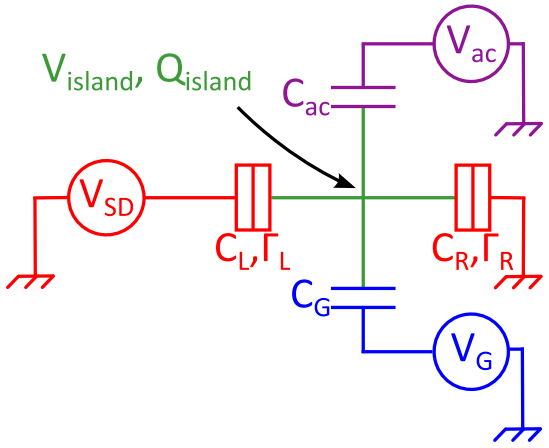

FIGURE 2.5: Quantum Dot circuit considered in this paper. The CNT contacted by two source-drain Pd electrodes (red) and capacitively coupled to a gate electrode (blue) forms an electronic island (green). It is also coupled to an AC voltage source which is the CPW resonator (purple). The charge on the island is quantized as $Q_{island} = -ne$ where n is the number of electrons on the dot. The island potential is $V_{island} = \frac{Q+\sum C_i V_i}{C_\Sigma}$, redistributing the charge on the different electrodes as $Q_i = -\alpha_i en + V_i C_i + \alpha_i(\sum_j C_j V_j)$. Here $\alpha_i = -C_i/C_\Sigma$

One single orbital level d of the dot is taken into account. To correctly express the dot Hamiltonian, the electrostatic energy on the dot must be properly defined

$$E = \frac{1}{2} C_\Sigma V_{island}^2 = \frac{(Q + \sum_i C_i V_i)^2}{2C_\Sigma} \tag{2.15}$$

If n_0 is the number of charges on the dot when $V_i = 0\ \forall i$ and $N = n - n_0$, then $Q = -Ne$ is the number of charges on the island compared to the electrostatic equilibrium. By choosing $E(n_0) = 0$, one gets

$$E(N) = E_c \left(N^2 - \frac{2N \sum_i C_i V_i}{e} \right) = E_c N^2 + eN \sum_i \alpha_i V_i \tag{2.16}$$

where the charging energy $E_c = \frac{e^2}{2C_\Sigma}$. The Hamiltonian of the system writes $H = H_D + H_{L(R)} + H_{T,L(R)}$ with

$$
\begin{aligned}
H_D &= \sum_{\sigma=\{\uparrow,\downarrow\}} \tilde{\xi}_{d\sigma} c^\dagger_{d\sigma} c_{d\sigma} + U n_{d\downarrow} n_{d\uparrow} \\
H_{L(R)} &= \sum_{k\in\nu_{L(R)},\sigma=\{\uparrow,\downarrow\}} \xi_{k\sigma} c^\dagger_{k\sigma} c_{k\sigma} \\
H_{T,L(R)} &= \sum_{k\in\nu_{L(R)},\sigma=\{\uparrow,\downarrow\}} t_{k\sigma} c^\dagger_{d\sigma} c_{k\sigma} + t^*_{k\sigma} c^\dagger_{k\sigma} c_{d\sigma}
\end{aligned}
$$

with $n_{d\sigma} = c^\dagger_{d\sigma} c_{d\sigma}$ and $\tilde{\xi}_{d\sigma} = \xi_{d\sigma} + e\sum \alpha_i V_i$. Here, $\alpha_i = -C_i/C_\Sigma$ and V_α is the potential on the reservoir α. $\nu_{L(R)}$ is the ensemble of electronic states in lead $L(R)$. The energies $\xi_{d\sigma}$ and $\xi_{k\sigma}$ are defined with respect to the Fermi energies of the dot and lead respectively. The conductance of the circuit can be calculated as [75]

$$
G = -\frac{e^2}{h} \sum_\sigma \int_{-\infty}^{+\infty} \frac{d\xi}{\hbar} \frac{\Gamma_{L\sigma}(\xi)\Gamma_{R\sigma}(\xi)}{\Gamma_{L\sigma}(\xi) + \Gamma_{R\sigma}(\xi)} A(d\sigma, \xi) \frac{\partial f(\xi)}{\partial \xi} \tag{2.17}
$$

with, for $l \in \{L, R\}$

$$
\Gamma_{l\sigma}(\xi = \xi_{k\sigma}) = 2\pi \left|t_{k\sigma}\right|^2 N_F^l \tag{2.18}
$$

and N_F^l the density of states at the Fermi level in lead l. The spectral density A is[3]

$$
A(d\sigma, \omega) = -2\,\mathrm{Im}[G^d_\sigma(\omega)] \tag{2.19}
$$

with

$$
\begin{cases}
G^d_\sigma(\omega) = \displaystyle\int_{-\infty}^{+\infty} G^d_\sigma(t) e^{i\omega t} d\omega \\
G^d_\sigma(t) = -i\theta(t) \left\langle \left\{ c_{d\sigma}(t), c^\dagger_{d\sigma}(0) \right\} \right\rangle
\end{cases}
$$

2.2.2 Equation of motion theory

For $T \gg T_K$, one can neglect electronic correlations between the dot and the leads [4]. Then, the equation of motion technique leads to (see Appendix D for details)

[3] with the conventions of [75]. Usually, it is defined as $A = -\frac{1}{\pi}\mathrm{Im}[G]$.

[4] The following approximations are made $\langle\{c^\dagger_{k\bar{\sigma}}(t) c_{k'\bar{\sigma}}(t) c_{d\sigma}(t), c^\dagger_{d\sigma}\}\rangle = \delta_{k,k'} f(\xi_{k\bar{\sigma}}) \langle\{c_{d\sigma}(t), c^\dagger_{d\sigma}\}\rangle$, $\langle\{c^\dagger_{d\bar{\sigma}}(t) c_{k'\bar{\sigma}}(t) c_{k\sigma}(t), c^\dagger_{d\sigma}\}\rangle = 0$, $\langle\{c^\dagger_{k'\bar{\sigma}}(t) c_{k\sigma}(t) c_{d\bar{\sigma}}(t), c^\dagger_{d\sigma}\}\rangle = 0$. This means that the Green's function expansion is up to first order in $c_d c_k$. Therefore, this calculation cannot treat Kondo correlations which require the summation over all correlation terms.

$$G^d_\sigma(\omega)/\hbar = \frac{1-\langle n_{d\bar{\sigma}}\rangle}{\hbar\omega - \xi_{d\sigma} - \Sigma^S_\sigma(\omega)} + \frac{\langle n_{d\bar{\sigma}}\rangle}{\hbar\omega - \xi_{d\sigma} - \Sigma^D_\sigma(\omega)} \tag{2.20}$$

with

$$\Sigma^S_\sigma(\omega) = \Sigma^0_\sigma - U\Sigma^1_{\bar{\sigma}}\left[\hbar\omega - \xi_{d\sigma} - U - \Sigma^0_\sigma - \Sigma^3_{\bar{\sigma}}\right]^{-1} \tag{2.21}$$

$$\Sigma^D_\sigma(\omega) = U + \Sigma^0_\sigma + U\Sigma^2_{\bar{\sigma}}\left[\hbar\omega - \xi_{d\sigma} - \Sigma^0_\sigma - \Sigma^3_{\bar{\sigma}}\right]^{-1} \tag{2.22}$$

with $\langle n_{d\sigma}\rangle$ the average occupation of orbital d by spins σ . Assuming that $\Gamma_{l\sigma}$ is energy independent (broad band approximation) and using (2.18), the self energy terms occurring at the right hand side of (2.21) and (2.22) are (see Appendix D)

$$\Sigma^0_\sigma = -i\Gamma_\sigma/2 \tag{2.23}$$

$$\begin{aligned}\Sigma^1_{\bar{\sigma}}(\omega) = &-i\frac{\Gamma_{\bar{\sigma}}}{2}\left[f(\xi_{d\sigma}+\xi_{d\bar{\sigma}}+U-\hbar\omega)+f(\hbar\omega+\xi_{d\bar{\sigma}}-\xi_{d\sigma})\right]\\ &+\frac{\Gamma_{\bar{\sigma}}}{2\pi}\,\mathrm{Re}\left[\Psi\left(\frac{1}{2}+i\beta\frac{\xi_{d\sigma}+\xi_{d\bar{\sigma}}+U-\hbar\omega}{2\pi}\right)\right]\\ &-\frac{\Gamma_{\bar{\sigma}}}{2\pi}\,\mathrm{Re}\left[\Psi\left(\frac{1}{2}+i\beta\frac{\hbar\omega+\xi_{d\bar{\sigma}}-\xi_{d\sigma}}{2\pi}\right)\right]\end{aligned} \tag{2.24}$$

$$\Sigma^3_{\bar{\sigma}} = -i\Gamma_{\bar{\sigma}} \tag{2.25}$$

$$\Sigma^2_{\bar{\sigma}}(\omega) = -i\Gamma_{\bar{\sigma}} - \Sigma^1_{\bar{\sigma}}(\omega) \tag{2.26}$$

with $\Gamma_\sigma = \Gamma_{L\sigma} + \Gamma_{R\sigma}$ and $\Psi(z) = \left(\sum_{k=1}^{+\infty}\frac{1}{k} - \frac{1}{k+z-1}\right) - \gamma$ the digamma function. The self-energy Σ^1 is the result of the EOM refinements. It gives corrections to the Lorentzian approximation that can be done for the energy levels. In the following section, this will be emphasized by comparing the predictions for both models. However, as already mentioned, this EOM description is an approximation which is not perfectly controlled as it diverges at half-filling, which is a signature of the appearing Kondo effect [5]. It can nevertheless be expanded to the description of the Kondo physics, as it has been done in [76].

The density of states $A_{d\sigma}(\omega)$ can be calculated from equation(2.20) as

$$A_{d\sigma}(\omega) = (1-\langle n_{d\bar{\sigma}}\rangle)A^S_\sigma(\omega) + \langle n_{d\bar{\sigma}}\rangle\, A^D_\sigma(\omega) \tag{2.27}$$

[5] Note that $\lim_{\beta\to 0}(\mathrm{Re}[\Psi(\frac{1}{2}+i\beta\frac{\xi_{d\sigma}+\xi_{d\bar{\sigma}}+U-\hbar\omega}{2\pi})] - \mathrm{Re}[\Psi(\frac{1}{2}+i\beta\frac{\hbar\omega+\xi_{d\bar{\sigma}}-\xi_{d\sigma}}{2\pi})]) = \log[\left|\frac{\xi_{d\sigma}+\xi_{d\bar{\sigma}}+U-\hbar\omega}{\hbar\omega+\xi_{d\bar{\sigma}}-\xi_{d\sigma}}\right|]$. At $T=0$, this limit diverges for $\xi_{d\sigma}+\xi_{d\bar{\sigma}}+U-\hbar\omega=0$ or $\hbar\omega+\xi_{d\bar{\sigma}}-\xi_{d\sigma}=0$.

with, for $j \in \{S, D\}$

$$A^j_\sigma(\omega)/\hbar = \frac{-2\,\mathrm{Im}[\Sigma^j_\sigma]}{(\hbar\omega - \xi_{d\sigma} - \mathrm{Re}[\Sigma^j_\sigma])^2 + \mathrm{Im}^2[\Sigma^j_\sigma]}$$

This allows to find a self-consistency equation to calculate the average occupation of the QD $\langle n_{d\sigma}\rangle$

$$\langle n_{d\sigma}\rangle = \frac{\langle n_{S\sigma}\rangle\,(1 - \langle n_{S\bar{\sigma}}\rangle) + \langle n_{S\bar{\sigma}}\rangle\,\langle n_{D\sigma}\rangle}{1 - (\langle n_{D\sigma}\rangle - \langle n_{S\sigma}\rangle)(\langle n_{D\bar{\sigma}}\rangle - \langle n_{S\bar{\sigma}}\rangle)} \tag{2.28}$$

with, for $j \in \{d, S, D\}$,

$$\langle n_{j\sigma}\rangle = \int_{-\infty}^{+\infty} \frac{d\omega}{2\pi} f(\hbar\omega) A^j_\sigma(\omega) \tag{2.29}$$

Spin degenerate situation

in the case where the spins are degenrate, the expression of $\langle n_d\rangle$ and $A_d(\omega)$ can be simplified. This is especially useful for numerical calculations. The summation over σ directly gives

$$\langle n_d\rangle = \frac{2n_S}{1 + n_S - n_D} \tag{2.30}$$

and the spectral density of states can be written

$$A_d(\omega) = (1 - \frac{\langle n_d\rangle}{2})A^S(\omega) + \frac{\langle n_d\rangle}{2}A^D(\omega) \tag{2.31}$$

2.2.3 Occupation of the QD

In this section, the occupation number of the dot is evaluated as a function of the applied gate voltage bias. At this point, it has been calculated within the frame of a full EOM development. While being rigorous, the results are obtained only through numerical evaluations. It is therefore instructive to look at a simpler version of the EOM technique in which the self-energies Σ_1 and Σ_2 are removed. This is equivalent to consider Lorentzian line-shape levels. The conductance of the QD therefore writes

$$G_\pm(\omega) = \frac{1 - \langle n_\mp\rangle}{\hbar\omega - \epsilon_\pm + i\Gamma/2} + \frac{\langle n_\mp\rangle}{\hbar\omega - \epsilon_\pm - U + i\Gamma/2} \tag{2.32}$$

The self-consistency equation on the occupation number of the QD, arising from the direct combination of equations (2.5) and (2.29) is

$$\langle n_{\pm}\rangle = -\frac{1}{\pi}\int_{-\infty}^{+\infty} d\omega f(\omega)\mathrm{Im}G_{\pm}(\omega) \tag{2.33}$$

Equation (2.33) is analytically solvable and the mean occupation number of the QD within this approximation at T=0 is (for details, see appendix D section D.4)

$$\langle n_{\pm}\rangle = \frac{\frac{1}{2} - \frac{1}{\pi}\arctan\left(\frac{2\epsilon_{\pm}}{\Gamma}\right) + \frac{\beta_{\pm}}{\pi}\left(\frac{1}{2} - \frac{1}{\pi}\arctan\left(\frac{2\epsilon_{\mp}}{\Gamma}\right)\right)}{1 - \frac{\beta_+\beta_-}{\pi^2}} \tag{2.34}$$

with $\beta_{\pm} = \arctan\left(\frac{2\epsilon_{\pm}}{\Gamma}\right) - \arctan\left(\frac{2\epsilon_{\pm}+2U}{\Gamma}\right)$. Equation (2.34) is particularly useful for fast computations and will be used later on in chapter 5 in the distant interaction model. In order to evaluate these quantities, experimentally relevant values are taken, $\Gamma = 1\text{meV}$, $U = 10\text{meV}$ and $T = 5\text{K}$. Therefore $\Gamma/U = 0.1$ and $U/kT = 23$ which is in agreement with the working hypothesis of EOM. As ϵ_d is tuned from 10mV to -20mV, the dot is successively filled with one electron at $\epsilon_d = -U/2$ and two electrons at $\epsilon_d = -3U/2$.

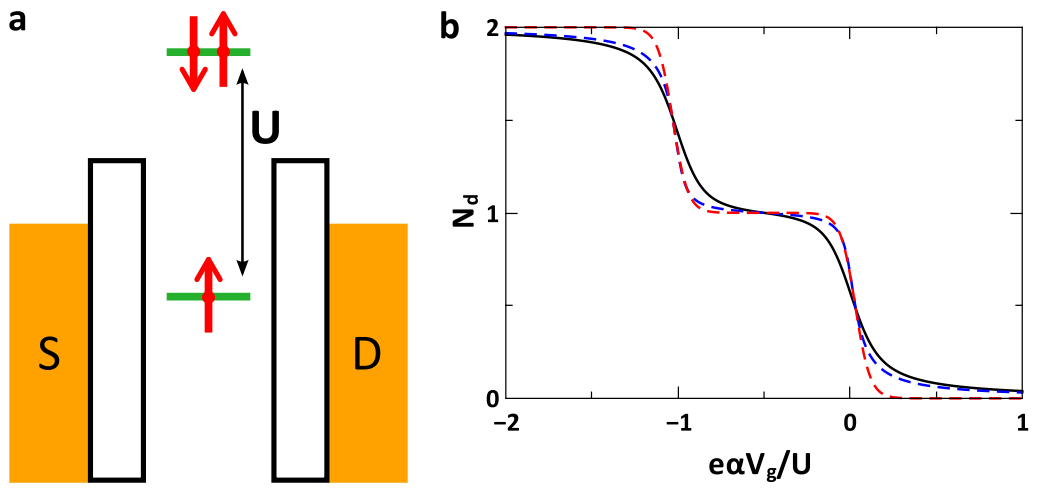

FIGURE 2.6: **a :** Scheme of the single orbital dot, with tunnel barriers and Fermi seas at Fermi energy on both sides. The energy between the single occupied and double occupied dot is the Coulomb energy U. **b :** Number of electron on the dot with regard to the dot energy $\tilde{\xi}_d/U$. Full EOM calculation using numerical evaluation of equation (2.28) (black curve), EOM with Lorentzian approximation at T=0, using analytical expression (2.34) (blue dashed curve) and sequential tunnelling regime using master equation approach (red dashed curve).

Figure 2.6 (b) shows the mean average occupation of the QD as a function of the gate voltage. Three different evaluations are shown. The black curve corresponds to the

full EOM calculation using numerical evaluation of equation (2.28). The blue dashed curve corresponds to the EOM with Lorentzian approximation at T=0, using analytical expression (2.34). Finally, the red dashed curve corresponds to the sequential tunnelling situation $\Gamma \ll kT$ solved with master equation technique for double occupancy single orbital (as treated in chapter 1). For this last case, the number of charges on the QD is directly given by

$$\langle n \rangle = \sum n_i p_i \tag{2.35}$$

with p_i defined by equations (B.3). The results presented here highlight the role of the full EOM treatment as the steps of the QD occupation are significantly smoothed, especially around $n = 1$.

2.2.4 Capacitance of the QD

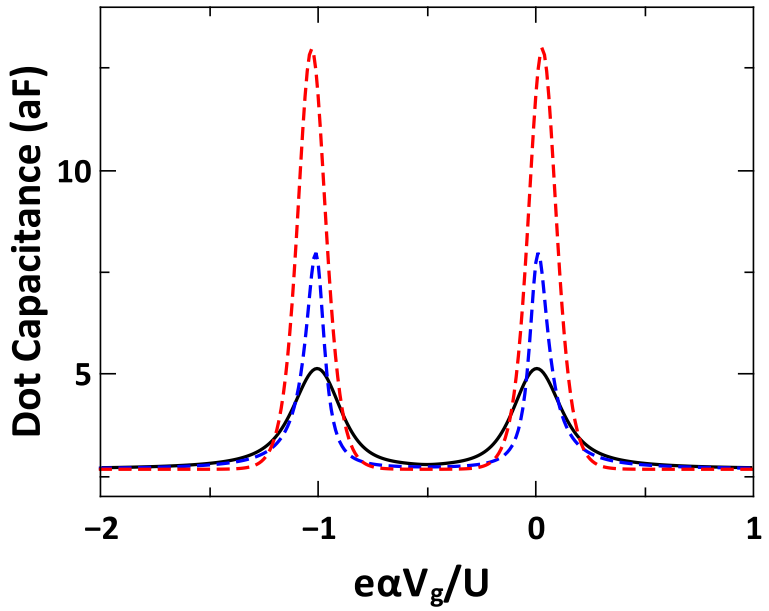

FIGURE 2.7: Mesoscopic capacitance of the QD responding to the AC voltage source in the three different situations addressed in this chapter. Full EOM calculation using numerical evaluation of equation (2.28) (black curve), EOM with Lorentzian approximation at T=0, using analytical expression (2.34) (blue dashed curve) and sequential tunnelling regime using master equation approach (red dashed curve).

Now that the average occupation number $\langle n_d \rangle$ on the QD versus the gate voltage has been determined, the effective capacitance of each capacitor due to the charge redistribution can be calculated. The average charge distribution on each capacitor plate reads

$$\langle Q_i \rangle = -\alpha_i e \langle n \rangle + V_i C_i + \alpha_i (\sum_j C_j V_j) \tag{2.36}$$

from which we it is easy to calculate the effective capacitance as

$$\begin{aligned} \tilde{C}_i &= \frac{\partial \langle Q_i \rangle}{\partial V_i} \\ &= -\alpha_i e \frac{\partial \langle n \rangle}{\partial \tilde{\xi}_d} \frac{\partial \tilde{\xi}_d}{\partial V_i} + C_i(1+\alpha_i) \\ &= -(\alpha_i e)^2 \frac{\partial \langle n \rangle}{\partial \tilde{\xi}_d} + C_i(1+\alpha_i) \end{aligned} \tag{2.37}$$

The mesoscopic capacitance responding to the AC voltage source is then as shown in figure 2.7 in the three different situations already discussdd in figure 2.6 for $\alpha_{AC} = 0.3$ and $C_{AC} = 2$aF. The height of the capacitance peaks, their width and positions are all affected by the considered model. As expected, for the full EOM treatment, the peaks are wide and small compared to the Lorentzian approximation and the sequential tunnelling regime.

It is important to compare the behaviour of the capacitance and of the differential conductance of the system, as both quantities are measured in the experiments performed in this work. Such study is presented in figures 2.8 and 2.9 for two sets of temperature $T = 2$K and $T = 5$K. The behaviour of the AC capacitance is similar to the one of the differential conductance. Nevertheless, by scaling the mesoscopic capacitance and the differential conductance, several differences in the two line shapes are visible, as shown in figure 2.9. First there is a significant difference between the relative peak heights. The peaks are also slightly shifted in $e\alpha V_g/U$ between dI/dV and $\tilde{C}$. Indeed at T=2K, the peaks are respectively found at $-U \pm 0.475U$ and $-U \pm 0.45U$ for the capacitance and the differential conductance, and at T=5K, $-U \pm 0.505U$ and $-U \pm 0.48U$ respectively.

2.2.5 Non-interacting limit and link between the capacitance and the spectral density

The EOM description is actually exact only in the non-interacting case $U = 0$. In this situation, the conductance simply writes

$$G_{\pm}(\omega) = \frac{1}{\hbar\omega - \epsilon_{\pm} + i\Gamma/2} \tag{2.38}$$

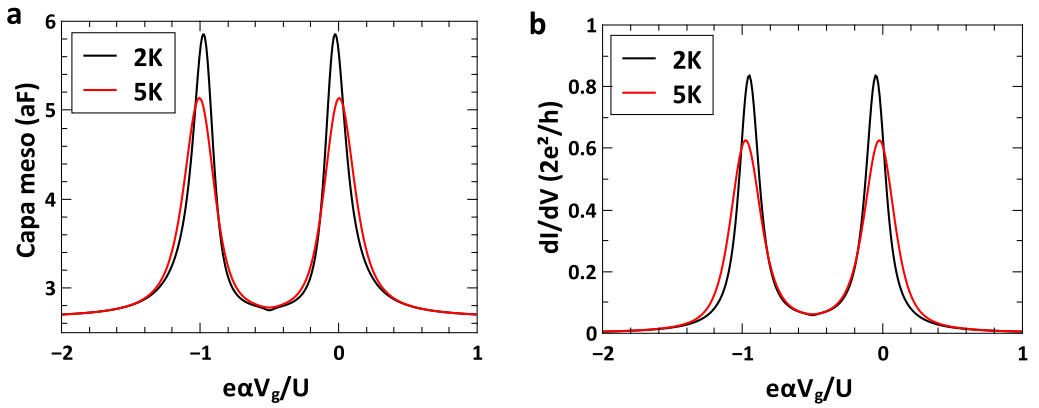

FIGURE 2.8: **a :** mesoscopic capacitance in regard with the AC voltage source versus $e\alpha V_g/U$ for two different temperatures T = 2 (black) and 5K (red). **b :** differential conductance through the dot in the same conditions in units of $2e^2/h$.

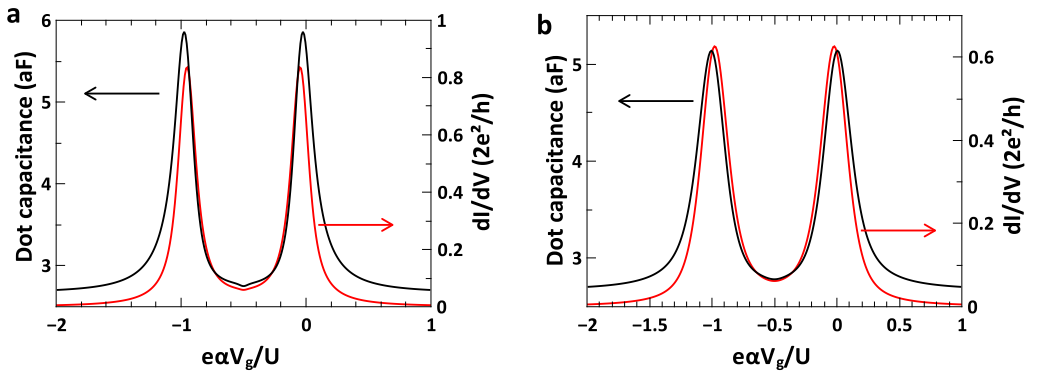

FIGURE 2.9: Comparison of the mesoscopic capacitance and the differential conductance with two different scales, C (black, left scale) and dI/dV (red, right scale). **a :** 2K and **b :** 5K.

which gives the following spectral density

$$A(\omega) = \frac{\Gamma}{2\pi} \frac{1}{(\hbar\omega - \epsilon_\pm)^2 + \Gamma^2/4} = \frac{2}{\pi\Gamma} \frac{1}{1 + \left(\frac{2\epsilon}{\Gamma}\right)^2} \tag{2.39}$$

Following the calculation steps detailed in appendix D.4, the average number of electron on the QD in the spin degenerate situation is

$$\langle n \rangle = 1 - \frac{2}{\pi} \arctan\left(\frac{2\epsilon}{\Gamma}\right) \tag{2.40}$$

which finally gives a quantum capacitance (following equation (2.37))

$$C_Q(U=0) = \frac{2e^2}{\pi\Gamma}\frac{1}{1+\left(\frac{2\epsilon}{\Gamma}\right)^2} \tag{2.41}$$

One directly see that the non-interacting capacitance $C_Q(U=0)$ is equal to the spectral density $A(\omega=0)$ (when proper dimension has been reintroduced in G). The introduction of interactions in the system, will make the weight of the capacitance to be less than the spectral density. Therefore, the full spectral density of a level constitutes an upper bound to the quantum capacitance value. As the spectral density of a level can be evaluated from its width from a spectroscopic measurement, it is straightforward to estimate this upper bound. This will be used in chapter 4 for the estimation of the electron-photon coupling in the Kondo regime.

Chapter 3

Experimental setup

3.1 Nanofabrication

An important part of the experimental work of this thesis is devoted to sample fabrication. Most of it has been done done in the clean room of the ENS and some thin film depositions were done at the clean room of the ESPCI (SBPC). As already emphasized, the challenge of the experiment was to combine two fields of mesoscopic physics, hence two different types of nanofabrication processes. On the one hand, there is the fabrication of superconducting coplanar waveguide resonators. On the other hand, the growth and contacting of carbon nanotubes. As we will see in this section, the merge of these two processes has been challenging as they are not really compatible. Indeed, superconducting films are not robust against the heating temperatures required to grow the carbon nanotubes by CVD. For their part carbon nanotubes are fragile to the usual etching techniques of superconducting resonators. The first process that we have developed was based on growing the carbon nanotubes inside the cavity, leading to the first sample we could measure, NTRES33a. The unreliable AC properties of the superconducting resonator and the low yield of contacted carbon nanotubes lead us to develop a reversed process where the quantum dots are done first, and the cavity is built as the last step. While challenging, this process lead to better success rates of functional quantum dots and the resonator suffered no alterations. In this section I will describe the different fabrication processes that I used to make the samples and I will detail the two different processes developed in my thesis.

3.1.1 Substrates

Choice of the substrate

The first stone of a nanodevice is the substrate on which the nano circuit is built. In our case, the choice of the substrate was determined by the resonator properties constrains. In order to achieve high quality factors, one must use highly resistive substrate to avoid at most dielectric losses. It has been recently demonstrated that internal quality factors between 10^6 at single photon level and 10^7 at high power are achievable with Al based CPW resonators on sapphire [77]. The other widely used substrate is passivated Si wafer with high resistivity. This kind of substrate allows lower quality factors resonator but still up to several 10^5 [78]. We chose to use the latter one as it is easier to manipulate and to perform e-beam lithography with reasonably small charging effects. Indeed, sapphire is so highly resistive that there is very little contrast in a scanning electron microscope (SEM) as the charges cannot escape through it, rendering every e-beam lithography difficult.

Characteristics and preparation of the wafers

Our wafer is 500μm thick highly resistive Si ($\rho \approx 10$kΩ.cm) with 500nm of thermally activated silicon oxyde SiO_2. Four inches wafers are diced in 10×10 square chips on which two devices will be processed. Every chip is labelled *NTRES#* and each of the two devices on a chip is labelled *a* or *b*. The CPW resonator is a macroscopic structure of several millimeters that requires the least amount of defects. It is thus important to first properly clean the substrate. It is done by cleaning the chips with the following recipe

Wafer cleaning

Acetone 10 min in ultrasonic bath

IPA 10 min in ultrasonic bath

Piranha acid (H_2SO_4/H_2O_2 with ratio 3:1) 15 min

3.1.2 Lithographies

The main purpose of nanofabrication is to make metallic structures that will define the device. In order to draw the device pattern, we use either electronic or optical

lithography. Although they technically differ, both relies on the same concept and the main steps of creating this metallic pattern with lithographies is schemed in figure 3.1. The polymeric bonds of the resists are altered either with an electron beam or by UV on specifically patterned regions. These exposed regions can then be removed with a specific developer, while the unexposed resist remains on the wafer.

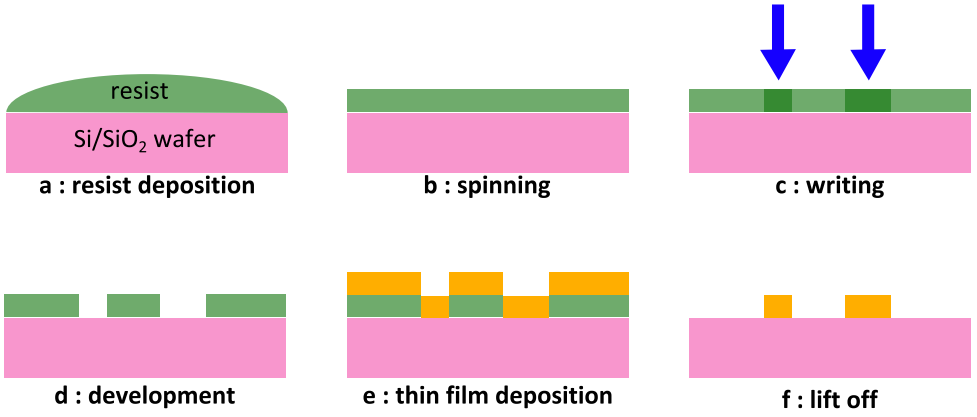

FIGURE 3.1: Nanofabrication processes. **a:** resist deposition on the substrate, **b:** spin coating of the resist to form an uniform layer of resist, **c:** exposure of the resist with either electron beam or UV, **d:** development of the resist to remove the exposed pattern, **e:** thin metallic film deposition on the sample, **f:** lift off to remove the unexposed resist and the metallic film upon it.

e-beam lithography

E-beam lithography is usually used for making nanometer to micrometer range structures as it offers a resolution close to few nanometers. We use it to build the quantum dot on carbon nanotube where electrodes of few hundreds of nanometer are made with a precision of fifty nanometer. In a first process, we also use e-beam lithography to build the resonator, even though this structure is millimetric in size. The resist that we use is poly-methyl-methacrylate (PMMA) diluted in anisol. It is an electronic positive resist, which means that what is exposed is being removed at the development step. We prepare the PMMA layer by depositing two to three drops of PMMA on the chip and spin coating it at 4000 rounds.min$^{-2}\times$ 4000 rounds.min^{-1} during 30s. It is then baked at 165°C for 15 minutes. This makes a PMMA layer of 500nm. It can also be useful for some steps to make thicker PMMA layer. It is achieved by repeating this process one more time, which leads to a 1000 μm layer.

Different parameters can be tuned to adapt the e-beam writing to one needs. They consist in the acceleration voltage of the gun, the aperture size of the beam, the dose of exposure and the step size of the beam. We use an acceleration voltage of 20kV for writing purposes and 2kV for observation of carbon nanotubes. The latter is necessary

in order to avoid damaging the nanotubes. The aperture size is an important parameter for writing speed. The smaller the size of the aperture, the more resolution we get but the longer the lithography will take. The exposure dose, expressed in μC.cm^{-2} reflects the amount of charges that is injected in the resist per area unit. For every couple of parameters of acceleration voltage and aperture size, the electronic current of the beam is measured. Then a step size is set, defining the resolution of the structure as the minimal area. Finally, the dwell time of the beam on each minimal area is calculated, knowing the beam current and the required dose. This exposure dose is actually a critical parameter of the e-beam lithography. Indeed, too small a dose results in a pattern that will not be developed due to under exposure. On the other hand, too high dose will result in enlarged structures that can overlap. It is thus advised to perform a dose test for every new process. Finally, the exposed pattern is removed by developing it in a methyl-isobutyl-ketone:isopropanol (MIBK ratio 1:3) solution during 2 minutes.

UV lithography

UV lithographies are usually used for large structure and offer a maximum resolution of 1μm. The main advantage of UV lithography over e-beam lithography is that it is much faster and can be operated easily on large wafers up to 4 inches. Once the process is optimized, it takes about 15 minutes to obtain a developed resist pattern. For example, writing a resonator with e-beam lithography takes about one hour while it takes only 15 minutes to write up to 50 resonators at with UV lithography. In the second device recipe, we used UV lithography to make the resonator as the final step of the process. The resist we use is the AZ5214E, which can be used as both positive (what is exposed is removed) or negative (what is exposed remains) resist. The process differs for each use. We use the same parameter for spin coating this resist on the sample but only cook it 1'30" at 120°C and obtain a 1200nm thick layer of resist. To draw the desired pattern, we need a mask that blocks up the UV except where we want to expose the resist. The pattern of the mask is made of chromium, which is put in contact with the resist of the sample. We use the AZ5214E resist as a negative resist and thus must perform several steps to obtain the desired result. First there is an exposition of the resist that breaks the bondings between the polymeric chains of the resist. The sample is then baked again for 1'30" at 125°C. New bonds are formed between the resist chains in these exposed regions. These are actually stronger than the unexposed ones. Then the sample is flooded with UV on all its surface in order to break the polymeric chains of the unexposed regions. Thus after development, only the resist where we first made make the exposure with the chromium mask remains.

UV lithography for resonator

1. 1.2μm thick AZ5214E resist : 4000/4000/30 spin coating + 1'30" of baking at 120°C).
2. UV exposure during 3s with hard contact (5s).
3. baking at 125°C for 1'30".
4. UV flooding during 30s.
5. development : MIF 746 for 15s

3.1.3 Thin films deposition

After lithography is done and the sample is developed, we usually deposit a metal layer on the sample as shown in figure 3.1 (**e**). This allows to create the metallic structures of the device. This is done in an evaporator where a metal ingot is heated above its melting temperature, creating a conical jet of atoms that deposits on the surface of the sample above. The thickness of the layer is controlled via a quartz inside the evaporator that lies within the evaporation cone. The sharp resonance of the quartz is modified by the mass of the evaporated layer, giving a precision on the evaporation rate up to 0.1Å.s^{-1}. The heating of the metal ingot can be achieved by either Joule effect or with an electron beam. Joule effect evaporator are usually small and easy to manipulate but only usable for metal with low melting point like gold or aluminium. For higher melting point metal like niobium, palladium or titanium, we use an electron beam evaporator at the ESPCI (SBPC).

The key point of evaporating thin films layer is to obtain the purest layers. To achieve this, we need high vacuum or even ultra high vacuum (UHV) in order to avoid at most the number of impurities in the layer. Heating the metal ingot induces desorption of impurities lying in the evaporator and increases the pressure inside it. It is therefore a competition between a high enough evaporating rate and a low enough pressure to ensure good thin films quality. The vacuum of the Joule evaporator of the ENS is made by a turbo molecular pump (TMP) and we usually reach 10^{-6} to 10^{-5} mbar during evaporation, which is enough for gold. On the other hand, some materials like niobium require sharper conditions. The value of the Tc and the residual resisitivity ratio (RRR) of niobium[1] depend strongly on the number of impurity in the layer. A rate of few Å.s^{-1}

[1]These two parameters are crucial to ensure good superconducting properties.

at around 10^{-7}mbar is needed. We achieve these constrains with a TMP, an ion pump and titanium sublimation to get a base vacuum of the order of 10^{-8}mbar.

3.1.4 Reactive ion etching

A fast and convenient method to make CPW resonator is reactive ion etching (RIE). Dry chemical etching of the metal layer is done by a plasma. The plasma is made with various different gases, depending on the metallic layer. For this process, the metallic layer is usually deposited on all the wafer's surface and lithography is done on top of it. The success of this process is that the metallic layer is etched faster than the resist layer. As niobium is easily etched by SF_6 plasma (200 nm in approximately 30 s). However, this technique is limited to a restricted number of metals as for example aluminium cannot be etched with it. O_2 plasma RIE is also widely used to clean samples by removing all organic deposit on the surface. It is often use to remove resist remains on the sample and especially in the gaps of the resonators. Carbon nanotubes thus do not resist this treatment and it is impossible to clean the gaps of the resonator with this technique. SF_6 plasma should not destroy CNTs in principle but can affect their atomic structure by adding defects or inclusions. This explains why the first process was based on growing the CNTs inside the already etched resonator.

3.1.5 Carbon nanotubes growth

The key ingredient of our devices is the carbon nanotube. Ijima in 1991 [79] was the first to control the growth and characterize carbon nanotubes. This material exhibits good physical, electrical and chemical properties. This work by Ijima initiated the development of various methods to produce carbon nanotubes such as arc discharge, laser ablation or chemical vapour deposition, boosted by the wide range of interest of this material. We use a chemical vapour deposition (CVD) technique based on methane and molybdenum oxide catalyst. We need single wall carbon nanotubes (SWNT) with semiconductor behaviour and the recipe we use was purposely developed to favour the synthesis of such.

Catalyst

The first ingredient we need is the catalyst. It is made of nanoparticles of three different types of oxides in solution. The exact composition is 39mg of $Fe(NO_3)_3$-H_2O, 7.9mg of MoO_2 and 32mg of Al_2O_3 diluted in 30mL of methanol. CNTs will actually grow from the nanoparticles deposited on the sample's surface. Where we want CNTs to grow, we

make square holes of 1μm are made by e-beam lithography in the resist. One to two drops of catalyst are deposited on the sample and it only remains on the surface where the square windows were made. It is important here to have two-layer thickness of PMMA in order to obtain well defined catalyst spots. Otherwise, the catalyst solution can leak near the hole, ending with a wide area of catalyst on the sample as shown in figure (3.2). Then lift-off is proceeded to remove the PMMA. In order to avoid redeposition of catalyst on the surface, the lift-off is made with several beaker of acetone. The overall detailed process is described in box (3.1.5).

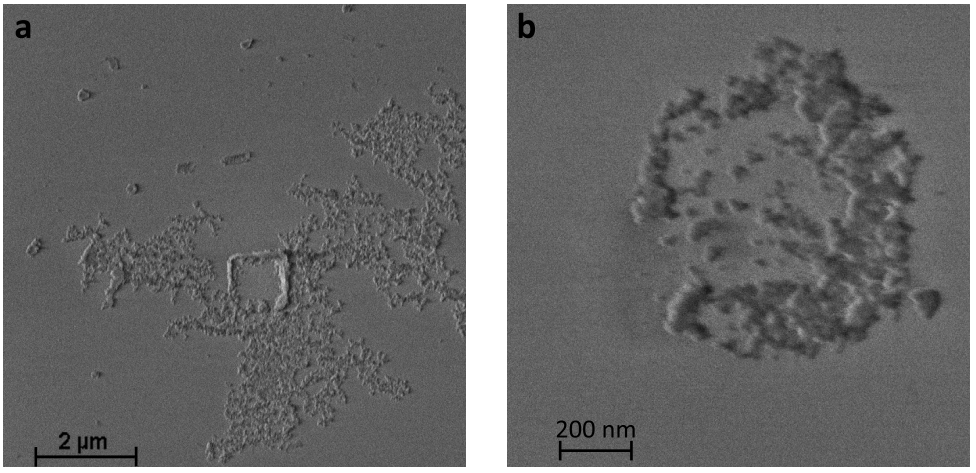

FIGURE 3.2: Catalyst deposition with (**a**) one layer of PMMA (500nm thickness) and (**b**) two layers of PMMA (1μm thickness). Catalyst spread away from the lithographied hole in the case of one layer of PMMA on an area up to 10μm×μm.

Catalyst deposition

Resist : 1μm thick layer of PMMA (two layers technique)

e-beam lithography : 1μm square holes. Acceleration voltage : 2kV, aperture : 10 μm, XY step size : 20nm, exposure dose : 300 μC.cm^{-2}. MIBK development : 2 minutes.

Catalyst solution : 1h of ultrasonics to break the particles clusters, then 45 min of settling.

Catalyst deposition : 1 or 2 drops of the upper part of the catalyst solution is deposited on the surface of the sample and is immediately dried with nitrogen flow.

Lift off : 4 successive beakers filled with acetone : 30"/60"/90"/180". The sample is then cleaned in IPA.

Step	**Time (min)**	**Temperature (°C)**	**Ar (mL/min)**	**H_2 (mL/min)**	**CH_4 (mL/min)**
purge	3	20	1500	220	1100
heating	$\sim$ 20	20 to 900	1500	0	0
H_2 flash	8	900	0	220	0
growth	10	900	0	220	1100
cooling (1st step)	$\sim$ 180	900 to $\sim$ 300	1500	220	0
cooling (2nd step)	$\sim$ 60	to 20	1500	0	0

TABLE 3.1: Carbon nanotube CVD growth process.

Chemical vapour deposition

Once catalyst is deposited on the sample, the growth of CNTs can be performed. The sample is put in an oven that reach 900°C. We use three different gases. Argon (Ar) as a neutral gas, hydrogen (H_2) as a reducer for catalyst nanoparticles and methane (CH_4) as the carbon source. The protocol for the growth is described in table (3.1).

Issues with superconducting resonators

As already mentioned, superconducting resonators and CNTs are quite incompatible. We first thought that growing CNTs inside the resonators would be the easiest way of making the device and we thus focused on this process. first, the high temperature required for CVD limits the type of superconductor that we can use. Aluminium films would indeed be severely altered as their melting point is 660°C. On the contrary, Niobium with its high melting point seems perfectly suited for this. Unfortunately, niobium does not resist CVD growth and even becomes non metallic after the process. The film is matted and looks greyish. To overcome this, we protect niobium with platinum (usually 30nm of Pt over 200nm of Nb). The interest of this process is that Pt becomes superconductor by proximity effects and the layer doesn't look altered after the growth. DC measurements of the Tc of the superconducting thin film shows a drop from 9.2K before the growth to 8K after the growth as shown in figure (3.3). However, the AC properties of the film turn out to be severely altered probably by the formation of grain boundaries at temperature above 600°C in the presence of impurities. These grain boundaries acts as scatterers that dissipates the AC excitations. This resulted in relatively low quality factors of our resonators, below 1000, compared to the expected 10000.

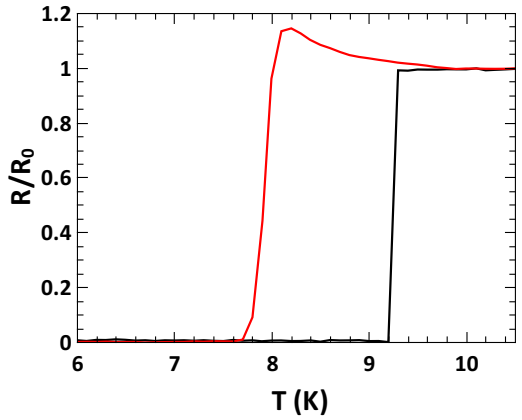

FIGURE 3.3: Van der Pauw measurement of Nb/Pt (200nm/30nm) thin films critical temperature before CNT growth (black line) and after CNT growth (red curve). The ratio between the resistance before transition R_0 and the measured resistance is plotted. The Tc drops from 9.2K to 8K after the CVD growth.

3.1.6 Contacting carbon nanotubes

The confinement of CNT to form the QD is achieved by contacting it with metallic electrodes. This step breaks the atomic structure of CNT at the contacts points, creating tunnel barriers from the electrodes to the CNT. This step is thus critical because the lithography parameters and choice of electrodes metal will ensure the best contact possible from the CNT QD to the external world.

Localizing carbon nanotubes

After the growth, a first observation of CNTs is made with the SEM (EHT : 2kV, aperture : 10μm, magitude $\leq$ 2k). The purpose of this step is to quickly take pictures of the different growth zone of each resonators and then determine which CNT will be contacted in each of the four available areas (see figure 3.4 a). Once this choice is made, precontacts and alignment crosses defining a 100μm$\times$100μm are made in gold for each of the four chosen CNTs (see figure 3.4 b). Finally, by aligning with the SEM on these crosses, precise pictures of the CNTs are taken. These SEM micrograph are inserted in the mask editor at the right coordinates and the electrodes are then directly drawn on top of the imaged CNTs as shown in figure 3.5.

Fine structures

Alignment of the e-beam writer is made on the same crosses as in the localization step in order to be in the same coordinate. To avoid any overlap between the 500 nm wide

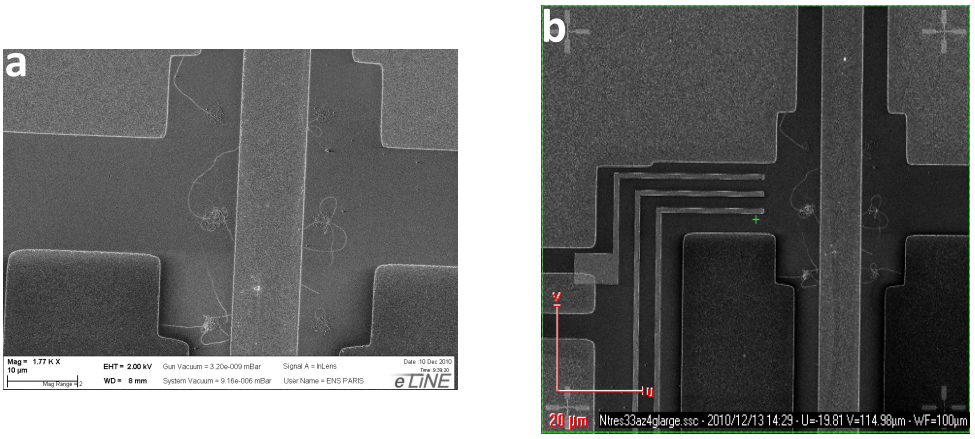

FIGURE 3.4: SEM observation of the CNTs. **a :** first rough observation of the CNTs after the CVD growth. We see CNTs grown from catalyst inside the gap of the CPW resonator. **b :** Fine localization of the CNT of the chosen zone. The localization is made by aligning on the gold alignment marks on each corner. The gold precontacts are also visible.

electrodes separated by 500 nm, the exposition dose must be of 250μC.cm^{-2}. However, all the resist must be removed on the CNT itself to ensure good galvanic contact. It is achieved by significantly increasing the exposition dose to 360μC.cm^{-2} at the contact point of each electrodes. The fine structures are made with standard parameters (EHT : 2kV, aperture : 10μm, XY step size : 20nm). CNTs are then contacted with Pd electrodes which provides the best coupling between the two structures (need ref here !). Once a CNT is contacted, it is exposed to electrostatic shocks and the greatest care must be undertaken to avoid damaging the CNTs.

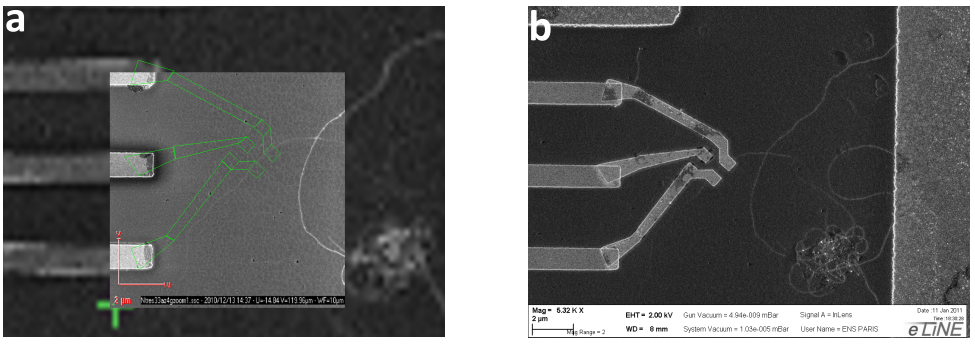

FIGURE 3.5: Fine structure contacting the CNT. **a :** mask drawing directly on the localization SEM micrograph. **b :** Pd fine structures after lithography, evaporation and lift-off.

3.1.7 Two recipies

As mentioned at the beginning of this section, two different processes where developed to make the devices. Although the second method we developed gave better quality samples, it is important to report both. Indeed, the first process was easier to implement with our initial knowledge and the first working sample we made that lead to the first measurement of the coupling of a CNT QD to a microwave resonator was made with it.

First recipe : Resonator before CNT growth

The major difficulty of this process was to make the superconducting film survive the CVD growth (at least in DC). It was requested that the protection layer can endure the high temperature without diffusing as well as it should not alter the superconductivity of the niobium. Several candidates were tried. We first tried to protect niobium with palladium but it acted as a catalyst for CNT growth and the CNT density was too high. Titanium was also tried but was similarly altered. The solution was found in platinum which becomes a superconductor by proximity effect and cannot be corroded.

1. **Wafer cleaning :** as described on page 64.
2. **Resonator**
   (a) **e-beam resonator**
      i. 1μm thick PMMA : 2 times (4000/4000/30 spin coating + 15 min of baking at 165°C).
      ii. e-beam lithography : voltage 20kV, aperture 120μm, XY step size 200nm, curve step size : 140nm, dose : 300μC.cm$^-$2.
      iii. development : MIBK:IPA (1:3) for 2 min.
   (b) **UV lithography resonator**
      i. 1.2μm thick AZ5214E resist : 4000/4000/30 spin coating + 1'30" of baking at 120°C).
      ii. UV exposure during 3s with hard contact (5s).
      iii. re baking at 125°C for 1'30".
      iv. UV flooding during 30s.
      v. development : MIF 746 for 15s
   (c) **Nb/Pt evaporation :** electron gun evaporation. 200nm of Nb at 2Å.s^{-1} and pressure P= 10^{-7}mbar. 30nm of Pt at 2Å.s^{-1} and pressure P= 10^{-7}mbar.

(d) **RIE :** SF_6/O_2 (25sccm/2sccm) plasma. It takes approximatively 3 min to remove the Pt layer and 30s to remove the Nb layer.

3. **CNT growth :** catalyst deposition as described on page 69 and CVD growth as described in table 3.1.

4. **CNT observation :** SEM imaging. voltage 2kV, aperture 10 μm, maximum magnification 1.5k.

5. **Precontacts and alignment marks (100μm $\times$ 100μm field)**

   (a) 500nm thick PMMA : 4000/4000/30 spin coating + 15 min of baking at 165°C.

   (b) e-beam lithography : voltage 20kV, aperture 10μm, XY step size 20nm, dose 250μm.cm^{-2}.

   (c) development : MIBK:IPA (1:3) for 2 min.

   (d) chromium/gold evaporation : Cr/Au (1.5nm/50nm). Chromium is used as an adhesion layer. Evaporation is performed in a joule effect evaporator. $P_{Cr} \approx 10^{-5}$mbar and $P_{Au} \approx 10^{-6}$mbar.

   (e) lift off in acetone at T=45°C.

6. **CNT localization :** SEM imaging with fine alignment on the alignment marks. voltage 2kV, aperture 10 μm, magnification 1k.

7. **Fine structures :**

   (a) 500nm thick PMMA : 4000/4000/30 spin coating + 15 min of baking at 165°C.

   (b) e-beam lithography : voltage 20kV, aperture 10μm, XY step size 20nm, dose 360μm.cm^{-2} on the CNT, 250μm.cm^{-2} elsewhere.

   (c) development : MIBK:IPA (1:3) for 2 min. It is critical to develop at least 2 min to be sure to remove all the resist on the CNT.

   (d) Pd evaporation : electron gun evaporation of 100nm of Pd at P$\approx 10^{-7}$mbar.

   (e) lift off in acetone at T=45°C.

Second recipe : CNT growth before resonator

It turns out that CVD significantly alters the AC properties of superconductor thin films. Better results can be obtained by reversing the process. The issue then is that we must align the contacted CNT with the resonator at micrometric precision. Since growth

is done before, RIE can't be used since it could damage the SWNTs. This constrain lead to the choice of a lift-off technique to make the resonator. UV lithography has been chosen to do so, as it is convenient for quickly developing a process. The quantum dot is built first (CNT + fine structures + precontacts) and is aligned it in the gap of the resonator. The choice of a negative UV process allows to see the QD structure inside the gap of the resonator during the alignment procedure. Then the tricky part is the lift off of Nb thin films. Indeed, the high temperature of Nb evaporation "bakes" the resist on the sample during deposition, hardening the resit. The lift-off becomes impossible, even with smooth evaporations. Thus, Al thin film resonators have been developed first because they are easily lifted. With this process, sample NTRES52a has been produced, in which two quantum dots where "alive" in the cavity and which results will be discussed in chapter. As the cryostat in use for this experiment is a VTI with a base temperature of 1.4K, and as aluminium Tc=1.19K, we continued to work on Nb and it was found that sputtered Nb thin film can be lifted with the right sputtering parameters.

1. **Wafer cleaning :** as described on page 64.
2. **Large alignment marks (1000μm $\times$ 1000μm field)**
   (a) 500nm thick PMMA : 4000/4000/30 spin coating + 15 min of baking at 165°C.
   (b) e-beam lithography : voltage 20kV, aperture 120μm, XY step size 200nm, dose : 300μC.cm$^-$2.
   (c) development : MIBK:IPA (1:3) for 2 min.
   (d) Ti evaporation. Ti has a good adhesion on Si/SiO_2 substrate and survives CVD.
   (e) lift off in acetone at T=45°C.
3. **CNT growth :** catalyst deposition as described on page 69 with alignment on the Ti marks and CVD growth as described in table 3.1.
4. **CNT observation :** SEM imaging. voltage 2kV, aperture 10 μm, maximum magnification 1.5k. To find the CNTs, it is necessary to find the Ti marks. The contrast between Ti and Si/SiO_2 substrate is very low. Nevertheless, the marks can easily be found by using looking at the secondary electron detector of the SEM.
5. **Precontacts and alignment marks (100μm $\times$ 100μm field)**

(a) 500nm thick PMMA : 4000/4000/30 spin coating + 15 min of baking at 165°C.

(b) e-beam lithography : alignment on the Ti marks with the secondary electron detector. voltage 20kV, aperture 10μm, XY step size 20nm, dose 250μm.cm^{-2}.

(c) development : MIBK:IPA (1:3) for 2 min.

(d) chromium/gold evaporation : Cr/Au (1.5nm/50nm). Chromium is used as an adhesion layer. Evaporation is performed in a joule effect evaporator. $P_{Cr} \approx 10^{-5}$mbar and $P_{Au} \approx 10^{-6}$mbar.

(e) lift off in acetone at T=45°C.

6. **CNT localization :** SEM imaging with fine alignment on the gold alignment marks. voltage 2kV, aperture 10 μm, magnification 1k.

7. **Fine structures :**

(a) 500nm thick PMMA : 4000/4000/30 spin coating + 15 min of baking at 165°C.

(b) e-beam lithography : voltage 20kV, aperture 10μm, XY step size 20nm, dose 360μm.cm^{-2} on the CNT, 250μm.cm^{-2} elsewhere.

(c) development : MIBK:IPA (1:3) for 2 min. It is critical to develop at least 2 min to be sure to remove all the resist on the CNT.

(d) Pd evaporation : electron gun evaporation of 100nm of Pd at P$\approx 10^{-7}$mbar.

(e) lift off in acetone at T=45°C.

8. **resonator**

(a) **UV lithography resonator aligned on the contacts**

i. 1.2μm thick AZ5214E resist : 4000/4000/30 spin coating + 1'30" of baking at 120°C).

ii. UV exposure during 3s with hard contact (5s). At this step, the alignment and overlap between precontacts and DC lines is made with the microscope of the UV masker.

iii. re baking at 125°C for 1'30".

iv. UV flooding during 30s.

v. development : MIF 746 for 15s

(b) Al evaporation

i. Al evaporation : 330nm at 10Å.$^{-1}$ at P $\approx 10^{-6}$mbar.

ii. lift off in hot acetone T=45°C.

(c) Nb sputtering

i. Nb sputtering (150nm) with Ar (5.5) : $P_{before} = 4.10^{-7}$mbar, $P_{sputtering} = 10^{-2}$mbar, rate = 20Å.$^{-1}$. Power supply : I=1.02A, V=328V.

ii. lift off in hot acetone T=45°C.

3.1.8 Typical sample

The samples fabricated and measured in this thesis present the same geometry and features, as presented in figure 3.6. The two antinodes regions of the CPW resonator present opening in the ground plane which are presented in 3.6 (b). For each region, 3 DC lines are lithographied in order to contact the SWNT. Therefore, up to 4 QDs can be contacted in the same cavity. Each antinode area presents 4 CNT growth windows on each side of the resonator's transmission line. In order to locate each contacted SWNT in a resonator, they are numbered by the window number, starting from the left of the resonator (ranging from 1 to 8) and by the side of the transmission line they lie (G for "gauche" - left- and D for "droite" -right). This leads to samples name like NTRES33bZ4D for example.

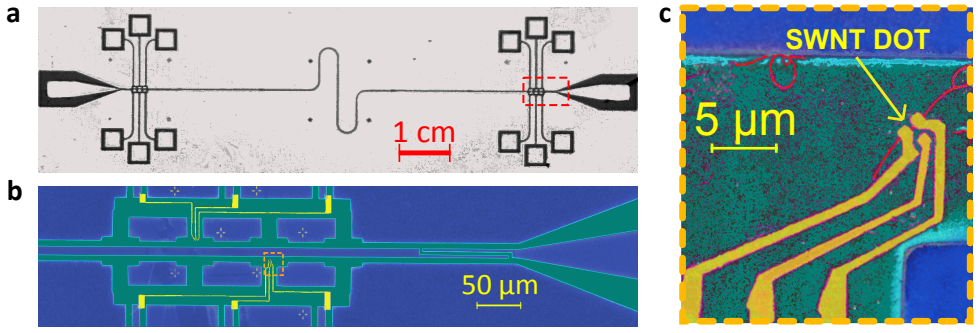

FIGURE 3.6: **a :** photograph of a CPW resonator in Nb/Pt or Al. **b :** optical micrograph close up in false colors of the ground plane openings where the SWNT QDs are contacted. The superconductor is in blue and the dielectric in green. **c :** SEM micrograph in false colors of the contacted QD with source, drain and gate electrodes. The blue represent the superconductor (transmission line and ground plane), the yellow is for the Pd electrodes, the SWNT is in red and the dielectric in green.

The coupling gaps of the resonator, as shown in figure 3.6 (b), are finger gaps, of length 100μm. They define a coupling capacitance of about 4fF, leading theoretically to quality factors up to 12000. Quality factors up to 8000 have been measured in raw resonators in Nb without any CNT growth as shown in figure 3.7. The cavity spectrum of complete devices with SWNT QDs will be presented in the following chapter.

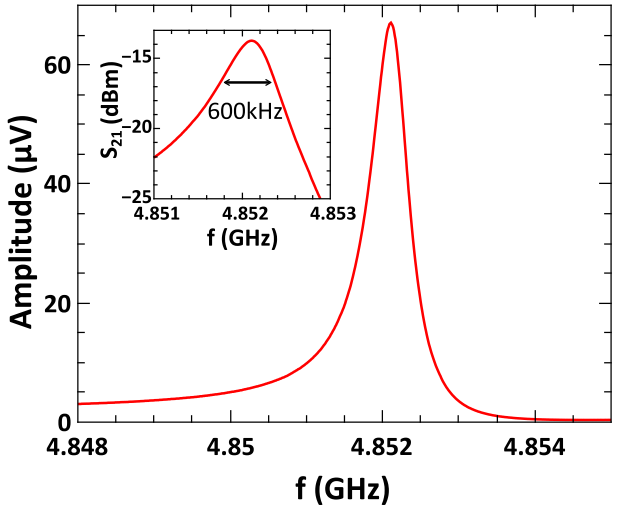

FIGURE 3.7: Amplitude of the transmitted microwave field through a Nb CPW resonator that did not get altered by CVD. In the insert is a zoom on the resonance, in units of transmission coefficient S_{21}. The arrows shows the width of the resonance at -3dB, giving a quality factor of about 8000.

The SWNT are contacted within 5μm of the transmission line, in the gap of the CPW resonator, as shown in the SEM micrograph of figure 3.6 (c).

3.2 Measurement techniques

3.2.1 Low noise measurements

We are interested in measuring the electronic properties of carbon nanotube based quatum dots (CNT QD). Thus we need to measure the current flowing through the system. As already described in chapter 1, driving the QD requires three electrodes. Source and drain electrodes to bias the QD and a gate electrode to tune its energy. The CNT is usually voltage biased and the generated current is measured. It is possible to either measure the current or the differential conductance directly. In this thesis, the measurement of the differential conductance was performed. It is done with a lock in demodulation technique that allows to significantly reduce the noise of the signal. The CNT is biased by a combination of a DC voltage V_{sd} and a low frequency AC signal $V_{AC} \ll V_{sd}$, V_G at frequency ω_{AC} generated by the lock in as shown in figure 3.8. The resulting bias is

$$V_{bias} = \frac{\frac{V_{sd}}{10k} + \frac{V_{AC}}{100k}}{\frac{1}{100} + \frac{1}{10k} + \frac{1}{100k}} \approx \frac{V_{sd}}{100} + \frac{V_{AC}}{1000} \tag{3.1}$$

The current I through the CNT can be expanded as

$$\begin{aligned} I(V_G, V_{bias}) &= I(V_G, V_{sd} + V_{AC}\cos(\omega_{AC}t)) \\ &= I(V_G, V_{sd}) + V_{AC}\cos(\omega_{AC}t)\frac{\partial I}{\partial V_{bias}}\bigg|_{V_G, V_{sd}} + O(V_{AC}^2\cos^2(\omega_{AC}t)) \\ &= I(V_G, V_{sd}) + V_{AC}\cos(\omega_{AC}t)\delta G(V_G, V_{sd}) + O(V_{AC}^2\cos^2(\omega_{AC}t)) \end{aligned} \tag{3.2}$$

with δG the differential conductance of the system. The homodyne demodulation of the lock-in removes all term that are not in $\cos(\omega_{AC}t)$ and we end measuring only $V_{AC}\delta G(V_G, V_{sd})$. V_{AC} is set to 100 mV so that the effective AC excitation of the system is 100μV.

We know that the conductance quantum corresponding to one electronic channel with unitary transmission is $G_0 = \frac{2e^2}{h} \approx 77\mu S$. One channel accounts for the spin degree of freedom. In CNT, there are four conduction channels, two for spin and two for orbital valleys. The maximum reachable conductance is then $G_{max} = \frac{4e^2}{h}$. considering our AC drive, the maximum possible current through the QD $I_{max} \approx 15$ nA. The current of small coupled CNT QD exhibiting strong Coulomb blockade regime can drop below 1pA. It is thus necessary to properly amplify this current with a transimpedance amplifier as shown in figure 3.8. The amplification is directly given by the negative feedback resistor R_a, converting a current I in a voltage $-R_aI$. To avoid the noise, the amplifier is connected the closest possible to the sample, at the cryostat head. It is also power supplied by battery to avoid the electrical network noise or power cut. We use a commercial amplifier *DL Instrument 1211 preamplifier* set on a transimpedance gain 10^6 as well as a homemade amplifier based on the OPA657. This setup allows to measure pico amps with noise of about 100 femto amps.

The gate voltage line is noise filtered by a high impedance resistor as shown in figure 3.8. This resistor in parallel with the capacitance of the DC line makes a RC filter with frequency cut at $f_c = \frac{1}{2\pi RC} \approx 80$Hz. It is important to place it on the cryostat head in order to filter the noise that has been caught by the BNC cable from the voltage source to the cryostat.

3.2.2 Microwave techniques

Simultaneously to the low frequency measurement of the differential conductance of the QD, the transmitted microwave signal through the CPW cavity is measured. This is

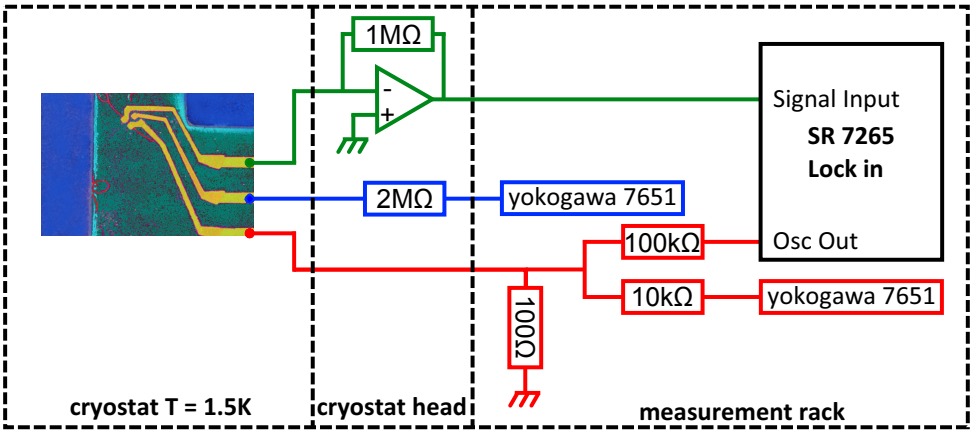

FIGURE 3.8: **Low frequency measurement setup.** The gate voltage line is represented in blue, the source and drain lines are respectively represented in red and green. The bias excitation (red) is the addition of a DC voltage source (yokogawa 7651) and a low frequency AC voltage from a lock-in amplifier. This bias creates a current in the CNT that is amplified by a trans-impedance amplifier at room temperature that converts current into voltage (green). The signal is demodulated in the lock-in. The gate voltage line (blue) is filtered by a 2MΩ resistance.

done with commercial microwave devices in a measuring chain that can be considered the electronic counterpart of optic tables. The RF measurement setup is presented in figure 3.9. The measurement principle is based on signal modulation and demodulation in order to extract both the in-phase (I) and out-of-phase (Q) quadratures of the transmitted microwave field. The up and down conversions are done with double balanced mixers. We use a signal generator (Agilent E8257D) to generate the local signal at frequency $\omega_{LO} \in$ [4;8] GHz at a power P_{in} =18dBm

$$\mathcal{A}_{LO} = A_{LO}\cos(\omega_{LO}t + \phi_{LO}) \tag{3.3}$$

The output power of the RF source is adjusted to adapt to the input power working points of the both the up-converter mixer and the IQ mixer[2]. This signal is mixed with a low frequency signal coming from a lock-in amplifier at frequency ω_{IF} =777.77Hz in an up-converter.

$$\mathcal{A}_{IF} = A_{IF}\cos(\omega_{IF}t + \phi_{IF}) \tag{3.4}$$

with A_{IF}=0.5V. The resulting RF two-tone sideband signal is

[2]respectively [7;10] dBm and [10:13] dBm

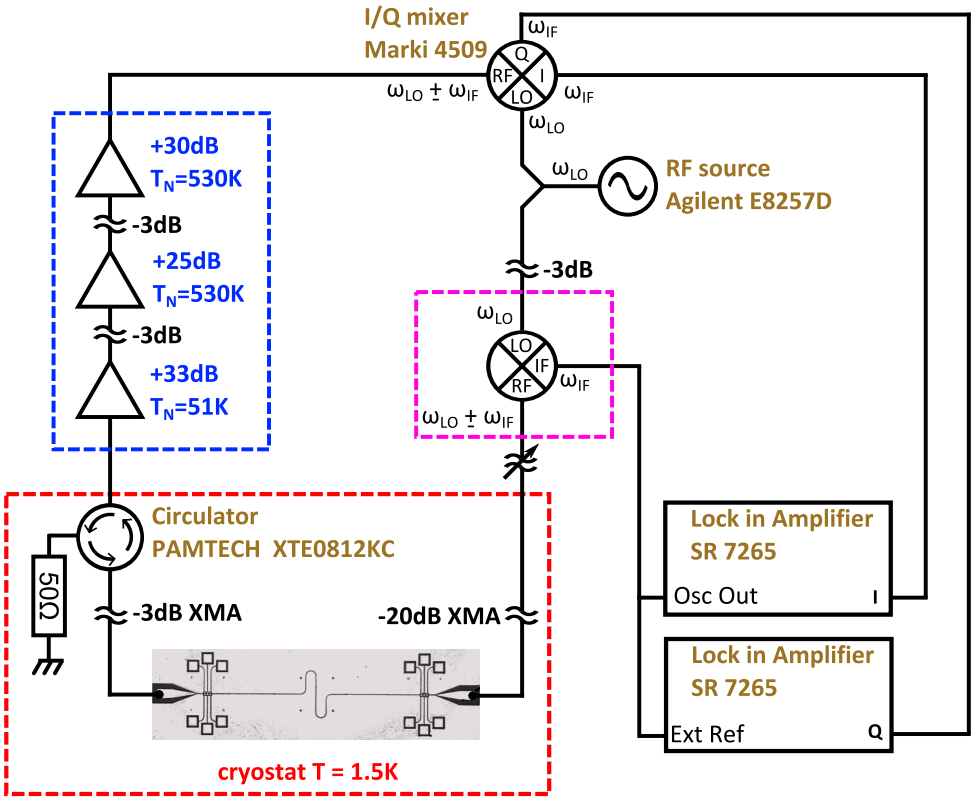

FIGURE 3.9: **RF measurement setup.** The RF local signal at 4GHz$\leq \omega_{LO} \leq$ 8GHz generated by an Agilent source E8257D is mixed with the AC signal of a lock-in amplifier at ω_{IF} =777.77Hz in a two side band up converter setup (dashed pink square). This generates a RF signal, modulated in amplitude at $\omega_{RF} = \omega_{LO} \pm \omega_{IF}$. The superconducting cavity in the cryostat is driven by this signal (dashed red square) at T=1.5K. At the output of the cavity is a cryogenic isolator that reduce the back action noise of the first amplifier by 18dB. The transmitted signal is amplified in an amplification chain of G=82dB (dashed blue square). A 3dB attenuator is put between every amplifier to kill resonant modes. The amplified signal is down converted with the RF local signal in an IQ mixer. The two in-phase (I) and out-of-phase (Q) quadratures of the field at frequency ω_{IF} are demodulated in the lock-in amplifier.

$$\mathcal{A}_{RF} = \frac{A_{LO}A_{IF}}{2}\left[\cos((\omega_{LO}-\omega_{IF})t+\phi_{LO}-\phi_{IF})+\cos((\omega_{LO}+\omega_{IF})t+\phi_{LO}+\phi_{IF})\right] \quad (3.5)$$

The power is then adjusted with attenuators in order to drive the resonator at the desired input power. We work with no cryogenic amplifier and at a rather high temperature of 1.5K. Therefore the signal we can measure is limited by the thermal noise of the measurement chain as well as the back action noise of the first amplifier. The room temperature attenuators of the setup generate a noise level equivalent to a 50Ω resistor. The bandwidth of the attenuator is B = 20GHz, leaving a noise level of $N_{V,V} = \sqrt{4k_B T_{room} RB} \equiv -65$dBm. For the excitation line, this noise level is attenuated

by the 20dB attenuator at 1.5K to -85dBm. This attenuator gives itself a noise level of $N_{V,V} = \sqrt{4k_B T_{sample} RB} \equiv -88$dBm. The resulting noise level at the input port is then $N_{V,V,in} = -83$dBm.

Amplification chain

The transmitted signal through the cavity is then amplified at room temperature by an amplification chain. Between the first amplifier and the cavity output port is a cryogenic circulator with a 50Ω resistor on the third port, in an isolator configuration. Amplifiers have a back action noise which is usually expressed as an effective temperature. This back action noise is thus absorbed by the 1.5K resistor. Nevertheless, the isolator is not perfect and the output port of the resonator sees the back action noise of the amplifier attenuated by 18dB in addition to the noise of the 1.5K resistor. It is important that the first amplifier of the chain has the least input noise. The first amplifier of our chain has a noise temperature of 51K. With the same reasoning that in the previous paragraph, the noise that enters the output port is fixed by the 1.5K thermalized 50Ω resistance of the isolator in addition to the back action noise of the first amplifier attenuated by the 18dB of the cryogenic circulator from port 2 to port 1. The overall is attenuated by the 3dB XMA attenuator between the isolator and the cavity. This gives a total noise level on the output port $N_{V,V,out} = -82$dBm[3]. The resonant modes that could arise between two amplifiers are destroyed with 3dB attenuators. Amplifiers are only linear up to a so called 1dB compression point at which they start to saturate. It usually happens around 10dBm. It is thus important to estimate the signal level as well as the noise level at the end of the amplification chain to avoid saturating it. We see from these noise level calculation that the driving power of the cavity cannot be less than roughly -80 dBm.

IQ demodulation

The amplified RF signal is down converted in an IQ mixer. The purpose of this device is to extract the two quadratures of the EM field as described in figure 3.10. The transmitted amplified signal $\mathcal{A}^{out}_{RF}(\omega_{LO} \pm \omega_{IF}, \phi_{out}) = G\tau\mathcal{A}^{in}_{RF}(\omega_{LO} \pm \omega_{IF}, \phi_{in})$ is down converted by the local oscillator signal. In the IQ mixer, both, $\mathcal{A}^{out}_{RF}(\omega_{LO} \pm \omega_{IF}, \phi_{out})$ and $\mathcal{A}^{out}_{RF}(\omega_{LO} \pm \omega_{IF}, \phi_{out} + \frac{\pi}{2})$ are down converted, to ω_{IF}. These two signals are then demodulated in two lock-in synchronized at ω_{IF}. We directly read the amplitudes of the in-phase and out-of-phase of the EM field with this technique.

[3]The bandpass of the isolator is 4GHz, thus the overall noise at the output port is $N_{V,out} = 10\log\left(\frac{S_{VV}(51K,4GHz)\text{“}-3dB\text{“}+S_{VV}(1.5K,4GHz)\text{“}-3dB\text{“}+S_{VV}(1.5K,20GHz)}{1mW}\right)$

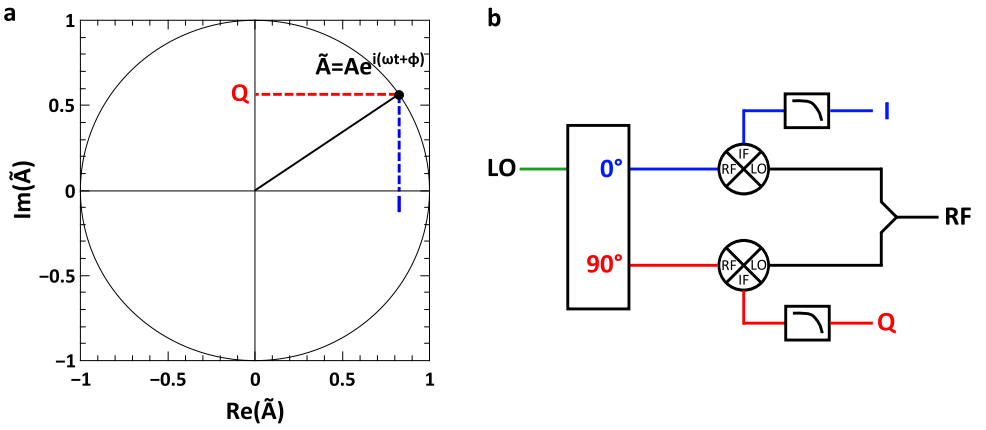

FIGURE 3.10: **a :** the electromagnetic field complex representation. The in-phase (I) and out-of-phase (Q) quadratures are respectively the real and imaginary parts of the EM field. **b :** IQ mixer principle. The RF signal enters a hybrid coupler that generates 0°and 90°phase shifted RF signals. Both are down converted and low-pass filtered, directly giving the amplitude of both quadratures.

The whole demodulation setup is calibrated by connecting the output of the up-converter to the amplification chain. The RF power entering the amplification is adjusted to not saturate the last amplifier nor the IQ down-converter. The calibration is made over the whole frequency span available on the microwave table f $\in$ [4.5;8]GHz. The amplitude and phase are extracted from the in-phase and out-of-phase quadratures as shown in figure 3.11. The amplitude is -12.5$\pm$1 dBm and the phase varies of 0.1 rad over the whole span.

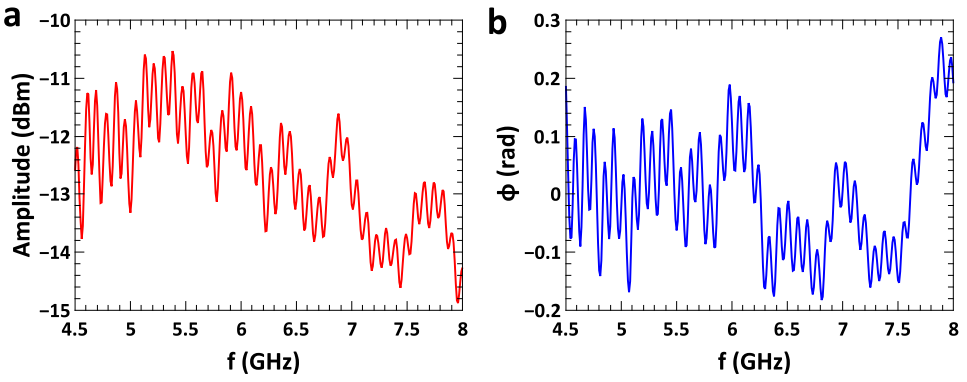

FIGURE 3.11: Calibration of the microwave table. Amplitude (**a**) and phase (**b**) of the RF demodulation setup vs frequency of the local oscillator with P=-87dBm entering the amplification chain. The output of the up-converter (dashed pink square of figure 3.9) is directly connected to the input of the amplification chain (dashed blue square of figure 3.9).

Phase drift compensation

The microwave phase is extremely sensitive to any external perturbation[4]. We will use it to probe the QD inside the cavity and as we will see in the following chapter, we measure $\Delta\phi \in [0.1; 3]$ mrad. We thus need to have the most stable phase possible. The two main sources of variations of the phase are the temperature (cryostat and room) and the current drifts of the RF amplifiers power supply. The latter can be reduced by properly grounding the setup. However, the smallest temperature variations of the experimental room will make the phase to drift, as schemed in figure 3.12. Data acquisition is rather long on CNT devices, especially with lock-in techniques and phase drifts need to be compensated.

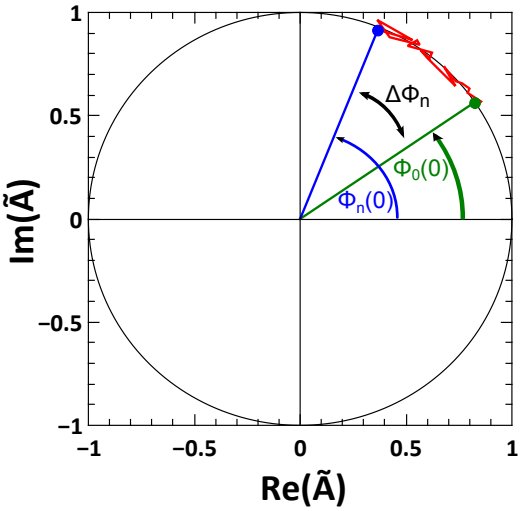

FIGURE 3.12: Scheme of the drift of the phase of the RF signal during a measurement. The drift of the phase is cancelled by defining a reference phase at a working point $\phi_0(0)$. At step n of the measurement, the phase $\phi_n(0)$ is measured at the same working point and the angle $\Delta\phi_n$ is added to the signal to compensate the drift.

The phase drift compensation is done by choosing a reference phase ϕ_0 at a particular working point $\vec{V_0}$ at the beginning of the measurement. Then each time it is necessary, usually at the beginning of each new sweep, the phase ϕ_n is measured again at $\vec{V_0}$ and a rotation angle $\Delta\phi = \phi_n - \phi_0$ is made. The phase drift protocol is detailed in the following box.

[4] e.g. the phase is sensitive to 10mK oscillations of the 1K pot

Phase drift compensation

1. **sweep 0 : reference phase determination**

$$\begin{cases} I_0(\vec{V_0}) \\ Q_0(\vec{V_0}) \end{cases} \Longrightarrow \begin{cases} A_0(\vec{V_0}) \\ \phi_0(\vec{V_0}) \end{cases}$$

2. **sweep n**

$$\begin{cases} I_n(\vec{V_0}) \\ Q_n(\vec{V_0}) \end{cases} \Longrightarrow \begin{cases} A_n(\vec{V_0}) \\ \phi_n(\vec{V_0}) \end{cases}$$

3. **sweep n : drift compensation**

$$\begin{cases} \Delta A_n = A_0(\vec{V_0}) - A_n(\vec{V_0}) \\ \Delta\phi_n = \phi_0(\vec{V_0}) - \phi_n(\vec{V_0}) \end{cases} \Longrightarrow \begin{cases} A_n^{cal}(\vec{V}) = A_n^{cal}(\vec{V}) + \Delta A_n \\ \phi_n^{cal}(\vec{V}) = \phi_n^{cal}(\vec{V}) + \Delta\phi_n \end{cases}$$

Chapter 4

Coupling a quantum dot to a microwave cavity

The coupling between SWNT QD devices and a microwave CPW resonator is discussed in this chapter. In this thesis, the measured samples exhibited the three different regimes observable in such systems. Thus the discussion will cover the coupling of the cavity to QDs in these three situations.

4.1 Quantum dot spectroscopy in the resonator's phase

As emphasized in section 2 of chapter 3, the two quadratures of the transmitted microwave field are measured simultaneously with the low frequency differential conductance of the QD. Measurements of both differential conductance and microwave field will be described in this section.

4.1.1 Three regimes

Fabry-Perot regime

The Fabry-Perot regime has been observed in sample *NTRES52aZ7D* as shown in figure 4.1 (a) where the differential conductance is represented in color scale plot, in the gate voltage V_G bias voltage V_{sd} plane. The Fabry-Perot pattern described in chapter 1 is observable, with a level spacing $\Delta \approx 5mV$ corresponding to a QD length of approximatively 350nm. We can note the non regularity of the pattern, especially in terms of level spacing. That could be attributed to a more complex situation than exposed in chapter 1, where orbital K and K' are differently coupled to the leads.

Figure 4.1 (b) and (c) shows the phase and amplitude variations of the transmitted microwave field simultaneously taken with 4.1 (a), at the resonance frequency of the cavity, $f = 5.75$GHz. Essentially all the spectroscopic features observed in the differential conductance are visible in both the phase and the amplitude spectroscopies. The phase spectroscopy evolves similarly to the conductance while the amplitude evolves oppositely. The latter can be easily understood as the conductance of the QD corresponds to a dissipative channel for the microwave field. Thus, the more the conductance, the more dissipation in the system and the less amplitude of the RF transmitted field.

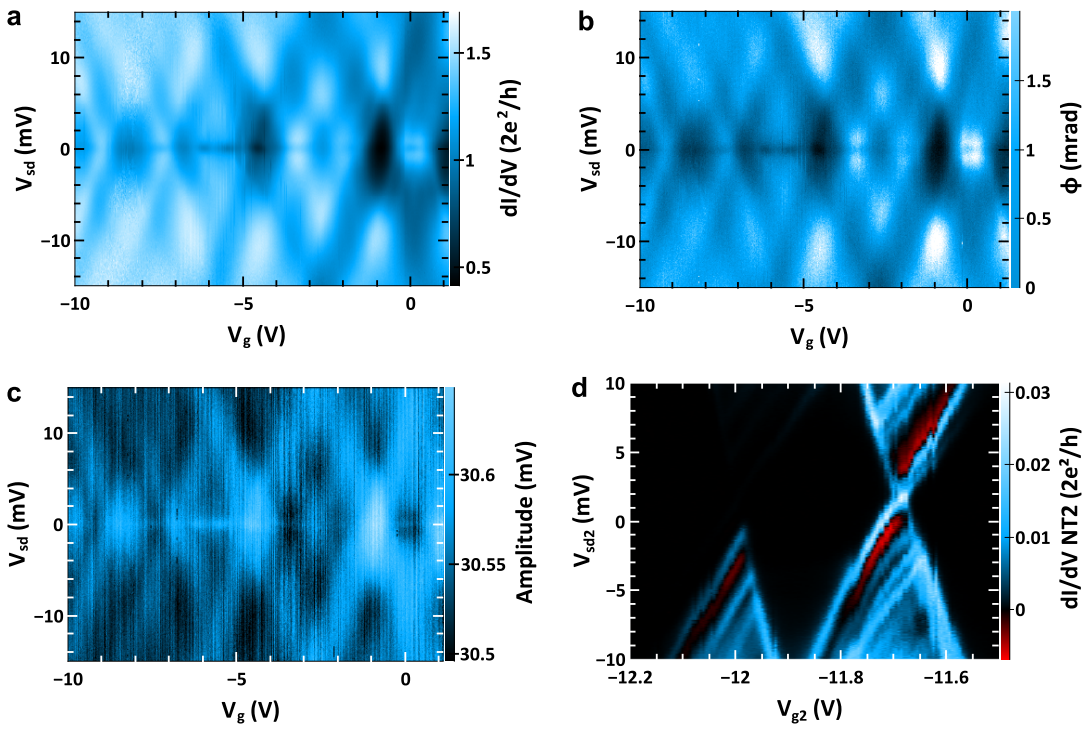

FIGURE 4.1: **a :** Color scale plot of the differential conductance of the SWNT QD *NTRES2aZ7D* in units of $2e^2/h$ in the gate/bias voltages plane in the Fabry-Perot regime. **b(c) :** Colour scale plot of the phase (amplitude) of the microwave field transmitted through the cavity at $f = 5.75$GHz taken simultaneously with (**a**). **d :** Color scale plot of the differential conductance of the SWNT QD *NTRES2aZ6G* in units of $2e^2/h$ in the gate/bias voltages plane in the Coulomb blockade regime. Excited states are visible as well as negative differential conductance peaks in red.

Coulomb blockade

The Coulomb blockade regime has been observed in two different devices, *NTRES33bZ4D* and *NTRES52aZ6G*. The conductance in one particular region of the latter is presented in figure 4.1 (d). A Coulomb diamond is visible, as well as excited states. These states are observed as parallel lines to the diamonds edges, at finite bias voltage. Negative differential conductance (NDC) zones are also visible in red. They can be explained for

example by a strong difference in the couplings Γ between the excited states and the leads (see *e.g.* [80]). Unfortunately, no phase nor amplitude spectroscopy were measured in this regime for the different considered here, at the time this manuscript has been written.

Kondo

Finally, Kondo effect was also measured, in sample *NTRES33bZ4D*. The corresponding differential conductance color scale plot is presented in figure 4.2 (a). Three Coulomb diamonds are visible and a Kondo ridge at zero bias is observed in the second diamond, for V_G between -2.5V and -2.0V. In the center of this Coulomb diamond, the Kondo ridge reaches $0.75\times(2e^2/h)$, close to the maximum possible value of 1. This indicates a well-developed Kondo resonance. A fit of this resonance in V_{sd} with the formula $G = G_0(1-(eV/kT_K)^2)$ gives a Kondo temperature $T_K \approx 2.9$K. The corresponding phase spectroscopy is shown in figure 4.2 (b). As in the case of Fabry-Perot, all the features observed in the conductance are visible in the phase spectroscopy. In particular, a finite ridge is visible at zero bias, corresponding to the Kondo ridge. Contrary to sample *NTRES52a*, the transmission of the cavity of sample *NTRES33b* was low ($S_{21} \approx -45dBm$ at resonance). The result of this is too small a signal-to-noise ratio of the transmitted RF signal amplitude variations, making such information not usable.

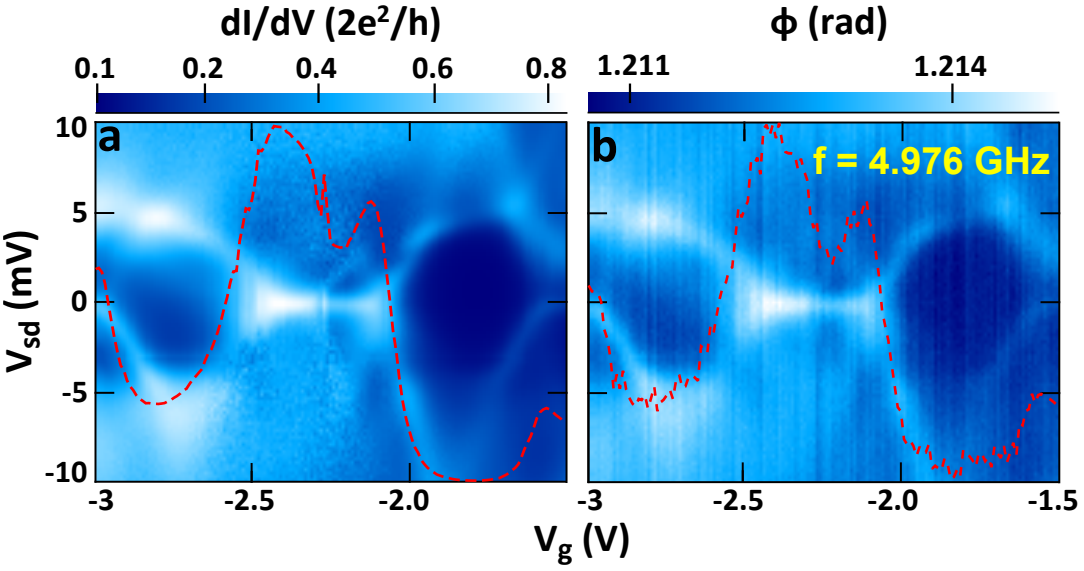

FIGURE 4.2: **a :** Color scale plot of the differential conductance of the SWNT QD *NTRES33bZ4D* in units of $2e^2/h$ in the gate/bias voltages plane. Three Coulomb diamonds are visible and a Kondo ridge at zero bias is observed in the middle diamond. **b :** Color scale plot of the phase of the microwave field transmitted through the cavity at $f = 4.976$GHz taken simultaneously with (**a**). In both colour scale plot, the dashed red line is a cut at zero bias.

An exotic Kondo effect region has also been observed in *NTRES33bZ4D* as shown by the differential conductance spectroscopy of figure 4.3 (a). A local fourfold degeneracy is visible, which is a signature of the two spins and two orbital channels available in SWNT. Kondo ridges are observable at zero bias in the three last Coulomb diamonds, corresponding to occupation of one, two or three electrons in the orbital being filled. This is consistent with SU(4) Kondo effect (see *e.g.* [46, 81]). Again, the phase spectroscopy of the same region (figure 4.3) exhibits the same features. Unfortunately, the spectroscopy of this region underwent irreversible modifications[1] before any precise study of this SU(4) Kondo could be undertaken.

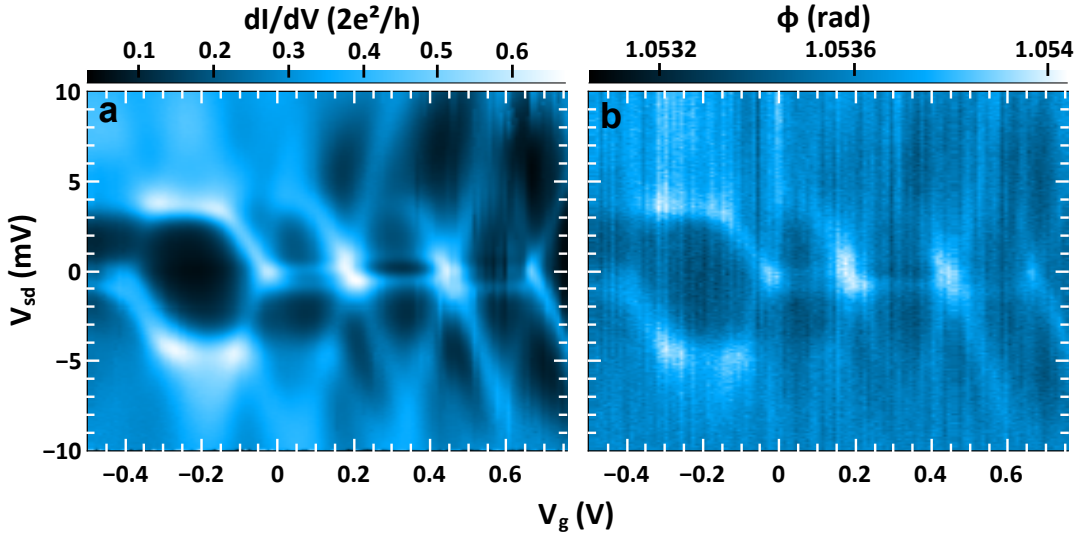

FIGURE 4.3: **a :** Colour scale plot of the differential conductance of a SWNT QD *NTRES33bZ4D* in units of $2e^2/h$ in the gate/bias voltages plane. The fourfold degeneracy of SWNT is visible in this spectroscopy. Four Coulomb diamonds are visible showing the filling of an orbital with 4 electrons. Kondo ridges are visible in three consecutive diamonds, suggesting both spin and orbital Kondo effect. **b :** Colour scale plot of the phase of the microwave field transmitted through the cavity at $f = 4.976$GHz taken simultaneously with (**a**).

4.1.2 Other possibilities

It should be possible with this device architecture to observe RF signal modulation while no differential conductance is observable. This could happen for example as in the situation depicted in figure 4.4. One of the leads is not contacted to the SWNT, or too weakly coupled. In this case, tunnelling from the QD to the right lead is impossible, therefore no signal can be measured in the standard low frequency differential conductance setup. However, Charge fluctuations between the left lead and the QD are possible, governed

[1] The spectroscopy can change after large gate sweeps which empty or fill charge traps in the oxide substrate.

by Γ_L. In the case of couplings Γ_L comparable with the frequency of the resonator f_0[2], different couplings from one level to another should leave a phase variation. Indeed, a effective capacitance can be attributed to the QD, taking into account both Γ_L and f_0 (see [28, 82]). The phase of the RF signal which is sensitive to the quantum capacitance associated to the electronic levels of the QD would thus show variations relative to the discrete spectrum of the QD.

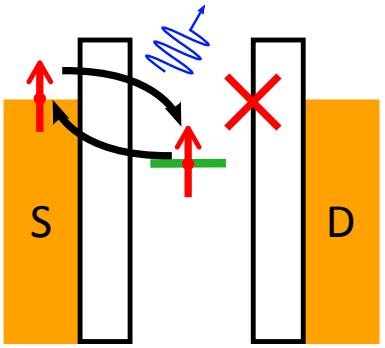

FIGURE 4.4: Scheme of a situation where the QD is contacted to one lead only. Charge fluctuations (represented by black arrows) from the contacted lead to the dot are possible, affecting the cavity field.

4.2 Cavity-Dot coupling

The observation of the QDs spectroscopies in the phase of the microwave signal implies that the QDs and the microwave field are coupled. In this section, the nature and strength of this coupling is discussed.

4.2.1 Capacitive coupling

"Photonic" Anderson-Holstein Hamiltonian

The cavity is capacitively coupled to the QD and interacts with it in two ways. The AC modulation of the cavity "shakes" both the leads and the energy levels of the QD. This coupling is represented in figure 4.5 where both coupling are respectively represented with red and blue capacitances.

The geometry of the QD with respect to the resonator transmission line is defined by the CNT growth direction. Hence the coupling of the leads to the cavity is asymmetric in most cases. This results in an asymmetric modulation of the chemical potential of both

[2] $f_0 \sim 6\text{GHz} \equiv 25\ \mu\text{eV}$, so Γ_L should be less than $250\mu\text{eV}$.

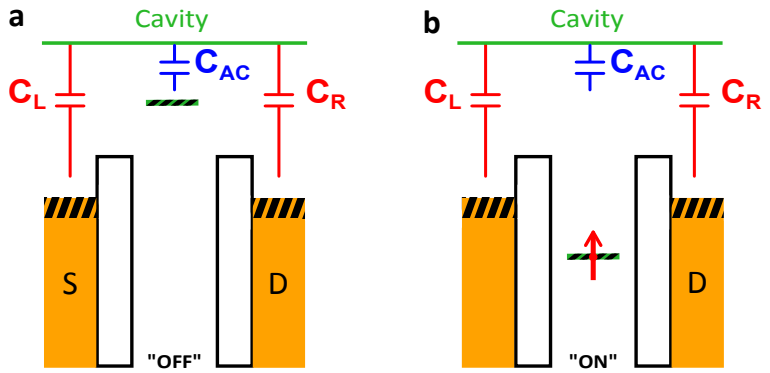

FIGURE 4.5: Scheme of the capacitive coupling of the QD to the cavity. Both the leads and the levels of the QD are coupled to the cavity (red and blue respectively). The dashed areas represent the "shaking" of the leads and energy level due to the AC modulation.

leads, and thus generates a finite current through the dot. This coupling is therefore responsible for dissipation in the cavity. There is a fundamental difference between this device and a standard cQED device. Here the electronic system is inherently an open quantum system as the Fermi seas of the leads are part of it. Photons are thus coupled to this open quantum system and can leak from the cavity through it[3]. This adds a new damping term to the cavity photons, which depends on the QD state.

The coupling of the cavity to the energy levels of the QD is a capacitive coupling related to a dipole-dipole coupling. The first dipole is the transmission line of the resonator facing the ground plane. The QD dipole is made by the charge of the QD in regard with the ground plane as well. Any change in the charge density of the QD modifies this dipole, thus the microwave field. This can be formulated by a photonic version of the Anderson-Holstein model

$$H = H_{dot} + H_{cav} + \sum_{k=K,K'} \lambda_k \hat{n}_k (\hat{a} + \hat{a}^\dagger) \tag{4.1}$$

with λ_k and $\hat{n}_k$, respectively, the electron-photon coupling and the number of electrons for each orbital $k = K, K'$ of the SWNT QD. $\hat{a}$ and $\hat{a}^\dagger$ are the annihilation and creation operators of the photon field. In general, $\lambda_K \neq \lambda_{K'}$ due to disorder [83]. This model actually is an extension of the Anderson model discussed in chapter 1 and 2. The purpose of this Hamiltonian is to treat the case of quantum impurities coupled to phonons. This model leads to effects known as the Franck-Condon effect [84, 85]. The current of the QD drops when the level separation matches the characteristic energy of the involved phonons, as in a dynamical Coulomb blockade effect. The phonon bath here can be

[3]Note that even in the case of a coupling purely on the QD level, the relaxation resistance of the QD is a damping for the photons as well.

replaced by any boson bath, and in particular photons in the situation of this thesis. The coupling involved in equation (4.1) is a capacitive coupling as the term $\lambda_k \hat{n}_k(\hat{a}+\hat{a}^\dagger)$ can be classically seen as a charge times a potential $Q_{dot}V_{field}$, therefore a capacitance of the QD towards the resonator.

The QD is spatially small compared to the leads to which it is contacted. One can therefore argue that the coupling to the electronic levels of the QD might be vanishingly small compared to the coupling to the leads. However, the coupling to the levels can be indirect. It is indeed equivalent to modulate the energy of the QD and to symmetrically modulate the chemical potential of the leads. In this picture, the capacitive coupling C_{AC} of figure 4.5 is the common mode of C_L and C_R. This point will reveal relevant when analysing the data.

Mapping onto Jaynes-Cummings Hamiltonian

While the model of equation (4.1) describes the coupling as a capacitive coupling, it is important to find a description equivalent to the one used in standard QED. This gives a mean of comparison between the different approaches. The usual description of the coupling relies on the Jaynes-Cumming Hamiltonian. In equation (4.1), the orbital degree of freedom is taken into account. Disorder in the SWNT structure can induce time-dependant valley mixing, thus orbital hybridization, as described in [83] and depicted in figure 4.6 (a) as a Bloch sphere with $|K\rangle$ and $|K'\rangle$ at each poles.

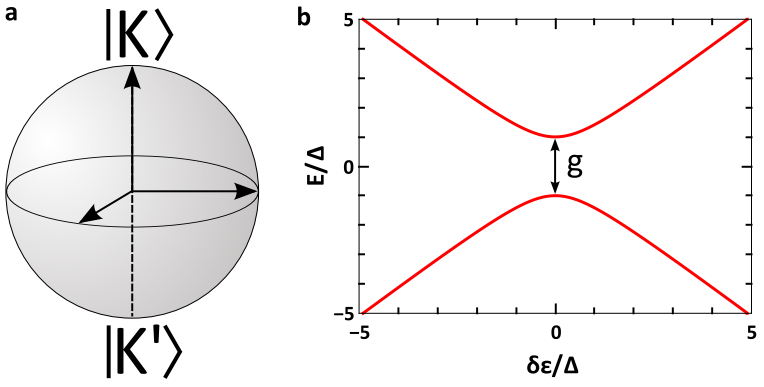

FIGURE 4.6: **a :** Bloch sphere of a two-level system $|K\rangle$ and $|K'\rangle$. This situation is possible in SWNT QD if the two orbital K and K' are hybridized. **b :** Energy dispersion of the TLS in presence of a bosonic bath. The level avoiding distance is related to the coupling g between the TLS and the bosonic bath.

It is therefore natural to consider both orbitals to be differently affected by the AC field. In this situation, H_{dot} of equation (4.1) writes as

$$H_{dot} = \sum_{k=K,K'} \epsilon_k \hat{d}_k^\dagger \hat{d}_k + U\hat{n}_\uparrow \hat{n}_\downarrow + \Delta_{KK'} \hat{d}_K^\dagger \hat{d}_{K'} + \Delta_{KK'}^\star \hat{d}_{K'}^\dagger \hat{d}_K \tag{4.2}$$

with $\Delta_{KK'}$ the orbital hybridization strength and $\hat{d}_k(\hat{d}_k^\dagger)$ the annihilation(creation) operator of an electron in orbital k on the QD. To simplify the calculations to the most, the case of a closed quantum dot with fixed number of electron $n = 1$ will be considered. This is implemented by taking $U = \infty$. The total Hamiltonian rewrites in the $\{|K\rangle, |K'\rangle\}$ basis

$$H_\phi = H_{cav} + \sum_{k=K,K'} |k\rangle\langle k| + \Delta_{KK'}|K\rangle\langle K'| + \Delta_{KK'}^\star |K'\rangle\langle K| + \sum_{k=K,K'} \lambda_k |k\rangle\langle k|(\hat{a}^\dagger + \hat{a}) \tag{4.3}$$

Defining $\frac{\epsilon_K + \epsilon_{K'}}{2}$ as the energy origin, the Hamiltonian can be diagonalized as

$$H_{dot} = \begin{pmatrix} \frac{\epsilon_K - \epsilon_{K'}}{2} & \Delta_{KK'}^\star \\ \Delta_{KK'} & -\frac{\epsilon_K - \epsilon_{K'}}{2} \end{pmatrix} = \sqrt{E^2 + \Delta^2} \begin{pmatrix} \cos\theta & \sin\theta e^{i\phi} \\ \sin\theta e^{-i\phi} & \cos\theta \end{pmatrix} \tag{4.4}$$

with $E = \frac{\epsilon_K - \epsilon_{K'}}{2}$, $\Delta^2 = \Delta_{KK'}^\star \Delta_{KK'}$, $\phi = \arg(\Delta_{KK'})$ and $\tan(\theta) = \frac{2|\Delta|}{\epsilon_K - \epsilon_{K'}}$. The eigenvalues and corresponding eigenvectors in the $\{|K\rangle, |K'\rangle\}$ basis are

$$\begin{cases} E_\pm = \pm\frac{1}{2}\sqrt{(\epsilon_K - \epsilon_{K'})^2 + \Delta^2} \\ |+\rangle = \cos\left(\frac{\theta}{2}\right)|K\rangle + \sin\left(\frac{\theta}{2}\right)e^{i\phi}|K'\rangle \\ |-\rangle = -\sin\left(\frac{\theta}{2}\right)e^{-i\phi}|K\rangle + \cos\left(\frac{\theta}{2}\right)|K'\rangle \end{cases} \tag{4.5}$$

The Energy spectrum of such a TLS system exhibits the standard avoiding levels as shown in figure 4.6 (b). The total Hamiltonian rewrites in the $\{|+\rangle, |-\rangle\}$ basis

$$H_\phi = H_{cav} + \frac{E_+ - E_-}{2}\hat{\sigma}_z + (\lambda_{K'} - \lambda_K)\cos\left(\frac{\theta}{2}\right)\sin\left(\frac{\theta}{2}\right)(\hat{\sigma}_+\hat{a} + \hat{a}^\dagger\hat{\sigma}_-) \tag{4.6}$$

with the σ matrices defined as

$$\begin{cases} \hat{\sigma}_+ = e^{-i\phi}|+\rangle\langle -| \\ \hat{\sigma}_- = e^{+i\phi}|-\rangle\langle +| \\ \hat{\sigma}_z = |+\rangle\langle +| - |-\rangle\langle -| \end{cases} \tag{4.7}$$

To obtain equation (4.6), the rotating wave approximation (RWA) has been done. It removes all non-resonant terms in the system. The standard Jaynes-Cumming Hamiltonian describing the coupling of a two-level system and a mode of an electromagnetic field is written

$$H_{JC} = H_C + E_0\sigma_z + \hbar g(\hat{\sigma}_+\hat{a} + \hat{a}^\dagger\hat{\sigma}_-) \tag{4.8}$$

Equations (4.6) and (4.8) have the same structure and direct comparison between the different terms is thus relevant. The coupling parameter g of the Jaynes-Cumming Hamiltonian describes the coupling strength between the EM mode and the TLS. In the situation considered here, with orbital hybridization in the SWNT QD, the corresponding coupling factor g is thus

$$g = (\lambda_{K'} - \lambda_K)\cos\left(\frac{\theta}{2}\right)\sin\left(\frac{\theta}{2}\right) \tag{4.9}$$

The strength of the coupling, as shown in equation (4.9), depends on the parameter θ which is related to the hybridization amplitude $\Delta_{KK'}$. For a maximal hybridization when $\epsilon_K = \epsilon_{K'}$, corresponding to $\theta = \pi/2$, the coupling is also maximum and is $g = \frac{1}{2}(\lambda_{K'} - \lambda_K)$. This mapping of the Anderson-Holstein Hamiltonian onto the Jaynes-Cumming Hamiltonian is important as it gives a mean to compare the results of this thesis to cQED experiments. Indeed, one of the goals of the experiments that have been performed in this thesis is to characterize the coupling strength between the QD device and the superconducting resonator in order to implement cQED-like manipulation of QD devices in the future.

Classical field description

As already mentioned, the quantum regime for photons is not achieved in this thesis, as the base temperature of the experiments is 1.5K[4]. The excitation power of the resonator is also big ($P_{in} \geq -80$dBm), and the number of photons in the cavity is large and far from the single photon regime. Furthermore, the QD is adiabatically driven by the resonator as the resonator's frequency is much smaller than all energies involved in the QD. Thus, it is relevant to treat the coupled system with classical electrodynamics. The overall equivalent electronic circuit of the device is presented in figure 4.7. The QD circuit (in blue) is in parallel of the equivalent RLC circuit of the resonator. The finite conductance

[4] 1.5K corresponds to a mean thermal occupation of 5 photons in a 6GHz cavity. However, the cavity is also connected to the external world and noise to the ports of the cavity determined in chapter 3 section 2 gives an average photon number of roughly 1000!

of the QD is described by a resistance $R_{dot} = 1/(dI/dV)$. Capacitances $C_{L/R}$ take into account both geometrical capacitance of the lead and quantum capacitance of the QD as $C_{L/R} = C_{L/R}^{geom} + C_{L/R}^{Q}$. Both R_{dot} and C^{Q} are variable lumped elements, as they are related to the QD states, thus to bias and gate voltages.

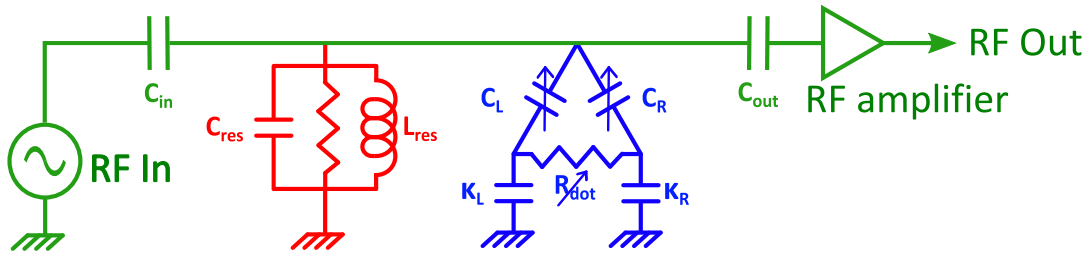

FIGURE 4.7: Equivalent electronic circuit of the QD coupled to a microwave resonator. The QD circuit (blue) is in parallel to the RLC equivalent circuit of the resonator (red). R_{dot} represents the dissipative channel of the SWNT QD (finite conductance) while C_L and C_R represents both geometrical and quantum capacitance from the QD and leads toward the cavity.

The QD admittance writes

$$Y_{dot} \approx \frac{\alpha}{R_{dot}} + j\omega C_{dot} \tag{4.10}$$

with

$$\alpha = \left(\frac{C_L}{C_L + \kappa_L} - \frac{C_R}{C_R + \kappa_R} \right)^2 \tag{4.11}$$

$$C_{dot} = \frac{C_L \kappa_L}{C_L + \kappa_L} + \frac{C_R \kappa_R}{C_R + \kappa_R} \tag{4.12}$$

Expression (4.10) holds for $(C_{L/R} + \kappa_{L/R}) R_{dot} \omega \gg 1$ and $\kappa_{L/R} R_{dot} \omega \gg 1$. Expression (4.11) is consistent with the previous symmetry argument about the dissipative effect of the QD as only an asymmetric coupling of the leads to the cavity makes the resistive term of the dot non-zero. The two different contributions of the QD admittance to the coupling in equation (4.10) are dissipative and dispersive. They respectively correspond to the in-phase and out-of-phase response of the QD. By adding this admittance in parallel to the RLC model of the resonator developed in chapter 1 section 2, the effective resonator's impedance Z_{eff} writes

$$Z_{eff}^{-1} = j\omega C' + \frac{1}{j\omega L} + \frac{1}{R'} + \frac{\alpha}{R_{dot}} + j\omega C_{dot} \tag{4.13}$$

The poles of Z_{eff} gives both the resonance frequency and width of the resonator. The positive pole is

$$z_0 = \omega_0 + j\frac{1}{2R'C'} - \frac{C_{dot}}{2C'}\omega_0 + j\left(\frac{\alpha}{2C'R_{dot}} - \frac{\omega_0}{2Q_L}\frac{C_{dot}}{C'}\right) \tag{4.14}$$

In equation (4.14), $\omega_0 + j\frac{1}{2R'C'}$ corresponds to the resonator alone, describing the resonance frequency and the finite width of its mode. It is interesting to note that the system resonance is given by the real part of the pole z_0 while the quality factor is given by the ratio of the real part and twice the imaginary part $Q_L = \frac{\mathrm{Re}(z_0)}{2\mathrm{Im}(z_0)}$. The two other terms are related to the QD and operate a dispersive shift

$$\delta f_R = -\frac{C_{dot}}{2C'} f_0 \tag{4.15}$$

and a dissipative shift

$$\delta f_D = \frac{\alpha}{2C'}\frac{dI}{dV}\frac{1}{2\pi} - \frac{f_0}{2Q_L}\frac{C_{dot}}{C'} \tag{4.16}$$

of the cavity mode. Note that the capacitive contribution to the dissipative shift behaves in $1/Q_L$ so that it is negligible for any large Q_L. Considering these dispersive and dissipative frequency shifts, the new frequency resonance and quality factor of the resonator write

$$\tilde{f}_0 = f_0 + \delta f_R \tag{4.17}$$

$$\tilde{Q}_L = \frac{f_0 + \delta f_R}{2\left(\frac{1}{2R'C'} + \delta f_D\right)} = Q_L \frac{1 + \frac{\delta f_R}{f_0}}{1 + \frac{2Q_L \delta f_D}{f_0}} \tag{4.18}$$

4.2.2 Disentangling dispersive and dissipative contributions

The QD has a double effect on the microwave field. One is purely related to the conductance of the QD, and so its information is somehow redundant with the low frequency differential conductance measurements (in the case of large quality factors). The dispersive effect of the QD related to its out-of-phase response consists however of a new information related to the capacitance of the QD. In general, both contributions are mixed in the amplitude and phase variation of the RF transmitted signal. The purpose of this subsection is to show how to extract these quantities from the measurements of the transmitted RF signal.

Phase signal only

First, the case of a low transmission cavity will be discussed as it was encountered in the first measured sample, *NTRES33bZ4D*. In this situation, the signal to noise ratio is too small to properly measure modulations in the RF signal amplitude. Thus only the phase of the RF signal is available for disentangling dispersive and dissipative contributions. Figure 4.8 (a) shows the theoretical phase variation of the transmitted RF signal through a cavity across the resonance, in different situations. The dashed black line is the case of a raw resonator with frequency resonance f_0 and width κ. This phase variation is defined as the reference phase. When applying a purely dispersive (resp. dissipative) shift to the cavity, the phase undergo a shift δf_R (resp. a broadening δf_D) as represented by the blue (resp. red) curve. The difference between both curves with the reference phase is defined as the phase contrast. Thise phase contrast is represented in figure 4.8 (b) with the same color code as in (a). The dispersive phase contrast presents a resonance shape centered on f_0 and is an even function. The dissipative phase contrast presents an odd function behaviour, centered as well on f_0.

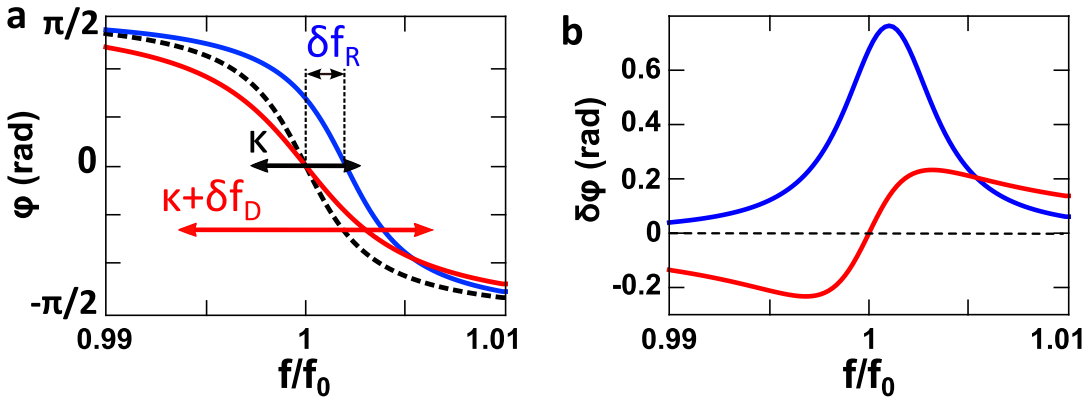

FIGURE 4.8: **a :** Phase of the transmitted microwave field through a CPW resonator versus frequency. The resonator's frequency is denoted f_0. The dashed black curve is the phase for a resonator alone. When coupled to a purely dispersive (resp. dissipative) system, the phase undergo a frequency shift in blue (resp. broadening in red). **b :** The phase contrast between purely dispersive (resp. dissipative) effect on the phase and the reference phase are represented versus frequency. A dispersive phase contrast shows a resonance (blue curve) centered on f_0 with same quality factor as the resonator mode. A dissipative phase contrast (red curve) shows an odd behaviour, centered on f_0.

The cavity transmission coefficient and phase write

$$\tau = -\frac{Q_L/Q_{ext}}{1 + 2iQ_L\left(\frac{f-f_0}{f_0}\right)} \tag{4.19}$$

$$\phi = -\arctan\left[2Q_L\left(\frac{f-f_0}{f_0}\right)\right] \tag{4.20}$$

Adding dispersive and dissipative frequency shifts with the conventions of equations (4.14), (4.15) and (4.16), the transmission coefficient writes

$$\begin{aligned}\tau' &= -\frac{\frac{\tilde{Q}_L}{Q_{ext}}}{1 + 2i\tilde{Q}_L\left(\frac{f-\tilde{f}_0}{\tilde{f}_0}\right)} \\ &= -\frac{\frac{Q_L}{Q_{ext}}\frac{1+\frac{\delta f_R}{f_0}}{1+\frac{2Q_L\delta f_D}{f_0}}}{1 + 2i\frac{Q_L}{1+\frac{2Q_L\delta f_D}{f_0}}\left(\frac{f-f_0-\delta f_R}{f_0}\right)}\end{aligned} \tag{4.21}$$

The phase follows as

$$\phi' = -\arctan\left[\frac{2Q_L}{1+\frac{2Q_L\delta f_D}{f_0}}\left(\frac{f-f_0-\delta f_R}{f_0}\right)\right] \tag{4.22}$$

Up to first order in δf, the resulting phase contrast thus reads

$$\delta\phi = \frac{2Q_L/f_0}{1 + 4Q_L^2\left(\frac{f-f_0}{f_0}\right)^2}\left(\delta f_R + 2Q_L\frac{f-f_0}{f_0}\delta f_D\right) + O(\delta f^2) \tag{4.23}$$

Equation (4.23) shows the contributions of dispersion and dissipation on the phase contrast, as an even and odd contribution respectively, with respect to f_0. The plot of both contributions is represented in figure 4.8 (b). The phase contrast is thus measured versus frequency as shown for example in figure 4.9 (a). The black curve is the phase contrast at one particular gate voltage along the Kondo ridge of figure 4.2. The extraction of the even and odd part with respect to $f_0 = 4.976$GHz is shown in figure 4.9 (b). The even, or dispersive contribution is represented by blue dots while the odd, or dissipative contribution is represented by red dots. There is a qualitative agreement between the raw data and the theoretical prediction of formula (4.23). The dispersive part exhibits a resonance shape with a width $\Delta f \approx 33$MHz corresponding to a quality factor of 150

as measured in the cavity transmission. The dissipative contribution however exhibits residual bumps due to imperfections in the amplification chain.

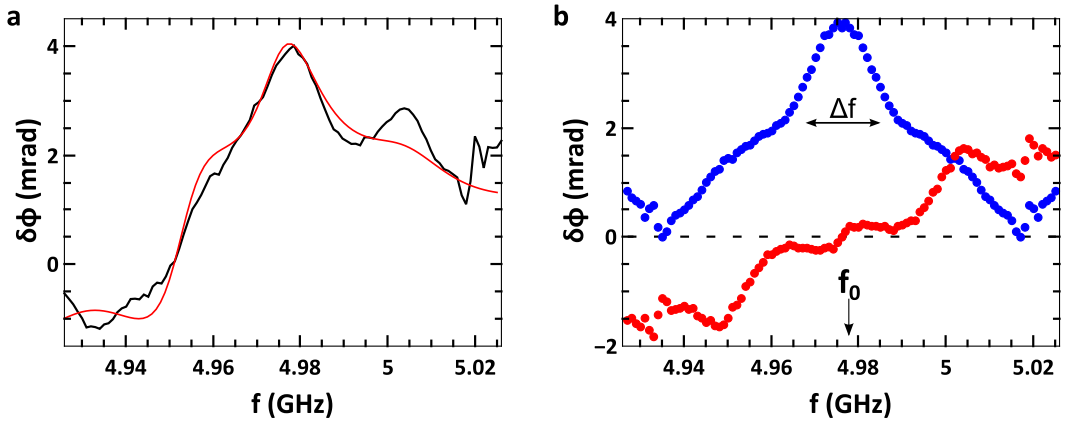

FIGURE 4.9: **a :** Phase contrast (black curve) along the Kondo ridge of figure 4.2. The phase reference is taken in the empty orbital at $V_G = -1.85$V. Red curve, model of a QD coupled to the cavity with Fabry-Perot mode to account for the modulations of the experimental data. **b :** even (blue curve) and odd (red curve) parts of the phase contrast in (**a**) in qualitative agreement with 4.8 (**b**).

Dispersive and dissipative frequency shifts are directly related to the area under respectively the even and odd contributions as

$$\int_{f_0(1-1/Q)}^{f_0(1+1/Q)} \frac{2Q_L/f_0}{1+4Q_L^2\left(\frac{f-f_0}{f_0}\right)^2}\delta f_R df = 2\arctan(2)\delta f_R \tag{4.24}$$

$$\int_{f_0}^{f_0(1+1/Q)} \frac{2Q_L/f_0}{1+4Q_L^2\left(\frac{f-f_0}{f_0}\right)^2} 2Q_L\frac{f-f_0}{f_0}\delta f_D df = \frac{\ln 5}{2}\delta f_D \tag{4.25}$$

The integration is centered on the resonance frequency with a width corresponding to 2 times the width of the resonance[5]. One important aspect of this method is that the integration acts as an averaging, thus removes the defects of the measurements such as these residual bumps. This allows one to obtain reliable values for δf_R and δf_D even with low quality resonators as it will be shown in the following.

[5] A more general integral between $f_0 - f_1$ and $f_0 + f_1$ respectively gives $2\arctan\left(2Q_L\frac{f_1}{f_0}\right)\delta f_R$ and $\frac{1}{2}\ln\left(1+4Q_L^2\frac{f_1^2}{f_0^2}\right)\delta f_D$.

Phase and amplitude signal

When amplitude variations of the RF transmitted signal are measurable [6], the full phase contrast method described above is not necessary to determine the dispersive and dissipative contributions of the QD. Indeed, while this technique is powerful, it takes long time to acquire data sets. The output amplitude of the RF signal is measured, which is expressed from the transmission coefficient as

$$\mathcal{A} = \mathcal{A}_{in}|\tau|G \tag{4.26}$$

with G the gain of the amplification chain and $\mathcal{A}_{in}$ the microwave field amplitude at the input port of the cavity. As $\mathcal{A}_{in}$ and G are difficult to calibrate, it is convenient to remove them by considering the relative variation of the amplitude which is thus directly related to the relative variation of the transmission coefficient

$$\frac{\delta\mathcal{A}}{\mathcal{A}} = \frac{\delta|\tau|}{|\tau|} \tag{4.27}$$

From equation (4.19) and (4.21), relative variation of the amplitude can thus be written up to first order as

$$\frac{\delta\mathcal{A}}{\mathcal{A}} = \frac{2Q_L/f_0}{1+4Q_L^2\left(\frac{f-f_0}{f_0}\right)^2}\left(-\delta f_D + 2Q_L\frac{f-f_0}{f_0}\delta f_R\right) + \frac{\delta f_R}{f_0} + O(\delta f^2) \tag{4.28}$$

Equation (4.28) is similar to equation (4.23), with inverted contribution for dispersive and dissipative contributions. As both $\delta\phi$ and $\frac{\delta\mathcal{A}}{\mathcal{A}}$ are measured, δf_R and δf_D are directly obtained by inverting the system. By considering that the measurements are done at the frequency resonance $f = f_0$, one gets

$$\delta f_R = \frac{f_0}{2Q_L}\delta\phi \tag{4.29}$$

$$\delta f_D = -\frac{f_0}{2Q_L}\frac{\delta\mathcal{A}}{\mathcal{A}} + \frac{f_0}{4Q_L^2}\delta\phi \tag{4.30}$$

The phase contribution to the dissipative shift is in $1/Q_L$. These expressions confirm the intuitive picture of the dispersive and dissipative shifts respectively related to phase

[6] *i.e* when the resonator's transmission is high enough so that the signal-to-noise ratio is good enough.

and amplitude variations. They are also useful within the frame of this thesis as the first order expansion is valid because of the small quality factors, hence relative cavity pull that is measured. However, it is possible to directly express both frequency shifts from the raw expression of $\frac{\delta\mathcal{A}}{\mathcal{A}}$ and $\delta\phi$. One finds

$$\delta f_R = \frac{f_0 \sin(\delta\phi)}{2Q_L(1+\frac{\delta\mathcal{A}}{\mathcal{A}}) - \sin(\delta\phi)} \tag{4.31}$$

$$\delta f_D = -\frac{f_0}{2Q_L} + \frac{f_0 \cos(\delta\phi)}{2Q_L(1+\frac{\delta\mathcal{A}}{\mathcal{A}}) - \sin(\delta\phi)} \tag{4.32}$$

4.2.3 Coulomb blockade peaks : a control experiment

For this subsection and the following, the discussion will treat sample *NTRES33bZ4D* where only the phase signal has been acquired. The dispersive and dissipative shifts are extracted from the phase contrast versus frequency. Color scale plots of the even and odd parts of the phase contrast are respectively presented in figure 4.10 (a). The measurement has been performed at zero bias along two Coulomb peaks. The even phase contrast plot exhibits two peaks, corresponding to the two Coulomb peaks in the conductance.

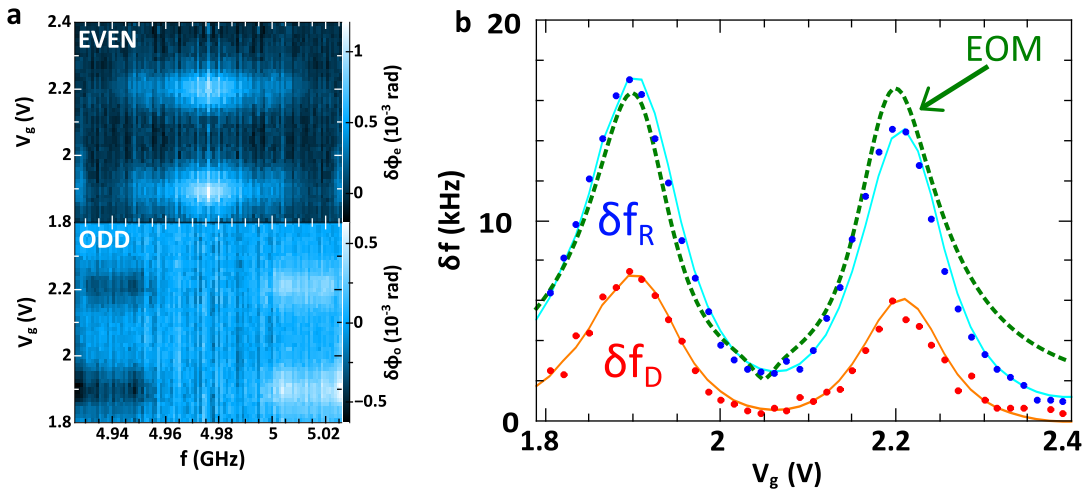

FIGURE 4.10: **a :** even and odd phase contrast versus gate voltage and frequency in a Coulomb blockade regime. **b :** dispersive (blue dots) and dissipative (red dots) frequency shifts extracted from (**a**). Light blue (resp. light orange) curves corresponds to the differential conductance expressed in units of dispersive (resp. dissipative) frequency shifts. The dashed green curve corresponds to a fit with the EOM model of chapter 2.

Frequency shifts are extracted from the area under each row of the even and odd color scale plots, with the help of equations (4.24) and (4.25). The extracted values are

represented by blue and red dots respectively, on figure 4.10 (b). δf_R and δf_D range from 0 to 17kHz and 7kHz respectively, so that the approximation $\delta f \ll f_0$ is satisfied. It is also noticeable that both contributions behaves like the conductance, represented by cyan and light orange curves. It was expected for the dissipative shift as $\delta f_D \propto dI/dV$ from equation (4.16). For the dispersive shift, an empirical formula fitting the data with the differential conductance can be written as

$$\delta f_R = \frac{C_0}{2C'} f_0 \frac{h}{2e^2} \frac{dI}{dV} \tag{4.33}$$

This allows to find an effective capacitance $C_0 = 18$aF of the QD in this region. The purpose of this measurement in the Coulomb blockade regime is that it can be compared to the EOM theory developed in chapter 2 section 2. The result of equation (2.37) is recalled

$$C_{dot} = -(\alpha_{AC} e)^2 \frac{\partial \langle n \rangle}{\partial \tilde{\xi}_d} + C_{AC}(1 + \alpha_{AC}) \tag{4.34}$$

where $-(\alpha_{AC} e)^2 \frac{\partial \langle n \rangle}{\partial \tilde{\xi}_d}$ corresponds to the variation of the capacitance of the QD ΔC_{dot} and $C_{AC}(1 + \alpha_{AC})$ corresponds to a geometric invariant capacitance. Thus, the EOM prediction for the dispersive shift reads

$$\delta f_R = (\alpha_{AC} e)^2 \frac{\partial \langle n \rangle}{\partial \tilde{\xi}_d} \frac{1}{2C'} f_0 \tag{4.35}$$

To fit data with the theoretical model (4.35), only one fitting parameter has to be adjusted, α, the geometrical factor of the device. Indeed, the other parameters necessary to compute EOM are known by the spectroscopy and consist of $U = 7$meV and $\Gamma = 1$meV. $C' = 0.7$pF on its part is defined by the CPW design and thus, lithography. Equation (4.35) shows that the dispersive frequency shift should be negative, as $\frac{\partial \langle n \rangle}{\partial \tilde{\xi}_d} \leq 0$, in contrast with the positive frequency shift observed in the measurements. However, as previously mentioned, the variation of $\tilde{\xi}_d$ can be effective and do to the common modulation of the chemical potential of the leads. As one have $\tilde{\xi}_d + \frac{\mu_L + \mu_R}{2} = cte$, therefore $\partial \tilde{\xi}_d = -\partial \left(\frac{\mu_L + \mu_R}{2} \right)$, which explains the observed sign of the dispersive frequency shift. The fit to the data, shown as a dashed green curve on figure 4.10 (b), agrees quantitatively with $\alpha_{AC} = 0.3$. The couplings $\lambda_{K/K'}$ of the Anderson-Holstein Hamiltonian, in equation (4.1), can be calculated from

$$\lambda_{K/K'} = e \alpha_{AC} V_{rms} \tag{4.36}$$

with V_{rms} the root mean square voltage of a single photon in the cavity mode $V_{rms} = \sqrt{\hbar\omega_0/2C'}$ (see [4, 5]). From this, one can obtain a coupling of $\lambda_{K/K'} \approx 111$MHz. This unexpectedly high value of the coupling is similar to the value obtained in cQED experiments with superconducting circuits [4][7]

4.2.4 A Kondo impurity coupled to a microwave cavity

The same method has then been applied to the Kondo ridge of figure 4.2. Color scale plots of the phase contrast versus gate voltage and frequency at zero bias are represented in figure 4.11 (a) for the even and odd contributions. A first observation can be done on the even phase contrast. It shows that, like for Coulomb blockade regime, the even phase contrast modulates similarly to the conductance. Indeed, the two Coulomb peaks are visible, with a finite contrast in between them, corresponding to the Kondo ridge.

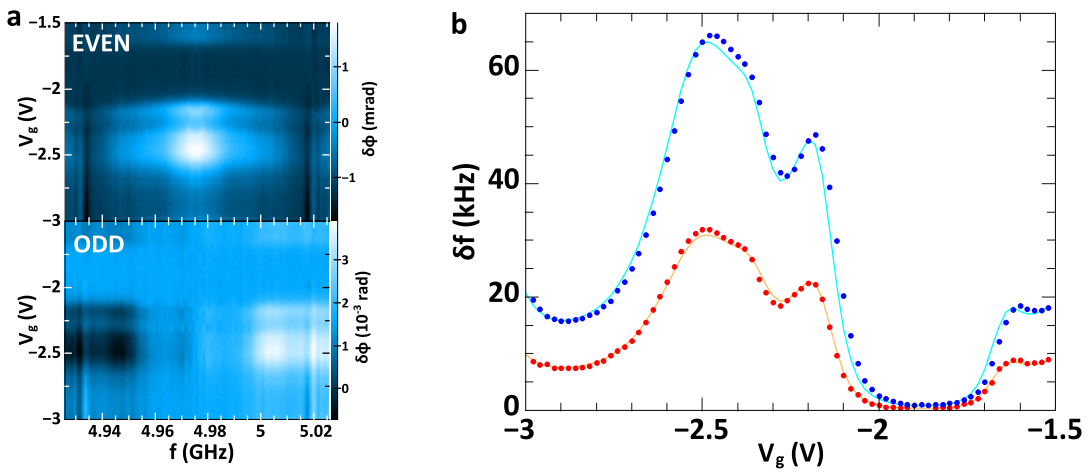

FIGURE 4.11: **a :** even and odd phase contrast versus gate voltage and frequency on the Kondo of figure 4.2. **b :** dispersive (blue dots) and dissipative (red dots) frequency shifts extracted from (**a**). Light blue (resp. light orange) curves corresponds to the differential conductance expressed in units of dispersive (resp. dissipative) frequency shifts.

Figure 4.11 (b) shows the frequency shifts extracted from the integration of each row of figure 4.11 (a). Dispersive and dissipative frequency shifts are represented by blue and red dots respectively. They both modulate up to 60kHz and 30kHz. From δf_R and equation (4.15), the QD capacitance on the Kondo ridge is found to be $C_{Kondo} = 16$aF. This value is taken at $V_G = -2.32$V, exactly in the middle of the two Coulomb peaks. Similarly to the Coulomb blockade case, it is possible to find an estimation of the

[7] In the paper related to this work [86], the coupling is strength is 140MHz as V_{rms} is considered to be 2μV, as in [4]. The resonator's capacitance, defined geometrically via finite elements theory in chapter 1 is $C' = 0.72 \pm 0.04$pF (The needed geometric parameters are extracted from the SEM micrograph of figure 3.4 (b) for example). The error on the parameter α_{AC} can be estimated to be of the order of 0.02. The ensued error on the coupling estimation is thus $\Delta\lambda = 10$MHz.

electron-photon coupling from this value. This "with the hands" argument relies on the estimation of the capacitance of the Kondo peak and the comparison to the measured value. The quantum capacitance associated to an electronic level is related to its spectral function. In the case of non-interacting QD, the quantum capacitance is given by the full spectral function (see [52] and chapter 2 section 1) as $C_K = 4e^2/\pi\Gamma_K \approx 200$ aF. Here $\Gamma_K \approx 1$meV, corresponding to a frequency of 250GHz, well above the frequency mode of the resonator. This allows us to provide an estimate of the electron-photon coupling in the Kondo regime as

$$\lambda_{K,K'} = eV_{rms}\sqrt{\frac{C_{dot}}{C_K}} \approx 102\text{MHz} \tag{4.37}$$

This coupling consist of the lower bound possible as we considered the theoretical value to be the maximum possible. It is nevertheless consistent with the value that has been found in the Coulomb blockade regime.

Another aspect of figure 4.11 (b) data is that both dissipative and dispersive shifts modulates like the conductance, like in the case of Coulomb blockade regime. While this remains expected for the former, it is more intriguing for the latter. The use of the empirical formula (4.33) gives an effective QD capacitance $C_{dot} = 22$aF. This observation seems seems counter intuitive at first glance. Indeed, the charge on the QD is fixed in the Kondo regime. This is expressed as a zero charge susceptibility $\chi_C = 0$ at the half-filling point, between the two Coulomb peaks. As the quantum capacitance is primarily related to χ_C, it could be expected that it also drops near to zero on the Kondo ridge. However, spin and orbital susceptibilities are not equal to zero[8]. While the spin degree of freedom is weakly coupled to the EM field via spin-orbit effects, it is not the case for the orbital degree of freedom. The orbital susceptibility χ_θ behaves like χ_C with a factor being roughly 1/16 (see [87]) and participate in C_{dot} as well. The relatively high Kondo temperature observed in this sample is compatible with the participation of orbital susceptibility in a SU(4) or SU(2)×SU(2) Kondo effect [46, 88]. This interpretation is reinforced by the probability to have orbital valley mixing in SWNT due to disorder, as developed in [83]. Therefore, even tough the information of the dispersive shift is different than the information contained in the conductance, its behaviour is similar with respect to the gate voltage.

[8] spin-flip processes only in the SU(2) situation, spin-filp and orbital "flips" for the SU(4) problem and they participate in the conductance.

4.2.5 Energy levels splitting : a direct observation of the coupling to the electronic states

The measurements presented in the precedent subsection have made it possible to estimate the coupling of the QD to the cavity mode. However, this estimation is rather indirect, especially compared to standard cQED experiments[9].

In this section, the effect of strong microwave power on the QD spectroscopy is studied. The discussion will focus on the closed QD in the Coulomb blockade regime *NTRES52a-Z6G*, which spectroscopy in one particular region of the gate voltage bias voltage plane is shown in figures 4.1 (d) and 4.12 (a), in the absence of microwave power. As the microwave power at the input port of the cavity is increased to -45dBm and -35dBm, energy levels split as shown in figures 4.12 (b) and (c) respectively.

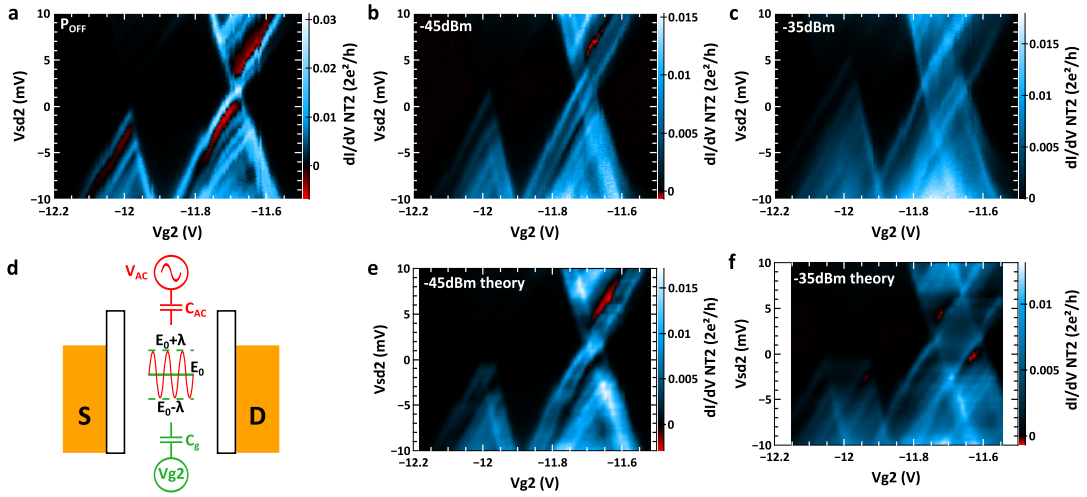

FIGURE 4.12: Evolution of a Coulomb diamond with increasing power at the input port of the microwave cavity. Input power is *Off* in **a**, -45dBm in **b** and -35dBm in **c**. **d :** scheme of the capacitive coupling action of the microwave field on the electronic level of the QD. The electronic level oscillates around its position without EM field E_0 with an amplitude λ. The averaging of this oscillation gives rise to two splitted levels at positions $E_0 \pm \lambda$. **e** and **f :** simulations of the averaged oscillation of the electronic level respectively for -45dBm and -35dBm.

This splitting, *e.g.* at $V_{G2} = -11.7$V, is 3meV at -45dBm and increases up to 10meV at -35dBm. This observation can firstly be explained classically by the "shaking" of the electronic levels at the cavity frequency, as already described in figure 4.5 and developed again in figure 4.12 (d). The QD electrons have a relaxation rate related to their coupling to the leads Γ. As $\Gamma \sim 1$meV corresponding to 250GHz, this relaxation rate is about 40 times higher than the microwave frequency of the cavity. Under this condition, the observed dynamical splitting can be explained by an averaging of the electronic level

[9] even tough as demonstrated formerly in this chapter, the Anderson-Holstein Hamiltonian maps onto the Jaynes-Cumming Hamiltonian.

position over several cycle of the microwave signal. The conductance of the QD under RF excitation of the cavity, $G_{RF=ON}$ can be written as

$$\begin{aligned} G_{RF=ON} &= f_0 \int_0^{1/f_0} G_{RF=OFF}(V_G + \lambda V_{AC}\cos(2\pi f_0 t), V_{sd})dt \\ &= \frac{1}{2\pi}\int_0^{2\pi} G_{RF=OFF}(V_G + \lambda V_{AC}\cos(\theta), V_{sd})d\theta \end{aligned} \tag{4.38}$$

This transformation is applied to the spectroscopy of figure 4.12 (a), measured without microwave drive, respectively for -45dBm and -35dBm, as represented in figure 4.12 (e) and (f). simulations reproduces data with $\alpha = 15.5$. The dynamical splitting and, in particular, the peculiar diamond emerging at the charge degeneracy point is well reproduced by this procedure. However, not all the spectroscopic feature of figures 4.12 (b) and (c) are reproduced. In particular, an excited states is observable in this newly formed diamond at $V_{G2} = -11.7$V, which is not visible in the simulation. The evolution of the Coulomb diamond bottom-left side (shaped as a triangle) is also not reproduced. Some of the excited states might thus have a different coupling mechanism to the photons than the ground state. The conclusion of this analysis is that the cavity mode couples mainly (but not only) to the electronic levels of the QD. This ensures that the phase measurements of the previous section [86] are not just another way to measure the conductance, even tough they both look similar.

A more specific way to decipher the origin of the coupling is to study the dependence of the level spacing with respect to the average number of photons dwelling in the cavity. Cuts at fixed gate voltage $V_{G2} = -1.8$V are done versus the input power of the cavity plane . This allows to directly read the energy level spacing without the capacitive lever arm of the gate voltage. The corresponding measurements are presented in figure 4.13 (a) and (b), respectively corresponding the Fabry-Perot QD *NTRES52aZ7D* (which spectroscopy is presented in figure 4.1 (a)) and the Coulomb blockaded QD *NTRES52aZ6G*. A characteristic funnel shape is observed for the energy level splitting, as the input microwave power is increased. With the help of equation (1.58) and cavity parameters extracted from figure 4.3, one can express the input power in terms of mean number of photons.

As shown in figure 4.13 (c) and (d), the splitting ΔE is linear with respect to the square root of the average number of photons $\sqrt{\bar{n}}$. This behaviour is reminiscent of the AC-Stark shift observed in cQED [3, 89], thus the observed splitting should read

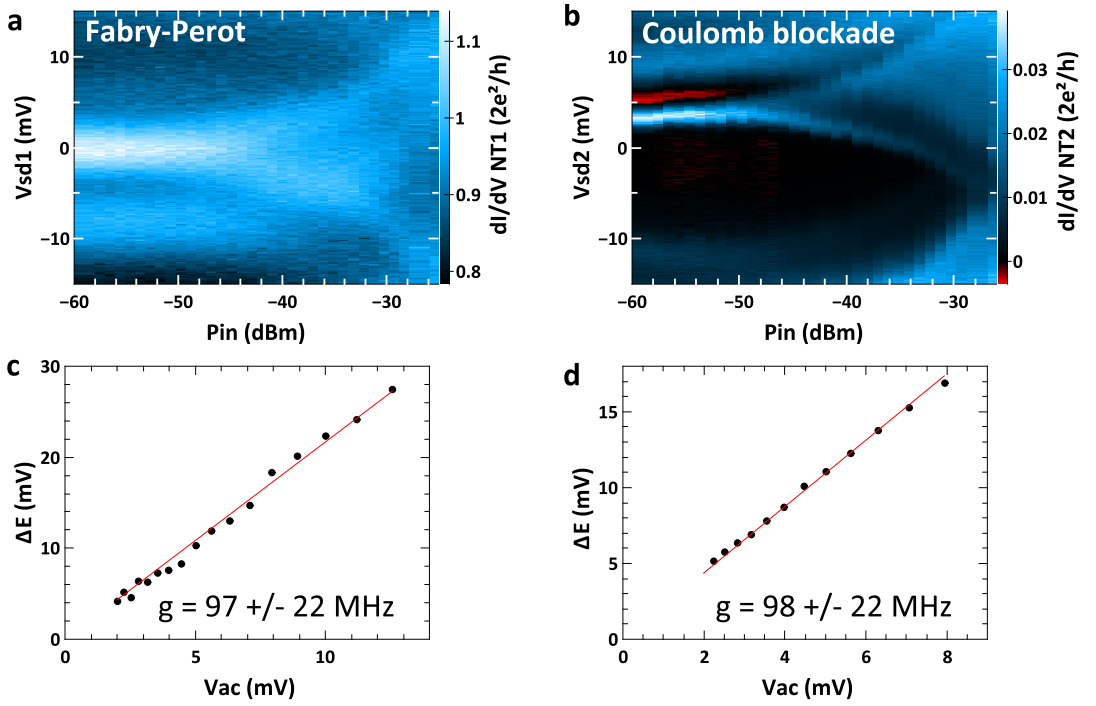

FIGURE 4.13: Energy level in bias voltage V_{sd} splitting versus RF power input P_{in}, in the case of Fabry-Perot (**a**) and Coulomb blockade (**b**) of figure 4.1. **c** and **d**, extracted energy level separation of respectively (**a**) and (**d**) versus V_{AC}. The linear dependence is directly related to the coupling g between the QD and the cavity.

$$\Delta E = 2g\sqrt{\bar{n}} \tag{4.39}$$

The fit of the linear dependence of ΔE with equation (4.39) gives $g = 97\text{MHz}\pm22\text{MHz}$ and $g = 98\text{MHz}\pm22\text{MHz}$ respectively. The relatively high uncertainty in the determination of g is due to systematic errors made in the exact determination of the power at the input port of the cavity, as well as the amplification chain[10]. This observation fully confirms the Anderson-Holstein vision of the problem, with the coupling g here being the formerly used parameter λ (in equation (4.1)). On an additional point, it should be noted that the parameter λ of equation (4.38) can be related to the coupling g. Indeed, the level splitting ΔE is also related to λV_{AC} of equation (4.38) as $\Delta E/2 = \lambda V_{AC}$. The coupling g in this case writes $g = \frac{\lambda e}{h}\frac{V_{AC}}{\sqrt{\bar{n}}}\frac{C_G}{C_\Sigma}$. The capacitive lever arm of this QD is extracted from the slope of one edge of the Coulomb diamond of figure 4.12 (a) and is $\frac{C_G}{C_\Sigma} = 0.125$. The resulting coupling strength is $g = 97\text{MHz}$, in agreement with the fit of the AC-Stark shift fit.

The fact that the electron-photon couplings of the 3 different QDs measured are similar can be puzzling at first. As already discussed, the coupling to the electronic levels can

[10]They have been respectively estimated to $\Delta P_{in} = \pm3\text{dBm}$ and $\Delta G = \pm3\text{dB}$.

be indirect via the common mode of the leads. All devices have basically the same design, especially the size of the electrodes and their positions in the gap of the resonator. Therefore, the coupling to the leads must be of the same magnitude for all samples. This is consistent with the sign of the dispersive frequency shift and the dynamical splitting model which showed that the cavity mode is coupled to the electronic levels of the QD.

Checking that the QDs are coupled to the cavity mode

To ensure that the QDs in which the level splitting is observed are coupled to the cavity mode, the splitting is measured versus frequency. The input power of the cavity is set to -45dBm, at which the splitting is already well developed, as shown in figure 4.13 (a) and (b) for both QDs. The frequency sweep associated to this splitting is shown in figure 4.14 for the QD in the Fabry-Perot regime (a) and the QD in the Coulomb blocakde regime (b). The data clearly show that the splitting occur at the cavity mode frequency $f_0 = 5.75$GHz in both case (see section *Samples IDs*). This additional observation gives thus a new clue that the QDs are indeed coupled to the resonator mode.

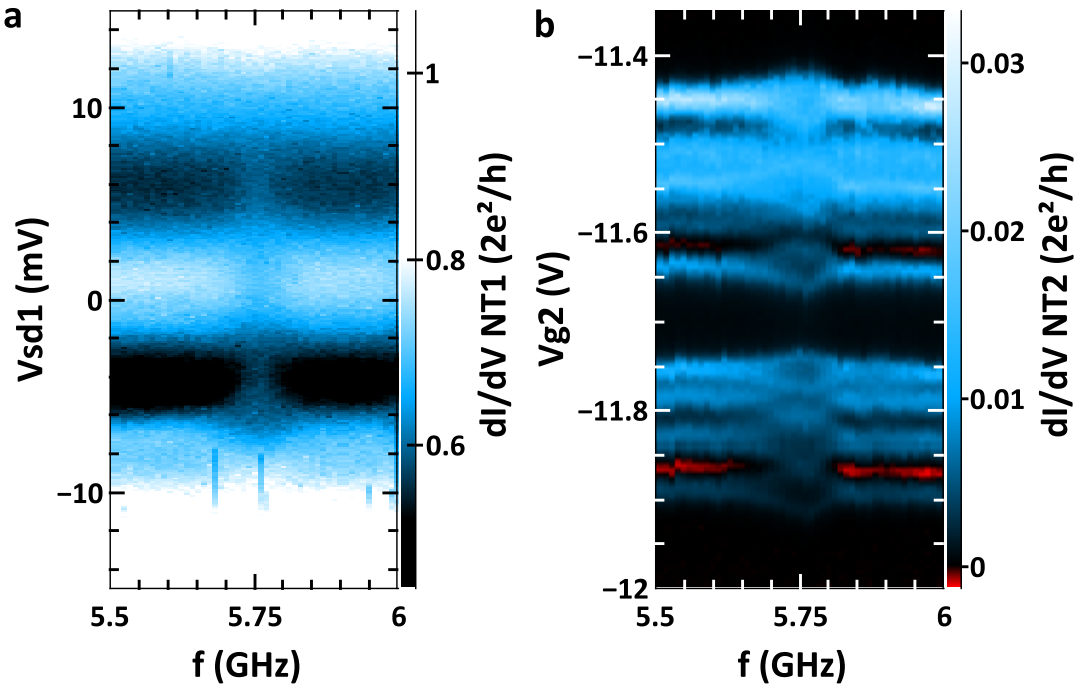

FIGURE 4.14: Splitting of the QD's energy levels versus frequency at a fixed input power of -45dBm. **a :** for the QD in the Fabry-Perot regime, corresponding to the splitting of figure 4.13 (a). **b :** for the QD in the Coulomb blockade regime, corresponding to the splitting of figure 4.13 (b).

4.3 Samples IDs

NTRES33b

Nanofabrication process First recipe, as described in chapter 3. Nb/Pt (200nm/30nm) CPW resonator etched by RIE first, then CNT growth by CVD inside the gaps of the resonator.

Cavity properties

Resonance frequency : $f_0 = 4.976$GHz

Quality factor : Q=150

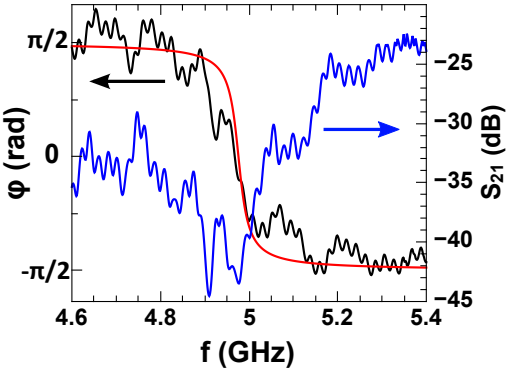

NTRES33bZ4D spectroscopy Coulomb blockade and Kondo effect. Differential conductance from 0.1 to 0.8 $\times 2e^2/h$. Charging energy $U \approx 7$meV. RF phase variation up to 3mrad.

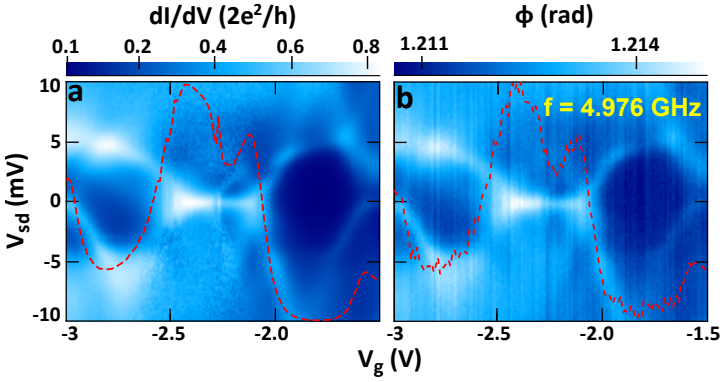

Electron-photon coupling $\lambda \approx 110$MHz

NTRES52a

Nanofabrication process Second recipe, as described in chapter 3. CNT growth by CVD and QD device fabrication first. UV lithography of Al (200nm) CPW resonator with optical alignment.

Cavity properties

Resonance frequency : $f_0 = 5.75$GHz

Quality factor : Q=40

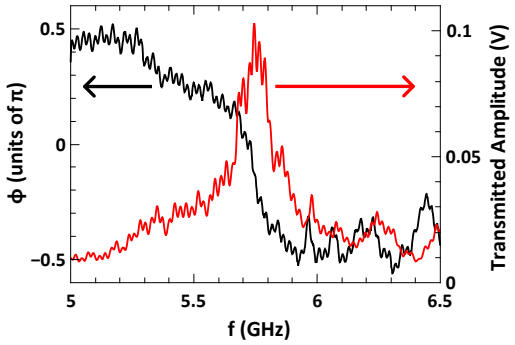

NTRES52aZ6G spectroscopy Coulomb blockade up to 0.03 $\times 2e^2/h$. Excited states observable. Charging energy $U \approx 12$meV.

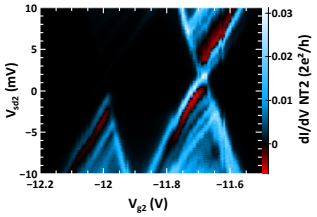

Electron-photon coupling $\lambda \approx 100$MHz.

NTRES52aZ7D spectroscopy Fabry-Perot regime with conductance up to $1.5 \times 2e^2/h$. Level spacing $\Delta \approx 7$meV.

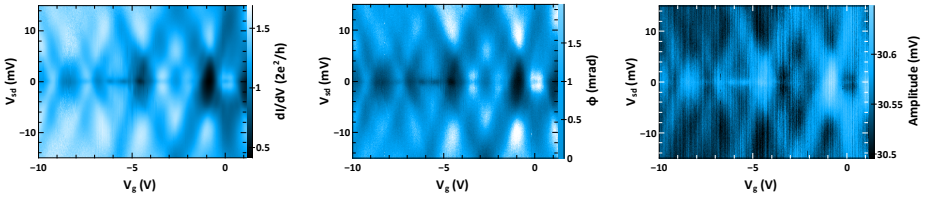

Electron-photon coupling $\lambda \approx 100$MHz.

Chapter 5

Interaction between two Quantum Dots

5.1 Embedding two quantum dots in one microwave cavity

As emphasized in chapter 4, the device architecture that has been developed in this thesis allows for coupling QD circuits to a microwave cavity. The electron-photon coupling strength g is of the order of the coupling found in superconducting circuits cQED [4, 36]. This is motivating enough to push a step further the investigation of such complex systems. One possible way was to reach the quantum limit for the microwave field. This regime should allow for studying the interaction between the two systems at the single photon level, as well as for performing coherent manipulations. This requires a dilution refrigerator in order to reach the millikelvin temperature range needed for it. However, there are also quantum features that can be investigated at moderate temperatures. Among the possible methods for coupling quantum dots [90–92], the use of photons is particularly attractive because they can mediate a potentially coherent interaction over macroscopic distances. In this sense, the direction that as been taken is to add another QD in the cavity and therefore investigate the interaction between the two QD devices, via the cavity photons, as schematically depicted in figure 5.1 (a). This has two potential applications. First, it provides a scalable architecture for performing quantum computation with spin qbit [15, 93]. Second, it also allows to simulate on-chip condensed matter situations like polaronic shifts, in a direct manner.

Thanks to the developed device architecture, it has been possible to make a device with 2 QDs embedded in a single microwave cavity, as shown in figure 5.1 (b). The sample (*NTRES52a*) has been made with the reversed process described in chapter 3 (second recipe). The resonator is made of aluminium (blue color in figure 5.1 (b)). While the

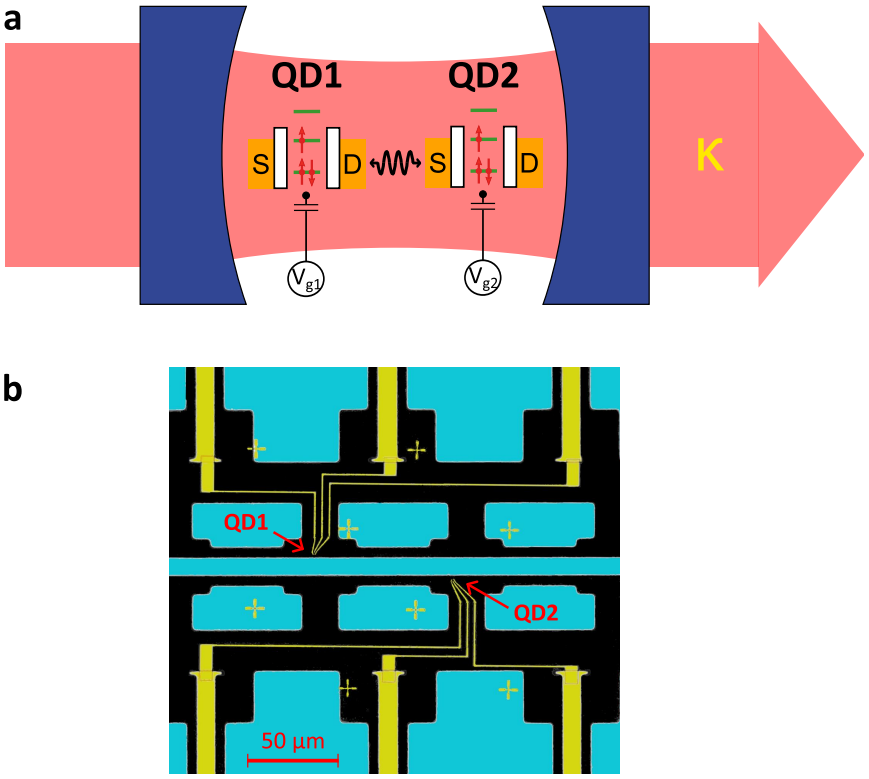

FIGURE 5.1: **a :** Scheme of two separate QDs interacting inside a microwave cavity. Both QDs are independently tuned and interact with the cavity mode. A distant interaction between the QDs can be mediated via the cavity photons. **b :** Optical micrograph in false colors of a device showing 2 QDs (yellow electrodes) embedded inside the same CPW superconducting resonator (in blue). The 2 QDs share the same anti-node of the electric field and are separated by about 80μm.

experiments are performed at temperature above its $T_C \approx 1.19$K, the cavity exhibits a resonance mode at $f_0 = 5.75$GHz with a quality factor $Q = 40$, as shown in chapter 4, in the samples IDs (see figure 4.3).

The 2 QDs, defined by the 3 contacting electrodes in Pd (yellow structures in figure 5.1 (b)) share the same anti-node of the EM field. In addition, they are separated by 80 μm, which is about 200 times their own size[1]. Therefore they constitute two independent QD circuits without direct tunnelling nor direct gate coupling from one QD to the other : the lever arm between a QD and the central conductor of the resonator is of the order of C_G/C_{res} ≈1aF/1pF≈ 10^{-5}. Each QD is contacted in the standard source-drain-gate electrodes geometry, allowing to measure them independently. This point is important and leads to two direct observations : first, this system is different from double QDs coupled to microwave cavities [25–27] as the 2 QDs here are neither tunnel

[1]The QDs are lithographically designed to measure 400nm, which yields a scaling factor of 200. Nevertheless, from the spectroscopy of the Fabry-Perot QD (figure 4.3), the length of this QD can be estimated to be of the order of 220nm. Therefore the scaling factor between the inter-dot distance and their size could be estimated to be about 350.

nor electronically coupled, and second, the independent tunability of each QD gives a mean to map the interaction between them.

5.2 Probing the distant interaction

As discussed in chapter 4, both the 2 QDs of this sample are coupled to the microwave field with electron-photon couplings $g_1, g_2 \approx 100$MHz. As both are coupled to the same EM field, they can a priori be coupled to each other, as depicted in figure 5.1 (a). In order to probe the coupling of the states of QD1 and those of QD2, QD2 is used as a detector[2] to measure the evolution of its energy levels via transport spectroscopy as its own gate, V_{g2}, and the distant gate of QD1, V_{g1}, are swept. Such a mapping is presented in figure 5.2, for a large span over each gate voltages. QD2's levels exhibit a strong dependence with respect to the gate voltage of the distant QD1. Level crossings (as in the region $(V_{g1}, V_{g2}) \approx (11V, -14V)$) and anticrossings (as in the region $(V_{g1}, V_{g2}) \approx (9.5V, -14V)$) are visible and will be studied in more details below. The strong slope of QD2's levels, of the order of 4V/V should also be noted.

Two points, already mentioned in the previous paragraph, find here their full meaning. First, the spectroscopy shown here suggest a strong interaction between the QDs circuits. Direct capacitive crosstalk between the two is vanishingly small thanks to the vanishingly small lever arm already discussed. Furthermore, any direct crosstalk should lead to QD2's levels to behave similarly with the same slope in the $V_{g1} - V_{g2}$ plane[3]. As QD2's levels undergo crossings and anticrossings, this possibility is thus eliminated. Secondly, crossings and anticrossings of levels could be reminiscent, at first, of the honeycomb structure of double QD devices spectroscopies [94]. However the system is made of two independent SWNT, therefore the situation investigated here is clearly different.

5.3 Polaronic shift

Trivial mechanisms that could explain the dispersion of QD2's levels have been removed. Therefore, the interaction should be mediated by the cavity photons, thanks to the couplings g_1 and g_2. A natural mechanism implying these couplings is the polaronic shift. A polaron is an electron system coupled to a phonon bath, but as usual this can be extended to the situation of an electron system coupled to any bosonic modes. The presence of a bosonic bath at frequency ω_0 coupled to the electronic system with a strength g shifts the energy levels of the electronic systems by [95]

[2] QD2 is in a Coulomb blockade regime with small energy levels broadening Γ.

[3] they should be on lines $V_{g2} + \alpha V_{g1}$ with α the lever arm between the to distant circuits.

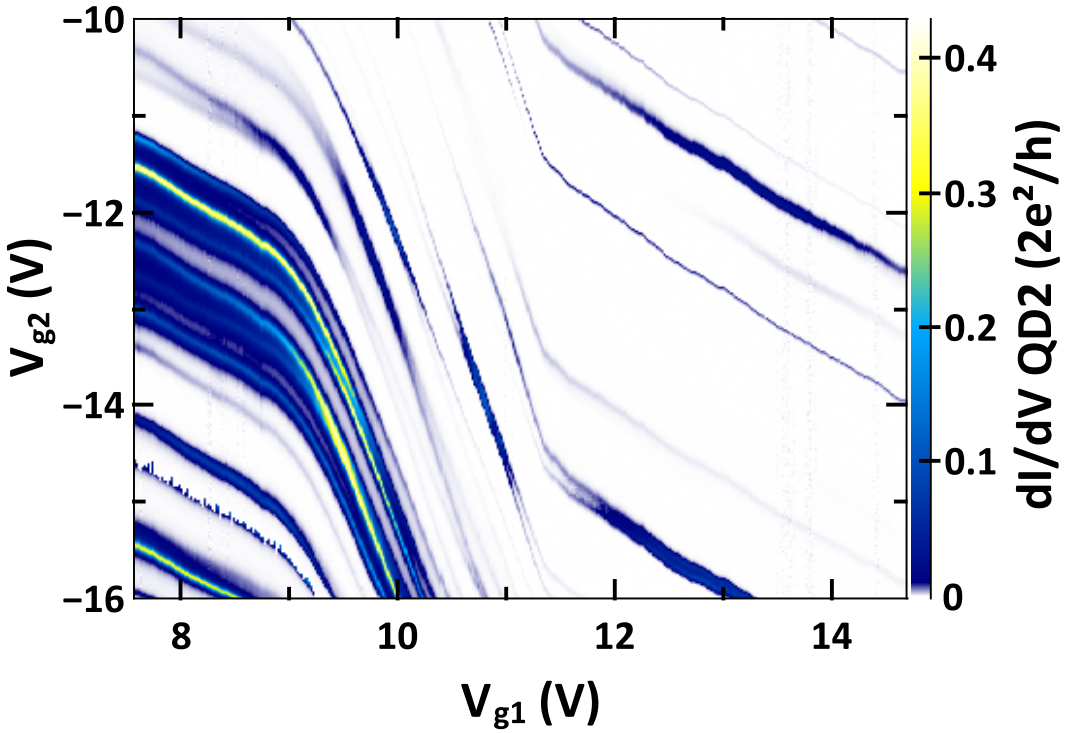

FIGURE 5.2: Color scale plot in the gate voltage of QD1 V_{g1} gate voltage of QD2 V_{g2} of the differential conductance of QD2. The energy levels of QD2 exhibits a strong dependence versus V_{g1}, showing anticrossings and crossings.

$$\Delta\epsilon = -\frac{2g}{\omega_0}\hat{n} \tag{5.1}$$

with $\hat{n}$ the operator number of electron of the electronic system. This shift is called the polaronic shift. In this section, the situation is extended to 2 QDs coupled to a photonic mode.

5.3.1 Theoretical approach with Green's functions

The effect of thermal and virtual photons from perturbation theory is investigated here. To help the reader not to be lost, QD2 refers to the coulomb blockaded QD, which is used as a detector, and QD1 refers to the Fabry-Perot QD. The theoretical approached that will be detailed here relies on Green's functions, as in chapter 2 section 2.

Renormalized photon Green's function

First, the renormalized interaction for QD2 as a consequence of QD1, using random phase approximation (RPA) is considered. The renormalized photon Green's function

$D(i\omega_n)$ can be found to be [15]

$$D^{-1}(i\omega_n) = D_0^{-1(i\omega_n)} - g_1^2\Pi_1(i\omega_n) \tag{5.2}$$

with $D_0(i\omega_n)$ the free photon Green's function

$$D_0(i\omega_n) = \frac{2\omega_0}{(i\omega_n)^2 - \omega_0^2} \tag{5.3}$$

and $\Pi_1(i\omega_n)$ the charge susceptibility of QD1. The renormalized photon Green's function thus writes

$$D(i\omega_n) = \frac{2\omega_0}{(i\omega_n)^2 - \omega_0^2 - 2g_1^2\omega_0\Pi_1(i\omega_n)} \tag{5.4}$$

Here, the term $\Omega^2 = \omega_0^2 + 2g_1^2\omega_0\Pi_1(i\omega_n)$ refers to the photon mode frequency square. It can be re-expressed as $\Omega \approx \omega_0(1+g_1^2/\omega_0\Pi_1(i\omega_n))$. One can recognize here the expression of the dispersive frequency shift δf_R, which is of the order of 100kHz, much smaller than the mode frequency which is about 6GHz. Therefore expansion with respect to this term is used.

Distant QDs direct interaction

The first process that can be thought of is the direct interaction between the 2 QDs, via a cavity photon. A photon at frequency $i\omega_n$ is emitted by QD2, interacts with QD1 and is re-absorbed by QD2 at the same frequency $i\omega_n$, as diagrammatically represented in figure 5.3.

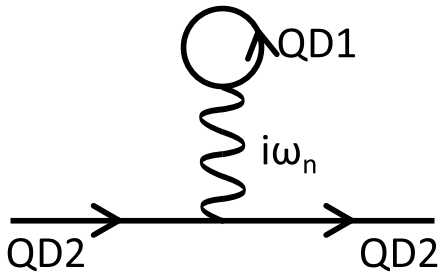

FIGURE 5.3: Diagrammatic representation of the distant interaction between QD1 and QD2 without photon renormalization. The plain lines with arrows refers to electronic propagators of QDs. The whirly line refers to photon propagator at frequency $i\omega_n$.

The corresponding self energy writes

$$D_1 = -kT \sum_{n=-\infty}^{\infty} \sum_j \left(-g_1 g_2 D(0) \frac{1}{i\omega_n - \epsilon_{1,j} + i\Gamma_{1,j}} \right) \tag{5.5}$$

Here ω_n refers to the fermionic Matsubara frequencies $(2n+1)\pi kT$, and j refers to the states of QD1 with energy $\epsilon_{1,j}$ and coupling $\Gamma_{1,j}$ to the leads. The photon Green's function is taken for $i\omega_n = 0$ as the re-absorbed photon is at the same frequency as the emitted photon. QD1 is assumed to be a non interacting QD, which is a reasonable hypothesis considering its Fabry-Perot behaviour. The sum $kT\sum_n (i\omega_n - \epsilon_{1,j} + i\Gamma_{1,j})^{-1}$ is the Fermi-Dirac distribution $f(\epsilon_{1,j} - i\Gamma_{1,j})$. One thus gets

$$D_1 = -g_1 g_2 \frac{2}{\omega_0 + 2g_1^2 \Pi_1(i\omega_n)} \sum_j f(\epsilon_{1,j} - i\Gamma_{1,j}) \tag{5.6}$$

By considering the atomic limit $\Gamma_{1,j} = 0$ and lowest order in g_1, the standard polaronic shift is recovered

$$D_1 = -2\frac{g_1 g_2}{\omega_0} N_{1,tot} \tag{5.7}$$

with $N_{1,tot}$ the total number of electrons on QD1. Note here that this is a perturbation theory approach. However, it recovers the results that can be found by using an exact calculation relying on the Lang-Firsov transformation (see appendix E). Indeed, as it will be shown later, $N_{1,tot}$ can be very large, leading to non-perturbative corrections.

5.3.1.1 Photon renormalization of QD2

The second process that must be considered is similar to the first one, except that the photon is renormalized by QD1 before being re-absorbed by QD2. Therefore, the emitted and re-absorbed photon have a different frequency. This is diagrammatically depicted in figure 5.4.

The corresponding self energy writes

$$D_2 = kT \sum_{n'=-\infty}^{\infty} \sum_j -g_2^2 D(i\omega_{n'}) \frac{1}{i\omega_n - i\omega_{n'} - \epsilon_{2,j} + i\Gamma_{2,j}} \tag{5.8}$$

As $\omega_0/(2\pi) \approx 6$GHz and $\epsilon_{2,j}, \Gamma_{2,j} \approx 1meV\equiv 250$GHz, therefore $\omega_0 \ll \epsilon_{2,j}, \Gamma_{2,j}$ and it is reasonable to omit the Matsubara frequency in the electron propagator of QD2. The

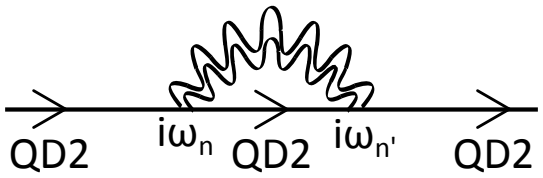

FIGURE 5.4: Diagrammatic representation of the distant interaction between QD1 and QD2 with photon renormalization. The plain lines with arrows refers to electronic propagators of QD2. The whirly double line refers to renormalized photon propagator, corresponding to equation eq (5.4).

sum over Matsubara frequencies is then just on the renormalized photon propagator D :

$$D_2 \approx kT \sum_j \frac{1}{i\omega_n - \epsilon_{2,j} + i\Gamma_{2,j}} (-g_2^2) \sum_{n'=-\infty}^{\infty} \frac{2\omega_0}{(i2\pi n' kT)^2 - \Omega^2} \tag{5.9}$$

where $\Omega^2 = \omega_0^2 + 2g_1^2\omega_0\Pi_1(0)$. In the expression of Ω, the charge susceptibility of QD1 is taken at $\omega_n = 0$ for the same reasons as above. Equation (5.9) rewrites

$$\begin{aligned} D_2 &= \sum_j \frac{1}{i\omega_n - \epsilon_{2,j} + i\Gamma_{2,j}} \frac{2g_2^2\omega_0}{4\pi^2 kT} \sum_{n'=-\infty}^{\infty} \frac{1}{n'^2 + \left(\frac{\Omega}{2\pi kT}\right)^2} \\ &= g_2^2 \frac{\omega_0}{\Omega} (1 + 2n_B(\Omega)) \sum_j \frac{1}{i\omega_n - \epsilon_{2,j} + i\Gamma_{2,j}} \end{aligned} \tag{5.10}$$

To obtain the last expression (5.10), the following relations are needed : $\sum_{n=0}^{\infty} \frac{1}{n^2+\alpha^2} = \frac{\pi\alpha\coth(\pi\alpha)+1}{2\alpha^2}$, $\sum_{n=-\infty}^{\infty} \frac{1}{n^2+\alpha^2} = 2\sum_{n=0}^{\infty} \frac{1}{n^2+\alpha^2} - \frac{1}{\alpha^2}$ and $\coth\left(\frac{\Omega}{2kT}\right) = 1 + 2n_B(\Omega)$, with n_B the Bose-Einstein distribution. Note here that the term $1 + 2n_B(\Omega)$ is made of two different contributions. The term "1" consists of a virtual process that involves a virtual photon, while the term "$2n_B$" refers to thermal photons processes. In the following, the case of a single orbital of QD2 will be considered. Furthermore, as the real Green's function is needed, analytical continuity $\omega_n = -i\omega + 0^+$ is performed, leaving

$$D_2(\omega) = g_2^2 \frac{\omega_0}{\Omega} (1 + 2n_B(\Omega)) \frac{1}{\omega - \epsilon_2 + i\Gamma_2} \tag{5.11}$$

Renormalized QD2's Green's function

The new electronic Green's function of QD2 for one orbital writes

$$G^{-1}(\omega) = G_0^{-1}(\omega) - D_2(\omega) \tag{5.12}$$

with $G_0^{-1}(\omega) = (\omega - \tilde{\epsilon}_2 + i\Gamma_2)$ the free electronic Green's function of QD2, where the polaronic shift has been taken into account in $\tilde{\epsilon}_2 = \epsilon_2 - D_1(\omega) = \epsilon_2 - 2g_1g_2/\omega_0 N_{1,tot}$. Equation (5.12) rewrites

$$G(\omega) = \frac{G_0(\omega)}{1 - \alpha^2 G_0(\omega)^2} \tag{5.13}$$

with $\alpha^2 = g_2^2(1 + 2n_B(\Omega))$. As $\alpha \in \mathbb{R}^+$, the electronic Green's function rewrites

$$G(\omega) = \frac{1}{2}\left(\frac{1}{G_0^{-1}(\omega) + \alpha} + \frac{1}{G_0^{-1}(\omega) - \alpha}\right) \tag{5.14}$$

Finally, from equation (5.14), the renormalized states of QD2 up to first order in g_1, g_2 write

$$\tilde{\epsilon}_{2,+/-} = \underbrace{\epsilon_0 + \alpha_0 C_{g2} V_{g2}}_{\text{term 1}} \underbrace{- 2\frac{g_1 g_2}{\omega_0}\left[N_{0,QD1} + \frac{C_{g1}V_{g1}}{e}\right]}_{\text{term 2}} \underbrace{\pm g_2\sqrt{1 + 2n_B(\omega_0)}}_{\text{term 3}} \tag{5.15}$$

In the last expression, all parameters have been expressed in terms of experimental parameters. Expression (5.15) is made of three different terms that need some explanation.

term 1 : this term has been previously noted ϵ_2. It is the standard QD2's levels modulation thanks to the external gate voltage V_{g2} applied to it with a lever arm α_0, with respect to an energy origin ϵ_0.

term 2 : this term is the polaronic shift of QD2's energy levels. It is the signature of the interaction between the two QDs, mediated via the cavity. The total number of electrons on QD1 has been expressed by the number of electrons due to electrochemical doping $N_{0,QD1}$ in addition to the number of electrons added when tuning the gate voltage V_{g1}. QD2's levels thus undergo a global shift due to its distant interaction with QD1.

term 3 : this term corresponds to a splitting of QD2's levels that were originally degenerate. Contrarily to the splitting discussed in chapter 4, which is a dynamical splitting, here it is due to exchange processes with the cavity photons. Both virtual and

thermal photons are involved in the mechanism. The relative slope between split levels is thus directly related to the coupling g_2 of QD2 to the microwave cavity.

Orders of magnitude and confrontation with experiment

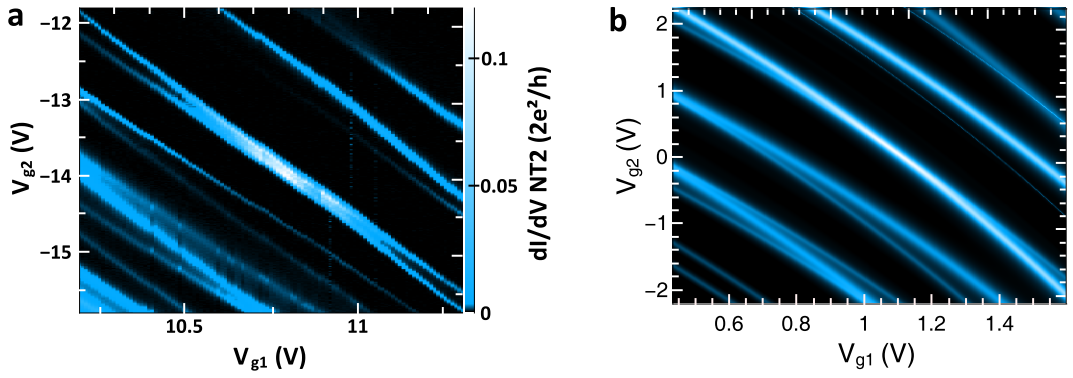

FIGURE 5.5: **a :** Close-up on one particular region of figure 5.2 where QD2's levels cross. QD2's levels are subject to 2 different slopes with respect to V_{g1}, in an alternate pattern. **b :** Simulation of (a) using equation (5.15) with the following parameters : : $\alpha_0 = 0.3$, $C_{g2} = 1\text{aF}$ $g_1 = 100(1 - 0.25V_1)$, $g_2 = 100(1 - 0.25V_2)$, $N_{0,QD1} = 10^6$, term 3 $= g_2 = 100(1 - 0.25V_2) \times 4\text{meV}$.

Figure 5.5 (a) presents a close-up in one particular region of figure 5.2 where levels crossings are observed, as well as an alternation of levels getting closer and away from each other. Figure 5.5 (b) presents a simulation of this spectroscopy using equation (5.15) in the presence of interactions. Interactions has been accounted for by using Lorentzian shape of width Γ for the levels, shifted by U for the two levels $+/-$ of one orbital, at $T = 0$. Similarly to the EOM description detailed in chapter 2, the self-consistency equations set

$$\begin{cases} G_{+/-} = \dfrac{1 - \langle n_{-/+} \rangle}{\omega - \tilde{\epsilon}_{2,+/-} + i\Gamma/2} + \dfrac{\langle n_{-/+} \rangle}{\omega - \tilde{\epsilon}_{2,+/-} - U + i\Gamma/2} \\ \langle n_{+/-} \rangle = -\dfrac{1}{\pi} \displaystyle\int d\epsilon f(\epsilon) \text{Im}[G_{+/-}(\epsilon)] \end{cases} \tag{5.16}$$

yields

$$\langle n_{+/-} \rangle = \frac{\frac{1}{2} - \frac{1}{\pi} \arctan \frac{2\tilde{\epsilon}_{2,+/-}}{\Gamma} + \frac{\beta_{+/-}}{\pi} \left(\frac{1}{2} - \frac{1}{\pi} \arctan \frac{2\tilde{\epsilon}_{2,-/+}}{\Gamma} \right)}{1 - \frac{\beta_+ \beta_-}{\pi^2}} \tag{5.17}$$

with

$$\beta_{+/-} = \arctan \frac{2\tilde{\epsilon}_{2,+/-}}{\Gamma} - \arctan \frac{2\tilde{\epsilon}_{2,+/-} + 2U}{\Gamma} \tag{5.18}$$

QD2 spectral function is calculated from the expression of $\langle n_{+/-} \rangle$ for several orbital (this is taken into account by changing the energy origin ϵ_0), which is shown in figure 5.5 (b). To recover the levels behaviour observed in figure 5.5 (a), several assumptions and orders of magnitude must be clarified.

electron-photon coupling dependence with the gate voltage To correctly account for the strong slope dependence of QD2's levels versus V_{g1} as well as the increasing splitting, it is necessary to consider that the electron-photon coupling of both QDs g_1 and g_2 are dependent on their own respective gate. This is taken into account by considering a linear dependence over a small span of V_g : $g_{1(2)}(V_{g1(2)}) = g_{1(2)}(1 - \alpha_{1(2)} V_{g1(2)})$. This assumption is reasonable considering the standard spectroscopies of each QD. Indeed, in the classical picture, the electron-photon coupling is the ratio between the capacitance of the QD to the resonator and the total capacitance of the island : C_{AC}/C_Σ. In chapter 4, in the discussion about sample *NTRES33b*, the effective capacitance of the QD varies from 18aF in the Coulomb blockade region to 22aF in the Kondo region. This corresponds to a change of about 22% of the coupling, induced by a change of the gate voltage. For the samples that are discussed here, this variation can be estimated from the standard spectroscopies by evaluating the ratio C_g/C_Σ from the slope of Coulomb diamonds edges or the slope between two bright spots of the Fabry-Perot checker board. As C_g is a geometric quantity, it does not vary, hence a variation of C_g/C_Σ indicates a change in C_Σ, therefore a change of the electron-photon coupling g. To reproduce the slope of figure 5.5 (a), both g_1 and g_2 need to vary of about 25% over the considered span. Both QD's spectroscopies indicate that such variations are reasonable. Furthermore, this dependence of $g_{1(2)}$ accounts well for the wide change of slope that is visible in figure 5.2. A dynamical splitting measurement of QD1 for several V_{g1} has shown a variation of more than 10% of g_1 over the range where the observed QD2 levels slope is the largest. Before and after this region, g_1 seems to be more or less constant. This feature thus reproduces the observed pattern. To properly simulate the data with good orders of magnitude, one needs to evaluate the other involved quantities.

Electron number on QD1 The global slope of 4V/V observed for QD2 levels is accounted for by considering a very large number of electrons on QD1 : $N_{0,QD1} \approx 10^6$. This value, while being huge, is compatible with the experiment. Indeed, QD1 is made out of a SWNT that is metallic[4]. The Fermi level of such metallic SWNT can a priori be

[4]No band-gap has been observed and only Fabry-Perot regime is accessible.

very high and could explain this large number of electrons on QD1. Note however that, like for a classical metal, these electrons do not contribute to the transport through the QD.

Thermal photons The second and last quantity to evaluate is the number of thermal photons in the cavity. A first contribution to this quantity comes from cavity mode population at the experiment temperature $T = 1.5$K. It reads $n_1 = n_B(\hbar\omega_0/kT) \approx 5$ photons[5]. The second contribution comes from the fact that the cavity is not isolated from the world but connected to input and output lines which brings thermal noise through thermalized attenuators. The calculation of the noise level of these attenuators has been performed in chapter 3 section 2. The number of corresponding photons is the integral of the spectral noise density at each port of the cavity over the the cavity. Equations (1.53), (1.54) and (1.56), are rearranged considering that power input at the 2 ports of the cavity, yielding

$$\langle n_{th} \rangle = \int_{\omega_1}^{\omega_2} \frac{4\gamma}{(\gamma+\gamma_L)^2 + 4(\omega-\omega_0)^2} \frac{S_{VV,in} + S_{VV,out}}{\hbar\omega} d\omega \tag{5.19}$$

The integration boundaries are respectively taken to 4GHz and 8GHz as they define the overall bandpass of the RF setup[6]. This term is temperature dependent via the attenuators that are thermalized at the sample temperature. The calculation gives $n_2 \approx 33$ photons at $T = 1.5K$. Therefore, the total number of thermal photons in the cavity is $N_{th} = n_1 + n_2 \approx 38$ photons. It is therefore better to speak in term of effective temperature for the cavity population[7], which in this case is $T_{eff} = 10$K.
This makes a level splitting $g_2\sqrt{1+2N_{th}} \approx 3\mu$eV, three orders of magnitude smaller than what is observed in figure 5.5. Actually, considering this contribution only, 5.10^6 thermal photons are needed to give the required 4meV splitting. However, as it will be discussed in the following section, an additional parameter can be added in the splitting term. It will reveal compatible with the observed orders of magnitude and the photonic processes will reveal negligible.

[5]This definition gives the number of photons at frequency ω_0, that dwell in the cavity for a time $2\pi/\Delta\omega$. This constitutes a basis for photons in the frequency-time plane. The previous result can be found differently by integrating the Bose-Einstein distribution times the spectral density of the cavity over all frequencies $\int n_B(\omega)\chi(\omega)d\omega$ with $\chi(\omega)$ the spectral density of the cavity.

[6]Note that in chapter 3, the noise power at the input and output port where calculated by integrating the noise spectral density over a flat band pass. This point is reasonable as the RF setup is basically flat over the 4GHz - 8GHz frequency span.

[7]It is possible to extrapolate a linear expression for the effective temperature $T_{eff} \approx 4.4 + 4.2T_{exp}$.

5.3.2 Energy level splitting

To make the splitting picture complete, it is important to look at the energy diagram presented in figure 5.6 (a). Energy levels of QD2 are schematically represented versus the energy of QD1 ϵ_1 and energy of QD2 ϵ_2. 2 orbitals are pictured, respectively in red and blue. The 2 spin degenerate levels are separated by U inside an orbital and two orbitals are separated by $\Delta + U$. The split levels must fulfil the Coulomb repulsion, therefore, inside an orbital, two levels cannot be separated by less than U. This avoids levels to come closer inside an orbital, as depicted by the crosses. However, between two orbitals, levels can come closer and even cross. Depending on the hybridization between orbitals, these levels can cross or anticross, as observed in the spectroscopy of figure 5.2 and 5.5. The resulting alternation of levels getting closer and away from each others is well observed in the measurements. Figure 5.6 (b) presents such measured diagram, extracted from figure 5.2. The position of each level in the plane $(V_{g1}, V_{g2}) \equiv (\epsilon_1, \epsilon_2)$ is reported. The overall slope is removed by taking one level as a reference ($\epsilon_2 = 0$, black level). Dashed levels are taken at $T = 1.5$K while plain levels are taken at $T = 3$K. The experimental diagram is in good qualitative agreement with the theoretical picture.

As previously discussed, the thermal photons term cannot explain the observed orders of magnitude. The difference in the slopes of the splitted levels at $T = 1.5$K and $T = 3$K (dashed and plain lines respectively), which is of the order of a factor 4 is not accounted by the estimation of thermal photons as well. Indeed, a $N_{th}(3\text{K}) \approx 1.6 N_{th}(1.5\text{K})$, therefore the slope variation should be around 30%. Nevertheless, it has already been mentioned that orbital levels can split in CNTs coupled to AC field, due to disorder valley mixing [83]. In this work, Palyi *et al.* describe this splitting by the following Hamiltonian (using the notation of this thesis)

$$H = \begin{pmatrix} \epsilon_2 & g_2 \Delta_{KK'} \\ g_2 \Delta^{\star}_{KK'} & \epsilon_2 \end{pmatrix} \tag{5.20}$$

where $\Delta_{KK'}$ is the valley mixing, or orbital hybridization term. The two eigenstates of such Hamiltonian are $\epsilon_{+/-} = \epsilon_2 \pm g_2 |\Delta_{KK'}|$. The splitting term of equation (5.15) rewrites $\pm g_2(\sqrt{1 + 2N_{th}} + |\Delta_{KK'}|)$. It is reasonable to say that $\Delta_{KK'}$ can be of the order of few meV. In addition, it should also be dependent with temperature via fluctuations of impurities, as this valley mixing term is due to disorder on the CNT. However, this issue is still open and needs more investigations, both theoretical and experimental, to settle it.

A closer inspection of one of the observed anti-crossings is presented in figure 5.7. Along the white dashed line following the anti-crossing (figure 5.7(a)), the corresponding QD2's

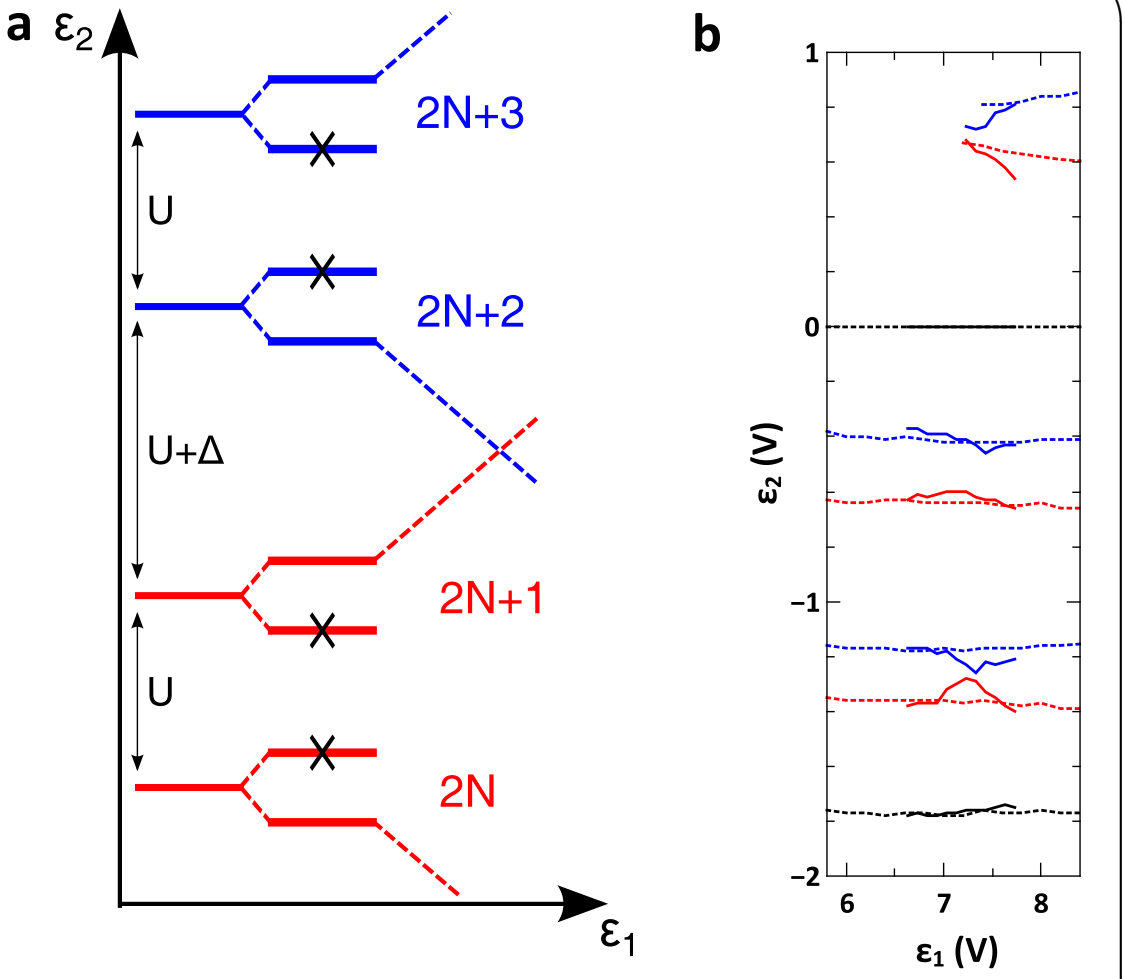

FIGURE 5.6: **a :** Energy levels diagram of a Coulomb blockaded QD, when there is a splitting. 2 orbitals are represented in red and blue. Inside an orbital, the energy levels are separated by the charging energy U. Two orbitals are separated by the level separation in addition to the charging energy $\Delta + U$. Inside an orbital, levels separated by less than U due to the splitting are forbidden (crossed levels). Levels from different orbitals can cross or anticross, depending on the hybridization between the orbitals levels. **b :** Experimental data showing the alternation of crossing or anticrossing levels depicted in (a). Data are taken from figure 5.2 at $T = 1.5K$ (dashed lines) and $T = 3K$ (plain lines). By increasing the temperature, the slope of the splitted levels increases roughly by a factor 4.

Coulomb diamond is measured. The cut in V_{sd2} in the middle of the diamond is reported in figure 5.7 (b), versus the gate voltage V_{g1} of QD1. The distance between the two peaks directly gives the level splitting ΔE in meV, which is reported in figure 5.7 (c). The data are well fitted with an avoided crossing expression

$$\Delta E/2 = \sqrt{\epsilon_1 + \Delta} + \Delta_0 \tag{5.21}$$

with $\Delta = 1.8$meV and $\Delta_0 = 1.8$meV. This confirms the mechanism of figure 5.6 in which

split levels from different orbitals can cross or anticross, depending on the hybridization between them. In the situation presently discussed, a finite coupling between the two measured orbital levels is responsible for the avoided crossing.

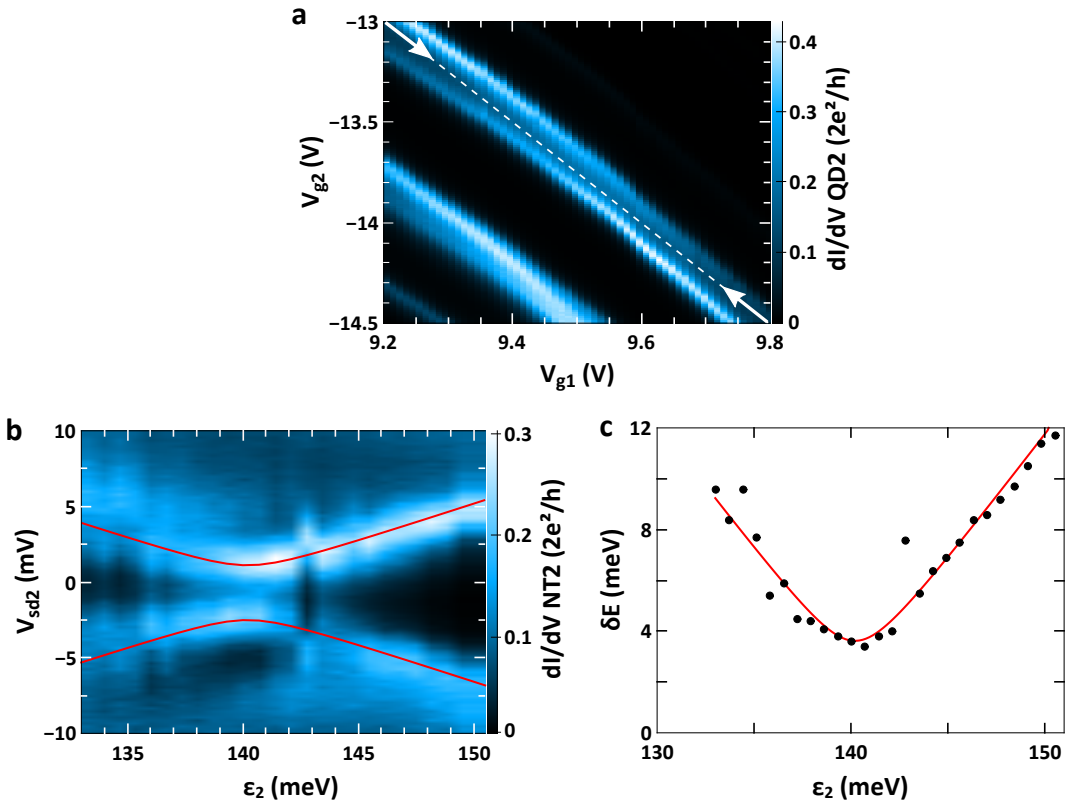

FIGURE 5.7: **a :** Close-up on one particular region of figure 5.2 where QD2's levels anticross. **b :** Color scale plot of the energy level splitting along the white dashed line of (a). For every gate voltage V_{g1}, a differential conductance scan in the gate voltage of QD2 V_{g2} bias voltage of QD2 V_{sd2} is taken. The cut in the middle of the corresponding Coulomb diamond is reported in (b). The red curves correspond to equation. **c :** Energy level separation ΔE extracted from (b) (black dots) and fit with equation (red curve).

5.3.3 Summary

The distant interaction between the 2 QDs, embedded inside the microwave cavity, has been investigated in this section. Figure 5.2, which gives a direct insight of it, seemed rather difficult to be interpreted at first. However, a picture has emerged and 3 mechanisms can explain it.

1. The overall slope of QD2's levels in the $V_{g1} - V_{g2}$ plane is due to a polaronic shift $-2g_1g_2/\omega_0 N_{tot,QD1}$, involving the coupling of both QDs to the microwave cavity. The number of electrons on the distant QD is a crucial parameter that explains

the large shift which is observed.

2. QD2's states, initially degenerates, undergo a splitting due to a renormalization by the cavity photons. The slope of the splitting, relative to the polaronic shift, is proportional to the coupling g_2 between QD2 and the cavity field.

3. The crossings or anticrossings of the different orbital levels gives an insight on the hybridization between these levels[8]. This last contribution is thus related to the inner structure of the QD discrete spectrum.

5.4 Joint read-out

In the previous section, the differential conductance of QD2 has allowed for probing the distant interaction between the 2 QDs. As they are both coupled to the cavity, they should both modulate the phase of the microwave field. The transmitted RF phase is thus measured in one particular region of the $V_{g1} - V_{g2}$ plane, where the anti-crossings are observed. Figure 5.8 shows such measurement. Levels of both QDs are visible, as indicated by the green arrows. The previously measured levels of QD2 are thin and undergo a strong slope with respect to V_{g1}, as previously seen. QD1's levels are also visible, large (due to the large Γ of the Fabry-Perot regime) and with a very small slope with respect to V_{g2}. This small slope can be interpreted by a much smaller number of electrons on QD2 compared to QD1[9].

The second observation to be made is that levels of both QD cross and show no avoided crossing. This is expected as the electronic and photonic systems are far detuned[10]. It has however the same origin as the mechanism leading to coherent SWAP manipulations for Rydberg atoms or superconducting qbits [3, 36, 96]. These coherent manipulations of qbits are essential for quantum computation purposes.

5.5 Tunable coupling

Electron-photon coupling of a QD modulates with its own gate voltage. This has been discussed in this chapter as a consequence of the QD's quantum capacitance variation

[8] No hybridization between 2 crossings levels and finite hybridization between anti-crossing levels.

[9] QD2 is way more blocked than QD1, therefore the number of electrons on the QD should be much smaller than on QD1.

[10] Let's recall that the characteristic frequency for the electronic system is of the order of 250GHz (1meV) while it is 6GHz for the cavity.

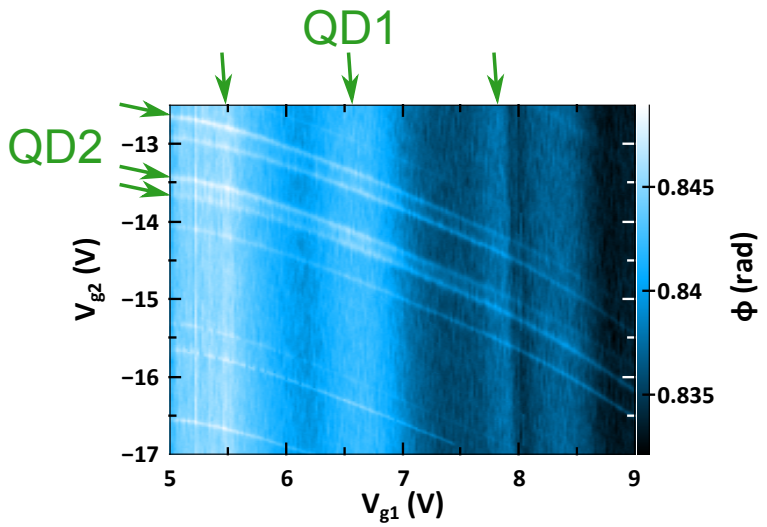

FIGURE 5.8: Joint Read-out of the energy levels of QD1 and QD2 (indicated by green arrows) in the phase of the transmitted microwave field.

with the gate voltage. This can be observed in the conductance spectroscopy as the pattern ratio between gate and bias voltage changes. Here the influence of the distant QD on the coupling is investigated.

5.5.1 Distant quantum dot as a "knob"

Figure 5.9 shows the relative value g_2/g_0 (with $g_0 = 111$MHz) versus the differential conductance of QD1. The value of the coupling g_2 is extracted from a dynamical splitting, as discussed in chapter 4. Such measurement has an uncertainty of the order of 20MHz, due to the uncertainty on the number of resident photons in the cavity. However, as it is a systematic error, the ratio between two couplings g has an uncertainty of about 2% only. The gate of QD1 is tuned between 9V and 14V. For each gate voltage V_{g1}, V_{g2} is adjusted in order to follow the same Coulomb diamond in QD2, the one studied in chapter 4 and shown in figure 4.12 for example. This allows to stay in the same spectroscopic region of QD2 and removes any influence of the inner variation of g_2.

The dashed blue line is a guide to the eye that shows the presumably linear dependence of g_2 with respect to $G_1 = dI/dV(QD1)$. Each black symbol is a measurement at zero bias at a different gate voltage V_{g1}. The green and red symbols represent two data sets where QD1 is biased, for two different V_{g1}. These ensure that the observed trend is effectively related to the conductance of QD1 and not to a trivial capacitive mechanism involving V_{g1}. The data suggest a linear dependence with a variation of about -28% of g_2 for a QD1's conductance variation of $2e^2/h$. This system thus controllably tune the

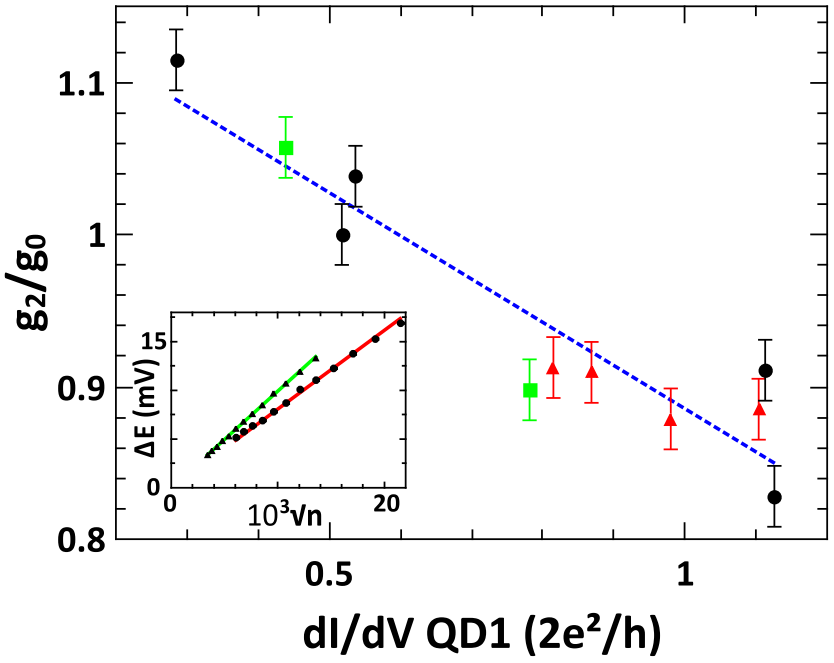

FIGURE 5.9: Variation of the coupling strength g_2 of QD2 to the microwave field, as a function of the differential conductance of QD1. g_2 is extracted from a power dependence of the energy level splitting, as described in chapter 4. The systematic error on the determination of g_2 is removed by plotting g_2/g_0, with $g_0 = 111$MHz. Black dots indicate coupling g_2 measured at different gates voltages V_{g1}. Green squares and red triangles indicate measurements at two data sets at finite bias voltage V_{sd1} for two particular gate voltages V_{g1}. The dashed blue line is a guide to the eye for a possible linear dependence $g_2/g_0 \propto dI/dVQD1$. The proportionality coefficient is -0.28, corresponding to a variation of 28% of g_2 when the conductance of QD1 varies of $2e^2/h$. **Bottom left inset :** Level spacing for the two extremal values of the main figure, $dI/dVQD1 = 1.13 \times 2e^2/h$ (dots, red fit) and $dI/dVQD1 = 0.28 \times 2e^2/h$ (triangles, green fit).

coupling between a QD and the photon field with significant magnitude. However, at this point, the mechanism explaining this behaviour has yet to be found.

5.5.2 Spectroscopic read-out of the tunable coupling

One way to confirm the previous measurement is to directly probe the tunability of g_2 from the spectroscopy of QD2. The cavity is driven with a power at its input port $P_{in} = -40$dBm. It induces a dynamical splitting of the QD's levels. As QD2's level separation writes

$$\Delta E_2 = 2g_2\sqrt{\bar{n}} \tag{5.22}$$

if g_2 varies with G_1, therefore, at a fixed value of the number of photons $\bar{n}$ (hence P_{in}), ΔE_2 should vary similarly. Measurement of QD2's conductance in the $V_{sd1} - V_{sd2}$ plane for $P_{in} = -40$dBm is presented in figure 5.10 (a), and the corresponding phase joint read-out in (b). Two levels are visible as horizontal lines, corresponding to a split level of QD2. The joint-read out measurement allows to simultaneously see QD1's levels as vertical broad lines.

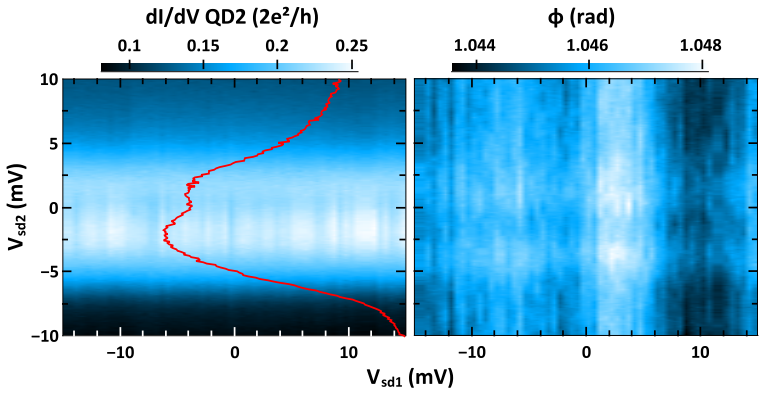

FIGURE 5.10: **a :** Color scale plot of QD2's differential conductance in the bias voltage of QD1 V_{sd1} bias voltage of QD2 V_{sd2} plane. Two peaks in the conductance are visible, as emphasized by the red curve which is a cut at $V_{sd2} = -4.8mV$. The power at the input port of the cavity is $P_{in} = -42$dBm. **b :** Corresponding joint read-out of the 2 QDs in the phase of the transmitted microwave field.

QD2's levels separation is presented in figure 5.11 as a red curve (right axis). Each point of the curve is measured independently on the spectroscopy of figure 5.10 (a). The corresponding differential conductance of QD1, G_1 is represented as a black curve (left axis), showing a variation of about $0.35 \times 2e^2/h$. Even though the measurement shows a lot of uncertainty (the spectroscopy is already the results of 5 global averages), the proportionality between ΔE_2 and G_1 is visible. The dependence extracted from the previous measurement presented in figure 5.9 is applied on the current differential conductance of QD1 and shown by the blue curve, which accounts well for the observations. For comparison, the green dashed curve corresponds to the linear fit of $\Delta E_2 \propto G_1$ for the current measurement. The coherence between the two experiments gives credit to the picture of a tunable electron-photon coupling at distance.

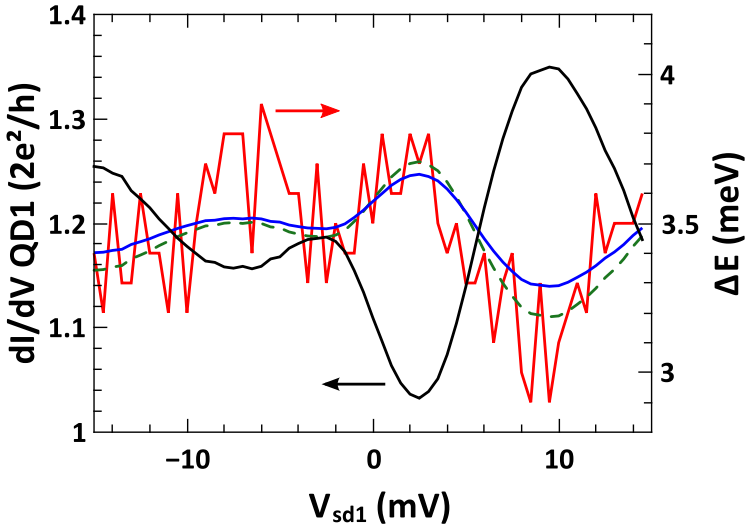

FIGURE 5.11: Energy level separation ΔE (red curve) between the two peaks of figure 5.10 (a) as a function of the bias voltage V_{sd1} applied on QD1. The corresponding QD1's differential conductance is shown as a black curve. The expected dependence $\Delta E(G1) = 2g_1(G1)\sqrt{n}$ with $g_1(G1)$ extracted from figure 5.9 is represented as a blue curve. The dashed green curve corresponds to the same formula with the linear regression taken from ΔE (red curve) as a function of $G1$ (black curve).

Chapter 6

Quantum capacitance out of equilibrium : preliminary measurements

Up to this point, measurements of the quantum capacitance have been performed at zero bias. The QD's capacitance is properly defined at equilibrium only. It is related to the charge susceptibility of the electronic system. At finite bias voltage drive, finite current passes through the QD. Therefore charges enter and exit the electronic island continuously. Definition of a QD's capacitance becomes thus less intuitive. New insights on QDs physics not accessible to conventional transport can be awaited from such regime investigations. In this chapter, preliminary results of such measurements are presented, obtained in sample *NTRES33bZ4D*. They already show a peculiar behaviour of the quantum capacitance out of equilibrium. Further investigations are required however, especially in a transport regime different than Kondo regime, where theoretical predictions can be more easily obtained.

6.1 Fourfold degeneracy playground

The spectroscopic region in which these preliminary measurements have been undertaken is presented in figure 6.1 (a). The differential conductance in units of $2e^2/h$ is shown in the gate voltage V_g bias voltage V_{sd} plane. It ranges from 0.2 to 0.8 $\times 2e^2/h$ and exhibits a typical fourfold degeneracy pattern. Two Kondo ridges are especially visible in the Coulomb diamonds corresponding to $N = 1$ and $N = 3$ electrons in the concerned orbital. In the $N = 2$ Coulomb diamond, conductance ridges are visible at finite bias voltage, corresponding to inelastic co-tunnelling. The interest of this region is that due

to the fourfold degeneracy, the electronic state within the orbital is well defined and known.

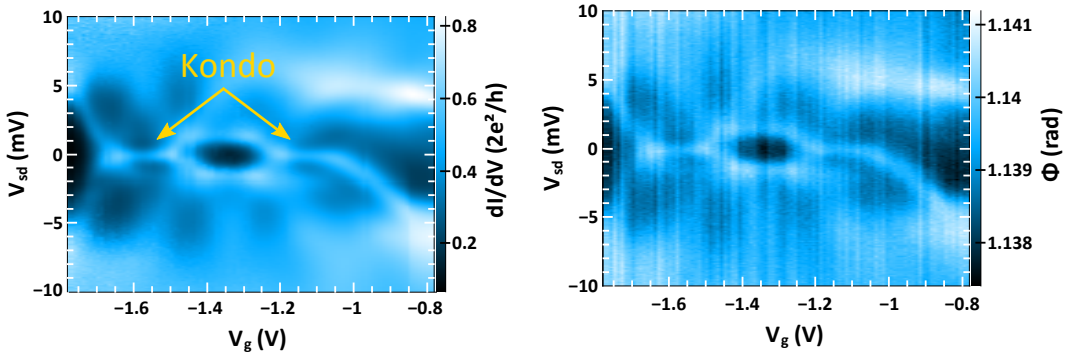

FIGURE 6.1: **a :** color scale plot of the differential conductance in unit of $2e^2/h$ in the gate voltage V_g bias voltage V_{sd} plane. Fourfold degeneracy is observable, with 2 Kondo ridges (orange arrows) corresponding to fillings N=1 and N=3 in the orbital. **b :** color scale plot of the transmitted RF signal's phase, simultaneously taken with (a).

As for the measurements presented in chapter 5, the phase of the transmitted RF signal is taken simultaneously, and gives a phase spectroscopy of the QD. It is presented in figure 6.1 (b). Similarly, the phase shows the same behaviour as the differential conductance, as every feature of the latter is visible in the former. First, a phase contrast measurement method is done at zero bias (as described in chapter 5 section 4.2.2). The dispersive and dissipative frequency shifts δf_R and δf_D obtained are presented in figure 6.2 with blue and red dots respectively. They respectively modulate up to 60kHz and 20kHz. The fits of δ_R and δf_D, using equations (4.33) and (4.16) gives an effective capacitance $C_0 = 22.8$aF and an asymmetry factor $\alpha = 0.004$, similar to the values obtained on the previous Kondo ridge study in chapter 5.

6.2 Out of equilibrium effective QD capacitance

The same kind of measurements is then performed versus bias voltage at fixed gate voltages. Out of equilibrium excursions are thus performed, as shown in figure 6.3 (a). The dispersive frequency shift and the differential conductance are represented on the same plot. The V_{sd} excursion is close to the equilibrium regime, as it spans from -400μV to 400μV. Once more, the frequency shift modulates like the conductance, which could be expected considering the phase spectroscopy of figure 6.1 (b) relative to the transport spectroscopy.

The linear dependence of δf_R with respect to the differential conductance dI/dV is shown in figure 6.3 (b) for two different gate voltages V_g. It is unambiguous that the slope of the

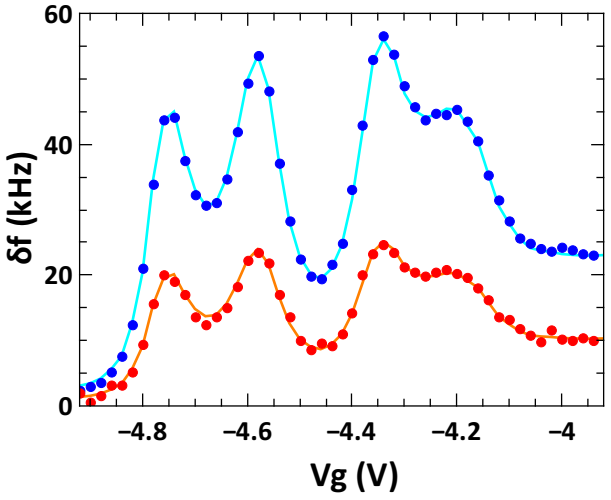

FIGURE 6.2: Dispersive (blue dots) and dissipative (red dots) frequency shifts at zero bias along the spectroscopy of figure 6.1 (a). The gate voltage V_g abscissa differs from the one of figure 6.1 (a) due to a gate voltage jump. the spectroscopy itself had remained unchanged. The differential conductance is represented in unit of dispersive (cyan curve) and dissipative (orange curve) frequency shift.

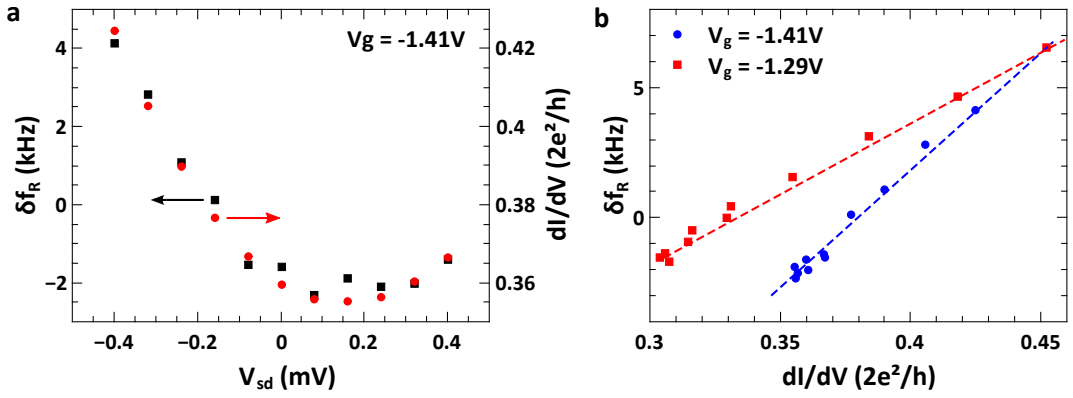

FIGURE 6.3: Out of equilibrium dispersive frequency shift δf_R measurements. **a :** dispersive frequency shift of the cavity (black squares, left axis) and differential conductance (red dots, right axis) versus the bias voltage V_{sd} at a particular gate voltage $V_g = -1.41$V of figure 6.1 (a). **b :** dispersive frequency shift versus differential conductance for 2 different gate voltages $V_g = -1.41$V (blue dots) and -1.29V (red squares). Linear fits with the formula (4.33) are represented for both data with blue and red lines respectively.

linear dependence is clearly different for the two considered gate voltages. Two different values of an effective capacitance are thus obtained, $C_0'(V_g = -1.29V) = 18 \pm 1$aF and $C_0'(V_g = -1.41V) = 25 \pm 1$aF. Not only these values differ from each other by more than the uncertainty estimation, but they also deviate from the value obtained at zero bias. It is thus a clear signature of the system behaving differently in the out of equilibrium situation. To have a clear vision of the whole evolution of the out of equilibrium effective

capacitance C_0', the measurements are performed along the whole fourfold degeneracy region, as showed in figure 6.4. The differential conductance at zero bias is represented as a red curve and the effective capacitance $C_0 = 22.8$aF found in this situation is represented by a blue horizontal line. The out of equilibrium effective capacitance C_0' has been measured via phase contrast protocol every 0.03V along V_g, as showed in figure 6.4 by the black squares.

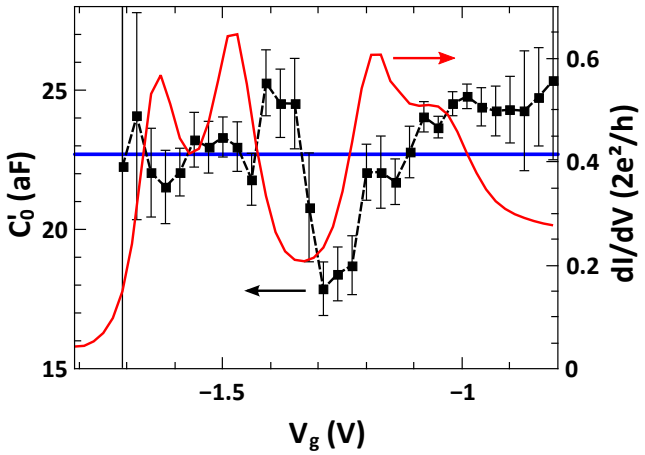

FIGURE 6.4: Effective QD capacitance C_0' (black squares, left axis) in the out of equilibrium regime. The value of C_0 is extracted from the linear dependence of δf_R versus the differential conductance, as shown in figure 6.3 (b). The corresponding differential conductance at zero bias is represented as a red curve (right axis). The value of $C_0 = 22.8$aF, at equilibrium, extracted from figure 6.2 is represented by the horizontal blue line.

$C_0'(V_g)$ shows a non trivial behaviour. For the first time, the capacitance of the QD does not modulate like the conductance. This result confirms the conclusion of chapter 4 that the cavity is coupled to the electronic levels of the QD. The measurement of the phase (and indirectly of δf_R) is clearly here not redundant with the differential conductance. More specifically, C_0' evolves around the value $C_0 = 22.8$aF found at equilibrium. The uncertainty on the value of C_0' is less than its variation[1]. Therefore it is possible to try finding a pattern in the evolution of C_0'. The most straightforward observation that can be done is that C_0' undergoes a drop of about 7aF (corresponding to a drop of 30%) in the $N = 2$ Coulomb diamond. It corresponds to the electron-hole symmetry point of the orbital. It is thus reasonable to cautiously say that the evolution of C_0' is related to the orbital filling.

[1]For the two first points, the error bars are big, which is due to the low differential conductance and thus low phase variation at these gate voltages. The linear regression between two signals with low SNR is inevitably very uncertain.

These preliminary results need to be complemented by more experimentation and theoretical modelling. It is therefore necessary to reproduce these measurements in different samples. Investigating less complex transport regime, and particularly Fabry-Perot regime, would allow to properly understand the behaviour of the system in the out of equilibrium regime. Furthermore, samples with better cavity allowing both the phase and amplitude of the RF signal to be measured will make it possible to acquire more rapidly new data.

Conclusion

This manuscript has addressed the development and study of microwave cavity embedded QDs, in a cQED architecture. Single wall carbon nanotubes have been chosen as the QD material because they offer a great versatility and a wide range of applications. Other groups have decided to study similar QD based cQED architecture with 2DEG [25, 26] or nanowires [27]. Several important results have been found during this work. First, a strong electron-photon coupling between SWNT QD devices and microwave cavities has been measured, of the order of 100MHz [86]. This high value is comparable with superconducting circuits based cQED. It is therefore a promising platform for developing quantum computation with QDs based Qbits. This point has been reinforced by the demonstration of the distant interaction between two QDs embedded inside the same microwave cavity. This should allow to perform gate operations which are necessary for quantum computing. Finally, the dispersive shift read-out technique used in this work gives a new probe to study new aspects of QDs. It especially allows for accessing their dynamic response and gives a direct way to measure the quantum capacitance of such systems.

The studied QD could be considered as charge Qbit. The charge having a very small coherence time, it is illusory to perform coherent manipulation of any charge state with the microwave field, hence quantum computation operations. However, QDs devices are suitable for making spin qbits [15, 90, 97] which have coherence times compatible with cQED. Reaching the strong coupling regime with such device is therefore the next and most important step. Nevertheless, this only constitutes one of the promising aspects of such architecture.

Both the measurements of the quantum capacitance in the Kondo regime and the distant interaction polaronic shift have shown that condensed matter situation are addressed with these devices. A wide variety of experiments can be performed with this cQED architecture. One can think of measuring the dynamics of the Kondo cloud, which experimental signature still remains to be demonstrated. This could be achieved by measuring a Kondo ridge of temperature around 300mK, corresponding to the 6GHz of

the resonator. Similarly, if the characteristic energy of the electronic system is comparable with the resonator frequency, one should be able to observe dynamical Coulomb blockade effect [98]. It should particularly address the non perturbative regime in the case of a single mode of the environment. Measurement of such situation has been recently done with an ohmic impedance [99].

Another promising aspect of such architecture is the recently predicted [21] possibility to probe the coherence of split Cooper pair. Such splitter can be made with CNTs [20] or nanowires [100]. Embedding such device in a microwave cavity of few thousand quality factor would reveal the coherence via a sub-radiance effect. Within the current keen interest for Majorana fermions, it has also been proposed to embed a Kitaev chain device (see *e.g* [101]) inside a microwave cavity [102]. This would allow for observing the topological transition and witness the signature of these particles. These few proposals show how rich the physics of this cQED with QD architecture is.

Appendix A

Scattering matrix in the Fabry-Perot regime

A.1 Scattering matrix of the Fabry-Perot

We start with the system described in the paragraph about Fabry-Perot regime with SWNT on page 20. We need to solve the system shown in figure A.1 (in order to lighten the notations, the subscript $SWNT$ used in the main text is replaced by W here)

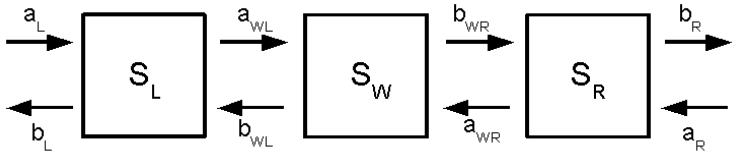

FIGURE A.1: Model of the system representing left (L) and right (R) contacts connnected by a wire (W) being the nanotube.

$$\begin{aligned} b_{WR} &= e^{i\delta} a_{WL} \\ &= e^{i\delta}(-i\sqrt{T_L}\ a_L + e^{-i\phi_L}\sqrt{1-T_L}\ b_{WL}) \\ &= e^{i\delta}(-i\sqrt{T_L}\ a_L + e^{i(\delta-\phi_L)}\sqrt{1-T_L}\ a_{WR}) \\ &= e^{i\delta}(-i\sqrt{T_L}\ a_L + e^{i(\delta-\phi_L)}\sqrt{1-T_L}(e^{-i\phi_R}\sqrt{1-T_R}\ b_{WR} - i\sqrt{T_R}\ a_R)) \end{aligned}$$

so that

$$b_{WR} = \frac{-ie^{i\delta}\sqrt{T_L}\ a_L - ie^{i(2\delta-\phi_L)}\sqrt{(1-T_L)T_R}\ a_R}{1-e^{i(2\delta-(\phi_R+\phi_L))}\sqrt{(1-T_L)(1-T_R)}}$$

we then get

$$b_R = \frac{-e^{i\delta}\sqrt{T_L T_R}\ a_L - e^{i(2\delta-\phi_L)}\sqrt{1-T_L}T_R\ a_R}{1-e^{i(2\delta-(\phi_R+\phi_L))}\sqrt{(1-T_L)(1-T_R)}} + e^{i\phi_R}\sqrt{1-T_R}\ a_R$$

This equation structure will be useful later. But for now, we will reduce to the same denominator to get

$$b_R = -\frac{e^{i\delta}\sqrt{T_L T_R}}{1-e^{i(2\delta-(\phi_R+\phi_L))}\sqrt{(1-T_L)(1-T_R)}}\ a_L + \frac{e^{i\phi_R}\sqrt{1-T_R} - e^{i(2\delta-\phi_L)}\sqrt{1-T_L}}{1-e^{i(2\delta-(\phi_R+\phi_L))}\sqrt{(1-T_L)(1-T_R)}}\ a_R$$

We get the same expression for b_L by inverting indexes R and L. Finally the full matrix reads

$$\mathbf{s_{Tot}} = \frac{1}{D}\begin{pmatrix} e^{i\phi_L}\sqrt{1-T_L} - e^{i(2\delta-\phi_R)}\sqrt{1-T_R} & -e^{i\delta}\sqrt{T_L T_R} \\ -e^{i\delta}\sqrt{T_L T_R} & e^{i\phi_R}\sqrt{1-T_R} - e^{i(2\delta-\phi_L)}\sqrt{1-T_L} \end{pmatrix}$$

with $D = 1 - e^{i(2\delta-(\phi_R+\phi_L))}\sqrt{(1-T_L)(1-T_R)}$

We note that the denominator becomes very small for specific phase value and that there is resonance phenomenon for the following condition

$$2\delta = \phi_L + \phi_R + 2\pi n$$

Assuming a weak coupling limit $T_\alpha \approx 0$

$$\begin{aligned} e^{i(2\delta-(\phi_R+\phi L))} &\simeq 1 + i(2\delta - (\phi_R+\phi_L)) \\ \sqrt{(1-T_R)(1-T_L)} &\simeq 1 - \frac{1}{2}(T_R+T_L) + \frac{T_R T_L}{4} \end{aligned}$$

Keeping only first order terms, we get

$$D \simeq \frac{1}{2}(T_R + T_L) - i(2\delta - (\phi_R + \phi_L))$$

Moreover, δ is the detuning due to the optical path in the cavity, so that we can express the excited energy levels with the help of the resonance condition

$$\delta = \frac{EL}{\hbar v_F} \tag{A.1}$$

$$E_n = \frac{\hbar v_F}{2L}(2\pi n + \phi_L + \phi_R) \tag{A.2}$$

Introducing the notation $\Gamma_\alpha = \frac{\hbar v_F}{2L} T_\alpha$ and $\Gamma = \Gamma_R + \Gamma_L$, the prefactor becomes

$$\begin{aligned} \frac{1}{1 - e^{i(2\delta - (\phi_R + \phi_L))}\sqrt{(1-T_L)(1-T_R)}} &= \frac{1}{\frac{1}{2}(T_R + T_L) - i(E - E_0)\frac{2L}{\hbar v_F}} \\ &= \frac{i}{\Delta(E)}\frac{\hbar v_F}{2L} \end{aligned}$$

with $\Delta(E) = E - E_0 + i\Gamma/2$.

We then find for transmission terms

$$s = -ie^{i\delta}\frac{\sqrt{\Gamma_R \Gamma_L}}{\Delta(E)}$$

and reflection terms

$$s_{R/L} = e^{i\phi_{R/L}}\Big(1 - i\frac{\Gamma_{R/L}}{\Delta(E)}\Big)$$

So that we find the final result

$$s_{\alpha\beta} = e^{i\frac{\phi_\alpha + \phi_\beta}{2}}\Big(\delta_{\alpha\beta} - i\frac{\sqrt{\Gamma_\alpha \Gamma_\beta}}{\Delta(E)}\Big) \tag{A.3}$$

Appendix B

Master equation solution of the double occupancy coulomb blockade regime

B.1 Probabilities in the stationary regime

We solve equation (1.21) for the stationary condition $\frac{d\vec{P}}{dt} = \vec{0}$. A additional equation must be added to make the system soluble, the sum of all probabilities is equal to one $\sum_n p_n = 1$. We consider spin degeneracy so that $p_\uparrow = p_\downarrow = p$. The system becomes

$$\begin{cases} 0 = -2\Gamma^+ p_0 + 2\Gamma^- p \\ 0 = \Gamma^+ p_0 - (\Gamma^- + \tilde{\Gamma}^+)p + \tilde{\Gamma}^- p_{\uparrow\downarrow} \\ 0 = 2\tilde{\Gamma}^+ p - 2\tilde{\Gamma}^- p_{\uparrow\downarrow} \\ 1 = p_0 + 2p + p_{\uparrow\downarrow} \end{cases} \tag{B.1}$$

Solving the system we find

$$p = \frac{\Gamma^+}{\Gamma^-} p_0, \quad p_{\uparrow\downarrow} = \frac{\tilde{\Gamma}^+\Gamma^+}{\tilde{\Gamma}^-\Gamma^-} p_0, \quad p_0 \left[1 + 2\frac{\Gamma^+}{\Gamma^-} + \frac{\tilde{\Gamma}^+\Gamma^+}{\tilde{\Gamma}^-\Gamma^-} \right] = 1 \tag{B.2}$$

By noting that $f(\xi) + f(-\xi) = 1$, we have $\Gamma^+_\alpha + \Gamma^-_\alpha = \tilde{\Gamma}^+_\alpha + \tilde{\Gamma}^-_\alpha = \gamma_\alpha$. We recall here that $\Gamma^\pm_\alpha = \gamma_\alpha f^\pm_\alpha(\xi + V_\alpha)$. The symmetrization of the problem is taken into account in writting $\Gamma^\pm = \Gamma^\pm_L + \Gamma^\pm_R$ and $\gamma = \gamma_L + \gamma_R$. The expression of the levels occupancy probabilities becomes

$$\begin{cases} p_0 = \dfrac{\tilde{\Gamma}^-\Gamma^-}{\gamma(\tilde{\Gamma}^- + \Gamma^+)} \\ p = \dfrac{\tilde{\Gamma}^-\Gamma^+}{\gamma(\tilde{\Gamma}^- + \Gamma^+)} \\ p_{\uparrow\downarrow} = \dfrac{\tilde{\Gamma}^+\Gamma^+}{\gamma(\tilde{\Gamma}^- + \Gamma^+)} \end{cases} \tag{B.3}$$

B.2 Expression of the current

The current is given by the following equation

$$I = 2e\left[\tilde{\Gamma}_L^+ p + \Gamma_L^+ p_0 - \Gamma_L^- p - \tilde{\Gamma}_L^+ p_{\uparrow\downarrow}\right] \tag{B.4}$$

By re-expanding the expressions of the Γ, many terms get simplified and one ends with the following compact expression

$$I = 2e\frac{\Gamma^+(\tilde{\Gamma}_L^+\tilde{\Gamma}_R^- - \tilde{\Gamma}_L^-\tilde{\Gamma}_R^+) + \tilde{\Gamma}^-(\Gamma_L^+\Gamma_R^- - \Gamma_L^-\Gamma_R^+)}{\gamma(\tilde{\Gamma}^- + \Gamma^+)} \tag{B.5}$$

This last expression can be expressed in terms of Fermi distribution as

$$I = \frac{2e}{h}\frac{\gamma_L\gamma_R}{\gamma_L + \gamma_R}\frac{\Gamma^+\left[\tilde{f}_L^+\tilde{f}_L^- - \tilde{f}_R^+\tilde{f}_R^-\right] + \tilde{\Gamma}^-\left[f_L^+ f_L^- - f_R^+ f_R^-\right]}{\Gamma^+ + \tilde{\Gamma}^-} \tag{B.6}$$

B.3 Linear regime

The linear regime is obtained for $eV/2 \ll kT$. In this situation, the Fermi distributions can be expanded as

$$f(x \pm \frac{eV}{2}) = f(x) \pm \frac{eV}{2}\frac{1}{4kT\cosh^2\left(\frac{x}{2kT}\right)} + O\left(\left(\frac{eV}{2}\right)^2\right) \tag{B.7}$$

and the product of Fermi distributions of equation (B.6) are expanded as

$$f(x \pm \frac{eV}{2}) f(-x \pm \frac{eV}{2}) = f(x)f(-x) \pm \frac{eV}{2} \frac{1}{4kT \cosh^2\left(\frac{x}{2kT}\right)} \left(f(x) + f(-x)\right)\right) + O\left(\left(\frac{eV}{2}\right)^2\right)$$
$$= f(x)f(-x) \pm \frac{eV}{2} \frac{1}{4kT \cosh^2\left(\frac{x}{2kT}\right)} + O\left(\left(\frac{eV}{2}\right)^2\right) \tag{B.8}$$

To first order in V, the current thus writes

$$I = \frac{2e}{h} \frac{\gamma_L \gamma_R}{\gamma_L + \gamma_R} V \frac{1}{\Gamma^+ + \tilde{\Gamma}^-} \left[\Gamma^+ \frac{1}{4kT \cosh^2\left(\frac{\xi + U}{2kT}\right)} + \tilde{\Gamma}^- \frac{1}{4kT \cosh^2\left(\frac{\xi}{2kT}\right)} \right] \tag{B.9}$$

$$= \frac{2e}{h} \frac{\gamma_L \gamma_R}{\gamma_L + \gamma_R} V \frac{1}{f(\xi) + f(-\xi - U)} \left[f(\xi) \frac{1}{4kT \cosh^2\left(\frac{\xi + U}{2kT}\right)} + f(-\xi - U) \frac{1}{4kT \cosh^2\left(\frac{\xi}{2kT}\right)} \right] \tag{B.10}$$

Note that a new definition for γ has been used here in order to make the planck constant appear $\gamma \to \gamma/h$. It now represent a tunnelling rate. On an additional note, it is not possible here to find an exact maximum peak height for the conductance.

Appendix C

Kinetic inductance

In the main text, we basically neglected losses in the superconductor in a microscopic point of view. They were actually introduced artificially as a damping port to the environment in the quantum description or as a resistive lumped element in the classical description. Superconductors are indeed not dissipation-less at AC frequencies. A simple vision of superconductors is the two fluids vision where both superconducting charge carriers (Cooper pairs) and normal charge carriers (quasiparticles excitations) coexist. Under DC excitation, only the superconducting charges contributes to the current, giving a lossless behaviour. To drive an AC current, an AC electric field is applied on the superconductor. While it generates an AC supercurrent, it also accelerates the normal charge carriers which scatter from impurities. This can be model as a complex conductivity $\sigma = \sigma_1 - i\sigma_2$. The superconducting channel behaves as a pure inductance while the dissipative channel is ohmic. This treatment is valid in the limit $\hbar\omega \ll \Delta$ where Δ is the gap of the superconductor. We can also add here that the dissipation is lowered by lowering the temperature as the density of normal charge carriers decreases exponentially $n_n \propto e^{-\Delta/kT}$.
Mattis and Bardeen found an analytical solution of this two fluids vision with the help of the BCS theory [103].

$$\frac{\sigma_1}{\sigma_n} = \frac{2}{\hbar\omega}\int_{\Delta}^{\infty}(f(E) - f(E+\hbar\omega))g(E)dE$$
$$\frac{\sigma_2}{\sigma_n} = \frac{2}{\hbar\omega}\int_{(max(\Delta-\hbar\omega,-\Delta))}^{\infty}(1-2f(E+\hbar\omega))g(E)dE$$

with σ_n the normal state conductivity, $f(E)$ the Fermi-Dirac distribution, Δ the superconductor's gap and

$$g(E) = i\frac{E(E+\hbar\omega)+\Delta^2}{\sqrt{(E+\hbar\omega)^2-\Delta^2}\sqrt{\Delta^2-E^2}}$$

As describe above, the surface impedance of the superconducting film is composed of an inductive and a resistive part. We have $Z_s = R_s + i\omega L_s$, which for a film of thickness d is given by

$$Z_s = \sqrt{\frac{i\mu_0\omega}{\sigma_1 - i\sigma_2}}\coth\left(\frac{d}{\lambda}\sqrt{1+i\frac{\sigma_1}{\sigma_2}}\right)$$

with λ the magnetic penetration depth $\lambda(\omega,T) = \frac{1}{\sqrt{\mu_0\omega\sigma_2}}$. Typically, we have $\sigma_1 \ll \sigma_2$, giving

$$R_s = \mu_0\omega\lambda\frac{\sigma_1}{2\sigma_2}\beta\coth\left(\frac{d}{\lambda}\right)$$
$$L_s = \mu_0\lambda\coth\left(\frac{d}{\lambda}\right)$$

where $\beta = 1 + \frac{2d/\lambda}{\sinh(2d/\lambda)}$ varying from 2 for a very thin film ($d \ll \lambda$) and 1 for bulky material. Therefore, we wee that this kinetic inductance term will add to the geometric inductance term of our transmission line. We have $L_\kappa = g_{CPW}L_s$ with g_{CPW} a factor taking into account the particular geometry of the CPW. Considering our CPW geometry, we can estimate $L_\kappa \approx 8nH.m^{-1}$, corresponding to a variation of 2% to the geometric inductance L_{res}. The treatment made by Watanabe [104] gives $L_\kappa = 7.8nH.m^{-1}$ in good accordance. However, it is not advised to rely on the geometry of the CPW to precisely evaluate the kinetic inductance. It is much more appropriate to measure it from the behaviour of the resonator. We have

$$\omega_0 = \frac{1}{l\sqrt{(L_{res}+L_\kappa)C_{res}}}$$

which relative variation is given by

$$\frac{\delta\omega_0}{\omega_0} = \frac{\alpha\beta}{4}\frac{\delta\sigma_2}{\sigma_2}$$

with $\alpha = L_\kappa/(L_{res} + L_\kappa)$. By integrating we find

$$\frac{\omega_0(T)}{\omega_0(0)} = \left(\frac{\sigma_2(T)}{\pi\Delta(0)/(\hbar\omega)}\right)^{\frac{\alpha\beta}{4}} \tag{C.1}$$

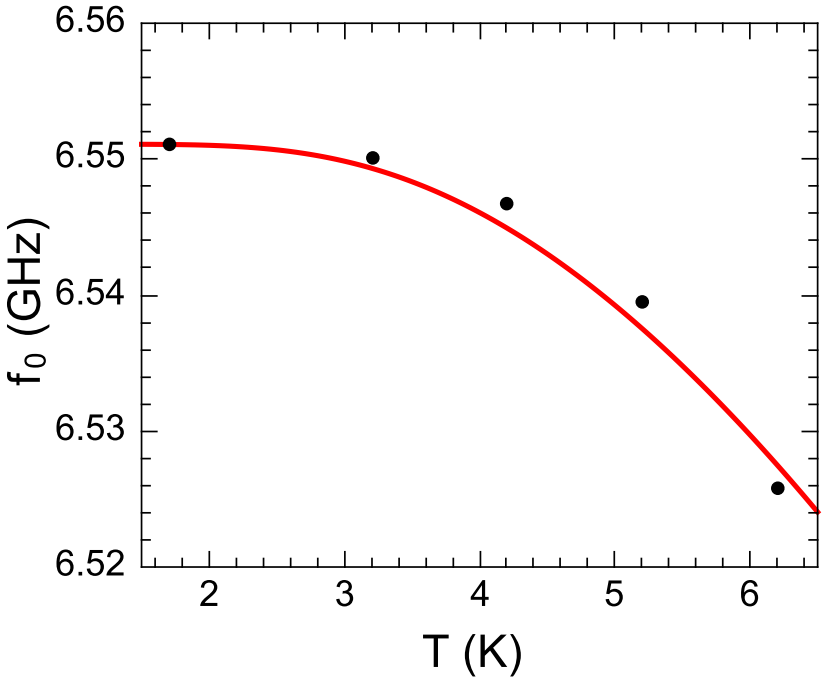

FIGURE C.1: Frequency resonance dependence versus temperature of a typical CPW superconducting on-chip resonator versus. The data (black dots) are well fitted with the Mattis-Bardeen theory (red line) giving $\alpha = 7\%$.

The resonator is made of a thin film of 150 nm of niobium topped with 25 nm of platinum. Platinum is not a superconductor but undergo a superconducting behaviour via proximity effect. Thus we chose $\Delta(0) = 1.4meV$ as it is the value of the superconducting gap of pure niobium. To take into account the presence of platinum, we add its height to the penetration length λ. The remaining two parameters are the normal state conductance σ_n and α. σ_n is bounded between $1/100\mu S.cm^{-1}$ and $1/22\mu S.cm^{-1}$ which are typical value for thin films which height vary from few angströms to bulk respectively (see [105]). In fact, the value of σ_n does not seem to affect the dependence of $\omega_0(T)$ significantly ans is then set to $\sigma_n = 1/22\mu S.cm^{-1}$ which is the bulk limit. As shown in figure C.1, the behaviour of the resonator is well fitted with the Mattis-Bardeen theory, and we find $\alpha = 7\%$, slightly higher than expected from geometric considerations but in

good accordance with usual value [72, 106]. This can be explained by both the imprecision of geometric dimensions during the process of nano fabrication and also the effect of CVD carbon nanotube growth that can alter significantly the physical properties of the film.

Appendix D

Equation of motion

D.1 Different Green Functions

This appendix gives the derivation of formulas (**??**,2.21,2.22,2.24). Due to the hybridization terms $H_{T,L}$ and $H_{T,L}$, the Hamiltonian H is not diagonal and the equations of motion couple $G^R_\sigma(d,t)$ to other Green's functions like

$$G^{kd}_\sigma(t) = -i\theta(t)\left\langle\left\{c_{k\sigma}(t), c^\dagger_{d\sigma}\right\}\right\rangle$$

$$D^d_\sigma(t) = -i\theta(t)\left\langle\left\{n_{d\bar{\sigma}}(t)c_{d\sigma}(t), c^\dagger_{d\sigma}\right\}\right\rangle$$

$$F^{kd}_\sigma(t) = -i\theta(t)\left\langle\left\{n_{d\bar{\sigma}}(t)c_{k\sigma}(t), c^\dagger_{d\sigma}\right\}\right\rangle$$

$$J^{kd}_\sigma(t) = -i\theta(t)\left\langle\left\{c^\dagger_{d\bar{\sigma}}(t)c_{k\bar{\sigma}}(t)c_{d\sigma}(t), c^\dagger_{d\sigma}\right\}\right\rangle$$

and

$$K^{kd}_\sigma(t) = -i\theta(t)\left\langle\left\{c^\dagger_{k\bar{\sigma}}(t)c_{d\bar{\sigma}}(t)c_{d\sigma}(t), c^\dagger_{d\sigma}\right\}\right\rangle$$

with $k \in \nu_{L(R)}$.

D.2 Equations of Motion

The exact equations of motions for G^d_σ, G^{kd}_σ and D^d_σ write

$$(\hbar\omega + i0^+ - \xi_{d\sigma})G^d_\sigma(\omega) = \hbar + UD^{d(\omega)}_\sigma + \sum_{k\in\nu_{L(R)}} t_{k\sigma}G^{kd}_\sigma(\omega),$$

$$(\hbar\omega + i0^+ - \xi_{k\sigma})G^{kd}_\sigma(\omega) = t^*_{k\sigma}G^d_\sigma(\omega)$$

$$(\hbar\omega+i0^+-\xi_{d\sigma}-U)D^d_\sigma(\omega) = \hbar\left\langle n_{d\bar{\sigma}}\right\rangle + \sum_{k\in\nu_{L(R)}} t_{k\sigma}F^{kd}_\sigma(\omega) + \sum_{k\in\nu_{L(R)}} t_{k\bar{\sigma}}J^{kd}_\sigma(\omega) - \sum_{k\in\nu_{L(R)}} t^*_{k\bar{\sigma}}K^{kd}_\sigma(\omega),$$

For $T \gg T_K$, one can neglect Kondo correlations. Then, the equations of motion for F^{kd}_σ, J^{kd}_σ and K^{kd}_σ write

$$(\hbar\omega + i0^+ - \xi_{k\sigma})F^{kd}_\sigma(\omega) = t^*_{k\sigma}D^d_\sigma(\omega)$$

$$(\hbar\omega + i0^+ - \xi_{d\sigma} + \xi_{d\bar{\sigma}} - \xi_{k\bar{\sigma}})J^{kd}_\sigma(\omega) = \sum_{k\in\nu_{L(R)}} t^*_{k\bar{\sigma}}\left[D^d_\sigma(\omega) - f(\xi_{k\bar{\sigma}})G^d_\sigma(\omega)\right],$$

and

$$(\hbar\omega + i0^+ - \xi_{d\sigma} - \xi_{d\bar{\sigma}} + \xi_{k\bar{\sigma}} - U)K^{kd}_\sigma\omega) = \sum_{k\in\nu_{L(R)}} t_{k\bar{\sigma}}\left[f(\xi_{k\bar{\sigma}})G^d_\sigma(\omega) - D^d_\sigma(\omega)\right],$$

D.3 Different Self Energies

Combining the different equations of motion leads to formulas (2.20,2.21,2.22), with self-energy terms

$$\Sigma^0_\sigma(\omega) = \sum_{k\in\nu_{L(R)}} \frac{|t_{k\sigma}|^2}{\hbar\omega - \xi_{k\sigma} + i0^+}$$

and, for $i \in \{1, 2, 3\}$

$$\Sigma^i_{\overline{\sigma}}(\omega) = \sum_{k\in\nu_{L(R)}} \mu_i(\xi_{k\overline{\sigma}})\,|t_{k\overline{\sigma}}|^2\,(\frac{1}{\hbar\omega - \xi_{d\sigma} + \xi_{d\overline{\sigma}} - \xi_{k\overline{\sigma}} + i0^+} + \frac{1}{\hbar\omega - \xi_{d\sigma} - \xi_{d\overline{\sigma}} - U + \xi_{k\overline{\sigma}} + i0^+})$$

Here, one has $\mu_1(\xi) = f(\xi)$, $\mu_2(\xi) = 1 - f(\xi)$ and $\mu_3 = 1$. Using (2.18), the self energies can be expressed using continuous sums as

$$\Sigma^0_\sigma(\omega) = \int_{-\infty}^{+\infty} \frac{d\xi}{2\pi} \frac{\Gamma_\sigma(\xi)}{\hbar\omega - \xi + i0^+}$$

and, for $i \in \{1, 2, 3\}$

$$\Sigma^i_{\overline{\sigma}}(\omega) = \int_{-\infty}^{+\infty} \frac{d\xi}{2\pi} \mu_i(\xi)(\frac{\Gamma_{\overline{\sigma}}(\xi)}{\hbar\omega - \xi_{d\sigma} + \xi_{d\overline{\sigma}} - \xi + i0^+} + \frac{\Gamma_{\overline{\sigma}}(\xi)}{\hbar\omega - \xi_{d\sigma} - \xi_{d\overline{\sigma}} - U + \xi + i0^+})$$

with $\Gamma_\sigma(\xi) = \Gamma_{L\sigma}(\xi) + \Gamma_{R\sigma}(\xi)$. If we eventually assume that $\Gamma_{k\sigma} = \Gamma_\sigma$ is energy independent, we find the expressions of the self energies indicated below Eq. (2.22).

D.4 Lorentzian approximation situation at T=0

The self consistency system between the the conductance and the average occupation of the dot is considered

$$G_\pm = \frac{1 - \langle n_\mp \rangle}{\omega - \epsilon_\pm + i\Gamma/2} + \frac{\langle n_\mp \rangle}{\omega - \epsilon_\pm - U + i\Gamma/2} \tag{D.1}$$

$$\langle n_\pm \rangle = -\frac{1}{\pi} \int_{-\infty}^{+\infty} d\omega f(\omega) \mathrm{Im} G_\pm(\omega) \tag{D.2}$$

Considering T=0, one has

$$\langle n_\pm \rangle = -\frac{1}{\pi} \int_{-\infty}^{0} d\omega \mathrm{Im} G_\pm(\omega) \tag{D.3}$$

and that

$$\int_{-\infty}^{0} d\omega \frac{1}{A^2 + (\omega - \omega_0)^2} = \frac{\pi}{2A} - \frac{1}{A} \arctan\left(\frac{\omega_0}{\omega}\right) \tag{D.4}$$

it gives

$$\langle n_{\pm}\rangle = \frac{1}{\pi}(1-\langle n_{\mp}\rangle)\left[\frac{\pi}{2} - \arctan\left(\frac{2\epsilon_{\pm}}{\Gamma}\right)\right] + \frac{1}{\pi}\langle n_{\mp}\rangle\left[\frac{\pi}{2} - \arctan\left(\frac{2\epsilon_{\pm}+2U}{\Gamma}\right)\right] \quad \text{(D.5)}$$

By defining $\beta_{\pm} = \arctan\left(\frac{2\epsilon_{\pm}}{\Gamma}\right) - \arctan\left(\frac{2\epsilon_{\pm}+2U}{\Gamma}\right)$, one has

$$\begin{cases} \langle n_{+}\rangle - \dfrac{\beta_{+}}{\pi}\langle n_{-}\rangle = \dfrac{1}{2} - \dfrac{1}{\pi}\arctan\left(\dfrac{2\epsilon_{+}}{\Gamma}\right) \\ -\langle n_{+}\rangle\dfrac{\beta_{+}}{\pi} + \langle n_{-}\rangle = \dfrac{1}{2} - \dfrac{1}{\pi}\arctan\left(\dfrac{2\epsilon_{-}}{\Gamma}\right) \end{cases} \quad \text{(D.6)}$$

Finally the system is solved and gives

$$\langle n_{\pm}\rangle = \frac{\frac{1}{2} - \frac{1}{\pi}\arctan\left(\frac{2\epsilon_{\pm}}{\Gamma}\right) + \frac{\beta_{\pm}}{\pi}\left(\frac{1}{2} - \frac{1}{\pi}\arctan\left(\frac{2\epsilon_{\mp}}{\Gamma}\right)\right)}{1 - \frac{\beta_{+}\beta_{-}}{\pi^2}} \quad \text{(D.7)}$$

Appendix E

Lang-Firsov transformation

E.1 Definitions

The following Hamiltonian is considered

$$H = H_0 + H_c \tag{E.1}$$

$$H_0 = \hbar\omega_r a^\dagger a + \sum_{d\sigma} \varepsilon_{d\sigma} c^\dagger_{d\sigma} c_{d\sigma} + H_{int} \tag{E.2}$$

$$H_c = \sum_{d\sigma} \lambda_d (a^\dagger + a) c^\dagger_{d\sigma} c_{d\sigma} \tag{E.3}$$

with d the orbitals of either QDs in the problem. The electron photon couplings λ_d are orbital dependant as the two QDs are at different positions.

E.2 Canonical Lang-Firsov transformation

E.2.1 Definition

Following the transformation found in [107], third edition, page 228, for every operator A, one defines

$$\widetilde{A} = e^S A e^{-S} \tag{E.4}$$

with

$$S = \sum_{d\sigma} \frac{\lambda_d}{\hbar\omega_r} (a^\dagger - a) c^\dagger_{d\sigma} c_{d\sigma} \tag{E.5}$$

By using the following relation

$$\widetilde{O} = O + [S, O] + \frac{1}{2!}[S, [S, O]] + \frac{1}{3!}[S, [S, [S, O]]] + ... \tag{E.6}$$

it is possible to evaluate this transformation.

E.2.2 Boson and electron operators transformation

$[S, a] = \sum_{d\sigma} \frac{\lambda_d}{\hbar\omega_r} c^\dagger_{d\sigma} c_{d\sigma} \left((a^\dagger - a)a - a(a^\dagger - a)\right) = \sum_{d\sigma} \frac{\lambda_d}{\hbar\omega_r} c^\dagger_{d\sigma} c_{d\sigma} \left(a^\dagger a - a a^\dagger\right) = -\frac{1}{\hbar\omega_r} \sum_{d\sigma} \lambda_d c^\dagger_{d\sigma} c_{d\sigma}$

$[S, [S, a]] = 0$

$[S, a^\dagger] = \sum_{d\sigma} \frac{\lambda_d}{\hbar\omega_r} c^\dagger_{d\sigma} c_{d\sigma} \left((a^\dagger - a)a^\dagger - a^\dagger(a^\dagger - a)\right) = \sum_{d\sigma} \frac{\lambda_d}{\hbar\omega_r} c^\dagger_{d\sigma} c_{d\sigma} \left(-a a^\dagger + a^\dagger a\right) = -\frac{1}{\hbar\omega_r} \sum_{d\sigma} \lambda_d c^\dagger_{d\sigma} c_{d\sigma}$

$[S, [S, a^\dagger]] = 0$

$[S, c^\dagger_{d\sigma} c_{d\sigma}] = 0$

where $n_{d\sigma} = \sum_\sigma c^\dagger_{d\sigma} c_{d\sigma}$

$$\widetilde{a} = a - \frac{1}{\hbar\omega_r} \sum_{d\sigma} \lambda_d n_{d\sigma}$$

$$\widetilde{a^\dagger} = a^\dagger - \frac{1}{\hbar\omega_r} \sum_{d\sigma} \lambda_d n_{d\sigma} = \widetilde{a}^\dagger$$

$$\widetilde{n_{d\sigma}} = n_{d\sigma}$$

$[S, c_{d\sigma}] = \frac{1}{\hbar\omega_r}(a^\dagger - a) \sum_{d'\sigma'} \lambda_{d'} \left(c^\dagger_{d\sigma'} c_{d\sigma'} c_{d\sigma} - c_{d\sigma} c^\dagger_{d\sigma'} c_{d\sigma'}\right) = -\frac{\lambda_d}{\hbar\omega_r}(a^\dagger - a)\,(c_{d\sigma})$

$[S, [S, c_{d\sigma}]] = -\frac{\lambda_d}{\hbar\omega_r}(a^\dagger - a)^2 \sum_{d'\sigma'} \frac{\lambda_{d'}}{\hbar\omega_r} \left(c^\dagger_{d\sigma'} c_{d\sigma'} c_{d\sigma} - c_{d\sigma} c^\dagger_{d\sigma'} c_{d\sigma'}\right) = \left(\frac{\lambda_d}{\hbar\omega_r}\right)^2 (a^\dagger - a)^2 c_{d\sigma}$

$[S, [S, [S, c_{d\sigma}]]] = -\left(\frac{\lambda_d}{\hbar\omega_r}\right)^3 (a^\dagger - a)^3 c_{d\sigma}$

$\widetilde{c_{d\sigma}} = c_{d\sigma}(1 - \frac{\lambda_d}{\hbar\omega_r}(a^\dagger - a) + \frac{1}{2!}\left(\frac{\lambda_d}{\hbar\omega_r}\right)^2 (a^\dagger - a)^2 - \frac{1}{3!}\left(\frac{\lambda_d}{\hbar\omega_r}\right)^3 (a^\dagger - a)^3 c_{d\sigma} + ...$

$\widetilde{c_{d\sigma}} = c_{d\sigma} \exp(-\frac{\lambda_d}{\hbar\omega_r}(a^\dagger - a))$

$$\widetilde{c_{d\sigma}} = c_{d\sigma} X \tag{E.7}$$

$$X_d = \exp(-\frac{\lambda_d}{\hbar\omega_r}(a^\dagger - a)) \tag{E.8}$$

$[S, c^\dagger_{d\sigma}] = \frac{1}{\hbar\omega_r}(a^\dagger - a)\sum_{d'\sigma'}\lambda_{d'}\left(c^\dagger_{d\sigma'}c_{d\sigma'}c^\dagger_{d\sigma} - c^\dagger_{d\sigma}c^\dagger_{d\sigma'}c_{d\sigma'}\right) = \frac{\lambda_d}{\hbar\omega_r}(a^\dagger - a)c^\dagger_{d\sigma}$

$[S, [S, c^\dagger_{d\sigma}]] = \frac{\lambda_d}{\hbar\omega_r}(a^\dagger - a)^2\sum_{d'\sigma'}\frac{\lambda_{d'}}{\hbar\omega_r}\left(c^\dagger_{d\sigma'}c_{d\sigma'}c^\dagger_{d\sigma} - c^\dagger_{d\sigma}c^\dagger_{d\sigma'}c_{d\sigma'}\right) = \left(\frac{\lambda_d}{\hbar\omega_r}\right)^2(a^\dagger - a)^2c_{d\sigma}$

$[S, [S, [S, c^\dagger_{d\sigma}]]] = \left(\frac{\lambda_d}{\hbar\omega_r}\right)^3(a^\dagger - a)^3c_{d\sigma}$

$\widetilde{c^\dagger_{d\sigma}} = c^\dagger_{d\sigma}(1 + \frac{\lambda_d}{\hbar\omega_r}(a^\dagger - a) + \frac{1}{2!}\left(\frac{\lambda_d}{\hbar\omega_r}\right)^2(a^\dagger - a)^2 + \frac{1}{3!}\left(\frac{\lambda_d}{\hbar\omega_r}\right)^3(a^\dagger - a)^3c_{d\sigma} + ...$

$\widetilde{c^\dagger_{d\sigma}} = c^\dagger_{d\sigma}\exp(\frac{\lambda_d}{\hbar\omega_r}(a^\dagger - a))$

$X^\dagger_d = \exp(-\frac{\lambda_d}{\hbar\omega_r}(a - a^\dagger)) = \exp(\frac{\lambda_d}{\hbar\omega_r}(a^\dagger - a))$

$$\widetilde{c^\dagger_{d\sigma}} = c^\dagger_{d\sigma}X^\dagger_d \tag{E.9}$$

One can verify that

$$X^\dagger_dX_d = X_dX^\dagger_d = 1$$

E.3 Hamiltonian transformation

$$\widetilde{a} = a - \frac{1}{\hbar\omega_r}\sum_\sigma\lambda_dn_{d\sigma}$$

$$\widetilde{a^\dagger} = a^\dagger - \frac{1}{\hbar\omega_r}\sum_\sigma\lambda_dn_{d\sigma} = \widetilde{a}^\dagger$$

$$\begin{aligned}
\widetilde{H} &= \hbar\omega_r\widetilde{a^\dagger}\widetilde{a} + \sum_{d\sigma}\varepsilon_{d\sigma}\widetilde{c^\dagger_{d\sigma}}\widetilde{c}_{d\sigma} + \widetilde{H_{int}} + \sum_{d\sigma}\lambda_d(\widetilde{a}^\dagger + \widetilde{a})\widetilde{c^\dagger_{d\sigma}}\widetilde{c}_{d\sigma} \\
&= \hbar\omega_r\left(a^\dagger - \frac{1}{\hbar\omega_r}\sum_{d\sigma}\lambda_dn_{d\sigma}\right)\left(a - \frac{1}{\hbar\omega_r}\sum_{d\sigma}\lambda_dn_{d\sigma}\right) \\
&+ \sum_\sigma\varepsilon_{d\sigma}c^\dagger_{d\sigma}c_{d\sigma} + H_{int} + \sum_{d\sigma}\lambda_d(a^\dagger + a - \frac{2}{\hbar\omega_r}\sum_{d'\sigma'}\lambda_{d'}n_{d\sigma'})n_{d\sigma} \\
&= \hbar\omega_ra^\dagger a - \sum_{d\sigma}\lambda_dn_{d\sigma}(a^\dagger + a) + \frac{1}{\hbar\omega_r}\left(\sum_{d\sigma}\lambda_dn_{d\sigma}\right)^2 \\
&+ \sum_\sigma\varepsilon_{d\sigma}c^\dagger_{d\sigma}c_{d\sigma} + H_{int} + \sum_{d\sigma}\lambda_d(a^\dagger + a)n_{d\sigma} - \frac{2}{\hbar\omega_r}\sum_{d\sigma}\lambda_d\sum_{d'\sigma'}\lambda_{d'}n_{d\sigma'}n_{d\sigma} \\
&= \hbar\omega_ra^\dagger a - \frac{1}{\hbar\omega_r}\left(\sum_{d\sigma}\lambda_dn_{d\sigma}\right)^2 + \sum_\sigma\varepsilon_{d\sigma}n_{d\sigma} + H_{int}
\end{aligned}$$

The interesting point here is that $\widetilde{H}$ is diagonal with respect to operators $a^\dagger a$ and $n_{d\sigma}$.

E.4 Transformed operators commutators

$$
\begin{aligned}
[\widetilde{a^\dagger}, \widetilde{a}] &= [a^\dagger - \frac{1}{\hbar\omega_r}\sum_{d\sigma}\lambda_d c^\dagger_{d\sigma}c_{d\sigma}, a - \frac{\lambda}{\hbar\omega_r}\sum_{d\sigma}\lambda_d c^\dagger_{d\sigma}c_{d\sigma}] \\
&= [a^\dagger, a] - \frac{1}{\hbar\omega_r}[a^\dagger, \sum_{d\sigma}\lambda_d c^\dagger_{d\sigma}c_{d\sigma}] - \frac{1}{\hbar\omega_r}[\sum_{d\sigma}\lambda_d c^\dagger_{d\sigma}c_{d\sigma}, a] + \left(\frac{1}{\hbar\omega_r}\right)^2[\sum_{\sigma}\lambda_d c^\dagger_{d\sigma}c_{d\sigma}, \sum_{\sigma}\lambda_d c^\dagger_{d\sigma}c_{d\sigma}] \\
&= -1
\end{aligned}
$$

$$
\{\widetilde{c^\dagger_{d\sigma}}, \widetilde{c_{d\sigma}}\} = \{c^\dagger_{d\sigma}X^\dagger_d, c_{d\sigma}X_d\} = c^\dagger_{d\sigma}X^\dagger_d c_{d\sigma}X_d + c_{d\sigma}X_d c^\dagger_{d\sigma}X^\dagger_d = c^\dagger_{d\sigma}c_{d\sigma}X^\dagger_d X_d + c_{d\sigma}c^\dagger_{d\sigma}X_d X^\dagger_d = c^\dagger_{d\sigma}c_{d\sigma} + c_{d\sigma}c^\dagger_{d\sigma} = 1
$$

Bibliography

[1] Jean-Michel Raimond and Serge Haroche. *Exploring the Quantum*. OUP Oxford, 2006.

[2] C. J. Hood, T. W. Lynn, A. C. Doherty, A. S. Parkins, and H. J. Kimble. The Atom-Cavity Microscope: Single Atoms Bound in Orbit by Single Photons. *Science*, 287(5457):1447–1453, February 2000. ISSN 00368075. doi: 10.1126/science.287.5457.1447. URL http://www.sciencemag.org/cgi/doi/10.1126/science.287.5457.1447.

[3] Jean-Michel Raimond, M. Brune, and S. Haroche. Manipulating quantum entanglement with atoms and photons in a cavity. *Reviews of Modern Physics*, 73(3): 565–582, August 2001. ISSN 0034-6861. doi: 10.1103/RevModPhys.73.565. URL http://rmp.aps.org/abstract/RMP/v73/i3/p565_1.

[4] Alexandre Blais, Ren-Shou Huang, Andreas Wallraff, S. M. Girvin, and R. J. Schoelkopf. Cavity quantum electrodynamics for superconducting electrical circuits: An architecture for quantum computation. *Physical Review A*, 69:062320, June 2004. ISSN 1050-2947. doi: 10.1103/PhysRevA.69.062320. URL http://link.aps.org/doi/10.1103/PhysRevA.69.062320.

[5] Andreas Wallraff, D I Schuster, Alexandre Blais, L. Frunzio, J. Majer, S Kumar, S. M. Girvin, and R. J. Schoelkopf. Strong coupling of a single photon to a superconducting qubit using circuit quantum electrodynamics. *Nature*, 431 (September):0–5, 2004. doi: 10.1038/nature02831.1. URL http://dx.doi.org/10.1038/nature02851.

[6] Max Hofheinz, H Wang, M Ansmann, Radoslaw C. Bialczak, Erik Lucero, Matthew Neeley, Aaron D O'Connell, Daniel Sank, J Wenner, John M. Martinis, and Andrew N Cleland. Synthesizing arbitrary quantum states in a superconducting resonator. *Nature*, 459(7246):546–9, May 2009. ISSN 1476-4687. doi: 10.1038/nature08005. URL http://dx.doi.org/10.1038/nature08005.

[7] J. M. Fink, M. Göppl, M. Baur, R. Bianchetti, P. J. Leek, Alexandre Blais, and Andreas Wallraff. Climbing the Jaynes-Cummings ladder and observing its nonlinearity in a cavity QED system. *Nature*, 454(7202):315–8, July 2008. ISSN 1476-4687. doi: 10.1038/nature07112. URL http://dx.doi.org/10.1038/nature07112.

[8] Daniel Loss and David P. DiVincenzo. Quantum computation with quantum dots. *Physical Review A*, 57(1):120–126, January 1998. ISSN 1050-2947. doi: 10.1103/PhysRevA.57.120. URL http://pra.aps.org/abstract/PRA/v57/i1/p120_1.

[9] Adriano Barenco, Charles Bennett, Richard Cleve, David P. DiVincenzo, Norman Margolus, Peter Shor, Tycho Sleator, John Smolin, and Harald Weinfurter. Elementary gates for quantum computation. *Physical Review A*, 52(5):3457–3467, November 1995. ISSN 1050-2947. doi: 10.1103/PhysRevA.52.3457. URL http://pra.aps.org/abstract/PRA/v52/i5/p3457_1.

[10] Mark A Reed. Quantum Dots. *Scientific American*, (January):118–123, 1993.

[11] Leo P. Kouwenhoven, Charles M. Marcus, Paul L. McEuen, Seigo Tarucha, and M Robert. Electron transport in quantum dots. *Proceedings of the NATO Advanced Study Institute on Mesoscopic Electron Transport*, pages 105–214, 1997.

[12] Tjerk H. Oosterkamp, Leo P. Kouwenhoven, A. Koolen, N. van der Vaart, and C. Harmans. Photon Sidebands of the Ground State and First Excited State of a Quantum Dot. *Physical Review Letters*, 78(8):1536–1539, February 1997. ISSN 0031-9007. doi: 10.1103/PhysRevLett.78.1536. URL http://prl.aps.org/abstract/PRL/v78/i8/p1536_1.

[13] Marc Bockrath, David H. Cobden, Paul L. McEuen, Nasreen G. Chopra, A. Zettl, Andreas Thess, and Richard E. Smalley. Single-Electron Transport in Ropes of Carbon Nanotubes. *Science*, 275(5308):1922–1925, March 1997. ISSN 00368075. doi: 10.1126/science.275.5308.1922. URL http://www.sciencemag.org/cgi/doi/10.1126/science.275.5308.1922.

[14] Nicolas Roch, Serge Florens, Vincent Bouchiat, Wolfgang Wernsdorfer, and Franck Balestro. Quantum phase transition in a single-molecule quantum dot. *Nature*, 453(7195):633–7, May 2008. ISSN 1476-4687. doi: 10.1038/nature06930. URL http://dx.doi.org/10.1038/nature06930.

[15] Audrey Cottet and Takis Kontos. Spin Quantum Bit with Ferromagnetic Contacts for Circuit QED. *Physical Review Letters*, 105:160502, October 2010. ISSN 0031-9007. doi: 10.1103/PhysRevLett.105.160502. URL http://link.aps.org/doi/10.1103/PhysRevLett.105.160502.

[16] W Liang, Marc Bockrath, D Bozovic, J H Hafner, M Tinkham, and H Park. Fabry - Perot interference in a nanotube electron waveguide. *Nature*, 411(6838):665–9, June 2001. ISSN 0028-0836. doi: 10.1038/35079517. URL http://www.nature.com/nature/journal/v411/n6838/full/411665a0.html.

[17] M. Buitelaar, A. Bachtold, T. Nussbaumer, M. Iqbal, and C. Schönenberger. Multiwall Carbon Nanotubes as Quantum Dots. *Physical Review Letters*, 88 (15), March 2002. ISSN 0031-9007. doi: 10.1103/PhysRevLett.88.156801. URL http://prl.aps.org/abstract/PRL/v88/i15/e156801.

[18] David H. Cobden and Jesper Nygå rd. Shell Filling in Closed Single-Wall Carbon Nanotube Quantum Dots. *Physical Review Letters*, 89(4), July 2002. ISSN 0031-9007. doi: 10.1103/PhysRevLett.89.046803. URL http://prl.aps.org/abstract/PRL/v89/i4/e046803.

[19] J. Nygå rd, David H. Cobden, and P.E. Lindelof. Kondo physics in carbon nanotubes. *Nature*, 408(6810):342–6, November 2000. ISSN 0028-0836. doi: 10.1038/35042545. URL http://www.nature.com/nature/journal/v408/n6810/full/408342a0.html.

[20] L. G. Herrmann, F. Portier, P Roche, Alfredo Yeyati, Takis Kontos, and C Strunk. Carbon nanotubes as cooper-pair beam splitters. *Physical review letters*, 104(2): 026801, January 2010. ISSN 1079-7114. URL http://prl.aps.org/abstract/PRL/v104/i2/e026801.

[21] Audrey Cottet, Takis Kontos, and Alfredo Yeyati. Subradiant Split Cooper Pairs. *Physical Review Letters*, 108:166803, April 2012. ISSN 0031-9007. doi: 10.1103/PhysRevLett.108.166803. URL http://prl.aps.org/abstract/PRL/v108/i16/e166803.

[22] Sangeeta Sahoo, Takis Kontos, Jürg Furer, Christian Hoffmann, Matthias Gräber, Audrey Cottet, and Christian Schönenberger. Electric field control of spin transport. *Nature Physics*, 1(2):99–102, October 2005. ISSN 1476-0000. doi: 10.1038/nphys149. URL http://www.nature.com/doifinder/10.1038/nphys149.

[23] Audrey Cottet, Chéryl Feuillet-Palma, and Takis Kontos. Multiterminal spin-dependent transport in ballistic carbon nanotubes. *Physical Review B*, 79:125422, March 2009. ISSN 1098-0121. doi: 10.1103/PhysRevB.79.125422. URL http://link.aps.org/doi/10.1103/PhysRevB.79.125422.

[24] Chéryl Feuillet-Palma, Thomas Delattre, P. Morfin, J.-M. Berroir, G. Fève, D. C. Glattli, B. Plaçais, Audrey Cottet, and Takis Kontos. Conserved spin and orbital phase along carbon nanotubes connected with multiple ferromagnetic

contacts. *Physical Review B*, 81:115414, March 2010. ISSN 1098-0121. doi: 10.1103/PhysRevB.81.115414. URL http://prb.aps.org/abstract/PRB/v81/i11/e115414.

[25] T. Frey, P. J. Leek, M. Beck, Alexandre Blais, Thomas Ihn, Klaus Ensslin, and Andreas Wallraff. Dipole Coupling of a Double Quantum Dot to a Microwave Resonator. *Physical Review Letters*, 108(4), January 2012. ISSN 0031-9007. doi: 10.1103/PhysRevLett.108.046807. URL http://prl.aps.org/abstract/PRL/v108/i4/e046807.

[26] H. Toida, T. Nakajima, and S. Komiyama. Circuit QED using a semiconductor double quantum dot. page 4, June 2012. URL http://arxiv.org/abs/1206.0674.

[27] K. D. Petersson, L. W. McFaul, M. D. Schroer, M. Jung, J. M. Taylor, A. A. Houck, and J. R. Petta. Circuit Quantum Electrodynamics with a Spin Qubit. May 2012. URL http://arxiv.org/abs/1205.6767.

[28] S. Chorley, J. Wabnig, Z. Penfold-Fitch, K. D. Petersson, J. Frake, C G Smith, and M. Buitelaar. Measuring the Complex Admittance of a Carbon Nanotube Double Quantum Dot. *Physical Review Letters*, 108(3), January 2012. ISSN 0031-9007. doi: 10.1103/PhysRevLett.108.036802. URL http://prl.aps.org/abstract/PRL/v108/i3/e036802.

[29] Jens Koch, Terri Yu, JM Gambetta, A. A. Houck, D I Schuster, J. Majer, Alexandre Blais, M. H. Devoret, S. M. Girvin, and R. J. Schoelkopf. Charge-insensitive qubit design derived from the Cooper pair box. *Physical Review A*, 76(4), October 2007. ISSN 1050-2947. doi: 10.1103/PhysRevA.76.042319. URL http://pra.aps.org/abstract/PRA/v76/i4/e042319.

[30] D. V. Averin and K. K. Likharev. Coulomb blockade of single-electron tunneling, and coherent oscillations in small tunnel junctions. *Journal of Low Temperature Physics*, 62(3-4):345–373, February 1986. ISSN 0022-2291. doi: 10.1007/BF00683469. URL http://www.springerlink.com/content/p1u31t7772500061/.

[31] T. Fulton and G. Dolan. Observation of single-electron charging effects in small tunnel junctions. *Physical Review Letters*, 59(1):109–112, July 1987. ISSN 0031-9007. doi: 10.1103/PhysRevLett.59.109. URL http://prl.aps.org/abstract/PRL/v59/i1/p109_1.

[32] M. R. Delbecq, V. Schmitt, F. D. Parmentier, Nicolas Roch, J. J. Viennot, G. Fève, B. Huard, Christophe Mora, Audrey Cottet, and Takis Kontos. Coupling a Quantum Dot, Fermionic Leads, and a Microwave Cavity on a Chip. *Physical Review Letters*, 107(25), December 2011. ISSN 0031-9007. doi: 10.1103/PhysRevLett.107.256804. URL http://prl.aps.org/abstract/PRL/v107/i25/e256804.

[33] Michael Pustilnik and L. I. Glazman. Kondo effect in quantum dots. *Order A Journal On The Theory Of Ordered Sets And Its Applications*, pages 1–27, January 2004. doi: 10.1088/0953-8984/16/16/R01. URL http://arxiv.org/abs/cond-mat/0401517.

[34] R. J. Schoelkopf, P. Wahlgren, A. A. Kozhevnikov, P. Delsing, and D. E. Prober. The Radio-Frequency Single-Electron Transistor (RF-SET): A Fast and Ultrasensitive Electrometer. *Science (New York, N.Y.)*, 280(5367):1238–1242, May 1998. ISSN 00368075. doi: 10.1126/science.280.5367.1238. URL http://www.sciencemag.org/content/280/5367/1238.abstract.

[35] Minchul Lee, Rosa Lopez, Mahn-Soo Choi, Thibaut Jonckheere, and Thierry Martin. Many-body Correlation Effect on Mesoscopic Charge Relaxation. page 5, January 2011. URL http://arxiv.org/abs/1101.0468.

[36] J. Majer, JM Chow, JM Gambetta, Jens Koch, B R Johnson, J A Schreier, L Frunzio, D I Schuster, A. A. Houck, Andreas Wallraff, Alexandre Blais, M. H. Devoret, S. M. Girvin, and R. J. Schoelkopf. Coupling superconducting qubits via a cavity bus. *Nature*, 449(7161):443–7, September 2007. ISSN 1476-4687. doi: 10.1038/nature06184. URL http://dx.doi.org/10.1038/nature06184.

[37] M. H. Devoret and John M. Martinis. Implementing Qubits with Superconducting Integrated Circuits. *Quantum Information Processing*, 3(1-5):163–203, October 2004. ISSN 1570-0755. doi: 10.1007/s11128-004-3101-5. URL http://dl.acm.org/citation.cfm?id=1032132.1032143.

[38] Seigo Tarucha, D. Austing, T. Honda, R. van der Hage, and Leo P. Kouwenhoven. Shell Filling and Spin Effects in a Few Electron Quantum Dot. *Physical Review Letters*, 77(17):3613–3616, October 1996. ISSN 0031-9007. doi: 10.1103/PhysRevLett.77.3613. URL http://prl.aps.org/abstract/PRL/v77/i17/p3613_1.

[39] B. van Wees, Leo P. Kouwenhoven, C. Harmans, J. Williamson, C. Timmering, M. Broekaart, C. Foxon, and J. Harris. Observation of zero-dimensional states in a one-dimensional electron interferometer. *Physical Review Letters*, 62(21):2523–2526, May 1989. ISSN 0031-9007. doi: 10.1103/PhysRevLett.62.2523. URL http://prl.aps.org/abstract/PRL/v62/i21/p2523_1.

[40] David Goldhaber-Gordon, Hadas Shtrikman, D. Mahalu, David Abusch-Magder, U. Meirav, and M. A. Kastner. Kondo effect in a single-electron transistor. *Nature*, 391(6663):156–159, January 1998. ISSN 0028-0836. doi: 10.1038/34373. URL http://dx.doi.org/10.1038/34373.

[41] Bertrand Reulet, Michel Ramin, Hélène Bouchiat, and Dominique Mailly. Dynamic Response of Isolated Aharonov-Bohm Rings Coupled to an Electromagnetic Resonator. *Physical Review Letters*, 75(1):124–127, July 1995. ISSN 0031-9007. doi: 10.1103/PhysRevLett.75.124. URL http://prl.aps.org/abstract/PRL/v75/i1/p124_1.

[42] L. C. Venema. Imaging Electron Wave Functions of Quantized Energy Levels in Carbon Nanotubes. *Science (New York, N.Y.)*, 283(5398):52–55, January 1999. ISSN 00368075. doi: 10.1126/science.283.5398.52. URL http://www.sciencemag.org/content/283/5398/52.abstract.

[43] Sean Washburn and Richard A. Webb. Aharonov-Bohm effect in normal metal quantum coherence and transport. *Advances in Physics*, 35(4):375–422, January 1986. ISSN 0001-8732. doi: 10.1080/00018738600101921. URL http://dx.doi.org/10.1080/00018738600101921.

[44] Yu. V. Nazarov and Yarosav M. Blanter. *Quantum Transport : introduction to nanoscience*. Cambridge University Press, 2009.

[45] Vincent Bouchiat, D. Vion, P. Joyez, D. Esteve, and M. H. Devoret. Quantum Coherence with a Single Cooper Pair. *Physica Scripta*, T76(1):165, 1998. ISSN 0031-8949. doi: 10.1238/Physica.Topical.076a00165. URL http://stacks.iop.org/1402-4896/1998/i=T76/a=024.

[46] Pablo Jarillo-Herrero, Jing Kong, Herre S J van der Zant, Cees Dekker, Leo P. Kouwenhoven, and Silvano De Franceschi. Orbital Kondo effect in carbon nanotubes. *Nature*, 434(7032):484–8, March 2005. ISSN 1476-4687. doi: 10.1038/nature03422. URL http://dx.doi.org/10.1038/nature03422.

[47] Michael J Biercuk, Shahal Ilani, Charles M. Marcus, and Paul L. McEuen. Electrical Transport in single-Wall Carbon Nanotubes. *Topic in Applied physics*, 111: 455–493, 2008. doi: 10.1007/978-3-540-72865-8_15. URL http://marcuslab.harvard.edu/papers/Biercuk_Topics_Review_2008.pdf.

[48] M. Stopa. Coulomb oscillation amplitudes and semiconductor quantum-dot self-consistent level structure. *Physical Review B*, 48(24):18340–18343, December 1993. ISSN 0163-1829. doi: 10.1103/PhysRevB.48.18340. URL http://prb.aps.org/abstract/PRB/v48/i24/p18340_1.

[49] M. Stopa. Quantum dot self-consistent electronic structure and the Coulomb blockade. *Physical Review B*, 54(19):13767–13783, November 1996. ISSN 0163-1829. doi: 10.1103/PhysRevB.54.13767. URL http://prb.aps.org/abstract/PRB/v54/i19/p13767_1.

[50] Dejan Jovanovic and Jean-Pierre Leburton. Self-consistent analysis of single-electron charging effects in quantum-dot nanostructures. *Physical Review B*, 49 (11):7474–7483, March 1994. ISSN 0163-1829. doi: 10.1103/PhysRevB.49.7474. URL http://prb.aps.org/abstract/PRB/v49/i11/p7474_1.

[51] M. Büttiker, A. Prêtre, and H. Thomas. Dynamic conductance and the scattering matrix of small conductors. *Physical Review Letters*, 70(26):4114–4117, June 1993. ISSN 0031-9007. doi: 10.1103/PhysRevLett.70.4114. URL http://prl.aps.org/abstract/PRL/v70/i26/p4114_1.

[52] A. Prêtre, H. Thomas, and M. Büttiker. Dynamic admittance of mesoscopic conductors: Discrete-potential model. *Physical Review B*, 54(11):8130–8143, September 1996. ISSN 0163-1829. doi: 10.1103/PhysRevB.54.8130. URL http://prb.aps.org/abstract/PRB/v54/i11/p8130_1.

[53] YA M Blanter and Markus Büttiker. Shot Noise in Mesoscopic Conductors. *Physics Reports*, 336(1-2):1–166, 1999. URL http://arxiv.org/abs/cond-mat/9910158.

[54] Paul L. McEuen, Marc Bockrath, David H. Cobden, Young-Gui Yoon, and Steven Louie. Disorder, Pseudospins, and Backscattering in Carbon Nanotubes. *Physical Review Letters*, 83(24):5098–5101, December 1999. ISSN 0031-9007. doi: 10.1103/PhysRevLett.83.5098. URL http://prl.aps.org/abstract/PRL/v83/i24/p5098_1.

[55] P. Anderson. Localized Magnetic States in Metals. *Physical Review*, 124(1):41–53, October 1961. ISSN 0031-899X. doi: 10.1103/PhysRev.124.41. URL http://prola.aps.org/abstract/PR/v124/i1/p41_1.

[56] Yigal Meir and Ned S Wingreen. Landauer formula for the current through an interacting electron region. *Physical Review Letters*, 68(16):2512–2515, April 1992. ISSN 0031-9007. doi: 10.1103/PhysRevLett.68.2512. URL http://link.aps.org/doi/10.1103/PhysRevLett.68.2512.

[57] W.J. de Haas, J. de Boer, and G.J. van dën Berg. The electrical resistance of gold, copper and lead at low temperatures. *Physica*, 1(7-12):1115–1124, May 1934. ISSN 00318914. doi: 10.1016/S0031-8914(34)80310-2. URL http://dx.doi.org/10.1016/S0031-8914(34)80310-2.

[58] Jun Kondo. Resistance Minimum in Dilute Magnetic Alloys. *Progress of Theoretical Physics*, 32(1):37–49, July 1964. ISSN 0033-068X. doi: 10.1143/PTP.32.37. URL http://ptp.ipap.jp/link?PTP/32/37/.

[59] J. P. Franck, F. D. Manchester, and D. L. Martin. The Specific Heat of Pure Copper and of Some Dilute Copper+Iron Alloys Showing a Minimum in the Electrical Resistance at Low Temperatures. *Proceedings of the royal society*, 263(1315):494–507, October 1961. ISSN 1364-5021. doi: 10.1098/rspa.1961.0176. URL http://rspa.royalsocietypublishing.org/cgi/doi/10.1098/rspa.1961.0176.

[60] KG Wilson. Renormalization Group - Critical Phenomena And Kondo Problem. *Reviews Of Modern Physics*, 47(4):773 – 840, 1975. URL http://www.citeulike.org/user/alexcabuz/article/6349859.

[61] M. Grobis, I. Rau, R. Potok, Hadas Shtrikman, and David Goldhaber-Gordon. Universal Scaling in Nonequilibrium Transport through a Single Channel Kondo Dot. *Physical Review Letters*, 100(24), June 2008. ISSN 0031-9007. doi: 10.1103/PhysRevLett.100.246601. URL http://prl.aps.org/abstract/PRL/v100/i24/e246601.

[62] Leo P. Kouwenhoven and L. I. Glazman. Revival of the Kondo effect. *Physics world*, pages 33–38, 2001.

[63] HC Manoharan, CP Lutz, and DM Eigler. Quantum mirages formed by coherent projection of electronic structure. *Nature*, 403(6769):512–5, February 2000. ISSN 1476-4687. doi: 10.1038/35000508. URL http://dx.doi.org/10.1038/35000508.

[64] A C Hewson. *The Kondo Problem to Heavy Fermions*. Cambridge University Press, 1997.

[65] Tai-Kai Ng. ac Response in the Nonequilibrium Anderson Impurity Model. *Physical Review Letters*, 76(3):487–490, January 1996. ISSN 0031-9007. doi: 10.1103/PhysRevLett.76.487. URL http://link.aps.org/doi/10.1103/PhysRevLett.76.487.

[66] Andrei Kogan, Sami Amasha, and M. A. Kastner. Photon-induced Kondo satellites in a single-electron transistor. *Science (New York, N.Y.)*, 304(5675):1293–5, May 2004. ISSN 1095-9203. doi: 10.1126/science.1096377. URL http://www.sciencemag.org/content/304/5675/1293.long.

[67] Christian Latta, F. Haupt, M. Hanl, Andreas Weichselbaum, M. Claassen, Wolf Wuester, Parisa Fallahi, Stefan Faelt, L. I. Glazman, J. von Delft, H. E. Türeci, and

Atac Imamoglu. Quantum quench of Kondo correlations in optical absorption. *Nature*, 474(7353):627–630, June 2011. ISSN 0028-0836. doi: 10.1038/nature10204. URL http://dx.doi.org/10.1038/nature10204.

[68] J. Basset, A. Kasumov, C. Moca, G. Zaránd, P. Simon, H. Bouchiat, and R. Deblock. Measurement of Quantum Noise in a Carbon Nanotube Quantum Dot in the Kondo Regime. *Physical Review Letters*, 108(4), January 2012. ISSN 0031-9007. doi: 10.1103/PhysRevLett.108.046802. URL http://prl.aps.org/abstract/PRL/v108/i4/e046802.

[69] Rainee Simons. *Coplanar waveguide circuits, components and systems*. John wiley & Sons, 2001.

[70] David M. Pozar. *Microwave engineering*. John Wiley and Sons, 2005.

[71] A. A. Clerk, S. M. Girvin, Florian Marquardt, and R. J. Schoelkopf. Introduction to quantum noise, measurement, and amplification. *Reviews of Modern Physics*, 82(2):1155–1208, April 2010. ISSN 0034-6861. doi: 10.1103/RevModPhys.82.1155. URL http://link.aps.org/doi/10.1103/RevModPhys.82.1155.

[72] Agustín Palacios-laloy. *Superconducting qubit in a resonator : test of the Leggett-Garg inequality and single-shot readout*. PhD thesis, 2010.

[73] Yarosav M. Blanter, F. Hekking, and M. Büttiker. Interaction Constants and Dynamic Conductance of a Gated Wire. *Physical Review Letters*, 81(9):1925–1928, August 1998. ISSN 0031-9007. doi: 10.1103/PhysRevLett.81.1925. URL http://prl.aps.org/abstract/PRL/v81/i9/p1925_1.

[74] Marc Bockrath, David H. Cobden, Jia Lu, Andrew G. Rinzler, Richard E. Smalley, Leon Balents, and Paul L. McEuen. Luttinger-liquid behaviour in carbon nanotubes. *Nature*, 397(6720):598–601, February 1999. ISSN 0028-0836. doi: 10.1038/17569. URL http://dx.doi.org/10.1038/17569.

[75] Yigal Meir, Ned S Wingreen, and P. J. Leek. Transport through a Strongly Interacting Electron System: Theory of Periodic Conductance Oscillations. *Physical Review*, 66(23):3048–3051, 1991. doi: 10.1103/PhysRevLett.66.3048. URL http://prl.aps.org/abstract/PRL/v66/i23/p3048_1.

[76] Raphaël Van Roermund, Shiue-yuan Shiau, and Mireille Lavagna. Anderson model out of equilibrium: Decoherence effects in transport through a quantum dot. *Physical Review B*, 81(16):165115, April 2010. ISSN 1098-0121. doi: 10.1103/PhysRevB.81.165115. URL http://link.aps.org/doi/10.1103/PhysRevB.81.165115.

[77] A Megrant, C Neill, R Barends, B Chiaro, Yu Chen, L Feigl, J Kelly, Erik Lucero, Matteo Mariantoni, P J J O Malley, Daniel Sank, A Vainsencher, J Wenner, T C White, Y Yin, J Zhao, C J Palmstrø m, and John M. Martinis. Planar superconducting resonators with internal quality factors above one million. *Applied Physics Letters*, 113510:11–14, 2012.

[78] M. Goppl, A Fragner, M. Baur, R. Bianchetti, S. Filipp, J. M. Fink, P. J. Leek, G Puebla, L. Steffen, and Andreas Wallraff. Coplanar waveguide resonators for circuit quantum electrodynamics. *Journal of Applied Physics*, 104(11):113904, 2008. ISSN 0021-8979. doi: 10.1063/1.3010859. URL http://dx.doi.org/10.1063/1.3010859.

[79] Sumio Iijima. Helical microtubules of graphitic carbon. *Nature*, 354:56–58, 1991. doi: 10.1038/354056a0. URL http://www.nature.com/nature/journal/v354/n6348/abs/354056a0.html.

[80] Axel Thielmann, Matthias Hettler, Jürgen König, and Gerd Schön. Super-Poissonian noise, negative differential conductance, and relaxation effects in transport through molecules, quantum dots, and nanotubes. *Physical Review B*, 71 (4), January 2005. ISSN 1098-0121. doi: 10.1103/PhysRevB.71.045341. URL http://prb.aps.org/abstract/PRB/v71/i4/e045341.

[81] A. Makarovski, A. Zhukov, J. Liu, and G. Finkelstein. SU(2) and SU(4) Kondo effects in carbon nanotube quantum dots. *Physical Review B*, 75(24):4–7, June 2007. ISSN 1098-0121. doi: 10.1103/PhysRevB.75.241407. URL http://link.aps.org/doi/10.1103/PhysRevB.75.241407.

[82] J Gabelli, G Fève, J-M Berroir, B Plaçais, A Cavanna, B Etienne, Y Jin, and D C Glattli. Violation of Kirchhoff's laws for a coherent RC circuit. *Science (New York, N.Y.)*, 313(5786):499–502, July 2006. ISSN 1095-9203. doi: 10.1126/science.1126940. URL http://www.sciencemag.org/content/313/5786/499.long.

[83] András Pályi and Guido Burkard. Disorder-Mediated Electron Valley Resonance in Carbon Nanotube Quantum Dots. *Physical Review Letters*, 106(8), February 2011. ISSN 0031-9007. doi: 10.1103/PhysRevLett.106.086801. URL http://prl.aps.org/abstract/PRL/v106/i8/e086801.

[84] Jens Koch, Felix von Oppen, and A. Andreev. Theory of the Franck-Condon blockade regime. *Physical Review B*, 74(20), November 2006. ISSN 1098-0121. doi: 10.1103/PhysRevB.74.205438. URL http://prb.aps.org/abstract/PRB/v74/i20/e205438.

[85] Renaud Leturcq, Christoph Stampfer, Kevin Inderbitzin, Lukas Durrer, Christofer Hierold, Eros Mariani, Maximilian G. Schultz, Felix von Oppen, and Klaus Ensslin. FranckCondon blockade in suspended carbon nanotube quantum dots. *Nature Physics*, 5(5):327–331, April 2009. ISSN 1745-2473. doi: 10.1038/nphys1234. URL http://dx.doi.org/10.1038/nphys1234.

[86] M. Delbecq. Coupling a Quantum Dot, Fermionic Leads, and a Microwave Cavity on a Chip. *Physical Review Letters*, 107(25), 2011. doi: 10.1103/PhysRevLett.107.256804. URL http://prl.aps.org/abstract/PRL/v107/i25/e256804.

[87] Y. Nishikawa, D. Crow, and A C Hewson. Renormalized parameters and perturbation theory for an n-channel Anderson model with Hunds rule coupling: Symmetric case. *Physical Review B*, 82(11):1–13, September 2010. ISSN 1098-0121. doi: 10.1103/PhysRevB.82.115123. URL http://link.aps.org/doi/10.1103/PhysRevB.82.115123.

[88] Thomas Delattre, Chéryl Feuillet-Palma, L. G. Herrmann, P Morfin, J.-M. Berroir, G. Fève, B. Plaçais, D. C. Glattli, Mahn-Soo Choi, Christophe Mora, and Takis Kontos. Noisy Kondo impurities. *Nature Physics*, 5(3):208–212, January 2009. ISSN 1745-2473. doi: 10.1038/nphys1186. URL http://www.nature.com/doifinder/10.1038/nphys1186.

[89] D I Schuster, Andreas Wallraff, Alexandre Blais, L. Frunzio, R.-S. Huang, J. Majer, S. M. Girvin, and R. J. Schoelkopf. ac Stark Shift and Dephasing of a Superconducting Qubit Strongly Coupled to a Cavity Field. *Physical Review Letters*, 94 (12), March 2005. ISSN 0031-9007. doi: 10.1103/PhysRevLett.94.123602. URL http://prl.aps.org/abstract/PRL/v94/i12/e123602.

[90] J. R. Petta, a C Johnson, J M Taylor, E a Laird, Amir Yacoby, M D Lukin, Charles M. Marcus, M P Hanson, and A. Gossard. Coherent manipulation of coupled electron spins in semiconductor quantum dots. *Science (New York, N.Y.)*, 309 (5744):2180–4, September 2005. ISSN 1095-9203. doi: 10.1126/science.1116955. URL http://www.sciencemag.org/content/309/5744/2180.long.

[91] Sylvain Hermelin, Shintaro Takada, Michihisa Yamamoto, Seigo Tarucha, Andreas D Wieck, Laurent Saminadayar, Christopher Bäuerle, and Tristan Meunier. Electrons surfing on a sound wave as a platform for quantum optics with flying electrons. *Nature*, 477(7365):435–8, September 2011. ISSN 1476-4687. doi: 10.1038/nature10416. URL http://dx.doi.org/10.1038/nature10416.

[92] R P G McNeil, M Kataoka, C J B Ford, C H W Barnes, D Anderson, G A C Jones, I Farrer, and D A Ritchie. On-demand single-electron transfer between distant

quantum dots. *Nature*, 477(7365):439–42, September 2011. ISSN 1476-4687. doi: 10.1038/nature10444. URL http://dx.doi.org/10.1038/nature10444.

[93] Mircea Trif, Vitaly N. Golovach, and Daniel Loss. Spin dynamics in InAs nanowire quantum dots coupled to a transmission line. *Physical Review B*, 77(4), January 2008. ISSN 1098-0121. doi: 10.1103/PhysRevB.77.045434. URL http://prb.aps.org/abstract/PRB/v77/i4/e045434.

[94] Wilfred G. van der Wiel, Silvano De Franceschi, Jeroen M. Elzerman, T. Fujisawa, Seigo Tarucha, and Leo P. Kouwenhoven. Electron transport through double quantum dots. *Reviews of Modern Physics*, 75(1):1–22, December 2002. ISSN 0034-6861. doi: 10.1103/RevModPhys.75.1. URL http://rmp.aps.org/abstract/RMP/v75/i1/p1_1.

[95] Jürgen König. *Quantum Fluctuations in the Single-ElectronTransistor*. PhD thesis, 1998.

[96] Guido Burkard and Atac Imamoglu. Ultra-long-distance interaction between spin qubits. *Physical Review B*, 74(4), July 2006. ISSN 1098-0121. doi: 10.1103/PhysRevB.74.041307. URL http://prb.aps.org/abstract/PRB/v74/i4/e041307.

[97] S Nadj-Perge, S. M. Frolov, E P A M Bakkers, and Leo P. Kouwenhoven. Spin-orbit qubit in a semiconductor nanowire. *Nature*, 468(7327):1084–7, December 2010. ISSN 1476-4687. doi: 10.1038/nature09682. URL http://dx.doi.org/10.1038/nature09682.

[98] Gert-Ludwig Ingold and Yu. V. Nazarov. Charge Tunneling Rates in Ultrasmall Junctions. In Grabert H. and Devoret M. H., editors, *"Single Charge Tunneling" NATO ASI Series B, Vol. 294*, pages 21–107. Plenum Press, New York, August 1992. URL http://arxiv.org/abs/cond-mat/0508728.

[99] F. D. Parmentier, A. Anthore, S. Jezouin, H. le Sueur, U. Gennser, A. Cavanna, D. Mailly, and F. Pierre. Strong back-action of a linear circuit on a single electronic quantum channel. *Nature Physics*, 7(12):935–938, September 2011. ISSN 1745-2473. doi: 10.1038/nphys2092. URL http://dx.doi.org/10.1038/nphys2092.

[100] L Hofstetter, S Csonka, J. Nygå rd, and Christian Schönenberger. Cooper pair splitter realized in a two-quantum-dot Y-junction. *Nature*, 461(7266):960–3, October 2009. ISSN 1476-4687. doi: 10.1038/nature08432. URL http://dx.doi.org/10.1038/nature08432.

[101] V. Mourik, K. Zuo, S. M. Frolov, S. R. Plissard, E. P. A. M. Bakkers, and A. A. Kozhevnikov. Signatures of Majorana Fermions in Hybrid Superconductor-Semiconductor Nanowire Devices. *Science*, 336(6084):1003–1007, April 2012. ISSN 0036-8075. doi: 10.1126/science.1222360. URL http://www.sciencemag.org/content/336/6084/1003.abstract.

[102] Mircea Trif and Yaroslav Tserkovnyak. Resonantly Tunable Majorana Polariton in a Microwave Cavity. page 11, February 2012. URL http://arxiv.org/abs/1202.2649.

[103] D. Mattis and J. Bardeen. Theory of the Anomalous Skin Effect in Normal and Superconducting Metals. *Physical Review*, 111(2):412–417, July 1958. ISSN 0031-899X. doi: 10.1103/PhysRev.111.412. URL http://prola.aps.org/abstract/PR/v111/i2/p412_1.

[104] Koki Watanabe, Keiji Yoshida, Takeshi Aoki, and Satoshi Kohjiro. Kinetic Inductance of Superconducting Coplanar Waveguides. *Japanese Journal of Applied Physics*, 33(Part 1, No. 10):5708–5712, October 1994. ISSN 00214922. doi: 10.1143/JJAP.33.5708. URL http://jjap.jsap.jp/link?JJAP/33/5708/.

[105] Takis Kontos. *Coherence et interférences quantiques dans des nanostructures supraconducteur/ferromagnetique*. PhD thesis, 2002.

[106] Rami Barends. *Photon-detecting superconducting resonators*. PhD thesis, 2009.

[107] Gerald D. Mahan. *Many particles physics*. 2000.